Ultrafast nonlinear acoustics in crystals and nanostructures

Universiteit Utrecht

Atom Optics and Ultrafast Dynamics,
Debye Instituut,
Departement Natuur- en Sterrenkunde,
Faculteit Bètawetenschappen,
Universiteit Utrecht

FOM

NWO
Nederlandse Organisatie voor Wetenschappelijk Onderzoek

Dit werk maakt deel uit van het onderzoekprogramma van de Stichting voor Fundamenteel Onderzoek der Materie (FOM), die financieel wordt gesteund door de Nederlandse Organisatie voor Wetenschappelijk Onderzoek (NWO)

ISBN 978-90-393-4881-9

Printed by PrintPartners Ipskamp B.V., Enschede, 2008

Ultrafast nonlinear acoustics in crystals and nanostructures

Ultrasnelle, niet-lineaire akoestiek in kristallen en nanostructuren

met een samenvatting in het Nederlands

PROEFSCHRIFT

ter verkrijging van de graad van doctor aan de Universiteit Utrecht, op gezag van de rector magnificus, prof.dr. J.C. Stoof, ingevolge het besluit van het college voor promoties in het openbaar te verdedigen op

woensdag 17 september 2008
des middags te 12.45 uur

door

Petrus Jacobus Stephanus van Capel

geboren op 24 maart 1978
te Noorden

Promotor: Prof.dr. J.I. Dijkhuis

"Drench yourself in words unspoken
Live your life with arms wide open
Today is where your book begins
The rest is still unwritten"

(Natasha Bedingfield,
Unwritten)

Voor mijn ouders
en grootouders

Contents

Chapter I

Introduction

Abstract

This introductory chapter serves as a background to the research presented in the following chapters, and to familiarize the reader with the field of physics and time and length scales that are involved. We show that coherent acoustics has long been a characterization method for solid state structures complementary to optical and electronic techniques; this applies both to continuous-wave and ultrashort, pulsed techniques. Furthermore, the recent developments in ultrafast acoustics are opening a window to *ultrafast nanophononics*, where high-frequency phonons are employed to manipulate nanometer-sized structures on a picosecond timescale.

I.1 Modern condensed matter physics: from bulk to nano

Classical experimental condensed matter has been concerned with understanding the properties of bulk crystalline systems present in nature [1]. During the explosive growth of the semiconductor industry from the 1970's on [2], and nanofabrication revolutions in the following decades [3], new, effectively lower-dimensional structures became available that show qualitatively different behavior compared to their bulk counterparts. Typical examples include (multi-)layered heterostructures (2D, Ch. VI), nanowires (1D, Ch. IX), and nanoparticles (0D) as elementary constituents, assembled in larger structures or devices. Here, the properties are dominated by quantum size effects, interface and boundary conditions or effects of the environment. An example of application is the giant magnetoresistance effect (important for hard-disk writing), the discovery of which was awarded the 2007 Nobel Prize in Physics [4, 5].

Parallel to the developments in deposition and growth techniques, spectros-

copy methods became available to study and understand the typical features of these structures. Apart from optical spectroscopy and microscopy, typical non-destructive testing techniques include atomic force microscopy (AFM) [6] and scanning electron microscopy (SEM) [7], both capable of supplying subnanometer structural information.

I.2 Ultrafast optics

If one chooses to examine dynamical rather than statical properties, i.e. reach high *temporal* rather than lateral resolution, the most convenient tools are pulsed laser-based techniques. Already several years after the development of the first laser, Q-switching by means of saturable absorbers allowed the generation of microsecond pulses in ruby and Nd-glass lasers [8]. In the 1970's, operation in the ultrafast ($<$ 10 ps) range became possible in dye lasers by applying active mode-locking techniques [9]. Time-resolved experiments at the subpicosecond timescale, and at much higher repetition rates (typically 80 MHz), became possible in the 1980's by the development of pulsed Ti-sapphire infrared laser systems. The Ti:sapphire laser also intensified a class of ultrafast experiments, usually denoted as *pump-probe spectroscopy*: a 'pump' pulse induces an effect in a material, and a delayed 'probe' measures the response and relaxation of the material at later times. Important advantages of this technique are the extreme time resolution, and the nondestructive and noncontact nature. Examples of pump-probe experiments presented in this thesis are sketched in Fig. I.1 a).

At present, through high-harmonic generation, the limits of ultrafast spectroscopy are pushed into the attosecond timescale, where it becomes possible to even probe electronic motion in condensed matter [10, 11, 12]. The Ti:sapphire-based systems have also evolved. On the one side, there is a push for ever higher pulse amplitudes at low repetition rates, by means of multi-step chirped pulse amplification [13]. Most experiments presented in this thesis made use of the "Hurricane", a single step amplified Ti-sapphire laser system, typically producing 100-femtosecond pulses at a 1-kHz repetition rate, with around 500 μJ output energy per pulse: 50,000 times higher than the powers available in usual 80-MHz experiments. On the other side, there are efforts to increase the pulse repetition rate at moderate power levels; the current 'record' reaching up to 6 GHz [14].

I.3 Ultrafast acoustics

It is instructive to follow the same path as we did for (ultrafast) lasers, when we sketch the development of coherent acoustics in solids.

Monochromatic phonon sources The first experiments with coherent CW phonon generation and detection by means of piezoelectric transducers and superconducting bolometers or tunnel junctions, respectively, were performed in the last century, extending from the MHz range [15], ultimately to 10 - 100 GHz [16, 17]. A dozen years later, research on the well-known electronic two-level system in ruby allowed optical generation of 870 GHz phonons [18]. Attempts have been made to develop this system into a single-frequency phonon laser (SASER) [19, 20, 21]. More recent efforts to generate monochromatic coherent phonons in the hundreds of gigahertz range were made by laser beam interference [22], and by using semiconductor multilayer structures, causing a zone-folding of the acoustic phonon branch [23, 24, 25, 26, 27]. The piezoelectric technique using microscale metallic transducers has recently been used to generate MHz frequency surface acoustic waves ($\sim \mu$m wavelengths) [28].

Generation and detection of pulsed phonon sources Pulsed phonon generation by electrical means is already as old as the first pulsed laser sources [29]. The research, where pressure pulses are generated on one side of a bulk crystal, and detected at the other side by bolometers, has been used very successfully in investigating ultrasound propagation, crystal anisotropy effects, and phonon focusing [30].

The development of the Ti:sapphire laser opened the way to generate and detect picosecond longitudinal acoustic pulses. This principle was first demonstrated and theoretically analyzed for metal films and semiconductors [31, 32, 33]. We have sketched the principle of this technique, that is nowadays referred to as *picosecond ultrasonics* [34] in Fig. I.1 a). A short laser pulse heats a thin transducer material, and through the thermoelastic effect (the heated material applies a stress to its surroundings), a coherent strain pulse is formed. This acoustic wave travels into the film, is partly reflected at the metal/substrate interface, and returns to the surface. By sending a delayed detection 'probe' pulse to the film surface, one can observe the change in optical properties, and the corresponding change in reflec-

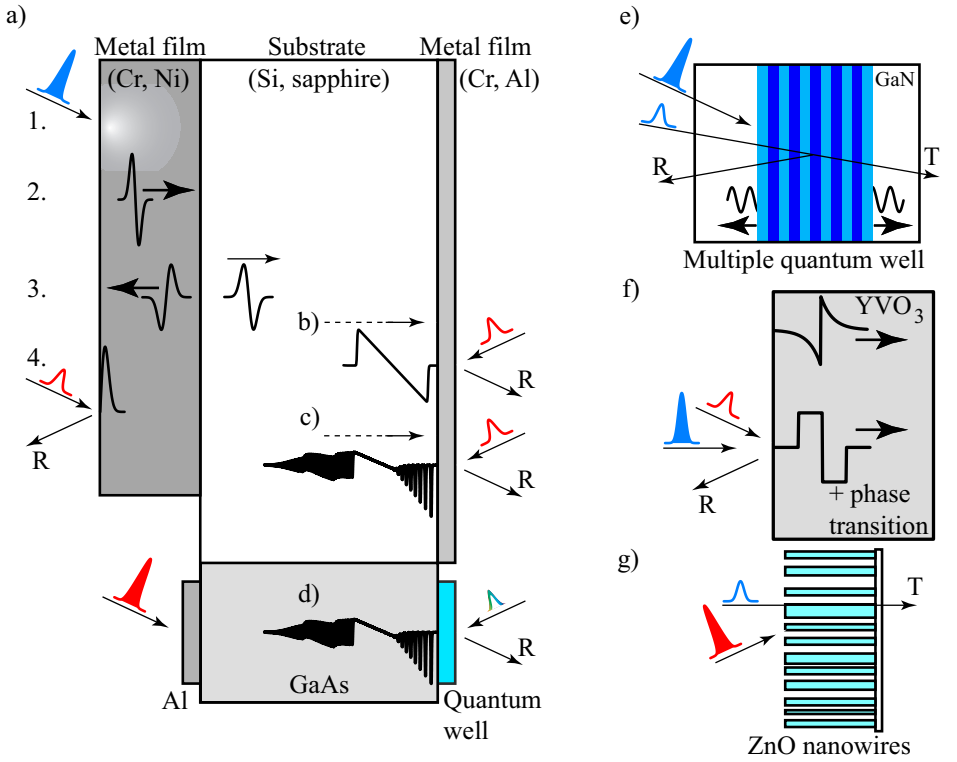

Figure I.1: Ultrafast pump-probe experiments in this thesis in a nutshell (Color figure: Fig. 1, p. 202)

a) Picosecond ultrasonics technique (Chs. II, III). 1. Absorption of energy from pump beam, and heating of the surface region. Coherent strain is generated by thermal expansion of the lattice. 2. The generated strain travels into the film. 3. Part of the wave is reflected at the metal/substrate interface. 4. The part that returns to the interface is detected by a delayed, weak probe pulse. b) Propagation of the high-amplitude acoustic wave launched into the substrate at room temperature: due to nonlinearity, the wave transforms into a N- or shock wave. The shock wave is detected at the other side by the same technique as in Fig. I.1 a). c) Like b) but now at low temperatures: the wave develops into a train of solitons, and high-frequency tail. d) Detection of soliton train by analyzing wavelength dependent reflection of a broadband colored pulse on a quantum well with a spectrometer. e) Reflection and transmission of multiple gallium nitride - indium gallium nitride quantum wells. Pumping leads to coherent vibrations, and acoustic wave propagation in the surrounding material. f) Generation of low-frequency, high amplitude acoustic waves in yttrium vanadate through structural phase transitions. g) Pump-probe transmission experiments on zinc oxide nanowires. First attempts are made to access the ultrafast carrier dynamics.

tivity due to the arriving acoustic reflection, as a function of time. We refer to Ch. III for a more detailed treatment of the generation process, and Chs. II - V for detection experiments. The range of accessible phonon frequencies is determined by the properties of the generator material, and is limited by either the optical penetration depth ζ or the electron diffusion length z_e (the typical depth over which heat is deposited) [35]. This allows generation of typically 100-GHz-bandwidth phonons, at strain amplitudes of the order of 10^{-5}.

Like for CW phonon sources, semiconductor heterostructures can be used for efficient generation of short phonon pulses. Here, the spectrum is determined by the thickness of the constituting layers, which can be an order of magnitude smaller than ζ and z_e. These heterostructures allow more control over the properties of the generated coherent wave [36]. In quantum well structures where strain is generated through piezeoelectric screening (see also Ch. VII), tunable phonon generation with a bandwidth of several hundreds of GHz has been demonstrated [37].

Generation mechanisms have since been extended to the high-amplitude regime through phase transitions in semiconductors [38, 39], and even into the destructive regime by ablation [40, 41, 42].

Acoustic solitons The study of picosecond ultrasonics entered a new stage when it was realized, that with the typical pulse widths and amplitudes, nonlinear propagation effects should occur over reasonable propagation distances. It is well known from elementary solid state physics that high-frequency phonons in crystalline structures suffer from dispersion [43]. This dispersion was experimentally investigated for several solids and propagation directions [44]. When the strain amplitudes become sufficiently large, the harmonic approximation of the atomic potential is not valid anymore and higher order elastic effects come into play [45]. This results in deformation of the strain wave and generation of higher frequencies. When damping can be ignored, it is the joint effect of nonlinearity and dispersion that leads to the formation of so-called acoustic *solitons*. In Fig. I.2 we sketch the formation process of an acoustic soliton. This subject will be treated more formally in Ch. V.

Solitons form a general physical phenomenon, and can be found in for example fluid dynamics [46, 47], plasmas [48], optics [49, 50, 51] and atomic physics [52, 53], and are both of experimental and theoretical interest [54, 55, 56]. The first detection of acoustic solitons in solids was reported for SiO_2, Si, Al_2O_3,

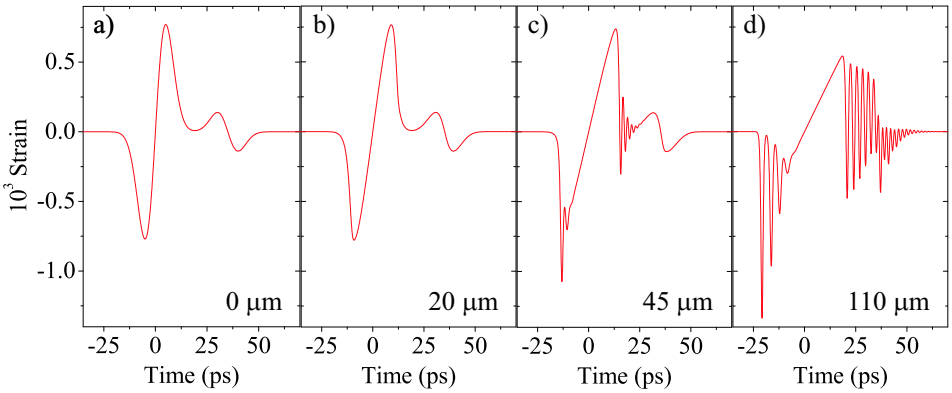

Figure I.2: Stages in formation of a train of solitons
a) Initial pulse. b) Self-steepening due to nonlinearity. c) Wave packet splitting into several solitons, and extreme dispersion of the rear (tensile) part. d) Fully formed soliton train. This calculation was performed for gallium arsenide, at a pump fluence of 10 mJ/cm^2 (Ch. VI) and for the indicated propagation distances.

and MgO in 2001 [57]. Acoustic solitons have since been observed by Brillouin scattering [58], two-level phonon spectroscopy [59], time-resolved reflectometric [60, 61] and interferometric [62] methods, and finally as surface propagating waves by beam deflection techniques [63].

It is now obvious why our experiments are performed with an amplified laser system. The induced effects can be orders of magnitude larger, since materials can be pumped close to their damage threshold. Moreover, since only a fraction of the pulse energy is required to reach this threshold, we can use pump beam sizes of the order of 200 μm, much larger than the 10 μm these experiments were originally performed with. This creates a quasi-1D propagation, and prevents complicating nonlinear diffraction effects [64, 65].

Advanced detection techniques After the initial reflection experiments [33], improvements of detection techniques have also been made. The reflection technique has been extended to include multicolor pump and probe, through the development of tunable laser sources [66, 67]. Diffraction experiments (where one looks at the beam displacement) [68, 69] and beam distortion techniques [70] were applied to bulk and surface acoustic wave detection. Polarization-sensitive detection allows the detection of shear acoustic waves [71, 72, 73]. A different class of tech-

niques makes use of diffraction of X-ray beams, and is sensitive to the position of single atomic planes [74, 75, 76, 77, 78, 79].

The current standard detection technique in picosecond ultrasonics is interferometry, either in single-shot [80] or non-destructive mode [35, 81, 82, 83], supplying information on both the amplitude and phase of the reflected or transmitted optical pulse (Ch. II). This technique has also been very successful in detection of vibrations of nanoparticles [84], and surface acoustic waves [85, 86, 87]. Very recently, results were obtained by XUV holography, which allows for improved lateral characterization of surface displacements [88].

Nanophononics The previous sections show, that the degree of control in ultrafast acoustics has developed to a stage where it has become a tool to study and manipulate functional solid state structures, rather than being the subject of research. First attempts of transferring optical techniques to the acoustic regime in recent years are shaping of pulsed phonon sources [89], and acoustical imaging of 2D nanostructures in the far field [90, 91]. Picosecond ultrasonics has been demonstrated to allow *in situ* characterization of film growth [92], and permits the determination of the presence of defects in nanostructures [93].

Even more interesting are demonstrations of manipulation of nanostructure properties. Surface acoustic waves are reported to generate optical superlattices with the prospect of creating tunable photonic crystals [28], and to induce exciton transport over micrometer distances [94]. Very recently, picosecond acoustic waves were reported to strongly modify the band gap properties of photonic crystals [95]. By virtue of resonant interactions, combined photonic/phononic structures open possibilities to strongly modify the material properties. First experiments showed the interplay between photonics and phononics at the nanoscale using either acoustic solitons [96] or selective excitation [97, 98] in nanocavities.

I.4 This thesis

The main subject of this thesis is the generation and detection of nanometer-sized phonon wavepackets. In particular, we explore the possibilities of generating THz frequency phonons, and applying them for nanostructure spectroscopy. All the experimental pump-probe schemes used in this thesis, are collected as sketches in Fig. I.1.

After discussing the experimental techniques in Ch. II, we will examine the

nonlinear generation of high-amplitude strain waves in chromium (Cr) and nickel (Ni) in Ch. III. These chapters will serve as a basis for Chs. IV and V, which are devoted to detection of linear, nonlinear (shock wave) and dispersive (soliton) propagation in crystalline materials. Ch. VI gives a first demonstration of utilizing a train of high-amplitude, ultrashort acoustic solitons to deform a semiconductor quantum well. The solitons are shown to act as ultrafast phase modulators and strongly modify the electron states and hence the reflection properties.

Chs. VII and VIII discuss alternative generation and detection methods of acoustic waves, i.e. without using metal films. Ch. VII shows results obtained on gallium nitride - indium gallium nitride (GaN/InGaN) multiple quantum well samples, demonstrating the emission of strain through piezoelectric screening. In Ch. VIII, we present measurements on yttrium vanadate (YVO_3), where strain is generated through ultrafast phase transitions and detected by means of time-resolved Brillouin scattering.

Ch. IX contains the only experiment in this thesis that does not involve acoustic, but rather electronic effects. We briefly discuss a possible future direction for ultrafast work using some of the presented techniques, by monitoring time-resolved transmission through zinc oxide (ZnO) nanowires.

References

1. D.L. Weaire and C.G. Windsor. *Solid state science: past, present and future*. IOP Publishing Ltd., 4th edition, 1987.
2. E. Braun and S. Macdonald. *Revolution in Miniature: The History and Impact of Semiconductor Electronics*. Cambridge University Press, 2nd edition, 1982.
3. G.M. Whitesides and J.C. Love. The art of building small. *Sci. Am.*, 285(3):38, 2001.
4. M.N. Baibich, J.M. Broto, A. Fert, F. Nguyen Van Dau, F. Petroff, P. Eitenne, G. Creuzet, A. Friederich, and J. Chazelas. Giant magnetoresistance of (001)Fe/(001)Cr magnetic superlattices. *Phys. Rev. Lett.*, 61(21):2472, 1988.
5. G. Binasch, P. Grünberg, F. Saurenbach, and W. Zinn. Enhanced magnetoresistance in layered magnetic structures with antiferromagnetic interlayer exchange. *Phys. Rev. B*, 39(7):4828, 1989.
6. G. Binnig, C.F. Quate, and Ch. Gerber. Atomic force microscope. *Phys. Rev. Lett.*, 56(9):930, 1986.
7. G. Binnig and H. Rohrer. Scanning tunneling microscopy - from birth to adolescence. *Rev. Mod. Phys.*, 59(3):615, 1987.

8. B.H. Soffer and R.H. Hoskins. Generation of giant pulses from a neodymium laser by a reversibly bleachable absorber. *Nature*, 204:276, 1964.
9. G. Steinmeyer, D.H. Sutter, L. Gallmann, N. Matuschek, and U. Keller. Frontiers in ultrashort pulse generation: pushing the limits in linear and nonlinear optics. *Science*, 286:1507, 1999.
10. A.L. Cavallieri, N. Müller, Th. Uphues, V.S. Yakovlev, A. Baltuška, B. Horvath, B. Schmidt, L. Blümel, R. Holzwarth, S. Hendel, M. Drescher, U. Kleineberg, P.M. Enchenique, R. Kienberger, F. Krausz, and U. Heinzmann. Attosecond spectroscopy in condensed matter. *Nature*, 449:1029, 2007.
11. M. Hentschel, R. Kienberger, Ch. Spielmann, G.A. Reider, N. Milosevic, T. Brabec, P. Corkum, U. Heinzmann, M. Drescher, and F. Krausz. Attosecond metrology. *Nature*, 414:509, 2001.
12. P.H. Bucksbaum. The future of attosecond spectroscopy. *Science*, 317:766, 2007.
13. M. Pittman, S. Ferré, J.P. Rousseau, L. Notebaert, J.P. Chambaret, and G. Chériaux. Design and characterization of a near-diffraction-limited femtosecond 100-TW 10-Hz high-intensity laser system. *Appl. Phys. B*, 74:529, 2002.
14. A. Bartels, R. Gebs, M.S. Kirchner, and S.A. Diddams. Spectrally resolved optical frequency comb from a self-referenced 5 GHz femtosecond laser. *Opt. Lett.*, 32(17):2553, 2007.
15. S.Y. Sokolov. Ultrasonic oscillations and their applications. *Tech. Phys.*, 2:1, 1935.
16. M.A. Breazale and J. Ford. Ultrasonic studies of the nonlinear behavior of solids. *J. Appl. Phys*, 36(11):3486, 1965.
17. J. Ilukor and E.H. Jacobsen. Generation and detection of coherent elastic waves at 114.000 Mc/sec. *Science*, 153(3740):1113, 1966.
18. P. Hu. Stimulated emission of 29-cm^{-1} phonons in ruby. *Phys. Rev. Lett.*, 44(6):417, 1980.
19. P.A. Fokker, J.I. Dijkhuis, and H.W. de Wijn. Stimulated emission of phonons in an acoustical cavity. *Phys. Rev. B*, 55(5):2925, 1997.
20. L.G. Tilstra, A.F.M. Arts, and H.W. de Wijn. Coherence of phonon avalanches in ruby. *Phys. Rev. B*, 68(14):144302, 2003.
21. L.G. Tilstra, A.F.M. Arts, and H.W. de Wijn. SASER action in optically excited ruby: angular and spectral distribution. *Jour. Phys.: Conf. Ser.*, 92:012011, 2007.
22. E.P.N. Damen, D.J. Dieleman, A.F.M. Arts, and H.W. de Wijn. Generation and propagation of coherent phonon beams. *Phys. Rev. B*, 64(17):4303, 2001.
23. N.M. Stanton, R.N. Kini, A.J. Kent, M. Henini, and D. Lehmann. Terahertz phonon optics in GaAs/AlAs superlattice structures. *Phys. Rev. B*, 68(11):113302, 2003.
24. S. Tamura, D.C. Hurley, and J.P. Wolfe. Acoustic-phonon propagation in superlattices. *Phys. Rev. B*, 38(2):1427, 1988.
25. A.J. Kent, R.N. Kini, N.M. Stanton, M. Henini, B.A. Glavin, V.A. Kochelap, and T.L. Linnik. Acoustic phonon emission from a weakly coupled superlattice under vertical electron transport: Observation of phonon resonance. *Phys. Rev. Lett.*,

96(21):215504, 2006.

26. A. Yamamoto, T. Mishina, Y. Masumoto, and M. Nakayama. Coherent oscillation of zone-folded phonon modes in GaAs-AlAs superlattices. *Phys. Rev. Lett.*, 73(5):740, 1994.
27. A.J. Kent, N.M. Stanton, L.J. Challis, and M. Henini. Generation and propagation of monochromatic acoustic phonons in gallium arsenide. *Appl. Phys. Lett.*, 81(18):3497, 2002.
28. M.M. de Lima Jr., R. Hey, P.V. Santos, and A. Cantarero. Phonon-induced optical superlattice. *Phys. Rev. Lett.*, 94(12):126805, 2005.
29. R.J. von Gutfeld and A.H. Nethercot. Heat pulses in quartz and sapphire at low temperatures. *Phys. Rev. Lett.*, 12(23):641, 1964.
30. J.P. Wolfe. *Imaging phonons. Acoustic wave propagation in solids*. Cambridge University Press, 2nd edition, 2005.
31. C. Thomsen, J. Strait, Z. Vardeny, H.J. Maris, J. Tauc, and J.J. Hauser. Coherent phonon generation and detection by picosecond light pulses. *Phys. Rev. Lett.*, 53(10):989, 1984.
32. G.L. Eesley. Generation of nonequilibrium electron and lattice temperatures in copper by picosecond laser pulses. *Phys. Rev. B*, 33(4):2144, 1986.
33. C. Thomsen, H.T. Grahn, H.J. Maris, and J. Tauc. Surface generation and detection of phonons by picosecond light pulses. *Phys. Rev. B*, 34(6):4129, 1986.
34. H.J. Maris. Picosecond ultrasonics. *Sci. Am.*, 86:278, 1998.
35. T. Saito, O. Matsuda, and O.B. Wright. Picosecond acoustic phonon pulse generation in nickel and chromium. *Phys. Rev. B*, 67:205421, 2003.
36. O. Matsuda, T. Tachizaki, T. Fukui, J.J. Baumberg, and O.B. Wright. Acoustic phonon generation and detection in GaAs/$Al_{0.3}Ga_{0.7}As$ quantum wells with picosecond laser pulses. *Phys. Rev. B*, 71(11):115330, 2005.
37. C.-T. Yu, K.-H. Lin, C.-L. Hsieh, C.-C. Pan, J.-I. Chyi, and C.-K. Sun. Generation of frequency-tunable nanoacoustic waves by optical coherent control. *Appl. Phys. Lett.*, 87(9):093114, 2005.
38. K. Sokolowski-Tinten, C. Blome, C. Dietrich, A. Tarasevitch, M. Horn von Hoegen, D. von der Linde, A. Cavalleri, J. Squier, and M. Kammler. Femtosecond X-ray measurement of ultrafast melting and large acoustic transients. *Phys. Rev. Lett.*, 87(22):225701, 2001.
39. H. Enquist, H. Navirian, T.N. Hansen, A.M. Lindenberg, P. Sondhauss, O. Synnergren, J.S. Wark, and J. Larsson. Large acoustic transients induced by nonthermal melting of InSb. *Phys. Rev. Lett.*, 98(22):225502, 2007.
40. K.T. Gahagan, D.S. Moore, D.J. Funk, R.L. Rabie, S.J. Buelow, and J.W. Nicholson. Measurement of shock wave rise times in metal thin films. *Phys. Rev. Lett.*, 85(15):3205, 2000.
41. D.J. Funk, D.S. Moore, K.T. Gahagan, S.J. Buelow, J.H. Reho, G.L. Fisher, and R.L. Rabie. Ultrafast measurement of the optical properties of aluminum during

shock-wave breakout. *Phys. Rev. B*, 64(11):115114, 2001.
42. Al.A. Kolomenskii, A.M. Lomonosov, R. Kuschnereit, P. Hess, and V.E. Gusev. Laser generation and detection of strongly nonlinear elastic surface pulses. *Phys. Rev. Lett.*, 79(7):1325, 1997.
43. C. Kittel. *Introduction to Solid State Physics*. John Wiley & Sons, 1st edition, 1996.
44. H.-Y. Hao and H.J. Maris. Study of phonon dispersion in silicon and germanium at long wavelengths using picosecond ultrasonics. *Phys. Rev. Lett.*, 84(24):5556, 2000.
45. F.D. Murnaghan. *Finite Deformations of an Elastic Solid*. John Wiley & Sons, 1951.
46. J.S. Russell. Report on waves. *British Association Reports*, 1844.
47. A.R. Osborne and T.L. Burch. Internal solitons in the Andaman Sea. *Science*, 208:451, 1980.
48. G.O. Ludwig, J.L. Ferreira, and Y. Nakamura. Observation of ion-acoustic rarefaction solitons in a multicomponent plasma with negative ions. *Phys. Rev. Lett.*, 52(4):275, 1984.
49. S.L. McCall and E.L. Hahn. Self-induced transparency. *Phys. Rev.*, 183(2):457, 1969.
50. L.F. Mollenauer, R. H. Stolen, and J.P. Gordon. Experimental observation of picosecond pulse narrowing and solitons in optical fibers. *Phys. Rev. Lett.*, 45(13):1095, 1980.
51. D.V. Skyrabin, F. Luan, J.C. Knight, and P.St.J. Russell. Soliton self-frequency shift cancellation in photonic crystal fibers. *Science*, 301:1705, 2003.
52. K.E. Strecker, G.B. Partridge, A.G. Truscott, and R.G. Hulet. Formation and propagation of matter-wave soliton trains. *Nature*, 417:150, 2002.
53. J. Denschlag, J.E. Simsarian, D.L. Feder, C.W. Clark, L.A. Collins, J. Cubizolles, L. Deng, E.W. Hagley, K. Helmerson, W.P. Reinhardt, S.L. Rolston, B.I. Schneider, and W.D. Phillips. Generating solitons by phase engineering of a Bose-Einstein condensate. *Science*, 287:97, 1999.
54. V.I. Karpman. *Non-linear Waves in Dispersive Media*. Pergamon Press, 1st edition, 1975.
55. D.J. Korteweg and G. de Vries. On the change of form of long waves advancing in a rectangular canal, and on a new type of long stationary waves. *Phil. Mag.*, 39:422, 1895.
56. R.K. Bullough and P.J. Caudrey, editors. *Solitons*. Springer, 1980.
57. H.-Y. Hao and H.J. Maris. Experiments with acoustic solitons in crystalline solids. *Phys. Rev. B*, 64:064302, 2001.
58. O.L. Muskens and J.I. Dijkhuis. High amplitude, ultrashort, longitudinal strain solitons in sapphire. *Phys. Rev. Lett.*, 89(28):285504, 2002.
59. O.L. Muskens, A.V. Akimov, and J.I. Dijkhuis. Coherent interactions of terahertz strain solitons and electronic two-level systems in photoexcited ruby. *Phys. Rev.*

Lett., 92(3):335503, 2004.
60. W. Singhsomroje and H.J. Maris. Generating and detecting phonon solitons in MgO using picosecond ultrasonics. *Phys. Rev. B*, 69(17):174303, 2004.
61. B.C. Daly, T.B. Norris, J. Chen, and J.B. Khurgin. Picosecond acoustic phonon pulse propagation in silicon. *Phys. Rev. B*, 70(21):214307, 2004.
62. E. Péronne and B. Perrin. Generation and detection of acoustic solitons in crystalline slabs by laser ultrasonics. *Ultrasonics*, 44(Suppl. 1):e1203, 2006.
63. A.M. Lomonosov, P. Hess, and A.P. Mayer. Observation of solitary elastic surface pulses. *Phys. Rev. Lett.*, 88(7):076104, 2002.
64. B.B. Kadomtsev and V.I. Petviashvili. On the stability of solitary waves in weakly dispersing media. *Sov. Phys. Dokl.*, 15(6):539, 1970.
65. O.L. Muskens and J.I. Dijkhuis. High-amplitude, ultrashort strain solitons in solids. In K.-T. Tsen, editor, *Non-equilibrium dynamics of semiconductors and nanostructures*, pages 15–45. CRC Press, 1st edition, 2005.
66. A. Devos and C. Lerouge. Evidence of laser-wavelength effect in picosecond ultrasonics: Possible connection with interband transitions. *Phys. Rev. Lett.*, 86:2669, 2001.
67. A. Devos, J.-F. Robillard, R. Cote, and P. Emery. High-laser-wavelength sensitivity of the picosecond ultrasonic response in transparent thin films. *Phys. Rev. B*, 74(6):064114, 2006.
68. O.B. Wright and K. Kawashima. Coherent phonon detection from ultrafast surface vibrations. *Phys. Rev. Lett.*, 69(11):1668, 1992.
69. A. Lomosonov, V.G. Mikhalevich, P. Hess, E.Yu. Knight, M.F. Hamilton, and E.A. Zabolotskaya. Laser-generated nonlinear Rayleigh waves with shocks. *J. Ac. Soc. Am.*, 105(4):2093, 1998.
70. N. Chigarev, C. Rossignol, and B. Audoin. Beam distortion detection technique for picosecond ultrasonics. *Jour. Phys.: Conf. Ser.*, 92:012178, 2007.
71. O. Matsuda and O.B. Wright. Theory of detection of shear strain pulses with laser picosecond acoustics. *Anal. Sci.*, 17:s216, 2001.
72. O. Matsuda, O.B. Wright, D.H. Hurley, V.E. Gusev, and K. Shimizu. Coherent shear phonon generation and detection with ultrashort optical pulses. *Phys. Rev. Lett.*, 93(9):095501, 2004.
73. D. Nounier, E. Morosov, P. Ruello, M. Edely, P. Babilotte, C. Mechri, J.-M. Breteau, and V. Gusev. Application of transient femtosecond polarimetry/ellipsometry technique in picosecond laser ultrasonics. *Jour. Phys.: Conf. Ser.*, 92:012179, 2007.
74. C. Rose-Petruck, R. Jimenez, T. Guo, A. Cavalleri, C.W. Siders, F. Ráksi, J.A. Squier, B.C. Walker, K.R. Wilson, and C.P.J. Barty. Picosecond-milliångström lattice dynamics measured by ultrafast X-ray diffraction. *Nature*, 398:310, 1999.
75. A. Cavalleri, C.W. Siders, F.L.H. Brown, D.M. Leitner, C. Tóth, J.A. Squier, C.P.J. Barty, K.R. Wilson, K. Sokolowski-Tinten, M. Horn von Hoegen, D. von der Linde, and M. Kammler. Anharmonic lattice dynamics in germanium measured with ul-

trafast x-ray diffraction. *Phys. Rev. Lett.*, 85(3):586, Jul 2000.
76. D.A. Reis, M.F. DeCamp, P.H. Bucksbaum, R. Clarke, E. Dufresne, M. Hertlein, R. Merlin, R. Falcone, H. Kapteyn, M.M. Murnane, J. Larsson, Th. Missalla, and J.S. Wark. Probing impulsive strain propagation with x-ray pulses. *Phys. Rev. Lett.*, 86(14):3072, 2001.
77. M. Bargheer, N. Zhavoronkov, Y. Gritsai, J.C. Woo, D. S. Kim, M. Woerner, and T. Elsaesser. Coherent atomic motions in a nanostructure studied by femtosecond X-ray diffraction. *Science*, 306(5702):1771, 2003.
78. S.H. Lee, A.L. Cavalieri, D.M. Fritz, M.C. Swan, R.S. Hegde, M. Reason, R.S. Goldman, and D.A. Reis. Generation and propagation of a picosecond acoustic pulse at a buried interface: Time-resolved X-ray diffraction measurements. *Phys. Rev. Lett.*, 95(24):246104, 2005.
79. Y. Hayashi, Y. Tanaka, T. Kirimura, N. Tsukuda, E. Kuramoto, and T. Ishikawa. Acoustic pulse echoes probed with time-resolved X-ray triple-crystal diffractometry. *Phys. Rev. Lett.*, 96(11):115505, 2006.
80. D.J. Funk, D.S. Moore, S.D. McGrane, J.H. Reho, and R.L. Rabi. Ultra-fast spatial interferometry: a tool for characterizing material phase and hydrodynamic motion in laser-excited materials. *Appl. Phys. A*, 81:295, 2005.
81. J.-P. Monchalin. Optical detection of ultrasound at a distance using a confocal Fabry-Perot interferometer. *Appl. Phys. Lett.*, 47(1):14, 1985.
82. T. Tachizaki, T. Muroya, O. Matsuda, Y. Sugawara, D.H. Hurley, and O.B. Wright. Scanning ultrafast Sagnac interferometry for imaging two-dimensional surface wave propagation. *Rev. Sci. Instr.*, 77(4):043713, 2006.
83. D.H. Hurley and O.B. Wright. Detection of ultrafast phenomena by use of a modified Sagnac interferometer. *Opt. Lett.*, 24(18):1305, 1999.
84. M.A. van Dijk, M. Lippitz, and M. Orrit. Detection of acoustic oscillations of single gold nanospheres by time-resolved interferometry. *Phys. Rev. Lett.*, 95(26):267406, 2005.
85. Y. Sugawara, O.B. Wright, O. Matsuda, M. Takigahira, Y. Tanaka, S. Tamura, and V.E. Gusev. Watching ripples on crystals. *Phys. Rev. Lett.*, 88:185504, 2002.
86. D.H. Hurley. Optical generation and spatially distinct interferometric detection of ultrahigh frequency surface acoustic waves. *Appl. Phys. Lett.*, 88(19):191106, 2006.
87. D.M. Profunser, O.B. Wright, and O. Matsuda. Imaging ripples on phononic crystals reveals acoustic band structure and Bloch harmonics. *Phys. Rev. Lett.*, 97(5):055502, 2006.
88. R.I. Tobey, M.E. Siemens, O. Cohen, M.M. Murnane, H.C. Kapteyn, and K.A. Nelson. Ultrafast extreme ultraviolet holography: dynamic monitoring of surface deformation. *Opt. Lett.*, 32(3):286, 2007.
89. J.D. Choi, T. Feurer, M. Yamaguchi, B. Paxton, and K.A. Nelson. Generation of ultrahigh-frequency tunable acoustic waves. *Appl. Phys. Lett.*, 87:081907, 2005.
90. B.C. Daly, N.C.R. Holme, T. Buma, C. Branciard, T.B. Norris, D.M. Tennant, J.A.

Taylor, J.E. Bower, and S. Pau. Imaging nanostructures with coherent phonon pulses. *Appl. Phys. Lett.*, 84(25):5180, 2004.

91. V. Tournat, D.M. Profunser, E. Muramoto, O. Matsuda, T. Takezaki, S. Sueoka, and O.B. Wright. Microscale multiple scattering of coherent surface acoustic wave packets probed with gigahertz time-reversal acoustics. *Phys. Rev. E*, 74(2):026604, 2006.
92. S. Kashiwada, O. Matsuda, J.J. Baumberg, R. Li Voti, and O.B. Wright. In situ monitoring of the growth of ice films by laser picosecond acoustics. *J. Appl. Phys.*, 100(7):073506, 2006.
93. G.A. Antonelli, H.J. Maris, S.G. Malhotra, and J.M.E. Harper. Picosecond ultrasonics study of the vibrational modes of a nanostructure. *J. Appl. Phys*, 91(5):3261, 2002.
94. J. Rudolph, R. Hey, and P.V. Santos. Long-range exciton transport by dynamic strain fields in a GaAs quantum well. *Phys. Rev. Lett.*, 99(4):047602, 2007.
95. A.V. Akimov, Y. Tanaka, A.B. Pevtsov, S.F. Kaplan, V.G. Golubev, S. Tamura, D.R. Yakovlev, and M. Bayer. Hypersonic modulation of light in three-dimensional photonic and phononic band-gap materials. *Phys. Rev. Lett.*, 101(3):033902, 2008.
96. A. Huynh, N.D. Lanzillotti-Kimura, B. Jusserand, B. Perrin, A. Fainstein, M.F. Pascual-Winter, E. Péronne, and A. Lemaitre. Subterahertz phonon dynamics in acoustic nanocavities. *Phys. Rev. Lett.*, 97(11):115502, 2006.
97. M.F. Pascual Winter, G. Rozas, A. Fainstein, B. Jusserand, B. Perrin, A. Huynh, P.O. Vaccaro, and S. Saravanan. Selective optical generation of coherent acoustic nanocavity modes. *Phys. Rev. Lett.*, 98(26):265501, 2007.
98. N.D. Lanzillotti-Kimura, A. Fainstein, A. Huynh, B. Perrin, B. Jusserand, A. Miard, and A. Lemaitre. Coherent generation of acoustic phonons in an optical microcavity. *Phys. Rev. Lett.*, 99(21):217405, 2007.

Chapter II

Ultrafast pump-probe reflectometry and interferometry

II.1 Introduction

The simple idea behind pump-probe spectroscopy is to send a "pump" laser pulse to excite the material under study, followed by a delayed "probe" pulse to monitor the time-dependent (optical) response to probe the processes that were initiated by the pump. One generally detects modulations of reflection from or transmission through a sample that are much smaller than the total signal itself. In this situation, differential measurements are performed, where the signal measurement is compared to a background measurement in absence of the pump.

Following Hurley *et al.* [1], we define the background electric field amplitude reflection of the sample as r_0, and the modulated reflection r' as $r_0(1+\rho)\exp(i\delta\varphi) \sim r_0(1+\rho+i\delta\varphi)$, as is depicted in Fig. II.1 a). When $\rho, \delta\varphi \ll 1$, terms of quadratic order can be neglected. In this expression we distinguish the two measurable components ρ (amplitude) and $\delta\varphi$ (phase). In the following chapters of this thesis, we describe the experiments and explain the underlying physical origins of the modulations. Here, we describe the optical scheme of the setups, the relation between the measured signals and ρ and $\delta\varphi$, and experiments defining the quality of our setup. The detailed operation of the relevant electronics is explained in App. A.

Our pump-probe setups run on the Spectra Physics "Hurricane", a 1-kHz, femtosecond amplified Ti-sapphire system operating at 800 nm. The total output power is around 500 mW, and the typical pulse length 110 fs (App. B).

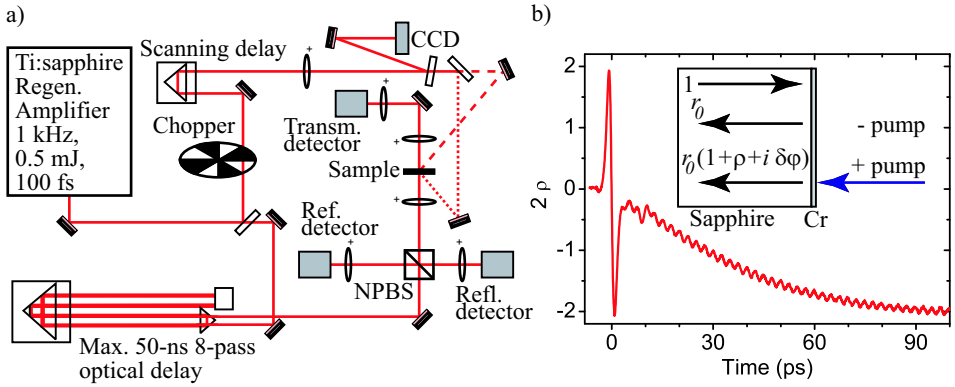

Figure II.1: Typical reflection and transmission setup
a) Experimental reflection/transmission setup. Long and short dashed paths indicate pump at back and front of the sample, respectively. b) Typical reflectometric pump-probe measurement. Inset shows the experimental geometry for this measurement, and the effects of the pump on the electric field amplitude and phase.

II.2 Reflection and transmission

In measurements of the absolute reflection and transmission, there is no reference for the phase, leaving it undefined. In reflection, one measures at the photodetector the intensities ${r'_0}^* r'$ and ${r_0}^* r_0$ for the signal and background measurement, respectively. Thomsen [2] defines the change in reflectivity (i.e. including the phase) as $r_0 + \Delta r$. Compared to the definition used here, which is more convenient when discussing interferometric detection, we can make the connection with the amplitude signal as $1 + \frac{\Delta R}{R} \equiv \frac{|\Delta r|^2 - |r_0|^2}{|r_0|^2} = \frac{|r_0(1+\rho+i\delta\varphi)|^2 - |r_0|^2}{|r_0|^2} \sim 1 + 2\rho$. A similar argument holds for the differential transmission $\Delta T/T$.

Figure II.1 a) shows a typical scheme of a reflection/transmission setup. The beam is split in a pump (90%) and a probe (10% and further attenuated) part. The pump is chopped to make a background measurement possible (App. A). Only one delay line is depicted in the pump path, although in fact two are present: one to get the timing approximately right, and the second to perform the scanning. Both delay lines in the pump are equipped with a retroreflector. The pump is focused with a 220-cm focal distance lens to obtain both a good Gaussian beam profile (the original beam quality is very poor and resembles a Gaussian only in the focal area) and a high pump fluence at the sample. The sample is located $\sim$ 35 cm before the focal point, giving beam waists of typically 100 - 400 μm, and maximum fluences

in the range of 15 - 200 mJ/cm^2 (depending on additional attenuation used in order to remain below the damage threshold of the specific sample). The beam profiles are measured with a CCD, inserted at the same distance from a beam splitter as the sample (Fig. II.1 a)).

A 2-m long eight-pass delay line is included in the probe beam, allowing a maximum optical delay of 50 ns. This is imperative for experiments where one side of the sample is pumped, and the generated strain is detected at the opposite side (Chs. IV and V). Before hitting the sample, part of the probe light is sent to a reference detector to correct for laser noise effects (App. A). The probe is focused on the sample in a perpendicular geometry, to make the probe spot as small as possible, typically in the range of 5 - 30 μm. The reflection or transmission is then collimated, and focused onto a photodetector. It is possible to measure differential reflection and transmission simultaneously, which also allows a direct determination of the absorption (Ch. VII).

In the case of pumping and probing at the same wavelength (Chs. IV and VIII), we use polarization filtering to reduce the amount of pump light on the detectors. When pumping and probing at different wavelengths color filters are used to reject pump light. The latter type of measurements generally yield better signal-to-noise ratio. A typical measurement result is shown in Fig. II.1 b). Here, we pump a chromium film deposited on sapphire, and probe it on the sapphire side (inset). The trace shows several sources of reflection changes:

- The bipolar pulse around $t = 0$ is due to a coherent strain pulse at the Cr-sapphire interface, modulating the optical constants of the metal through the elasto-optic effect. This effect is discussed in more detail in Chs. III - V.

- The long-living oscillation of $\sim$100 GHz frequency is the so-called Brillouin oscillation, arising from interference between light reflecting from the metal film surface and from the strain pulse moving in the sapphire. The subject is treated in Chs. VII and VIII.

- The slow decrease in background level after $t = 0$ is due to the propagation of heat generated by absorption of pump light in the Cr film. The heat pulse consists of incoherent high-frequency phonons and travels slower due to dispersive effects, scattering and diffusion [3].

II.3 Interferometry

To also obtain $\delta\varphi$, we must compare the phase of the signal pulse to a reference pulse. This can be done in an *interferometer*. Although several types exist (e.g. Mach-Zehnder, Michelson) [4], the common-path character of the Sagnac interferometer [1, 5, 6, 7] ensures that many noise sources (such as those connected to vibrations in the table) cancel.

II.3.1 Setup

Our setup is presented in Fig. II.2 a), and is a slightly modified version of type B presented in Ref. [5]. The delay line and chopper part is identical to that presented in Fig. II.1 a). Probing in the interferometer is at 800 nm. Polarization filtering is not possible and pumping is always at 400 nm. The incoming probe light is polarized at an angle of 45 degrees with respect to the main axes of the polarizing beam splitter (PBS). The reference signal is split off at the non-polarizing beam splitter (NPBS). At the PBS central in the setup, the incoming probe beam is divided into two counterpropagating beams. The quarter-wave plates (QWP) are used to rotate the polarization of a pulse entering an arm, so that each reflection at the center PBS is followed by a transmission, *vice versa*. This results in beam paths for the two polarizations that are shown in Fig. II.2 b) and c). The important point is that the beams with different polarization arrive at the sample at different times, but exit the interferometer at exactly the same time, thus having spatiotemporal overlap while carrying different information. The two pulses are merged after the central PBS again and mixed with a QWP after reflection at the NPBS. Finally the signal is split with a PBS, and the two contributions are measured by photodetectors D1 and D2.

The addition of focusing lenses in both sidearms (probably reducing the sensitivity for mirror alignment) and the use of a third photodetector for reference measurements before entering the interferometer appeared to be crucial and decreases the noise level by an order of magnitude.

II.3.2 Theory

When encountering polarization effects, the analysis can best be performed by using the Jones formalism [8]. Here, the two-component Jones vector describes the amplitude and phase of the two (horizontal and vertical) polarization components

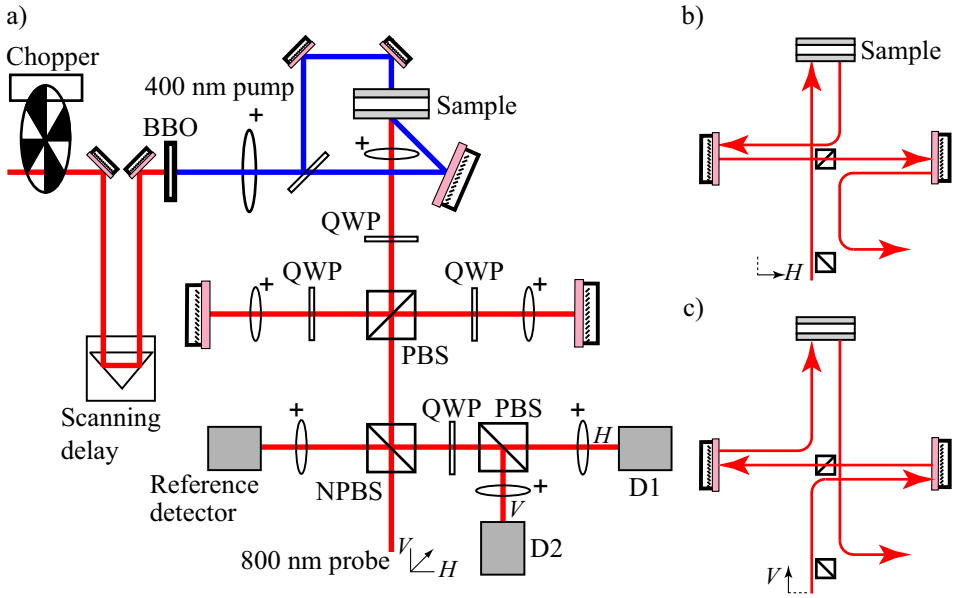

Figure II.2: Interferometric detection setup
a) Sketch of the interferometric pump-probe setup. NPBS: non-polarizing beam splitter, PBS: polarizing beam splitter, QWP: quarter waveplate. b) Sketch of the beam path for horizontal polarization, in the interferometer setup. c) Like b), but now for the vertical polarization.

of the electric field, and each modification in either amplitude or phase induced by an optical element corresponds to multiplication by a 2×2 Jones matrix. For this type of setup, the analysis is conscientiously performed in Ref. [5]. We will summarize the main points here.

Before entering the interferometer setup through the NPBS, we put the incoming polarization at 45° with respect to the principal polarization directions:

$$\frac{1}{\sqrt{2}} \begin{pmatrix} 1 \\ 1 \end{pmatrix}. \tag{II.1}$$

In the experiments, we use the vertical (V) polarization for the signal probe, and the horizontal (H) for the reference. When exiting the interferometer after following the paths indicated in Fig. II.2 b) - c), the former experiences the modulated reflection r', and the latter the equilibrium reflection coefficient r_0. The expressions for the amplitudes after reflection at the NPBS are then

$$\frac{-r_0}{2\sqrt{2}}\begin{pmatrix}1+\rho+i\delta\varphi\\1\end{pmatrix}. \tag{II.2}$$

The phase signal $\delta\varphi$ can be extracted by either using a polarizer at an angle of 45° and 135° with respect to the principal polarization axes, or by using a QWP and a PBS [5]. We have chosen the second option, since this allows for the easiest way of data processing, and simultaneous measurement of ρ and $\delta\varphi$. When the QWP is at 45°, the polarization amplitudes are given by

$$\frac{r_0}{8}\begin{pmatrix}-2-\rho-\delta\varphi+i(\rho-\delta\varphi)\\-2-\rho+\delta\varphi+i(-\rho-\delta\varphi)\end{pmatrix}. \tag{II.3}$$

The final PBS separates the two polarization components; the horizontal component is transmitted and goes to detector D1, while the vertical is reflected and goes to D2 (Fig. II.2 a)). Finally, we calculate the absolute value $I_{\mathrm{D1}} = {E_{\mathrm{D1}}}^* E_{\mathrm{D1}}$ and $I_{\mathrm{D2}} = {E_{\mathrm{D2}}}^* E_{\mathrm{D2}}$ to obtain the measured light intensities at the diodes:

$$I_{\mathrm{D1}} = \frac{{r_0}^2}{16}(1+\rho+\delta\varphi+\frac{\rho^2}{2}+\frac{\delta\varphi^2}{2}), \text{ and} \tag{II.4}$$

$$I_{\mathrm{D2}} = \frac{{r_0}^2}{16}(1+\rho-\delta\varphi+\frac{\rho^2}{2}+\frac{\delta\varphi^2}{2}). \tag{II.5}$$

The sum and difference of these intensities give the amplitude (neglecting higher order effects) and phase signal, respectively:

$$I_{\mathrm{D2}}+I_{\mathrm{D1}} = \frac{{r_0}^2}{8}(1+\rho), \tag{II.6}$$

$$I_{\mathrm{D2}}-I_{\mathrm{D1}} = \frac{{r_0}^2}{8}\delta\varphi. \tag{II.7}$$

In both cases, the normalization by a background measurement ensures that we obtain the absolute ρ and $\delta\varphi$. In general, the interferometric contrast does not reach the maximum of 100%, but is reduced (among others) by abberations in lenses, residual reflections of optical components, alignment imperfections, and beam quality [5].

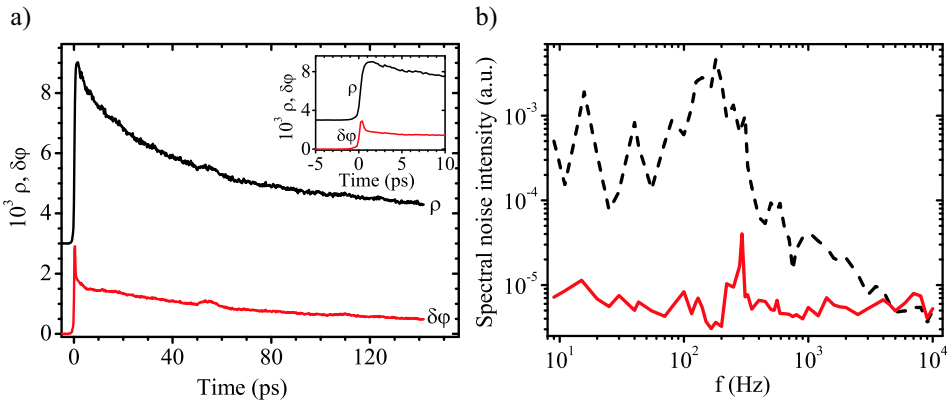

Figure II.3: Typical interferometer measurement and noise characteristics
a) Typical result for ρ and $\delta\varphi$, obtained in a pump-probe experiment on a Cr film deposited on a Si substrate (see also Ch. III). Inset shows the subpicosecond response upon arrival of the pump, and the temporal resolution of the setup. b) Noise stability in common-path interferometric (solid line) and simple interferometric (dashed line) case.

II.3.3 Experimental characterization

This section presents a series of characterization measurements demonstrating the virtue of the interferometer.

In Fig. II.3 a), a typical measurement result for ρ and $\delta\varphi$ is shown. Here we pump with 400 nm and probe interferometrically with 800 nm on a chromium (Cr) layer of ∼200-nm thickness deposited on a silicon (Si) substrate (Ch. III). The bump at 55 ps is due to the coherent acoustic wave that was generated by the pump at $t = 0$, reflected at the Cr/Si interface and returned to the Cr film surface. The fact that this feature is much clearer in the $\delta\varphi$ signal than in the ρ signal demonstrates the advantage of the experimental access to phase information. Comparing with previous measurements on the same structure [9], we deduce an interferometric contrast around 85%. The value below 100% can be traced back to the poor probe beam quality. The beam is somewhat elliptic, and its profile shows spatial deviations from the ideal Gaussian profile. The typical noise level is $\sim 10^{-5}$ for both amplitude and phase signal (corresponding to surface displacements of the order of 1 pm), for an integration time of 1 second. We note that for high signals the noise is larger, due to slow variations in pump intensity and/or beam pointing, amounting to ∼2% of the total signal amplitude. The inset in Fig. II.3 a) shows

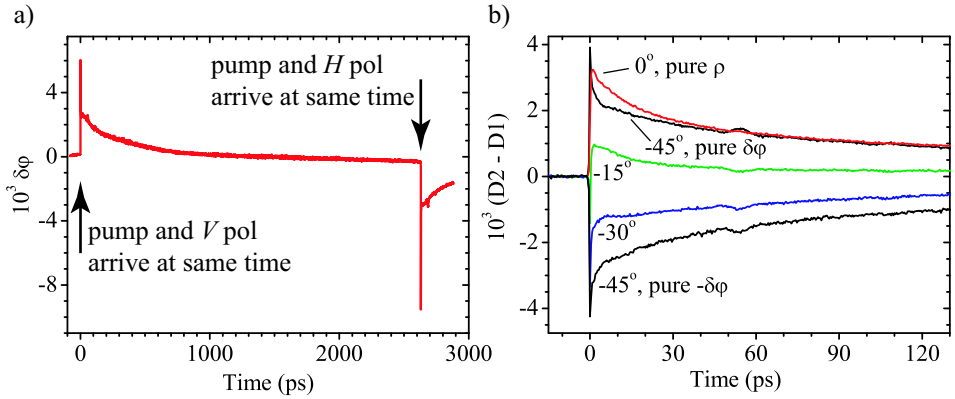

Figure II.4: Interferometer timing and contrast characteristics
a) Two-pulse experiment, using either the first or the last pulse to arrive at the sample as signal pulse. The time difference of 2630 ps is consistent with two times the length of the interferometer sidearms. The sign change is due to the fact that the modulation is in a different polarization component. b) Dependence of the difference signal D2−D1 on the orientation of the final quarter-wave plate.

the fast response at $t = 0$, due to rapid heating of the electron gas. From the response time of the phase signal, we can conclude that the temporal resolution in this geometry is better than 300 fs.

Fig. II.3 b) shows the improvement in noise level by going from non-common-path (using only two side arms, i.e. a Michelson-like geometry) interferometric to common-path (Sagnac) interferometric operation. This experiment was performed with a 780-nm CW diode laser, and the spectral intensity was measured at detector D2. The noise differs more than two orders of magnitude, 10^{-5} being the detection limit of the spectrum analyzer. Driving the table with an acoustic frequency generator showed that the peaks in the spectrum correspond to vibrational modes of the optical table. This demonstrates the inherent stability of the Sagnac interferometer.

In Fig. II.4 a), we prove that indeed two pulses travel through the interferometer. Apart from a minus sign, it does not matter which polarization acts as probe and which as reference. This implies that the arrival of the pump should be detected twice, with the temporal spacing equal to the difference in path length, being twice the length of the side arms. Fig. II.4 a) shows this in the form of two responses: the first (positive) in the case where the H-polarization acts as ref-

erence and the V-polarization as signal (standard operation), and the second *vice versa*. The two peaks are separated by 2.630 ns. This interval time obviously limits the detection window. We measured the total side arm length to be 37 cm, of which 2.54 cm through the glass PBS, $2 \times .93$ cm through the glass lenses, and $2 \times .8$ mm through the quartz QWP, and the remainder through air, making a total delay of 2.626 ns for the full passage, in agreement with the result from the pump-probe measurement.

Fig. II.4 b) shows the effect of rotating the final QWP on $\mathrm{D2} - \mathrm{D1}$ (normalized to the background). At $+45^\circ$ and -45°, the phase signals are maximum but with opposite sign, while at 0°, there is no interference and the signal is a pure amplitude signal ρ (as can be derived from the theoretical analysis). Note the reduced visibility of the acoustic reflection at 55 ps in this case, as in Fig. II.3 a). At intermediate angles, some of which are also shown, these two signals are nontrivially mixed.

References

1. D.H. Hurley and O.B. Wright. Detection of ultrafast phenomena by use of a modified Sagnac interferometer. *Opt. Lett.*, 24(18):1305, 1999.
2. C. Thomsen, H.T. Grahn, H.J. Maris, and J. Tauc. Surface generation and detection of phonons by picosecond light pulses. *Phys. Rev. B*, 34(6):4129, 1986.
3. B. Perrin, E. Péronne, and L. Belliard. Generation and detection of incoherent phonons in picosecond ultrasonics. *Ultrasonics*, 44(Suppl. 1):e1277, 2006.
4. W. Lauterborn, T. Kurz, and M. Wiesenfeldt. *Coherent optics*. Springer-Verlag, 1995.
5. T. Tachizaki, T. Muroya, O. Matsuda, Y. Sugawara, D.H. Hurley, and O.B. Wright. Scanning ultrafast Sagnac interferometry for imaging two-dimensional surface wave propagation. *Rev. Sci. Instr.*, 77(4):043713, 2006.
6. J.-Y. Duquesne and B. Perrin. Ultrasonic attenuation in a quasicrystal studied by picosecond acoustics as a function of temperature and frequency. *Phys. Rev. B*, 68:134205, 2003.
7. M.C. Gabriel, N.A. Whitaker Jr., C.W. Dirk, M.G. Kuzyk, and M. Thakur. Measurement of ultrafast optical nonlinearities using a modified Sagnac interferometer. *Opt. Lett.*, 16:1334, 1991.
8. E. Hecht. *Optics*. Addison Wesley, 3rd edition, 1998.
9. T. Saito, O. Matsuda, and O.B. Wright. Picosecond acoustic phonon pulse generation in nickel and chromium. *Phys. Rev. B*, 67:205421, 2003.

Chapter III

High-amplitude strain generation in Ni and Cr

Abstract

This chapter describes both theory and interferometric experiments on ultrafast generation of coherent strain pulses in chromium and nickel metal films. Experiments show that the strain amplitudes increase superlinearly with pump fluence, while the pulse widths increase at fluences above $\sim 70\%$ of the damage threshold. Detailed numerical simulations were performed, based on the two-temperature model in the non-equilibrium case. The measured amplitude effects can be attributed to the temperature dependence of the expansion coefficient. At the highest fluences, a sudden increase in strain amplitude and width is detected in chromium, related to damaging of the surface layer.

III.1 Introduction

Picosecond ultrasonics [1], the characterization of materials by dynamical strain in the sub-THz regime generated and detected by ultrashort optical pulses, has frequently been applied to metallic films. Metals form an ideal model system for ultrafast experiments, because the thermalization times following a pump pulse ($\sim$ 1 ps), the generated coherent phonon pulse widths ($\sim$ 5 ps), and the acoustic travel times through the deposited layers ($\sim$ 100 nm thick, typically taking 15 ps) are all in the picosecond range.

The dynamics in a metal film following optical excitation is sketched in Fig. III.1. In the *two-temperature model*, the electron gas and phonon bath are treated as separate, but coupled heat reservoirs [2]. Upon excitation, the electrons in the surface layer of the film absorb part of the pump pulse energy, leaving the lattice temperature at its equilibrium value (Fig. III.1 b)). The electron excess energy can escape by two processes: diffusion of hot electrons to the interior of the film,

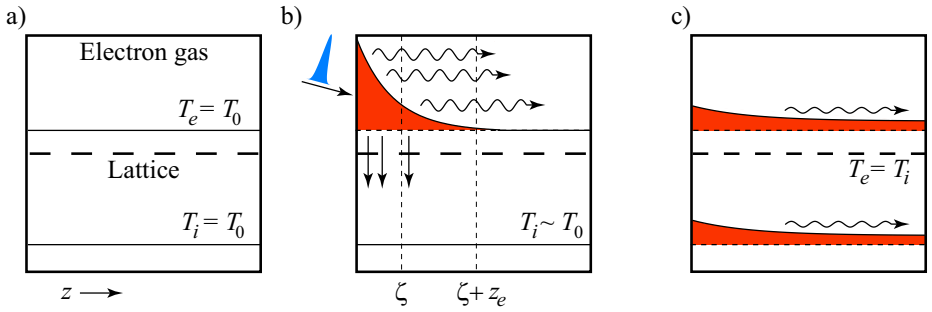

Figure III.1: Heat dissipation in metals: two-temperature model
a) Initial equilibrium state. Electron gas and lattice have the same temperature T_0. b) At and just after arrival time of the pump pulse at $t = 0$. Absorption of pump pulse energy by the electrons within the optical penetration depth ζ. Energy is transferred either into the bulk by hot carrier diffusion over a typical length z_e, or by coupling to the lattice. c) Long (> 10 ps) after pump pulse arrival. Quasi-equilibrium situation: the electron gas and lattice have the same temperature $T_e = T_i$ at all positions. After this time, there is slow ($\sim$ ns timescale) heat diffusion further into the metal and underlying substrate.

and coupling to (heating of) the lattice. Not only incoherent heat but also coherent strain is generated in this two-step heating process. Both the temperature rise of the electron gas δT_e and that of the lattice δT_i contribute to a thermoelastic stress $\delta\sigma$, of which in general the second contribution is dominant. This impulsive stress in turn leads to a travelling strain δs. The full coherent strain wave is formed by the sum of all generated strain components. A detailed analysis of these dynamics can be found in Sec. III.5.

Metals with a relatively large electron-phonon coupling constant g and low thermal conductivity κ yield a coherent phonon spectrum with a bandwidth mainly determined by the optical penetration depth ζ. This is for example the case in nickel [3, 4], chromium [4], molybdenum [5], and wolfram [6]. On the other hand, in metals like gold and silver electron propagation is quasi-ballistic [7], electrons diffuse over larger distances, and the excited phonon frequencies become relatively low [8, 9]. Aluminum forms a special case. Here, the slow electron-electron scattering with respect to electron-phonon coupling causes strong non-equilibrium electron diffusion [10]. Most experiments and analyses in literature are performed in the "quasi-equilibrium" regime, where constant thermal and mechanical parameters are assumed and only the electron and lattice temperatures vary. We will see that the pump fluences used in the experiments in this thesis may drive the gen-

eration in the non-equilibrium regime, where the material parameters depend on temperature and thus on time.

The purpose of this chapter is to provide insight into the strain-generating processes in the non-equilibrium regime. To this end, interferometric pump-probe reflection experiments are performed on nickel and chromium metal films. We distinguish three power regimes. First, the case of linear generation, where we calculate the strain by analytical evaluation of the equilibrium two-temperature model [11]. Second, the non-equilibrium regime, where the strain amplitudes increase superlinearly with fluence, caused by temperature-dependent expansion coefficients, and where we numerically evaluate the two-temperature model. Finally, the extremely high-power regime, where effects deviate from the two-temperature model results and nonthermal processes occur in the surface layer of the metal [2].

III.2 Detection

Before addressing the experimental results and the generation process, we start by analyzing the physics underlying the interferometric detection process. As discussed already in Ch. II, an interferometric measurement yields both amplitude (ρ) and phase ($\delta\varphi$) information. In the experiments in this chapter, a coherent strain $s(z,t)$ is generated at the metal surface, travels into the metal film, and is partly transmitted into the substrate, while higher-order reflections at the metal-substrate interface return to the film surface. We detect at both sides of the metal film. The relevant question here is how the strain emerging at the detection surface affects the film reflection properties. A detailed analysis of the detection process in reflection for the amplitude is given in Ref. [3], while Ref. [12] additionally discusses interferometric contributions. The most important results are summarized here.

III.2.1 Bulk contributions

The amplitude signal $\rho = \rho_{metal}$ originates from the change in optical constants $n+i\kappa$ of the metal by the presence of strain. A similar contribution is also present in the phase signal $\delta\varphi = \delta\varphi_{metal} + \delta\varphi_{surface}$. The bulk contributions ρ_{metal} and $\delta\varphi_{metal}$ as a function of time can be expressed in a weighted integration of the strain over all depths in the film:

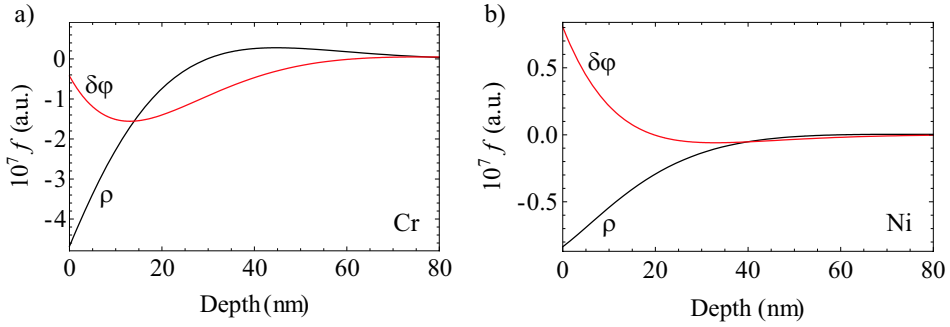

Figure III.2: Sensitivity functions
a) Calculated amplitude (ρ) and phase ($\delta\varphi$) sensitivity functions for chromium at a probe wavelength of 800 nm. b) Like a), but now for nickel. The parameters used in the calculations are taken from Ref. [4]. We have assumed the elasto-optical constants the same for 800 nm and 830 nm because of an expected weak wavelength dependence in this range.

$$\rho_{metal}(t) = \int_0^\infty f_\rho(z)s(z,t)\mathrm{d}z, \tag{III.1}$$

$$\delta\varphi_{metal}(t) = \int_0^\infty f_{\delta\varphi}(z)s(z,t)\mathrm{d}z, \tag{III.2}$$

with z the inward direction of the film, and $z = 0$ at the film surface. The function $f(z)$ is usually called the sensitivity function. It is an oscillatory function which decays as $\exp(-z/\zeta)$, with an amplitude mainly determined by the elasto-optical constants $\frac{\partial n}{\partial s} + i\frac{\partial \kappa}{\partial s}$ at the probe wavelength. The functions for Cr and Ni at a wavelength of 800 nm are plotted in Fig. III.2 a) and b), respectively.

III.2.2 Surface displacement

In addition to the bulk contribution a phase signal is generated by the surface displacement $\delta\varphi_{surface}$. With z as defined in the previous section, the phase shift $\delta\varphi(t)$ for the geometry of Fig. III.3 (insets) can be expressed in terms of the surface displacement $\delta z(t)$ from the equilibrium position $z = 0$ by

$$\delta\varphi_{surface}(t) = 2 \times \frac{2\pi}{\lambda}\delta z(t). \tag{III.3}$$

The relation between the surface displacement $\delta z(t)$ and strain $s(0,t)$ passing the (detection) surface is

Material	Mass density ρ (10^3 kg/m^3)	Longitudinal sound velocity v_s (10^3 m/s)	Acoustic impedance Z (10^7 kg/m^{2}s)
Si	2.33	8.48	1.98
Al_2O_3	3.97	11.23	4.46
Ni	8.9	5.89	5.24
Cr	7.2	6.65	4.79

Table III.1: Material parameters determining the acoustic reflection coefficients

$$\frac{\mathrm{d}\delta z(t)}{\mathrm{d}t} = 2 \times v_s s(0,t), \tag{III.4}$$

with v_s the longitudinal speed of sound in the metal. The multiplication factors of 2 arise from the fact that strain reflects at the free surface and undergoes a sign change. In our experiments, we measure the integrated $\delta\varphi(t)$. When the step size is Δt, the calculated discrete difference is proportional to the strain at the surface:

$$\delta\varphi(t+\Delta t) - \delta\varphi(t) = \frac{8\pi}{\lambda} v_s \Delta t s(0,t), \tag{III.5}$$

The surface displacement contribution is usually several factors larger than the bulk contribution. Moreover, the excursion of the surface is an integral rather than a derivative signal. This is advantageous when detecting very rapid signals like those from solitons (Ch. V).

III.3 Samples

The silicon (Si) (100) and sapphire (Al_2O_3) (0001) subtrates were cleaned by acetone or an eight-hour heating process in an oven ($\sim$ 1000 °C), respectively, to remove surface pollution. After this, the samples were introduced into a thermal evaporation chamber, which was evacuated to below 10^{-5} mbar. The samples were irradiated by UV-radiation to evaporate any residual organic components. During evaporation, the thickness of the deposited layer was monitored with a quartz oscillator crystal mounted inside the chamber.

The acoustic impedance Z of a material is given by ρv_s, with ρ the mass density. The values for materials used in this chapter are collected in Table III.1. For an acoustic wave travelling from material i to j, the impedance mismatch

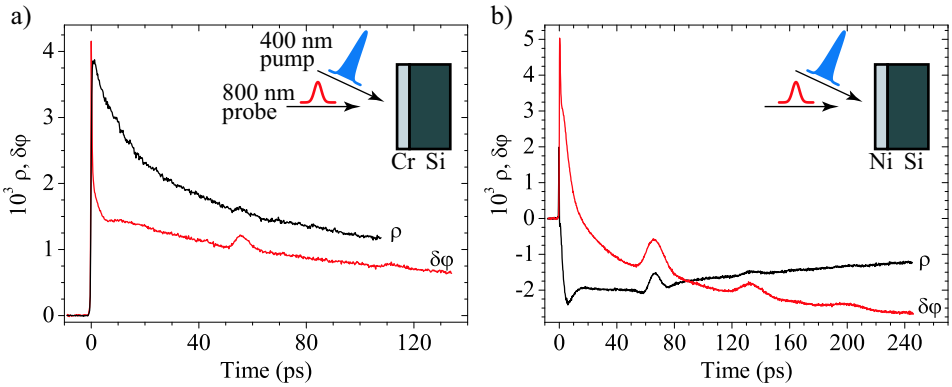

Figure III.3: Typical pump-probe signals for Cr and Ni
a) Measured ρ and $\delta\varphi$ signals for chromium at a fluence of 3.9 mJ/cm^2. b) Measured ρ and $\delta\varphi$ signals, for nickel at a fluence of 10.9 mJ/cm^2. Insets show the pump-probe configuration.

between the two materials determines the acoustic reflection coefficient: $r_{ac} = (Z_j - Z_i)/(Z_j + Z_i)$. The combination of metals and substrates was optimized for specific pump-probe experiments.

We have deposited Cr and Ni metal films of thickness $\sim$ 200 nm on a Si substrate for both pump and probe on the front side of the film, see insets Fig. III.3 a) and b). The low acoustic impedance of Si with respect to Ni and Cr ensures large amplitude acoustic reflection coefficients of -0.42 and -0.43, respectively. In the case of experiments where pumping occurs on the front side and probing on the back (insets Figs. III.6 d) and III.7 d)), we deposited 100-nm layers on (transparent) Al_2O_3. Acoustic reflection coefficients for Ni and Cr are then only -0.08 and 0.04, respectively. This allows us to capture a pure image of the generated acoustic wave, without the need for large corrections to the measured signal due to higher order reflections.

III.4 Pump-probe experiments on chromium and nickel

III.4.1 Interferometric contrast

The maximum interferometric contrast of 100% for the interferometric setup presented in Ch. II is in practice limited by several factors [13]. Fig. III.3 shows our measurements on ρ and $\delta\varphi$ for both Ni and Cr on Si. The obtained signals can

be compared qualitatively to results available in literature [4]. Acoustic echoes at multiples of 66 ps in the case of Ni, and multiples of 56 ps in the case of Cr, return from the metal/substrate interface. By comparing the amplitude of these bumps in the amplitude and phase signal to the ones in Ref. [4], the contrast reached in this setup may be estimated at a value between 85% and 90%.

III.4.2 Pump-probe experiments at the metal surface

Sets of measurements were performed as a function of fluence, both for Cr and Ni deposited on Si, at room temperature and 30 K. The main purpose of these measurements is to obtain information on the propagation of the generated strain waves in the metal films, most importantly the acoustic attenuation. Further, we search for a fluence dependence of the strain pulse shape, to be explored to better advantage when performing pump and probe measurements at opposite sides.

The results for the Cr film are collected in Fig. III.4. Fig. III.4 a) shows clear first and second acoustic echoes in the background corrected $\delta\varphi$ traces obtained at room temperature. The inset shows the average of the arrival times of these echoes for all measurements, yielding multiples t_r of 55.3 ps with an error below 200 fs. Using the sound velocity v_s for Cr (Table III.1) we can derive a film thickness d_{Cr} of $v_s t_r/2 = 184$ nm, in reasonable agreement with measurements during the deposition process.

In order to analyze the generation and propagation on a more quantitative basis, we describe the pulse shape by a Gaussian derivative function

$$s(t) = s_0 \frac{2\sqrt{e}}{\tau} t \exp\left(\frac{-2t^2}{\tau^2}\right). \tag{III.6}$$

This definition differs slightly from an earlier one [14], in the sense that the maximum amplitudes $\pm s_0$ are at $\pm\tau/2$. We define τ as the temporal width of the wave for the remainder of this thesis.

Ignoring the bulk contribution to the phase signal, the measured acoustic pulse echo i is found to follow $a_i\tau_i \exp\left(-2t^2/\tau_i^2\right)$, i.e. a Gaussian function. The measured echoes $i = 1,2$ in $\delta\varphi$ of Fig. III.4 a) and d) were fitted to this function. The results for the widths τ_i are plotted in Figs. III.4 b) and e), and for the amplitudes a_i in Figs. III.4 c) and f). The widths increase with increasing fluence, from 4.5 ps at the lowest fluence to 7 ps at the highest measured fluence at room temperature, and to 6 ps at low temperatures. The width of the second reflection is larger

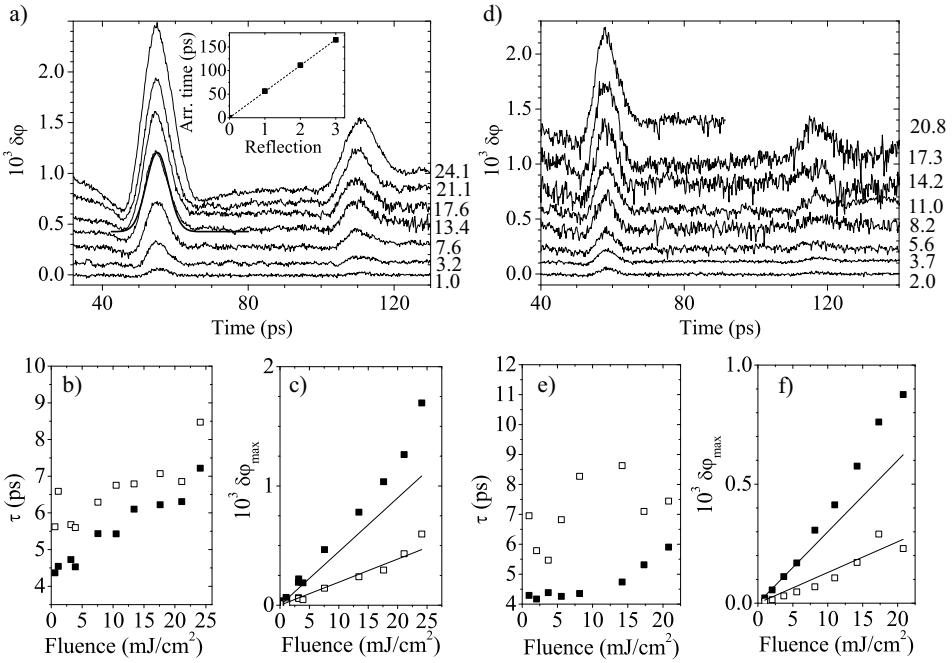

Figure III.4: Phase signals for Cr at room temperature and 30 K
a) Phase signals at various fluences for Cr on Si at room temperature, showing acoustic reflections at 55 ps and 110 ps. Numbers at the right axis indicate the pump fluence in mJ/cm^2. Inset shows determined arrival times of the various reflections, along with a linear fit on the data (dashed line). A Gaussian fit is indicated in the trace for 13.4 mJ/cm^2 by a thick solid line. b) Temporal width τ of the first (filled squares) and second (open squares) acoustic reflection versus pump fluence. Increased values for the second reflection are caused by acoustic attenuation. c) Amplitude of the first (filled squares) and second (open squares) echo as a function of fluence. Solid line through points for first reflection is a fit to low fluence amplitudes. Solid line through points for second reflection is a multiplication of this fit by the expected 0.43 amplitude reflection coefficient at the Cr/Si interface. d) - f) As for figures a) - c), but now at a temperature of 30 K.

than that of the first, which is a signature for acoustic attenuation, as we will see. The amplitudes of the second acoustic reflection (Fig. III.4 c), open squares) are found to be minutely lower than the amplitude of the first reflection multiplied by the 0.43 amplitude reflection coefficient, showing that attenuation is low. At the highest fluence, both amplitude and width show a sharp increase.

The results for Ni are plotted in Fig. III.5. The reflection arrival times of

multiples of 67.6 ps yield a film thickness d_{Ni} of 199 nm, again corresponding well to the expected 200 nm. Fig. III.5 b) shows that for Ni, τ does not increase sharply with increasing fluence. The temporal widths are larger than in the Cr case, but the second reflection is still much broader in time than the first. Furthermore, the amplitude of the second reflection is lower than that of the first reflection multiplied by the 0.42 amplitude reflection coefficient. Both observations indicate that the damping for our Ni films is large. In contrast to the Cr film signals, showing a sharp increase in signal at the highest fluences, the Ni film signal drops sharply.

A final observation is that the behavior at low temperatures deviates slightly from that at room temperatures. Although we will not discuss the details of the low-temperature results, the data suggest that for each temperature (as well as each fluence) the wave shape should be characterized separately to be able to properly describe acoustic wave propagation in the substrate (Chs. IV - VI).

III.4.3 Acoustic attenuation

The properties of the second acoustic echoes shown in Figs. III.4 and III.5 compared to the first one can be used to determine the acoustic attenuation of the metal. The signal-to-noise ratio of the third echo unfortunately did not allow to use the ratio of the third relative to the second. We will assume that damping of the phonon angular frequency component ω in the phonon spectrum $\tilde{s}(\omega)$ depends exponentially on the propagation distance z multiplied by the frequency-dependent attenuation coefficient $\alpha(\omega)$:

$$\tilde{s}(\omega) = \tilde{s}_0 \exp(-\alpha(\omega)z). \tag{III.7}$$

There are several sources of ultrasonic attenuation in metals. In solids at finite temperatures scattering with thermal phonons, so-called Akhieser damping, and thermoelastic damping are important [15]. The corresponding attenuation factors are proportional to ω^2 and strongly temperature dependent. In addition, in metals, there is a contribution $\propto \omega$ due to electron-phonon interaction [16]. We have estimated the typical acoustic frequencies that will be affected in Ni and Cr films of these thicknesses to be above 500 GHz so that this effect can readily be neglected. The leading contribution comes from the polycrystalline film structure, giving rise to grain-boundary scattering. This contribution does not necessarily show an ω^2-dependence [15]. An AFM measurement for a thin Cr film is shown in Fig. IV.1

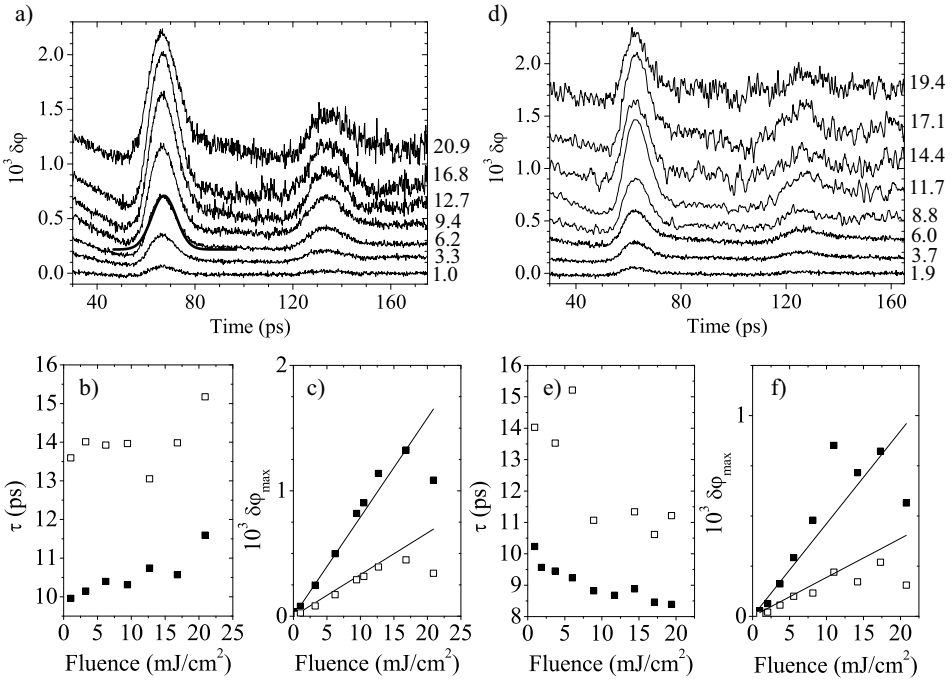

Figure III.5: Phase signals for Ni at room temperature and 30 K
a) Phase signals for Ni on Si, at room temperature and as a function of fluence. Numbers at the right axis indicate the pump fluence in mJ/cm^2. A sample Gaussian fit result is shown in the trace for 6.2 mJ/cm^2 by a thick solid line. b) Temporal width τ of the first (filled squares) and second (open squares) acoustic reflection, as a function of pump fluence. c) Amplitude of the first (filled squares) and second (open squares) as a function of fluence. Solid line through points for first reflection is a fit to low fluence amplitudes. Solid line through points for second reflection is a multiplication of this fit by the expected 0.42 amplitude reflection coefficient at the Ni/Si interface. d) - f) As for figures a) - c), but now obtained at 30 K.

b). The typical grain size d_{gr} is ~ 30 nm. A reasonable estimate would be that this grain size effects frequencies around $v_s/2d_{gr}$, yielding a value of 110 GHz for Cr, indicating that this effect is important.

For now, we will assume that α is proportional to ω^2. Once the Gaussian width τ_1 and amplitude a_1 of the first echo are determined, the Gaussian can be Fourier transformed, and multiplied by the acoustic attenuation $\exp\left(-\alpha_d\omega^2\right)$, with α_d the frequency-independent attenuation coefficient for a propagation dis-

Material	Cr	Cr	Ni	Ni
Temperature	295 K	30 K	295 K	30 K
α_0 (GHz^{-2}m^{-1})	145 ± 17	150 ± 24	395 ± 15	471 ± 66

Table III.2: Attenuation coefficients derived from experiments
Frequency-dependent attenuation is defined as $\alpha(f) = \alpha_0 f^2$, with f in GHz.

tance $2d$. Transforming back to the time domain, we find for the second echo

$$s_2(t) = a_1 \frac{\tau_1^2}{\sqrt{8\alpha_d + \tau_1^2}} \exp\left(\frac{-2t^2}{8\alpha_d + \tau_1^2}\right). \tag{III.8}$$

Finally, we wish to express the damping as $\exp\left(-\alpha_0 f^2 z\right)$, with $f = 2\pi\omega$. Then, $\alpha_0 = 2\pi^2\alpha_d/d$. The attenuation factors α_0 extracted from the data are collected in Table III.2, for the determined film thicknesses, echo widths, and amplitudes. For both Cr and Ni no significant temperature dependence is found. Attenuation can thus be attributed to scattering on grains in the metal film. We will touch upon this subject again in Chs. IV and V. For Cr, the determined value agrees excellently with the literature value $\alpha_0 = 150$ GHz^{-2}m^{-1} [4]. The value for Ni differs significantly from literature values [4, 17]: if the value of Ref. [17] is extrapolated, a value $\alpha_0 = 26$ GHz^{-2}m^{-1} is found. Given the fact that the attenuation depends strongly on film quality [17], this suggests that our film quality is poor.

III.4.4 Pump-probe experiments at opposite side

All presented measurements suffer from an electronic contribution $\delta\varphi_{metal}$ according to Eq. (III.2) in the phase signal (in particular in the Cr case), a poorly defined background level, and a large noise due to strong heating of the surface at high fluences (Fig. III.3). We have therefore resorted to a geometry that separates the acoustic signal from the thermal one, reducing the noise and background bias. Probing is performed opposite to the pump side of the metal film through a transparent substrate, as depicted in the insets of Fig. III.6 d) and Fig. III.7 d).

For Cr, we focus on the amplitude (ρ) measurements, since the large sensitivity allows for a reliable analysis. Measurements for indicated fluences are shown in Fig. III.6 a), up to the damage threshold of ~ 22 mJ/cm^2. At $t = 0$, heating effects are induced by the pump in the bulk of the film, sensed from the other side.

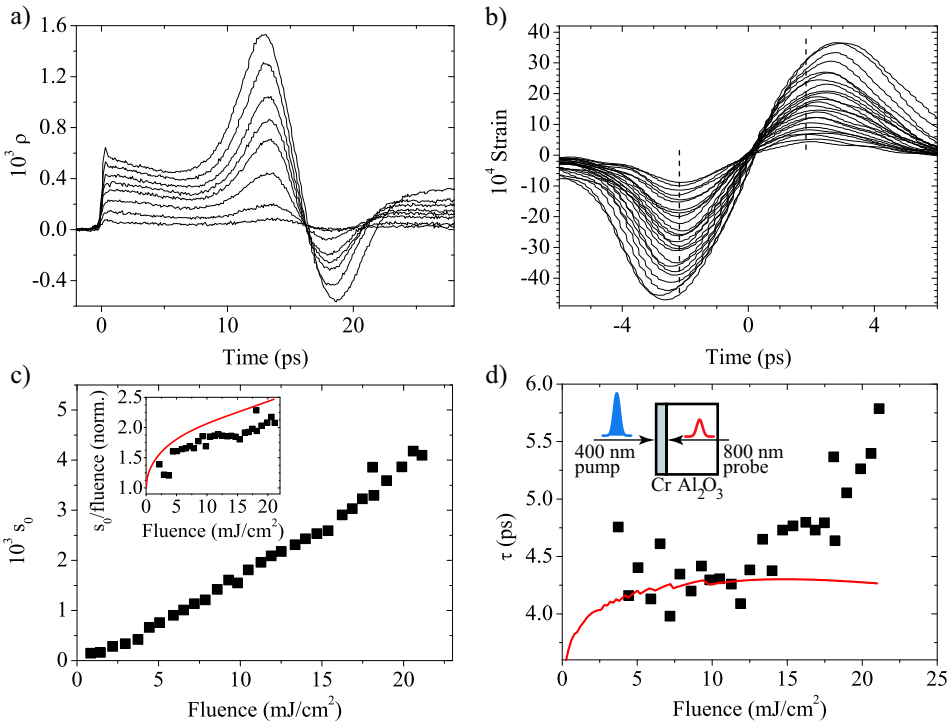

Figure III.6: Results for Cr film on sapphire at room temperature
a) Measured ρ wave traces for indicated pump fluences. b) Extracted strain pulse shape, for fluences from 4.4 mJ/cm^2 up to 21.1 mJ/cm^2, increasing in steps of 0.7 mJ/cm^2. Dashed lines indicate positions of maximum amplitude for low fluences. c) Maximum strain amplitude s_0 versus fluence. Inset shows maximum strain amplitude, divided by fluence and normalized to 1 at the lowest fluences. Solid line indicates width as calculated from the nonlinear model presented in Sec. III.5. d) Temporal width τ versus fluence (points: measured, solid line: calculated). Inset shows pump-probe geometry.

It takes the generated strain at the outer film surface around 15 ps to travel through the Cr film. From this travel time, the film thickness was determined at 104 nm.

To extract the strain profile, the measured signals are deconvoluted according to Eq. (III.1). Here, the different interface properties with respect to detection at the Cr/air interface (affecting the reflection properties and redefining the sensitivity function of Fig. III.2 a)) were taken into account. The 0.04 acoustic reflection coefficient at the Cr/sapphire interface was accounted for by defining $f(-z) = 0.04\,f(z)$ and expressing the measured signal in a simple convolution in-

tegral $\int_{-\infty}^{\infty} f(z)s(z,t)\mathrm{d}z$. The signal amplitude was multiplied by $(1-R_{\mathrm{air/Al_2O_3}})^{-2}$ to correct for the reflections $R_{\mathrm{air/Al_2O_3}} \sim 7.5\%$ on the sapphire/air interface that do not probe the Cr/sapphire interface. High-frequency noise filtering was applied to the data with a cut-off frequency of 200 GHz. At this frequency, the spectral intensity of the coherent wave was found to be below that of the noise. The obtained waveforms are presented in Fig. III.6 b). Strains with a typical width of 5 ps, and a maximum amplitude of 4.2×10^{-3} are found. The wave profiles are characterized by the amplitude s_0 (defined as half the difference of minimum and maximum strain amplitude) and the width τ (defined as the distance in time between these two extrema). Fig. III.6 c) and d) summarize the derived values. As is clearly demonstrated in the inset in Fig. III.6 c), the amplitude s_0 increases superlinearly above 7 mJ/cm^2, up to $\sim 70\%$ above the low fluence extrapolation. In the same range, the temporal width τ stabilizes at ~ 4 ps up to 17 mJ/cm^2, where it sharply increases to 6 ps at a fluence of 21 mJ/cm^2.

Because the Ni metal film sensitivity functions are very low (Fig. III.2), we resorted to $\delta\varphi$ measurements. Results for Ni are collected in Fig. III.7 a). The $t = 0$ point was determined from the high-fluence measurements in Fig. III.8 b), yielding a film thickness of 110 nm. Because the bulk contribution Eq. (III.2) is small, calculating the derivative of the measured signal according to Eq. (III.5) yields an accurate measure for the strain. Like for the Cr case, a correction factor to Eq. (III.5) has to be taken into account due to the different geometry:

$$\delta\varphi(t+\Delta t) - \delta\varphi(t) = c\frac{8\pi}{\lambda} v_s \Delta t s(d_{\mathrm{Ni}}, t) \times n_{\mathrm{Al_2O_3}} \times \frac{(1-r_{ac})^2}{4} \times (1-R_{\mathrm{air/Al_2O_3}})^2, \qquad \text{(III.9)}$$

where c is the interferometer contrast. The sapphire index of refraction $n_{\mathrm{Al_2O_3}} = 1.76$ accounts for the different wavelength in sapphire, $\frac{(1-r_{ac})^2}{4}$ for the partial acoustic reflection $r_{ac} = -0.08$ at the Ni/sapphire interface ($z = d_{\mathrm{Ni}} = 110$ nm), and $(1-R_{\mathrm{air/Al_2O_3}})^2$ for the non-interfering optical reflections at the sapphire surface. Again, high-frequency filtering was applied to reduce noise. The transient strain profiles as a function of fluence are collected in Fig. III.7 b). Importantly, the generated strain amplitudes are a factor of three higher than for Cr, leading to a maximum strain amplitude of 1.4% at a lower damage threshold. The superlinearity in amplitude, shown in Fig. III.7 c), is smaller than for Cr, and becomes apparent only at higher intensities. The width τ in Fig. III.7 d) is nearly indepen-

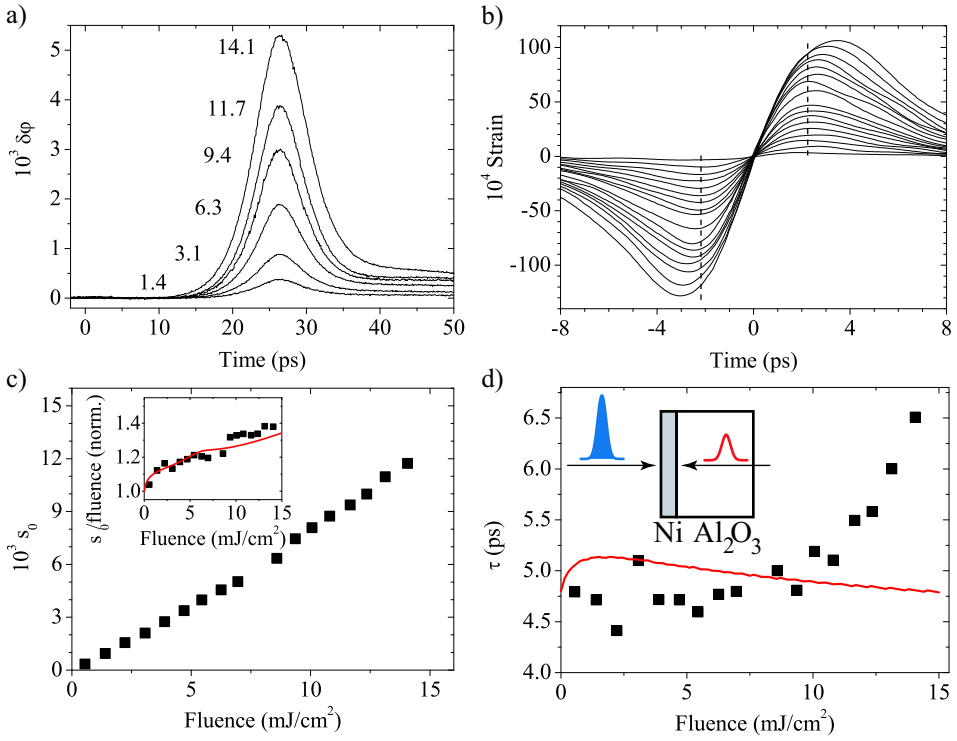

Figure III.7: Results for Ni film on sapphire at room temperature
a) Measured $\delta\varphi$ wave shapes for indicated fluences. b) Extracted strain wave shape for fluences 1.4 mJ/cm^2 - 14.1 mJ/cm^2, increasing in steps of 0.7 mJ/cm^2. Dashed lines indicate positions of maximum amplitude for low fluences. c) Maximum strain amplitude s_0 versus fluence. Inset shows maximum strain amplitude, divided by fluence and normalized to 1 at the lowest fluences. Solid line indicates width as calculated from the nonlinear model presented in Sec. III.5. d) Temporal width τ versus fluence (points: measured, solid line: calculated). Inset shows pump-probe geometry.

dent of fluence up to 10 mJ/cm^2, where it sharply increases.

The measured signals above the damage threshold are presented in Fig. III.8. For both metals, a damaged point can be observed by eye. Strain generation appeared to be irreversible as well. From the observed decrease in heat pulse arrival time as well as that of the coherent strain, we conclude that the total heat penetration depth has increased. In the case of Cr, up to a fluence of 27 mJ/cm^2 the signal amplitudes keep increasing, as does the width of the wave, boosting the strain generation efficiency with respect to the undamaged situation. Above this

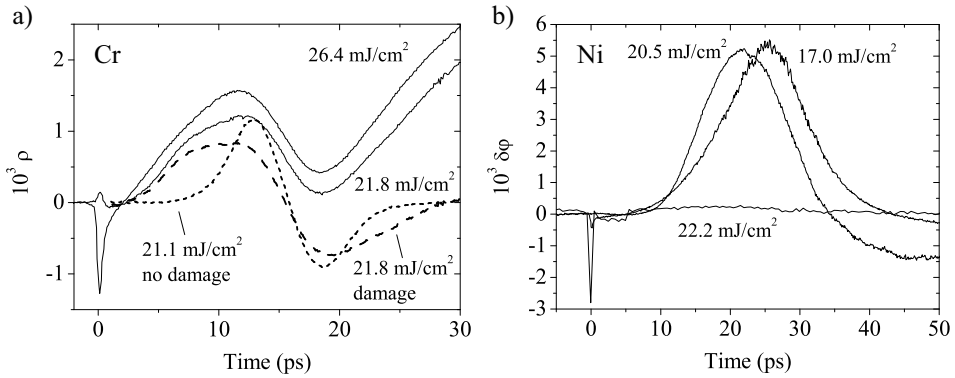

Figure III.8: Measured signals for Cr and Ni in the destructive regime
a) Measured amplitude signals for Cr above the damage threshold of 21 mJ/cm^2 (solid lines). The long and short dashed line signals are the background corrected contributions due to coherent strain just above and below the damage threshold, respectively. b) Measured phase signals for Ni, above the damage threshold of 14.5 mJ/cm^2.

fluence, the coherent strain signal disappeared. The efficient strain generation was exploited in Ch. IV to promote nonlinear propagation. For Ni above the damage threshold, the strain generation does not increase anymore, to decline to zero at a value of 22 mJ/cm^2.

III.5 Generation process

The strain generation at high pump fluences shows distinct nonlinear behavior both of the amplitude and of the temporal width. In order to explain this, we now examine the generation mechanism. The first theoretical model applied to ultrafast heating of metals can be found in Ref. [3]. Here, the effect of the optical pump pulse was taken to be instantaneous and the resulting heat profile and strain profile were calculated taking into account heat diffusion. The electron gas and lattice were taken to be in local equilibrium at all times. More recent approaches take the dynamics into account that occurs *within* the pump pulse duration, and permit a considerable difference of electron and lattice temperature during a period of time [4, 9, 18]. We will employ this so-called two-temperature model, already introduced in the beginning of this chapter.

Most relevant Ni and Cr material properties can be found in Ref. [4]. Other parameters will be explicitly stated here. All results presented and assumptions

used in our analysis are valid as long as the electron temperature $T_e < 0.1T_F$ (T_F the Fermi temperature) [2, 19]. The Fermi energies for Cr and Ni are 11.7 eV and 9.2 eV, respectively [20], which means that our calculations are valid for $T_e < 10^4$ K.

III.5.1 Two-temperature model

Because $\zeta, z_e, d \ll w_{pump}$, the relevant dynamics is essentially one-dimensional [21]. The two coupled differential equations governing the time- and space-dependent electron temperature $T_e(z,t)$ and lattice temperature $T_i(z,t)$ read

$$C_e \frac{\partial T_e}{\partial t} = \frac{\partial}{\partial z}\left(\kappa_0 \frac{\partial T_e}{\partial z}\right) - g(T_e - T_i) + \frac{S(t)}{\zeta}\exp\left(-\frac{z}{\zeta}\right), \tag{III.10}$$

$$C_i \frac{\partial T_i}{\partial t} = g(T_e - T_i). \tag{III.11}$$

In these equations, C_e and C_i are the electron and lattice heat capacities, respectively, and κ_0 the thermal conductivity of the material. In the right part of Eq. (III.10) three terms can be distinguished. The first describes hot electron diffusion, the second the energy loss from the electron gas due to coupling to the lattice, and the third the energy absorbed from the pump excitation pulse (source term). When the center of the pump pulse arrives at $t = 0$ and the Gaussian temporal width is τ_p, $S(t)$ is related to the pump fluence I_0 as

$$S(t) = I_0(1-R)\frac{1}{\sqrt{2\pi}\tau_p}\exp\left(-\frac{t^2}{2\tau_p^2}\right). \tag{III.12}$$

The source term is normalized such that $\int\int S(t)/\zeta \exp(-z/\zeta)\mathrm{d}z\ \mathrm{d}t = I_0(1-R)$, the absorbed energy per pulse and per unit area. The stress $\delta\sigma(z,t)$ that is exerted due to the transient temperature changes $\delta T_e(z,t)$ and $\delta T_i(z,t)$, is [10]

$$\delta\sigma(z,t) = -\frac{2}{3}C_e\delta T_e(z,t) - \gamma_i C_i \delta T_i(z,t), \tag{III.13}$$

where $\gamma_i = 3B\beta(T)/C_i$ is the Grüneisen constant, with B the bulk modulus and $\beta(T)$ the temperature-dependent thermal expansion coefficient [22, 23, 24]. The room temperature values for these parameters are specified in Table III.3. The lattice contribution to stress generation is in general much larger than the electronic

	Cr	Ni
Grüneisen constant γ_i	1.24 [25]	1.84 [25, 26]
Bulk modulus B (10^{11} N/m^2)	1.90 [25, 27]	1.86 [27]
Thermal expansion coeff. β (10^{-5} K^{-1})	0.41 [23]	1.29 [24]

Table III.3: Room temperature values of mechanical parameters for Cr and Ni

contribution.

The generated strain $\delta s(z,t,t')$ is a travelling contribution, depending on generation time t, position z, and propagation time t':

$$\delta\sigma(z,t) \rightarrow \frac{1}{2\rho {v_s}^2}\delta s(|z-v_s(t'-t)|,t')\ \mathrm{sgn}(z-v_s(t'-t)), \tag{III.14}$$

where $\rho {v_s}^2$ is equal to the elastic constant of the material. The factor 1/2 stems from the fact that stress is applied in the positive and negative z-directions, resulting in two strain contributions travelling in opposite directions. The sign function in this expression ensures that one of these contributions travels to the free surface and reflects with sign -1. In order to calculate the total coherent strain that is generated in this process, the contributions δs are integrated over all generation times t:

$$s(z,t') = \int_{-\infty}^{\infty} \delta s(|z-v_s(t'-t)|,t')\ \mathrm{sgn}(z-v_s(t'-t))\mathrm{d}t. \tag{III.15}$$

In this model (fast) ballistic electron propagation and (slow) heat diffusion carried by phonons are neglected, but electron diffusion is taken into account [4]. These effects can broaden the final coherent strain wave packet. Since some of the parameters involved in calculating the temperature profiles and the strain wave shape are not known from literature for 30 K, we limit ourselves to room temperature results.

III.5.2 Linear regime

For a small temperature rise, the material parameters can be assumed constant and, neglecting the electronic strain contribution, an exact solution of the coupled differential equations Eqs. (III.10) - (III.11) can be found [11]. The resulting strain spectrum reads

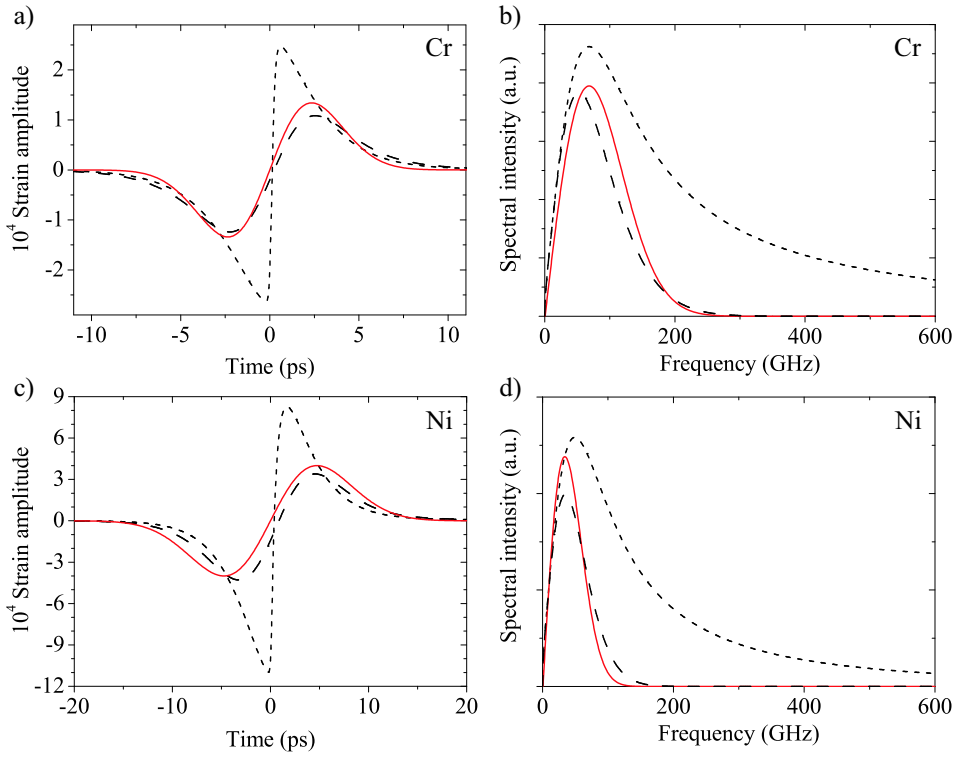

Figure III.9: Generated strains calculated by the linear model
a) Strain temporal profile in Cr as calculated from Eq. (III.16), for a fluence of 1.0 mJ/cm^2. Short dash: at generation position. Long dash: *Idem*, after propagation over $2d_{\mathrm{Cr}} = 368$ nm, given the value determined for α_0 (Table III.2). Solid line: Gaussian derivative, of width $\tau = 4.8$ ps, with arbitrary amplitude scaling. b) Spectra of the profiles indicated in a), represented by the same line styles. c) Calculated strain temporal profile in Ni, for a fluence of 1.0 mJ/cm^2. Short dash: at generation position. Long dash: *Idem*, after propagation over $2d_{\mathrm{Ni}} = 398$ nm, given the determined value for α_0 in Table III.2. Solid line: Gaussian derivative, of width $\tau = 10$ ps, with arbitrary amplitude scaling. d) Spectra of the profiles indicated in c), represented by the same line styles.

$$\tilde{s}(z,\omega) = \frac{3B\beta\tilde{S}(\omega)\omega^2 \exp[\frac{i\omega z}{v_s}]}{\rho\kappa_0 {v_s}^4 (1-\frac{i\omega C_i}{g})(1+\left(\frac{\zeta\omega}{v_s}\right)^2)} \times \frac{1}{p}\left(\frac{1}{p^2+(\frac{\omega}{v_s})^2}+\frac{\zeta^2}{1+\zeta p}\right), \text{ with} \tag{III.16}$$

$$p = \left(-\frac{i\omega C_e}{\kappa_0}\left(1+\frac{\frac{C_i}{C_e}}{1-\frac{i\omega C_i}{g}}\right)\right). \tag{III.17}$$

Here, $\tilde{S}(\omega)$ is the Fourier transform of $S(t)$ in Eq. (III.12). The value of g for Cr is constant for room temperature experiments and at low fluences [28]. A recent publication shows that for Ni, g can vary by a substantial amount already for a small temperature rise [29]. We estimate an average value for Ni of g of 9×10^{17} $\mathrm{Wm^{-3}K^{-1}}$ for the current pump fluence [30], although the calculations did not show statistical difference between using this value and the value of 4.4×10^{17} $\mathrm{Wm^{-3}K^{-1}}$ used in Ref. [4].

The calculated spectra according to Eqs. (III.16) - (III.17) were Fourier transformed to obtain the temporal profiles. The temporal and spectral results for Cr and a pump fluence $I_0 = 1$ mJ/cm^2 are presented in Fig. III.9 a) and b), respectively, and for Ni in Fig. III.9 c) - d). A large difference in strain amplitude is observed between these materials, mainly caused by the factor of three difference in thermal expansion coefficient (Table III.3). Both metals show an initially sharp temporal profile, and a peak in the spectrum ~ 65 GHz with a slowly decaying spectral intensity for increasing frequencies. These high frequencies are efficiently taken out of the coherent wave by acoustic attenuation while traversing ~ 400 nm of metal, thereby increasing the characteristic width to ~ 5 ps in Cr and ~ 10 ps in Ni.

Although the initial temporal and spectral shape strongly deviate from a Gaussian derivative as defined in Eq. (III.6), the solid lines in Fig. III.9 demonstrate that for large enough travel distances through the metal film a description by a Gaussian derivative is applicable for all practical purposes, by virtue of acoustic attenuation. The precise amplitude and width of this function therefore depend on film thickness and pump fluence.

It is also possible to follow the opposite path as in Figs. III.6 - III.7, i.e. take the calculated strain profile for a low fluence and a propagation distance of ~ 100 nm, determine the differential amplitude and phase signals, and compare these to

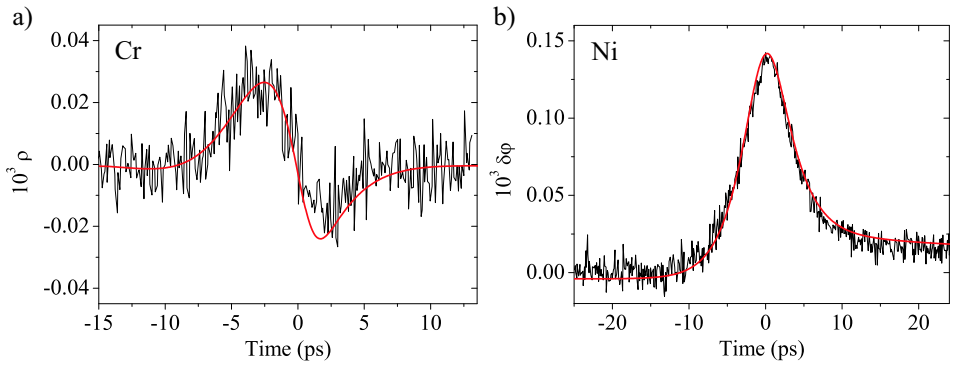

Figure III.10: Comparison between calculation and experiment, linear regime
a) Measurement (thin line) of ρ signal for Cr and a fluence of 0.84 mJ/cm^2, and calculation (thick line) for the same fluence according to Eqs. (III.1), (III.16) and (III.17). b) Measurement (thin line) and calculation (thick line) of $\delta\varphi$ signal for Ni at a fluence of 0.54 mJ/cm^2.

the measured curves. The result is shown in Fig. III.10 a) for a ρ measurement on Cr and b) for a $\delta\varphi$ measurement on Ni, both for a fluence < 1 mJ/cm^2. In both cases, excellent agreement is achieved. Note that for these low fluences, the deconvolution and derivative procedures used for Figs. III.6 b) and III.7 b) do not yield reliable results. The differences in the trailing part of Fig. III.10 a) can be caused by slightly different values for the elasto-optical constants for 800 nm as compared to 830 nm. In conclusion, the linear model describes the results fairly well at these moderate fluences [4].

III.5.3 Nonlinear regime I: Simple model

The assumption that the material parameters remain constant is valid only for very low pump fluences. The electronic heat capacity can change by an order of magnitude, since it scales in first approximation as $C_e(T) = C_{e,0} \times T_e$ [27]. An estimate for the fluence $I_{0,e}$ at which C_e is significantly changed (for example by 50%) for Cr and Ni is $I_{0,e} \sim (0.5 C_e(T_0) T_0 \zeta)/(1-R)$, yielding fluences of 0.04 and 0.12 mJ/cm^2, respectively. Because of the much larger heat capacity of the lattice, the fluence $I_0 = I_{0,i} \sim (0.5 C_i T_0 \zeta)/(1-R)$ at which the lattice temperature is significantly increased is much larger: $I_{0,i}$ equals 1.2 and 1.5 mJ/cm^2 for Cr and Ni, respectively.

The parameters related to the lattice, C_i, κ_0 and β, in general depend non-

Parameter	Units	Ni Reference	Cr Reference
C_e	J m^{-3} K^{-1}	[4, 29]	[4]
C_i	J m^{-3} K^{-1}	[33]	[34]
κ_0	W/(m K)	[4, 35]	[4, 35]

Table III.4: References for temperature dependence of important parameters
A phenomenological temperature dependence is derived from the experimental data, presented in the references in the table. The temperature dependence for the thermal expansion coefficient β can be found in the references in Table III.3.

trivially on temperature and no functional forms are known. For example, nickel shows a magnetic phase transition at around 620 K [24], affecting both the expansion coefficient and heat capacity. References are collected in Tables III.3 and III.4. With an empirical function a fit to the measured or calculated data was made which appeared to deviate less than 10% from the experimentally determined values.

When $T_e \neq T_i$, the electron thermal conductivity can be described by [31, 32]

$$\kappa_T(T_e, T_i) = \kappa_0(T_i) \frac{T_e}{T_i(1-\alpha) + \alpha {T_e}^2/T_0}, \tag{III.18}$$

where the conductivity prefactor κ_0 depends exclusively on T_i. The numerator in the fraction takes into account that electron diffusion increases for elevated electron temperatures $\propto T_e$. The two terms in the denominator contain model electron-phonon scattering and electron-electron scattering terms, respectively, with α the ratio of the electron-electron and electron-phonon collision frequencies at room temperature. In general $\alpha \ll 0$, and electron-phonon collisions are dominant at low pump fluences [32]. In transition metals, the value of α is around 10% [31]. Then, electron-electron collision processes start to limit electron diffusion when $T_e \sim T_0/\alpha^{1/2}$, typically at electron temperatures < 1000 K, which we expect to reach in our experiments already at moderate fluences. For the moment, we leave α as free parameter.

One expects a significant change in strain wave shape when either the heat diffusion length (determining the pulse width) or the expansion coefficient $\beta(T)$ averaged over the lattice temperatures reached (determining the pulse amplitude) change substantially. To obtain estimates for the increase in amplitude and width,

the following crude model is used. First, the maximum electron temperature

$$T_{max,e}(I_0) \sim T_0 \sqrt{1 + \frac{2I_0(1-R)}{C_{e,0}{T_0}^2 z_{eff}(T_{max,e})}} \tag{III.19}$$

and the effective heat deposition depth $z_{eff}(T_{max,e}) \sim (\zeta^2 + z_e(T_{max,e})^2)^{1/2}$, with $z_e(T_{max,e}) \sim \sqrt{\kappa_T(T_{max,e}, T_0)}$, were selfconsistently derived [36]. Knowing $z_{eff}(I_0)$, the maximum lattice temperature $T_{max,i}$ is determined from

$$\frac{I_0(1-R)}{z_{eff}(I_0)} = \int_{T_0}^{T_{max,i}} C_i(T)\mathrm{d}T, \tag{III.20}$$

and the resulting average thermal expansion coefficient from

$$\bar{\beta}_I(I_0) = \frac{\int_{T_0}^{T_{max,i}} \beta(T)\mathrm{d}T}{T_{max,i} - T_0}. \tag{III.21}$$

The relative change in effective deposition depth $z_{eff}(I_0)/z_{eff}(0)$ and relative expansion coefficient $\bar{\beta}_I(I_0)/\beta_I(0)$ are used to rescale the width and amplitude of the low-fluence wave packets shown in Fig. III.8. The known propagation distance through Cr and Ni and acoustic attenuation are incorporated to obtain the final width τ and relative amplitude as a function of pump fluence.

The results for these two parameters are shown as solid lines in the insets of Figs. III.6 c) and III.7 c) (relative amplitude), and Figs. III.6 d) and III.7 d) (τ). In these calculations, we used values of $\alpha = 0.5\%$ for Cr, much lower than expected, and 10% for Ni. We note that the result for Cr is not very reliable since in that case the assumptions in our model are not quite valid [36].

The widths τ derived from the quasi-equilibrium calculation Eqs. (III.16) - (III.17) are 3.2 ps for Cr and 4.8 ps for Ni, respectively. The amount of change of both width and amplitude in Cr is much larger than in Ni. The stronger increase in width in Cr at low fluences originates from its factor of five smaller electronic heat capacity, so that less energy is required to modify the effective diffusion depth. Note that the calculated increase in width saturates already < 2 mJ/cm^2 fluences for both metals, due to significant increases in lattice temperature and electron-electron scattering, limiting the electron diffusion length (Eq. (III.18)). The stronger amplitude increase in Cr with respect to Ni is due to the strong temperature dependence of the expansion coefficient over the accessed temperature range (for Cr, the change is more than a factor of two, for Ni only 40%).

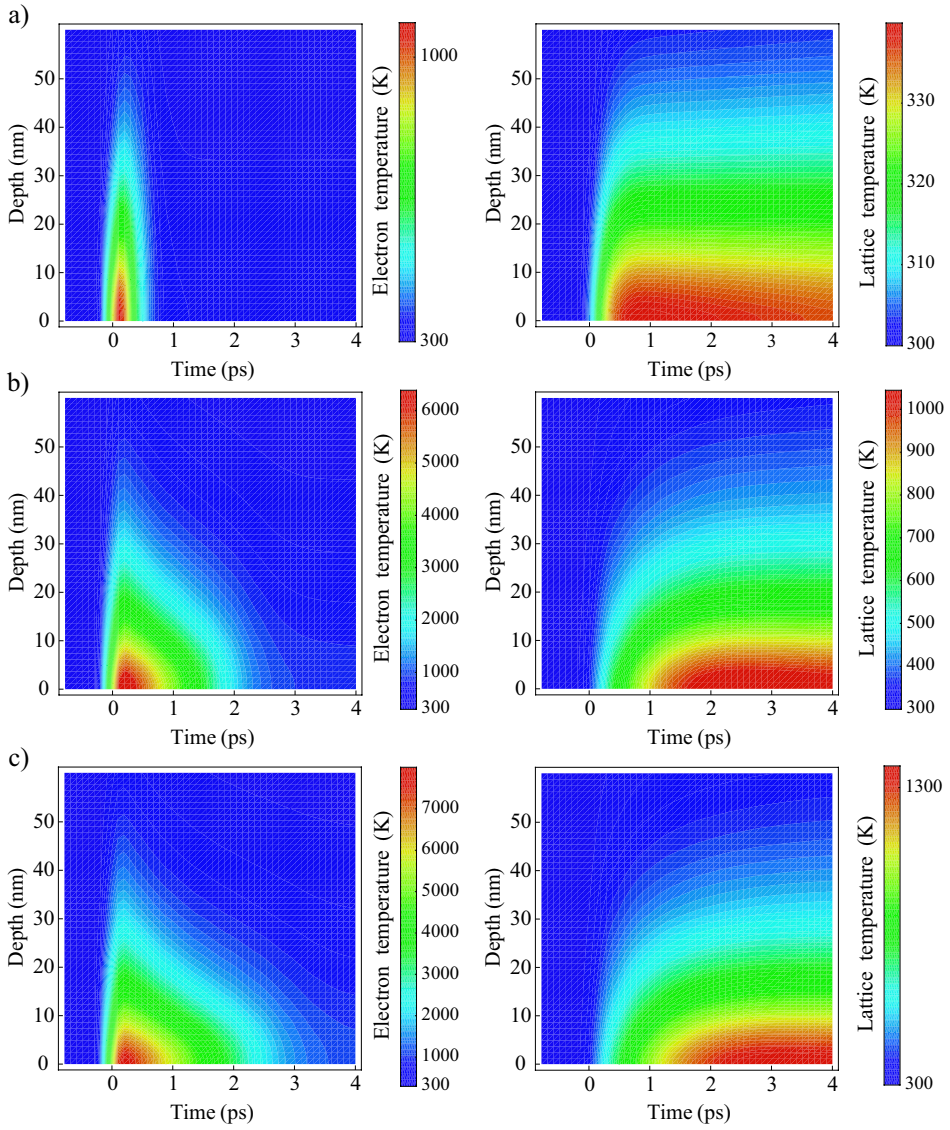

Figure III.11: Nonlinear temperature dynamics in Cr (Color figure: Fig. 2, p. 203) Electron (left panel) and lattice (right panel) temperatures for Cr as a function of time and position in the film, for pump fluences a) $I_0 = 0.83$ mJ/cm^2, b) $I_0 = 14.0$ mJ/cm^2, and c) $I_0 = 20$ mJ/cm^2.

This simple model explains the qualitative characteristics up to fluences of 16 mJ/cm^2 for Cr, and 10 mJ/cm^2 for Ni. Above these fluences, the measured widths rapidly increase, suggesting enhanced electron diffusion. From this model, we estimate $T_{max,e} \sim 7300$ K and $T_{max,i} \sim 1070$ K for Cr, and $T_{max,e} \sim 2700$ K and $T_{max,i} \sim 1200$ K for Ni at the measured damage threshold. The lattice temperatures are much lower than the melting temperatures of 2120 K (Cr) and 1726 K (Ni), mostly assumed to be the point at which damage occurs [2]. It should be noted that this model estimates the average temperatures in the surface layer several picoseconds after the pump pulse. The temperatures in the first nanometers of the film and shortly after pumping can exceed the calculated averages by a substantial amount.

III.5.4 Nonlinear regime II: Exact solution

In order to make a more accurate prediction of the generated wave, a full numerical evaluation of Eqs. (III.10) - (III.15) was performed, taking due account of the temperature dependences of all relevant material parameters. For Ni, the temperature dependence of g and C_e as calculated by Ref. [29] was incorporated. Since we have no information about the temperature dependence of g and C_e for Cr, we assume that the room temperature value and the $\propto T_e$-behavior are valid up to the estimated maximum electron temperatures in the previous section [37]. α was again left as free fit parameter in the calculations.

The numerical solution of Eqs. (III.10) - (III.11) was performed in Fortran, for a time window -1 ps - 6 ps around the pump pulse arrival time $t = 0$. Fig. III.11 shows contour plots of the calculated T_e and T_i in Cr as a function of time and depth in the film, for three fluences. The lowest fluence was taken equal to the one depicted in Fig. III.10 a), to allow for a comparison. At the highest pump fluence of 20.6 mJ/cm^2, the maximum lattice temperature at the surface was ~ 1400 K, larger than the estimates in the previous section, and approaching the melting temperature.

We fit a value of $20 \pm 10\%$ for α, much larger than in the simple model of the previous section, but in agreement with estimates of Refs. [31, 32]. This makes electron-electron scattering the dominant contribution in Eq. (III.18) at $T_e \sim 700$ K. The results of Fig. III.11 a) show that this value is reached already at the pump fluence of 0.83 mJ/cm^2. Due to electron-electron scattering, the effective penetration depth does not increase significantly for higher fluences, as is also observed in Fig. III.11 b) and c). Analogous results for the temperature profiles

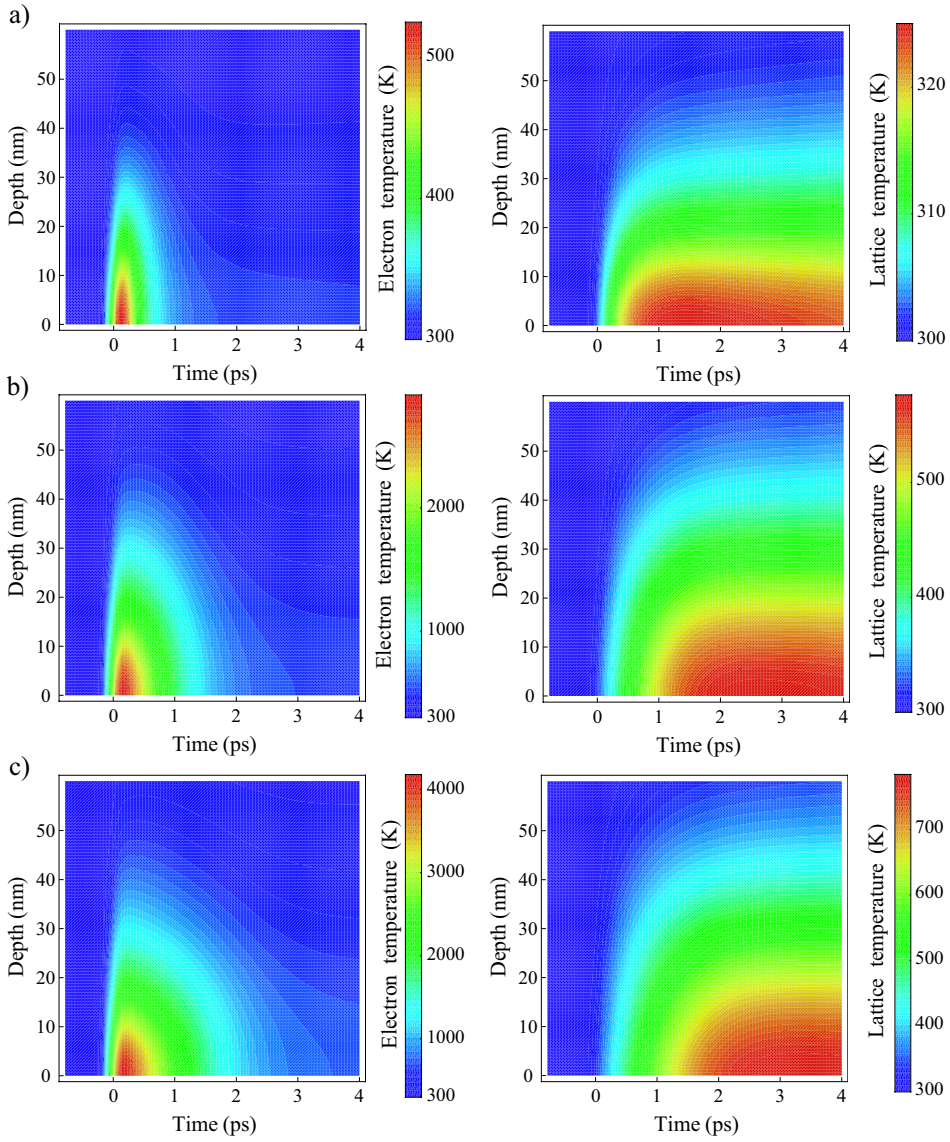

Figure III.12: Nonlinear temperature dynamics in Ni (Color figure: Fig. 3, p. 204)
Electron (left panel) and lattice (right panel) temperatures for Ni as a function of time and position in the film, for pump fluences a) $I_0 = 0.54$ mJ/cm^2, b) $I_0 = 8.56$ mJ/cm^2, and c) $I_0 = 14.1$ mJ/cm^2.

for Ni are shown in Fig. III.12. We derive a value of α of $5 \pm 3\%$. The step in amplitude at 9 mJ/cm^2 in Ni visible in the inset in Fig. III.7 c) is possibly due to the phase transition in Ni [24], since Fig. III.12 b) demonstrates that the phase transition temperature of ~ 620 K is reached at 8.6 mJ/cm^2.

The calculated ρ for Cr signals are shown in Fig. III.13 a) - c) for the three fluences presented in Fig. III.11, where we take into account the effects of propagation through 104 nm. The calculated $\delta\varphi$ signals for Ni are shown in Fig. III.13 d) - f). The calculations for the lowest fluence agree qualitatively with the result of the analytical solution shown in Fig. III.10. However, Fig. III.13 shows that the numerical calculation underestimates the volume of the compressive part by $\sim 15\%$ for both Cr and Ni, and cannot explain the asymmetric wave. The reason for this is unclear, and will be investigated in the near future. Fig. III.13 b) shows the calculated signal shapes for both $\alpha = 0\%$ and $\alpha = 20\%$, demonstrating the need to take into account electron-electron scattering to track the measured traces reliably. From the fact that the agreement between measurement and calculation is reasonable at the intermediate fluences of 14 mJ/cm^2 for Cr, and 8.6 mJ/cm^2 for Ni, we conclude that the superlinear growth in strain amplitude due to the expansion coefficient β growing with T_i is taken into account properly.

Since in the current model the diffusion is limited by electron-electron scattering processes, effectively *decreasing* the diffusion length for larger pump fluences, it cannot explain the strong increase in width at the highest fluences for both metals. Possibly, this is due to a significant modification of the thermal Fermi distribution, affecting all material "constants" to a large extent [10, 29]. It is beyond the scope of this thesis to examine this effect further.

III.6 Conclusions

In this chapter, we have examined strain generation and propagation in thin nickel and chromium films as a function of pump fluence. The strain wave shape changes significantly while increasing the fluence. In a simple model, this can be explained by the increase of the thermal conductivity and expansion coefficient with temperature. A full theoretical analysis, performed in both the linear and nonlinear regime accounts for the transient electron and lattice temperatures and non-equilibrium effects in the generation layer. A quantitative comparison between theoretical results and experiments yields good agreement up to 70% of the damage threshold. At this point, the dynamics apparently becomes nonthermal and

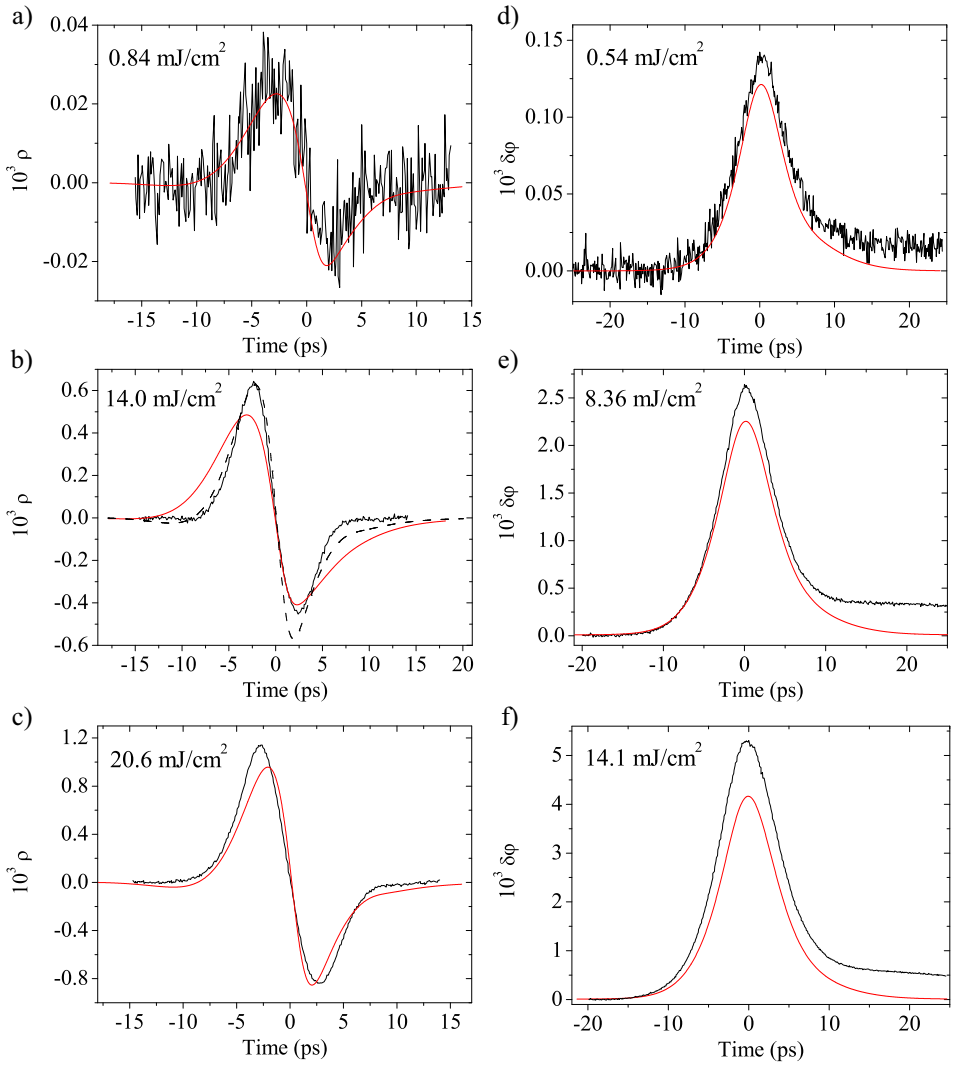

Figure III.13: Comparison of numerical calculations and experimental results
a) Measured ρ data (black line) and simulated trace (gray line, with $\alpha = 20\%$) for Cr and the indicated fluence. b) Measured ρ data (black line) at indicated fluence. Taking into account electron-electron scattering (dashed line, $\alpha = 20\%$, gray line, $\alpha = 0$) in calculations significantly improves agreement to measured data. c) Measurement (black line) and calculation for $\alpha = 20\%$ (gray line) diverge for the highest, nondestructive pump fluences. d) - f) Measured $\delta\varphi$ data (black line) and simulated trace (gray line) for Ni and the indicated fluences. $\delta\varphi$. Calculations were performed with $\alpha = 0.05$.

cannot be described by the two-temperature model anymore. Strain amplitudes are generated up to 1.4% in Ni, and 0.4% in Cr, without damaging the metal film. These are the highest nondestructive strains ever generated in metals. In Cr, the integrated strain increases even more when going above the damage threshold.

This way, a consistent picture of the strain generation process is obtained. The results are relevant for the following chapters, where we monitor the propagation of the generated strains in the sapphire substrate as a function of fluence and temperature. We now know that it is not possible to define a fixed wave shape with an amplitude depending linearly on fluence in high-amplitude picosecond acoustics. In Ch. IV, where strain is generated in Cr films, we therefore leave the strain amplitude (showing the strongest fluence dependence) as free fitting parameter. In Ch. V, the width of the input wave is also allowed to vary. The initially generated strain pulse strongly deviates from a Gaussian derivative shape. Modelling the propagating wave in this way, however, is validated from the fact that acoustic attenuation in the generation film removes the highest phonon frequencies from the generated wave packet, and reshapes the pulse to resemble a Gaussian derivative.

References

1. H.J. Maris. Picosecond ultrasonics. *Sci. Am.*, 86:278, 1998.
2. L. Jiang and H.-L. Tsai. Improved two-temperature model and its application in ultrashort laser heating of metal films. *J. Heat Transfer*, 127:1167, 2005.
3. C. Thomsen, H.T. Grahn, H.J. Maris, and J. Tauc. Surface generation and detection of phonons by picosecond light pulses. *Phys. Rev. B*, 34(6):4129, 1986.
4. T. Saito, O. Matsuda, and O.B. Wright. Picosecond acoustic phonon pulse generation in nickel and chromium. *Phys. Rev. B*, 67:205421, 2003.
5. O.B. Wright and K. Kawashima. Coherent phonon detection from ultrafast surface vibrations. *Phys. Rev. Lett.*, 69(11):1668, 1992.
6. A. Devos and C. Lerouge. Evidence of laser-wavelength effect in picosecond ultrasonics: Possible connection with interband transitions. *Phys. Rev. Lett.*, 86:2669, 2001.
7. S.D. Brorson, J.G. Fujimoto, and E.P. Ippen. Femtosecond electronic heat-transport dynamics in thin gold films. *Phys. Rev. Lett.*, 59(17):1962, 1987.
8. O.B. Wright and V.E. Gusev. Ultrafast acoustic phonon generation in gold. *Physica B*, 219-220(1-4):770, 1996.
9. O.B. Wright. Ultrafast nonequilibrium stress generation in gold and silver. *Phys. Rev. B*, 49(14):9985, 1994.
10. G. Tas and H.J. Maris. Electron diffusion in metals studied by picosecond ultrason-

ics. *Phys. Rev. B*, 49:15046, 1994.
11. O.B. Wright and V.E. Gusev. Ultrafast generation of acoustic waves in copper. *IEEE Trans. Ultrason. Ferroelectr. Contr.*, 42:331, 1995.
12. D.H. Hurley and O.B. Wright. Detection of ultrafast phenomena by use of a modified Sagnac interferometer. *Opt. Lett.*, 24(18):1305, 1999.
13. T. Tachizaki, T. Muroya, O. Matsuda, Y. Sugawara, D.H. Hurley, and O.B. Wright. Scanning ultrafast Sagnac interferometry for imaging two-dimensional surface wave propagation. *Rev. Sci. Instr.*, 77(4):043713, 2006.
14. O.L. Muskens and J.I. Dijkhuis. Interactions of ultrashort strain solitons and terahertz electronic two-level systems in photoexcited ruby. *Phys. Rev. B*, 71(10):104304, 2005.
15. B.A. Auld. *Acoustic Fields and Waves in Solids*, volume 1. Robert E. Krieger Publishing Company, 2nd edition, 1990.
16. J.W. Tucker and V.W. Rampton. *Microwave Ultrasonics in Solid State Physics*. North-Holland Publishing Company, 1st edition, 1972.
17. W. Sigle and O. Weis. Phase velocity and attenuation of 9 GHz hypersound in polycrystalline nickel films as a function of quartz-substrate temperature. *Z. Phys. B: Cond. Mat.*, 53:75, 1983.
18. T. Saito, O. Matsuda, and O.B. Wright. Ultrafast acoustic phonon pulse generation in chromium. *Physica B*, 316-317:304, 2002.
19. N.W. Ashcroft and N.D. Mermin. *Solid State Physics*. Holt, Rinehart and Winston, 1976.
20. V.L. Moruzzi, Y.F. Yanak, and A.R. Williams. *Calculated electronic structure and properties of solids*. Pergamon, 1978.
21. T. Dehoux, N. Chigarev, C. Rossignol, and B. Audoin. Effect of lateral electronic diffusion on acoustic diffraction in picosecond ultrasonics. *Phys. Rev. B*, 77(21):214307, 2008.
22. The factor of 2/3 is derived for a free electron gas, and forms a reasonable approximation for our metal films.
23. N.A. Dubrovinskaia, L.S. Dubrovinsky, S.K. Saxena, and B. Sundman. Thermal expansion of chromium (Cr) to melting temperature. *Calphad*, 21(4):497, 1997.
24. T. G. Kollie. Measurement of the thermal-expansion coefficient of nickel from 300 to 1000 K and determination of the power-law constants near the Curie temperature. *Phys. Rev. B*, 16(11):4872, 1977.
25. J.M. Wills and W.A. Harrison. Interionic interactions in transition metals. *Phys. Rev. B*, 28(8):4363, 1983.
26. C.V. Pandya, P.R. Vyas, T.C. Pandya, and V.B. Gohel. Volume variation of Gruneisen parameters of *fcc* transition metals. *Bull. Mat. Sci.*, 25(1):63, 2002.
27. C. Kittel. *Introduction to Solid State Physics*. John Wiley & Sons, 1st edition, 1996.
28. T.Q. Qiu and C.L. Tien. Short-pulse laser heating on metals. *Int. J. Heat Mass Transfer*, 35(3):719, 1992.

29. Z. Lin, L.V. Zhigilei, and V. Celli. Electron-phonon coupling and electron heat capacity of metals under conditions of strong electron-phonon nonequilibrium. *Phys. Rev. B*, 77(7):075133, 2008.
30. E. Beaurepaire, J.-C. Merle, A. Daunois, and J.-Y. Bigot. Ultrafast spin dynamics in ferromagnetic nickel. *Phys. Rev. Lett.*, 76(22):4250, 1996.
31. M.J. Laubitz. Electron-electron scattering in the high-temperature thermal resistivity of the noble metals. *Phys. Rev. B*, 2(6):2252, 1970.
32. P.B. Corkum, F. Brunel, N.K. Sherman, and T. Srinivasan-Rao. Thermal response of metals to ultrashort-pulse laser excitation. *Phys. Rev. Lett.*, 61(25):2886, 1988.
33. Y. Takahashi. High-temperature heat-capacity measurement up to 1500 K by the triple-cell DSC. *Pure & Appl. Chem.*, 69(11):2263, 1997.
34. J.-O. Andersson. Thermodynamic properties of chromium. *Int. J. Thermophys.*, 6(4):411, 1985.
35. *http://www.efunda.com*, and references supplied there.
36. Silent and simplifying assumptions in this model are that the heated zone $0 < z < z_{eff}$ can be considered to be uniformly heated, and that the energy relaxation time to the lattice $\tau_e = C_e/g$ is slow with respect to electron diffusion. The latter assumption is more valid in the case of Ni (where $\tau_e \sim 1$ ps is long) than for Cr ($\tau_e \sim 200$ fs) [4]. The variations of $\kappa_0(T_i)$ and g are for now neglected.
37. Lin [29] calculates the electron DOS for a range of metals. The electronic structure of Cr mostly resembles that of tungsten, with a partly filled electronic d-band. For this metal, g shows only minor $< 20\%$ deviations, and $C_e(T_e) \sim C_{e,0}T_e$ for $T_e <$ 3000 K. Based on these calculations, our assumption seems reasonable at least for fluences < 10 mJ/cm^2.

Chapter IV

The formation of acoustic shock waves in sapphire at room temperature

Abstract

Using both pump-probe reflectometry and interferometry, we study the propagation of laser-excited longitudinal, high-amplitude, coherent picosecond acoustic phonon wave packets in thin sapphire slabs at room temperature. We excite high-amplitude acoustic strain waves in a chromium film deposited on a thin sapphire slab, by 160-fs pulses from a 1-kHz Ti:sapphire regenerative amplifier. The bipolar strain pulse that is launched into the crystal, gradually transforms into a shock wave when attenuation by thermal phonons is weaker than the nonlinear action. These shock waves are detected at the opposite side of the slab. We observe significant stretching of the wave packet to several tens of picoseconds, accompanied by strong steepening of the wavefronts. The results demonstrate the supersonic and subsonic nature of propagation in viscous nonlinear media and the presence of acoustic frequencies in the wave packet as high as 500 GHz. All experimental data are in excellent agreement with simulations based on Burgers' equation.

IV.1 Introduction

Coherent acoustic pulses of picosecond time duration can be generated and detected using metallic transducers and ultrafast laser techniques [1]. This picosecond ultrasonics technique is widely used to investigate mechanical properties of thin films, electronic devices, and nanostructures [2, 3, 4, 5, 6]. Recently, the nonlinear character of acoustic wave propagation has been addressed using these techniques. For extremely high initial acoustic amplitudes, self-steepening takes place on submicrometer propagation distances and devastating laser-induced shock waves are formed [7, 8]. These shock waves are useful for examining ma-

terials under extreme conditions [9, 10, 11] and, when for example propagating through a photonic crystal, are predicted to be capable of capturing light and produce other stunning phenomena [12, 13, 14]. For moderate, nondestructive acoustic strains, propagating over long distances in crystals at cryogenic temperatures, lattice dispersion may balance self-steepening, ultimately leading to the formation of acoustic solitons [15] and ultrashort acoustic soliton trains [16]. These low-temperature experiments suggest soliton widths in sapphire as short as a few hundred femtoseconds [17] and in fact have opened up the field of *femtosecond ultrasonics*. This subject will be further explored in Ch. V.

It is important to identify the relevance of femtosecond ultrasonics for applications. Therefore, we examine nonlinear acoustic propagation at room temperature in nondestructive experiments. The generation of shock fronts in sapphire as steep as 1.2 ps will be demonstrated. Further, the nonlinear and viscous wave propagation at room temperature will be described quantitatively using Burgers' equation.

IV.2 Theory

To properly account for the observed signals, we have to discuss generation, propagation and detection mechanisms in more detail. Generation and detection of coherent longitudinal strain waves have been examined extensively in theoretical models [2, 3], and in Ch. III. We approximate the injected strain profile as the derivative of a Gaussian with a width of 5.1 ps [18], which faithfully tracks the wave shape observed at low fluences. In calculations, the width is fixed at this value, and the strain amplitude is left as the only free fit parameter as a function of fluence. Although taking a fixed width does not agree completely with the results obtained in Ch. III, this pragmatic approach suffices because the deviation will appear to be small compared to the stretched shock wave width. Theory shows that for our case in point, the tensile part may be somewhat smaller than the compressive part, but earlier work [19, 20] did not show any significant deviations of the calculated signal due to this asymmetry.

In order to describe propagation of high-amplitude wave packets at room temperature, one needs to modify the linear wave equation for propagation of a strain $s(z,t)$ by adding a term describing nonlinearity and a term accounting for scattering with thermal phonons:

	Sample thickness d_{sample}	Shock formation length λ_{nonl}	Attenuation length λ_{att}	Diffraction length λ_{diff}
Expression		$\frac{v_s^3\rho}{3\pi\lvert\alpha\rvert s_0 f}$	$\frac{c_{33}^{3/2}}{2\pi^2\rho^{1/2}\eta f^2}$	$\frac{w_{pump}^2 f}{v_s}$
Value	$\pm$ 120 μm	8.1 μm	352 μm	>97 mm

Table IV.1: Typical lengths over which wave deformation effects become apparent
The calculations are valid for propagation in sapphire along the c-axis. These estimates were made for an input strain wave of amplitude $s_0 = 1 \times 10^{-3}$ and central frequency $f = 40$ GHz.

$$\frac{\partial^2 s}{\partial t^2} = v_s^2 \frac{\partial^2 s}{\partial z^2} - \frac{\alpha}{\rho}\frac{\partial}{\partial z}\left(s\frac{\partial s}{\partial z}\right) + \frac{\eta v_s}{\rho}\frac{\partial^3 s}{\partial z^3}. \tag{IV.1}$$

The strength of the nonlinear term is measured by the nonlinearity constant α, and that of the scattering term by the viscosity η. At room temperature damping of high phonon frequencies dominates dispersive effects. Therefore, dispersion can be neglected in the description. By transforming to the moving coordinate frame ($x = z - v_s t$), one ends up at

$$\frac{\partial s}{\partial t} = -\frac{\alpha}{2\rho v_s} s\frac{\partial s}{\partial x} + \frac{\eta}{2\rho}\frac{\partial^2 s}{\partial x^2}. \tag{IV.2}$$

This modified wave equation is called the Burgers equation, and can be solved analytically in the limit of large propagation times [21]. However, we prefer numerical simulations to be able to describe the propagation over finite distances.

Measured parameters for sapphire along the c-axis were inserted for the sound velocity $v_s = 11.23 \times 10^3$ m/s, the mass density $\rho = 3.97 \times 10^3$ kg/m^3, the elastic constant $c_{33} = 4.97 \times 10^{11}$ N/m^2, nonlinear coefficient $\alpha = -18.5 \times 10^{11}$ N/m^2 [22], and the viscosity parameter $\eta = 6 \times 10^{-4}$ Ns/m^2 [23, 24] in the calculations for propagation. Estimates for the typical propagation distances for diffraction, attenuation, and nonlinearity to become apparent for a typical strain found in this experiment [19], are stated in Table IV.1. Diffraction is sufficiently small to allow for a 1D approach, and the nonlinear action is dominant at the highest powers, and the sample thickness used here. We note, that also nonlinear diffraction takes place [25]. Although much stronger than ordinary linear diffraction, calculations in Ref. [25] suggest that it is still negligible at these sample thicknesses, pump

beam diameters and propagation distances .

IV.3 Sample and setup

Details concerning the experimental technique can be found in Ch. II.

IV.3.1 Reflection experiment

In the reflection experiment, a sapphire slab of dimensions 7×4 mm$^2 \times 115$ μm was used, with the c-axis (perpendicular to the slab) as propagation direction. A 50-nm Cr generation layer was evaporated at one side (Ch. III), and an 80-nm Al detection layer at the opposite side to probe the differential reflectivity $\Delta R/R$. The Al/sapphire interface acoustic reflection coefficient can be calculated at 0.43, corresponding well to what is found in these experiments.

The 160-fs pump beam carries a maximum energy of 500 μJ per pulse, and was loosely focused to $w_{pump} = 380$ μm to produce an acoustic beam. The weak probe was focused down to $w_{probe} \sim 15$ μm at the aluminum transducer precisely opposite the pump beam. The eight-pass delay line was positioned around 38 cm from its origin, in order to bridge the 10-ns travel time for the acoustic wave through the crystal. The glass prisms in this delay line stretch the probe pulse to 275 fs (App. B).

Through analyzing optical reflections of the wafer surfaces, we estimated the angle δ between front and rear plane to be around 0.12°. Due to the finite size of the probe, this will result into an acoustic arrival time spread of $w_{probe} \times \tan\delta/v_s = 2.8$ ps.

IV.3.2 Interferometric experiment

Interferometric experiments were performed on a sapphire substrate of dimensions 7×4 mm$^2 \times 126$ μm, again with the c-axis perpendicular to the slab. The strain is generated in a 200-nm thick Cr layer, and detected on a 30-nm Cr layer at the other side of the sapphire slab. The impedance mismatch between sapphire and Cr was found to be 6%, so that a good interfacial bonding between the two materials can be assumed.

The pump light was frequency doubled to 400 nm (pulse length < 300 fs) before sending it to the sample, and focused to a waist w_{pump} of 165 μm, to obtain pump fluences as high as 30 mJ/cm^2. The probe pulses were sent through the

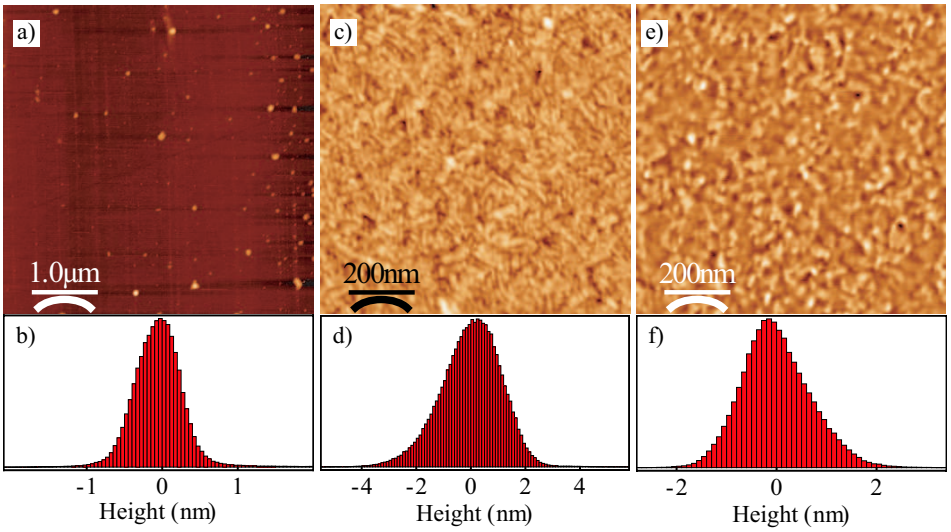

Figure IV.1: AFM measurements
a) Typical AFM scan of the sapphire substrate surface. b) Distribution of the measured heights. The typical measured thickness variation is 0.4 nm; this is an upper estimate, because of dust particles (white speckles) present at the surface. c) Typical scan of a 30-nm Cr film. d) Film thickness distribution. The typical thickness variation is 0.7 nm. e) Typical scan of an 80-nm Al film. f) Film thickness distribution. The typical thickness variation is found to be 1.1 nm.

eight-pass delay line, resulting in a pulse stretching to 180 fs (App. B), and were focused down to $w_{probe} \sim 10\ \mu$m. Since the optical reflection coefficient for Cr is almost the same for 800 nm and 400 nm (R = 0.50 and 0.48, respectively [3]), as are the temporal profiles of the pump pulses, the results from the two different experiments should be comparable.

The angle between front and rear plane was determined at $\delta = 0.076°$, corresponding to an arrival time difference of 1.2 ps over the probe spot.

IV.3.3 Film characterization

We have performed AFM measurements on the sapphire substrate and the deposited metal detection films; the results are shown in Fig. IV.1. The sapphire substrate was found to be almost atomically flat. The typical spread in detection film thickness is less than 1 nm, corresponding to a small variation in arrival time of the acoustic wave at the surface of 1 nm/v_m (v_m the sound velocity in the

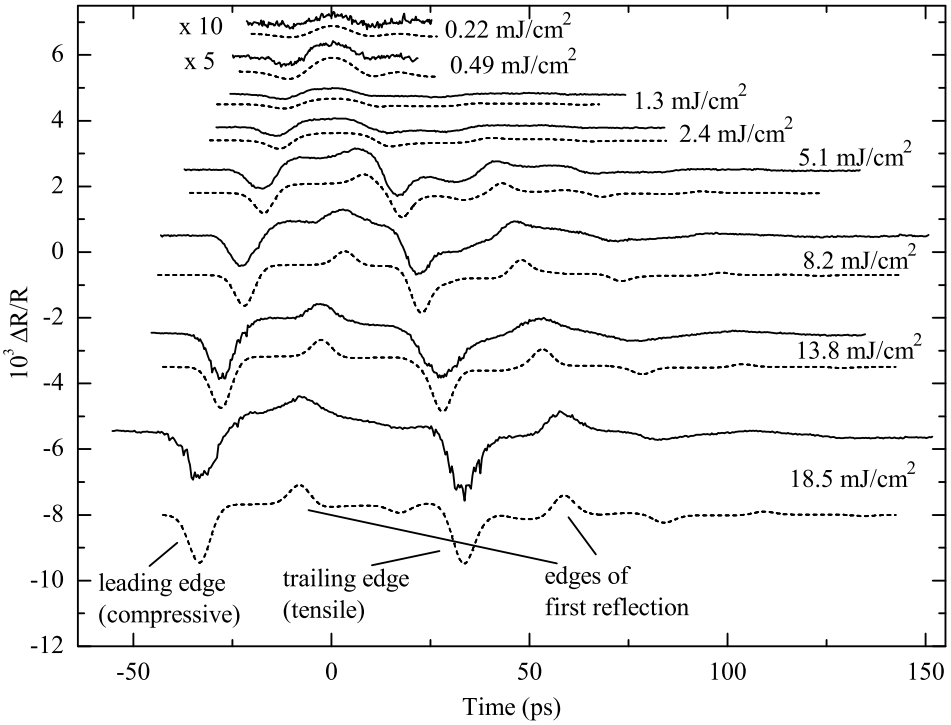

Figure IV.2: Reflectivity traces
Measured differential reflectivity traces (solid lines), and results from simulation of strain propagation through 115 μm of sapphire (dashed lines), for the indicated range of pump fluences.

metal film), around 160 fs. More important than the thickness variations are the randomly stacked grains that are clearly visible [26]. The typical diameter of the grains is ~ 30 nm, of the same order as the thickness and the acoustic wavelengths in the shock wave.

IV.4 Reflectometry experiments

Fig. IV.2 (solid lines) shows the measured differential reflectivity $\Delta R/R = 2\rho$ for pump fluences ranging from 0.2 to 18.5 mJ/cm^2. Clear temporal stretching and changes in shape depending on pump fluence are found. As was defined in Eq. (III.1), the detected signal $\Delta R/R$ as a function of delayed probe time t is the convolution of the strain $s(z,t)$ propagating in the (inward) z-direction of

the film, and the sensitivity function $f_\rho(z)$, which contains all relevant optical and elasto-optical properties of Al [2]. In this case, the width of the strain pulse is much larger than the optical penetration depth ($\sim$9 nm in Al), and the signal reduces to the (positive) spatial derivative of the strain near the surface. At low fluences, we can thus determine the strain directly from the observed signal as a smooth, bipolar function. At high fluences, the wave becomes stretched, and its edges become sharper, indicating self-steepening of the leading and trailing edge. Subsequent peaks and dips, indicated in Fig. IV.2, are reflections of these edges returning from the Al-sapphire interface.

Calculating the effect of the arriving strain profile on the reflectivity of the Al detection layer requires knowledge of the complex index of refraction $n + i\kappa$, and its derivative with respect to strain, $\frac{\partial n}{\partial s} + i\frac{\partial \kappa}{\partial s}$, at the probe wavelength. For the index of refraction, we use the tabulated values $n = 1.99$ and $\kappa = 7.05$ [27]. Since Al has an absorption band near 800 nm [5, 28], it is very sensitive to the presence of strain. As a result, the elasto-optical constants are relatively high. From results reported by Hao and Maris [15], and Daly *et al.* [29], we estimate the ratio of the latter two parameters, which fixes the shape of the transient reflection signal, as $\frac{\partial n}{\partial s} \sim -2\frac{\partial \kappa}{\partial s}$. The absolute values determine the signal amplitude and are adjusted to fit the measured time traces.

The dashed lines in Fig. IV.2 represent the calculated differential reflectivity signals for the given shape of the input strain wave. Over the full pump fluence range, the simulations agree well with the measured data. The simulated data yield for $\frac{\partial n}{\partial s}$ and $\frac{\partial \kappa}{\partial s}$ values of -28 and 15, respectively [30]. The absolute values of the elasto-optical constants agree within 30% with the values obtained by Jiles [31], and the values reported in Ref. [32]. This is acceptable, given the strong wavelength dependence around 800 nm and the dependence on film morphology.

Fig. IV.3 a) shows the calculated strain wave shape after propagation through 115 μm of sapphire, for the same pump fluences as presented in Fig. IV.2. For comparison, the initial strain profile for the highest pump fluence is also given (dashed line). A clear stretching of the wave in the time domain with increasing pump intensity is visible, as well as a steepening of the leading and trailing edges. For the highest fluence, the steepening of the wave front leads to a 10 - 90% rise time of 1.2 ps, corresponding to shock fronts as short as 9 lattice spacings. Fig. IV.3 b) shows the corresponding acoustic spectra. The nonlinear action increases the acoustic frequencies from 100 GHz up to 500 GHz. Fig. IV.3 c) shows the initial strain amplitude s_0 in sapphire, obtained from the simulations, for a larger

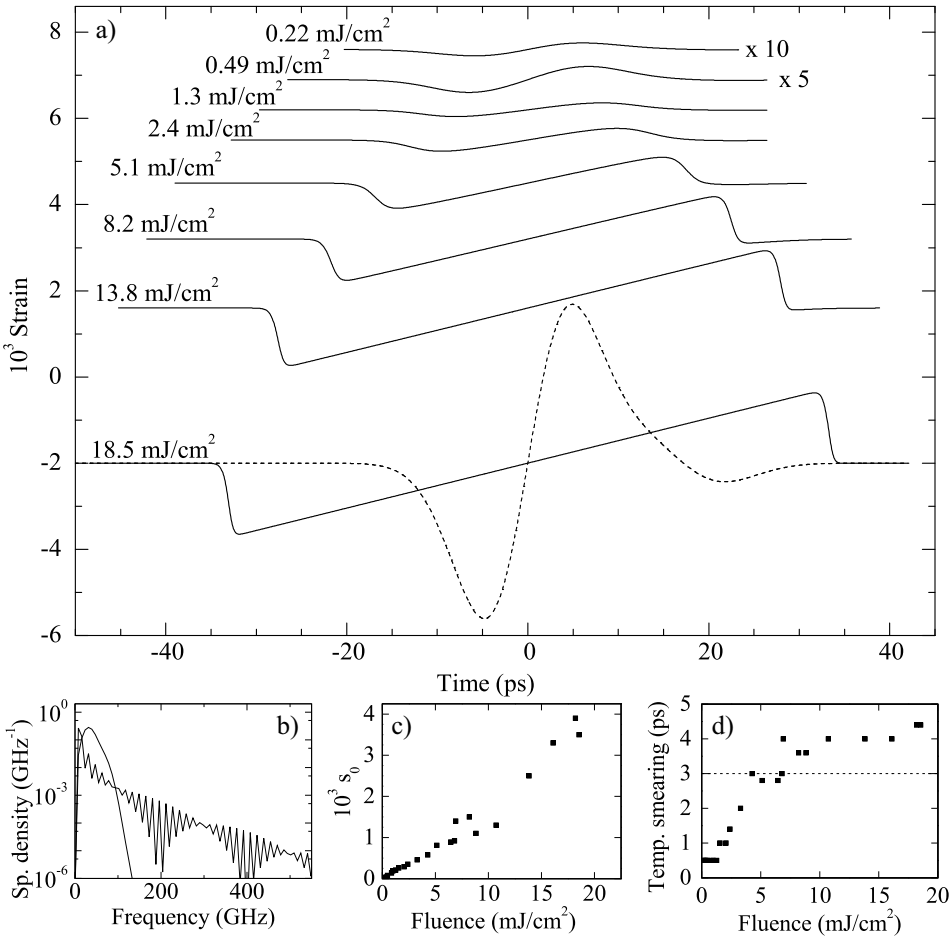

Figure IV.3: Nonlinear propagation calculations
a) Calculated strain traces after propagation through 115 μm of sapphire (solid lines), and injected strain pulse for the highest pump fluence (dashed line). b) Spectra of the initial strain profile (gray line) and after propagation through sapphire (black line), for a fluence of 18.5 mJ/cm^2. c) Input strain amplitude s_0 as a function of fluence. d) Temporal broadening, required to obtain a best fit, as a function of fluence. The dashed line indicates the optimal resolution, mainly limited by the parallelism of the generation and detection plane.

set of measurements. The strain amplitude increases linearly with pump fluence in the low fluence regime, and rises superlinearly at the highest fluences. The values and behavior are in good agreement with those obtained in Ch. III, when taking into account the different sound velocities in Cr and sapphire and the Cr/sapphire interface reflection. The arrival times of the supersonic front and the subsonic rear of the shock wave depend strongly on the input strain, making the input strain a well-defined parameter.

The simulations produce sharper temporal profiles than the measured ones for the highest fluences, suggesting that the high-frequency parts of the signal are suppressed or averaged out. In Fig. IV.3 d), the temporal broadening (defined as two times the standard deviation of the required distribution of times) that was used in the simulations in Fig. IV.2, is plotted as a function of pump fluence. These results will be discussed after presenting the interferometric results.

IV.5 Interferometric experiments

In Fig. IV.4 a), the detected phase signal $\delta\varphi$ after propagation is shown for a range of fluences, up to 26 mJ/cm^2. For the highest fluence, the 1% phase signal change corresponds to a surface displacement as high as 0.6 nm. Fig. IV.4 b) shows the typical pulse width after propagation through the sapphire. At low powers, the temporal width has broadened slightly ($\pm$ 2 ps) with respect to that obtained at the generation film (Ch. III), due to attenuation in the sapphire substrate that mainly affects the high frequencies in the wave packet, and the limited parallelism of the substrate front and rear planes.

At the highest fluences, the increase in pulse width is roughly a factor of six with respect to that of the incoming pulse. The nonlinear dependence on pump fluence is caused by the nonlinear increase of the generated strain amplitude and width, discussed in Ch. III. With respect to the reflectometry measurements [33], the broadening of the acoustic wave is of the same order. The inset in Fig. IV.4 c) shows a typical N-wave strain profile in the sapphire substrate for 26.4 mJ/cm^2 after 126 μm of propagation. Since the sample traversal time t_{travel} is 11.2 ns and the decrease in arrival time δt is around 30 ps for this fluence, the average Mach number is $(1 + \delta t/t_{travel}) = 1.0027$. The inset of Fig. IV.4 c) shows that the degree of supersonicity corresponds to the average strain amplitude during traversal of the sample.

A clear illustration of nonlinear action can also be seen in the inset in Fig. IV.4

a), showing the reflection from the 200-nm Cr generation layer/sapphire interface, arriving ~ 75 ps after the main pulse. Since the sign of this wave is opposite to the original one, here nonlinearity does not broaden but narrow the original pulse, giving rise to a more sharply peaked signal.

We can analyze the measurement for the highest fluence in Fig. IV.4 a), on several levels of detail. On a very simple level, we can consider the shock wave as being a pure N-wave. Knowing that the phase signal is dominated by the surface displacement, i.e. the integrated strain that has passed the surface, the measured signal equals the integral of a linear rise over a finite interval, a parabolic shape. The signal was fitted with such a a shape, which in first approximation is quite correct.

A more advanced method is to take the derivative of the phase signal according to Eq. (III.5), and compare this to a simulation. The results are shown in Fig. IV.4 c). Because of the limited signal-to-noise ratio in our experiments, the derivative signal was averaged over three points. In the propagation calculation according to Eq. (IV.2), we have used an input wave width of 5.1 ps [18], and an amplitude $s_0 = 3.65 \times 10^{-3}$. The result is shown in the inset in Fig. IV.4 c). To obtain the correct strain amplitude in the Cr film, the strain in sapphire has to be multiplied by a factor $(1-r)v_s/v_{s,\mathrm{Cr}} = 1.59$. Here, $r = 0.06$ is the acoustic reflection coefficient at the interface and $v_{s,\mathrm{Cr}} = 6.65 \times 10^3$ m/s the sound velocity in Cr. For this specific experiment, the time step Δt was 330 fs, and thus the multiplication factor $8\pi v_{s,\mathrm{Cr}}\Delta t/\lambda$ derived in Eq. (III.5) yields 0.069. Although the agreement is very good in the large part of the trace, it shows deviations mainly at the front and rear. This is because this method (as did the previous) neglects the fact that the phase signal also contains a metal film contribution $\delta\varphi_{metal}$ (Ch. III). This contribution will be large when the strain at the surface is rapidly changing with respect to the travel time through the penetration depth, i.e. at the shock wave edges.

To take this effect into account, we have taken the strain waveform as shown in Fig. IV.4 c), calculated both $\delta\varphi_{metal}$ and $\delta\varphi_{surface}$, and compared this to the measured signal. The additional surface displacement contribution improves the fit in the form of the positive contributions at the front and rear of the main signal, which are not present in the simple parabolic approximation in Fig. IV.4 a). In this procedure, a Gaussian broadening, i.e. temporal smearing, was included with a value of 6 ps, of the same order as for the highest fluence in the reflectometric case, shown in Fig. IV.3 d).

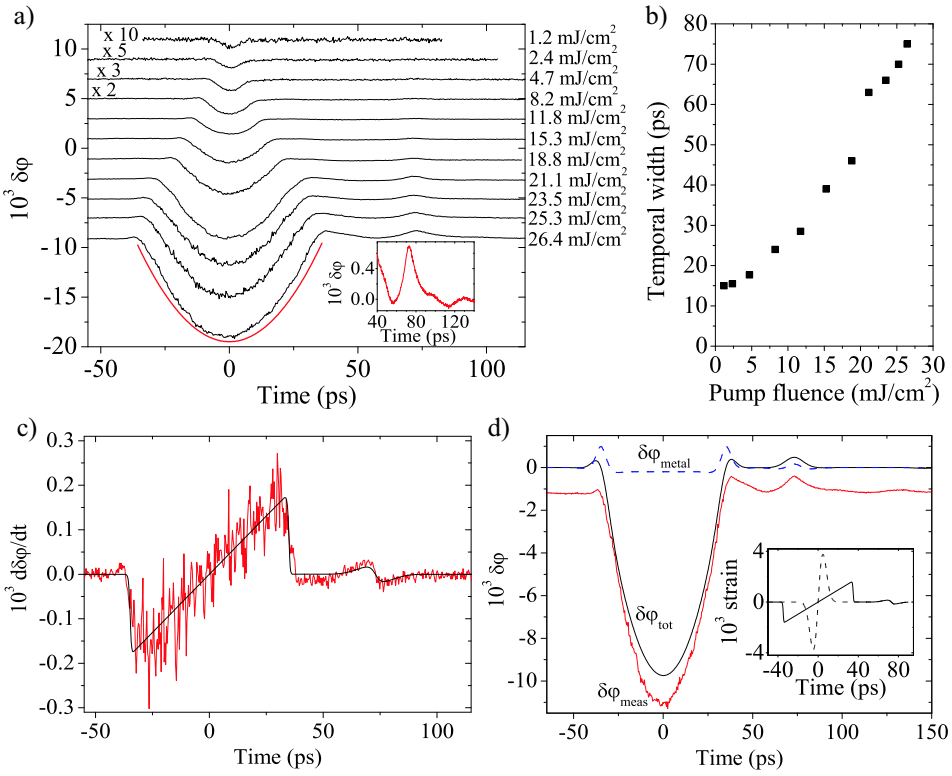

Figure IV.4: Interferometric measurements and calculations
a) Phase signal obtained by probing the sapphire crystal opposite the pump spot, as a function of pump fluence. Gray line shows parabolic fit to the highest fluence trace. Inset shows the $\sim 6\%$ amplitude reflection from the 200-nm Cr (generation layer)-sapphire interface for the highest fluence. b) Typical width (defined as distance between onset and point of full passage of $\delta\varphi$ signal) as determined from the traces shown in Fig. IV.4 a). c) Derivative of the measured phase signal (thin line), and the scaled result for the strain, calculated for propagation through 126 μm of sapphire, and evaluated in the metal film (thick line), for a fluence of 26.4 mJ/cm^2. d) Calculation of the bulk phase signal contribution $\delta\varphi_{metal}$ (dashed line) to the total phase signal $\delta\varphi_{tot}$, and comparison to the measured signal $\delta\varphi_{meas}$. The measured signal is displaced by 10^{-3} to enhance visibility. Inset shows the initial wave shape (dashed line), and the wave shape after propagation through 126 μm of sapphire (solid line), obtained from the calculation.

IV.6 Discussion

The most important aspect of these measurements to be discussed, is the temporal broadening, i.e. the loss of high-frequency information, in the experiments. The resolution of the reflectometric and interferometric measurements is limited by the largest of the probe pulse length, the surface roughness, and the parallelism of the sample planes. In both cases, the latter is the limiting factor, yielding a lower-limit on broadening of 2.8 ps for the reflectometric case (as shown in Fig. IV.3 d)), and 1.2 ps for the interferometric case. The maximum values found in the experiment are a factor two to five higher. The additional broadening is not due to diffraction (see Table IV.1), or the variation of pump intensity over the probe spot (giving rise to arrival time differences of only 300 fs).

In the analysis, phonon attenuation in the detection film was not taken into account. We have no information on acoustic attenuation in Al. For Cr, we may use the value of 150 $\mathrm{GHz}^{-2}\mathrm{m}^{-1}$ for attenuation in Cr, determined in Ch. III, to make an estimate of the cut-off frequency for the Cr detection film used in the interferometric experiment. Given the film thickness of 30 nm, the frequency that is attenuated by a factor of e is found to be 370 GHz. This would correspond to a temporal broadening around 2.7 ps. Although significant, this is still a factor of two lower than what is observed in the interferometric experiment. Moreover, the results of the reflectometric experiments in Fig. IV.3 d) suggest that the amount of time broadening depends on pump fluence. Linear damping cannot explain this intensity dependence.

It would be good to consider the nonlinear propagation itself as a source of broadening. Figs. IV.2 and IV.4 b) show that the width of the arriving shock wave depends on pump fluence. As a consequence, intensity variations will influence the arrival times of the compressive and tensile shock fronts, also the parts that carry the high-frequency information. We have made estimates of the magnitude of the nonlinear effects on the shock front arrival times. First of all, simulations were performed for a $\pm 1\%$ fluctuation in pump intensity (laser specifications) on an injected strain of 2×10^{-3} at a fluence of ~ 13 mJ/cm^2, see Fig. IV.3 c). This variation results in a ± 1 ps jitter in arrival time of the wavefronts. This effect, added to the 3 ps due to the lack of parallelism and other spurious effects, can explain the 4 ps required to get agreement with the experimental data.

An alternative estimate of the magnitude of this nonlinear broadening effect can be made by examining the width of the strain wave packet as a function of

fluence in Fig. IV.4 b). We estimate that at a fluence of 26.4 mJ/cm^2, $\pm 1\%$ in fluence corresponds roughly to a variation of ± 1.2 ps in wave packet width. Since the pump light is frequency-doubled, in first approximation the intensity noise in the pump increases to $\pm 2\%$. The 4.8 ps, in combination with the 2.7 ps due to phonon attenuation in the detection film and the 1.2 ps due to lack of parallelism, again approaches the broadening of 6 ps required in the calculations.

Despite the fact that the phonon frequencies generated in this experiment are in the several hundreds of GHz range, as quantitatively supported by calculations, and that the ultimate temporal resolution can be of the order of 1 ps, we conclude that the detection bandwidth is limited to at best 250 GHz because of nonlinear temporal smearing, and to a lesser degree high-frequency phonon scattering. Improved instrumental resolution requires a higher-quality detection layer, and a more stable laser source. We note that laser stability is an inherent limiting factor in amplifier-based experiments, but a much smaller problem in high-repetition-rate systems, where the pulse-to-pulse noise is an order of magnitude smaller.

The subject of nonlinear temporal broadening will be encountered again in Ch. V, when we discuss experiments performed at low temperatures.

IV.7 Conclusions

In conclusion, we have demonstrated nonlinear propagation of longitudinal high-amplitude acoustic wave packets in a thin sapphire slab at room temperature using picosecond ultrasonic techniques. Simulations of the nonlinear propagation of the wave packets based on Burgers' equation quantitatively track the measured traces over two orders of magnitude of pump fluences. The injected bipolar strain pulse is seen to stretch up by a factor of six for the highest pump powers, signifying the supersonic and subsonic nature of the propagation of the compressive and tensile part of the wave packet, respectively. Calculations show that the shock wave maintains frequencies up to 500 GHz after propagation over 120 micrometers at room temperature, resulting in a picosecond rise time of the shock wave front.

References

1. H.J. Maris. Picosecond ultrasonics. *Sci. Am.*, 86:278, 1998.
2. C. Thomsen, H.T. Grahn, H.J. Maris, and J. Tauc. Surface generation and detection of phonons by picosecond light pulses. *Phys. Rev. B*, 34(6):4129, 1986.

3. T. Saito, O. Matsuda, and O.B. Wright. Picosecond acoustic phonon pulse generation in nickel and chromium. *Phys. Rev. B*, 67:205421, 2003.
4. H.-N. Lin, H.J. Maris, L.B. Freund, K.Y. Lee, H. Luhn, and D.P. Kern. Study of vibrational modes of gold nanostructures by picosecond ultrasonics. *J. Appl. Phys.*, 73(1):37, 1993.
5. A. Devos and C. Lerouge. Evidence of laser-wavelength effect in picosecond ultrasonics: Possible connection with interband transitions. *Phys. Rev. Lett.*, 86:2669, 2001.
6. O. Matsuda, T. Tachizaki, T. Fukui, J.J. Baumberg, and O.B. Wright. Acoustic phonon generation and detection in GaAs/$Al_{0.3}Ga_{0.7}$As quantum wells with picosecond laser pulses. *Phys. Rev. B*, 71(11):115330, 2005.
7. K.T. Gahagan, D.S. Moore, D.J. Funk, R.L. Rabie, S.J. Buelow, and J.W. Nicholson. Measurement of shock wave rise times in metal thin films. *Phys. Rev. Lett.*, 85(15):3205, 2000.
8. S.D. McGrane, D.S. Moore, D.J. Funk, and R.L. Rabie. Spectrally modified chirped pulse generation of sustained shock waves. *Appl. Phys. Lett.*, 80(21):3919, 2002.
9. R. Evans, A.D. Badger, F. Falliès, M. Mahdieh, T.A. Hall, P. Audebert, J.-P. Geindre, J.-C. Gauthier, A. Mysyrowicz, G. Grillon, and A. Antonetti. Time- and space-resolved optical probing of femtosecond-laser-driven shock waves in aluminium. *Phys. Rev. Lett.*, 77(16):3359, 1996.
10. A.M. Lomonosov and P. Hess. Impulsive fracture of silicon by elastic surface pulses with shocks. *Phys. Rev. Lett.*, 89(9):095501, 2002.
11. D.G. Hicks, P.M. Celliers, G.W. Collins, J.H. Eggert, and S.J. Moon. Shock-induced transformation of Al_2O_3 and LiF into semiconducting liquids. *Phys. Rev. Lett.*, 91(3):035502, 2003.
12. E.J. Reed, M. Soljačić, and J.D. Joannopoulos. Color of shock waves in photonic crystals. *Phys. Rev. Lett.*, 90(20):203904, 2003.
13. E.J. Reed, M. Soljačić, and J.D. Joannopoulos. Reversed Doppler effect in photonic crystals. *Phys. Rev. Lett.*, 91(13):133901, 2003.
14. E.J. Reed, M. Soljačić, R. Gee, and J.D. Joannopoulos. Coherent optical photons from shock waves in crystals. *Phys. Rev. Lett.*, 96(1):013904, 2006.
15. H.-Y. Hao and H.J. Maris. Experiments with acoustic solitons in crystalline solids. *Phys. Rev. B*, 64:064302, 2001.
16. O.L. Muskens and J.I. Dijkhuis. High amplitude, ultrashort, longitudinal strain solitons in sapphire. *Phys. Rev. Lett.*, 89(28):285504, 2002.
17. O.L. Muskens, A.V. Akimov, and J.I. Dijkhuis. Coherent interactions of terahertz strain solitons and electronic two-level systems in photoexcited ruby. *Phys. Rev. Lett.*, 92(3):335503, 2004.
18. This value is $1/\sqrt{2}$ that of the value stated in publications [33, 34], because of the different definition of τ used in this thesis.
19. P.J.S. van Capel, O.L. Muskens, E.W. Hesselink, and J.I. Dijkhuis. Towards ul-

trafast pump-probe spectroscopy on trains of strain solitons. *Phys. Stat. Sol. (c)*, 1(11):2753, 2004.

20. O.L. Muskens and J.I. Dijkhuis. Inelastic light scattering by trains of ultrashort acoustic solitons in sapphire. *Phys. Rev. B*, 70(10):104301, 2004.
21. V.I. Karpman. *Non-linear Waves in Dispersive Media*. Pergamon Press, 1st edition, 1975.
22. Landolt-Bornstein. In K.H. Hellwege and A.M. Hellwege, editors, *New Series: Group III/11*. Springer, 1979.
23. B.A. Auld. *Acoustic Fields and Waves in Solids*, volume 1. Robert E. Krieger Publishing Company, 2nd edition, 1990.
24. This value differs 16% from that used in the next chapter. The difference lies in the fact, that here the value was an average value over the relevant frequency range, assuming attenuation $\propto \omega^2$, while in the next capter the attenuation was taken to be the experimentally determined $\propto \omega^{1.9}$, yielding a slightly lower prefactor.
25. O.L. Muskens and J.I. Dijkhuis. High-amplitude, ultrashort strain solitons in solids. In K.-T. Tsen, editor, *Non-equilibrium dynamics of semiconductors and nanostructures*, pages 15–45. CRC Press, 1st edition, 2005.
26. I. Petrov, P.B. Barna, L. Hultman, and J.E. Greene. Microstructural evolution during film growth. *J. Vac. Sci. Technol. A*, 21(5):S117, 2003.
27. Landolt-Bornstein. In K.H. Hellwege and A.M. Hellwege, editors, *II/8*. Springer, 6th edition, 1962.
28. F. Szmulowicz and B. Segall. Calculation of optical spectra of aluminum. *Phys. Rev. B*, 24(2):892, 1981.
29. B.C. Daly, T.B. Norris, J. Chen, and J.B. Khurgin. Picosecond acoustic phonon pulse propagation in silicon. *Phys. Rev. B*, 70(21):214307, 2004.
30. P.J.S. van Capel and J.I. Dijkhuis. Erratum: "Optical generation and detection of shock waves in sapphire at room temperature" [Appl. Phys. Lett. [88], 151910 (2006)]. *Appl. Phys. Lett.*, 89(13):139903, 2006.
31. D.C. Jiles and M.P. Staines. Piezo optic properties of aluminum. *Sol. St. Comm.*, 47(1):37, 1983.
32. O.L. Muskens. *High-amplitude, ultrashort strain solitons in solids*. PhD thesis, Utrecht University, 2004.
33. P.J.S. van Capel and J.I. Dijkhuis. Optical generation and detection of shock waves in sapphire at room temperature. *Appl. Phys. Lett.*, 88(15):151910, 2006.
34. P.J.S. van Capel, H.P. Porte, G. van der Star, and J.I. Dijkhuis. Interferometric detection of acoustic shock waves. *Jour. Phys.: Conf. Ser.*, 92:012092, 2007.

Chapter V

Time-resolved detection of ultrashort strain solitons in sapphire

Abstract

In this chapter the propagation of high-amplitude acoustic waves in sapphire is studied, as a function of sample temperature, sample thickness, and pump fluence. Strain waves are generated in a 100-nm thick chromium film, and launched into the sapphire. For temperatures < 60 K, damping can be neglected and propagation is dominated by the nonlinear and dispersive properties of the sapphire substrate. The interferometric technique presented in Ch. II is used to detect the wave on an epitaxially grown ~ 20-nm thick Cr film at the opposite side of the sample.

At the lowest temperature of 18 K, a train of up to seven solitons is detected in sapphire for a pump fluence of 11 mJ/cm^2. From the soliton amplitudes and velocities, we infer soliton temporal widths as short as 200 fs (< 2 nm). A theoretical analysis based on numerical solution of the Korteweg - de Vries - equation gives excellent agreement to all experiments presented. Deviations can be explained by pump intensity variations, directly affecting the (nonlinear) propagation properties.

V.1 Introduction

In the previous chapter, the formation of acoustic shock waves in sapphire at room temperature was examined. Here, damping due to scattering with thermal phonons prevents nonlinear generation of high frequencies, and lattice dispersion can be neglected in the formalism described by Eq. (IV.1). When lowering the temperature of the sample, wave propagation changes in a remarkable way, as is shown in Fig. I.2. The most striking feature is that supersonic acoustic solitons split off at the front of the wave. A first theoretical description of the soliton was

given by Korteweg and De Vries as early as 1895 [1]. The theoretical background of soliton formation and propagation will be discussed in Sec. V.3.

Solitons have been observed in numerous fields of physics [2, 3, 4, 5]. First experimental proof of acoustic solitons in solids was obtained by Hao and Maris in 2001, using picosecond ultrasonics techniques [6]. This groundbreaking work was followed by a series of picosecond ultrasonics experiments improving the understanding of acoustic wave propagation in the nonlinear and dispersive regime [7, 8, 9]. Muskens and Dijkhuis have used spectroscopic techniques to examine soliton propagation in sapphire and ruby [10, 11], and demonstrated a number of six solitons with a frequency content exceeding 870 GHz.

From an experimental point of view, high-repetition rate picosecond ultrasonics experiments are inherently limited in available pump power, requiring a tiny ($< 10\ \mu$m) pump beam waist to induce nonlinear effects. Then, propagation can not be considered one-dimensional because of nonlinear diffraction [12]. The transverse energy diffusion leads to decreased soliton generation efficiency and effectively two-dimensional propagation [13]. The intent of the present experiments, where large pump pulse energies are available, is to combine maximum nonlinear propagation effects with large acoustic beams, thus increasing the number of solitons while reducing diffraction effects.

In this chapter, we present the first time-resolved experiments on soliton generation using a 1-kHz repetition-rate laser system. After discussing the sample preparation specifics, some of which were crucial for experimental success, interferometric pump-probe experiments on three sapphire samples of different thickness are presented. Propagation is monitored as a function of temperature and pump intensity. The experimental traces are analyzed and discussed using the numerical calculation model presented in Ch. IV, but now including dispersive effects.

V.2 Sample and setup

V.2.1 Setup

The operation and resolution of our high-sensitivity interferometric pump-probe setup are explained in detail in Ch. II and App. A. The 400-nm pump beam waist was measured to be $\sim 170\ \mu$m at the sample for each set of measurements, with an accuracy $\pm 5\%$. The experimental geometry is sketched in the inset of Fig. V.1

b). The experimental setup is essentially the same as in Ch. IV, but extended with a continuous flow cryostat (Oxford Optistat CF) allowing the sample temperature to be set from 295 K (room temperature) to 5 K, with a stability of $\pm$ 0.1 K during a typical experimental run on a single sample (taking $\pm$ 24 hours). Experiments were performed at 295 K, 200 K, 100 K, 60 K, and 18 K. The interferometer was aligned such to prevent probe beam reflections off the cryostat windows to enter the detection system and reduce contrast. Pump fluences ranged from 1 to 12 mJ/cm^2 in steps of $\sim$ 1 mJ/cm^2. Above 12 mJ/cm^2, measurements became unstable and no clear soliton signals could be measured anymore. Reasons for this will be discussed in Sec. V.5.

V.2.2 Samples and preparation

The sample design is equivalent to the one presented in Ch. IV, and is depicted in the inset of Fig. V.1 b). We use three sapphire (Al_2O_3) (0001)-oriented samples (acoustic wave propagation along the sapphire *c*-axis), with measured thicknesses d_{sample} of 123 μm, 307 μm, and 405 μm. The front and rear planes of the samples have angles of 0.089°, 0.064°, and 0.038°, respectively. Assuming a probe beam diameter of $w_{probe} \sim 10$ μm, this translates in a spread in arrival time τ_p of the strain pulses over the probe spot amounting to 1.39 ps, 0.99 ps, and 0.59 ps.

Since sapphire is transparent for the probe wavelength of 800 nm, a metal film on the probe side is required. In Chs. III and IV we concluded that for the in-house grown chromium films grain formation and corresponding interface scattering probably are responsible for high-frequency phonon attenuation. In other experiments, the highest phonon frequencies detected were around 250 GHz, and a good sample surface quality appeared to be essential to reach these values [7, 14]. Since the frequencies in a typical soliton wavepacket can exceed 1 THz (Sec. V.4), high-frequency phonon scattering and attenuation would greatly reduce the detection efficiency.

For this reason, high-quality thin chromium films were grown by Dr. M. Highland in the group of Prof. Dr. D. Cahill at the University of Illinois at Urbana-Champaign. The films are grown epitaxially, and are nearly single-crystalline [15]. In this case, attenuation is not limited by metal film grains or Cr/sapphire interface scattering, but by more fundamental damping processes [16, 17]. The thickness of the Cr probe films is $\sim$ 20 nm, while the Cr films at the pump side are $\sim$ 100 nm thick.

Given the film thickness and quality we estimate the cutoff frequency for

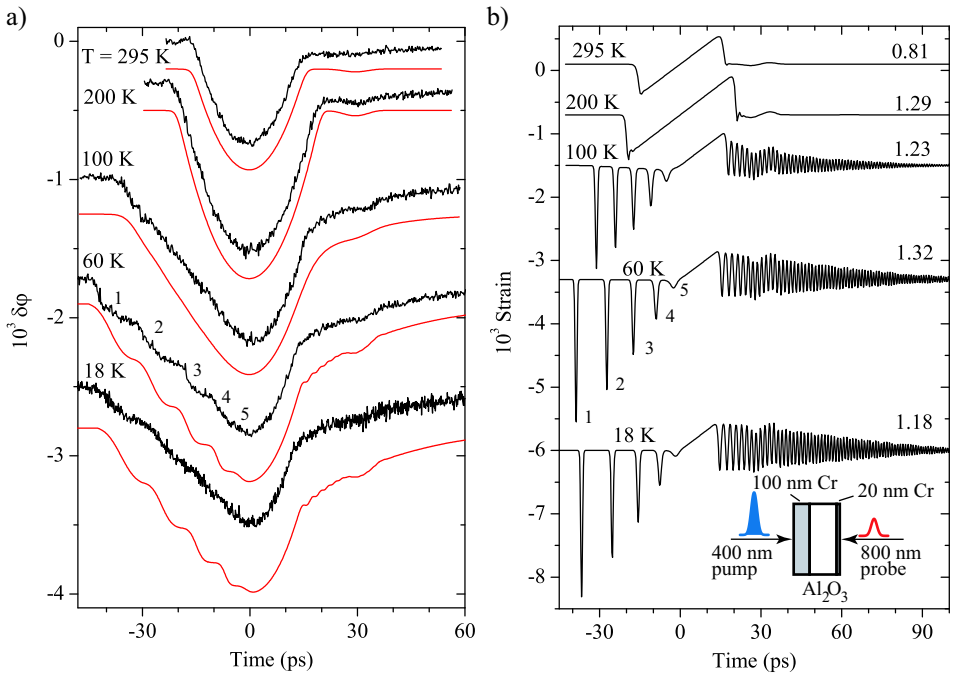

Figure V.1: Temperature dependence of phase signal and wave shape for propagation through 307 micron of sapphire

a) Measured (black line) and calculated (gray line) phase signals for room temperature (upper trace), and cooling via 200 K, 100 K, 60 K to 18 K (bottom trace) for a sapphire sample thickness of 307 μm and a constant pump fluence of 9.7 mJ/cm^2. Calculations include broadening effects. Numbers $i = 1,\ldots,5$ at 60 K trace correspond to arrival of i^{th} soliton at the detection surface. b) Calculated strain wave shape after propagation through 307 μm of sapphire, given the input strain amplitude $s_0(\times 10^3)$ required to reach agreement with the measurements in a). Inset: sketch of experimental geometry.

transmission through the probe metal film to be > 600 GHz, of the same order as $1/\tau_p$.

V.3 Theory

V.3.1 Korteweg - de Vries - Burgers - equation

In order to take lattice dispersion into account in first order, a term has to be added to the Burgers equation Eq. (IV.1) [6]. Transforming to the moving coordinate

frame results in

$$\frac{\partial s}{\partial t} = -\frac{\alpha}{2\rho v_s} s \frac{\partial s}{\partial x} - \beta \frac{\partial^3 s}{\partial x^3} + \frac{\eta}{2\rho} \frac{\partial^2 s}{\partial x^2}, \tag{V.1}$$

the Korteweg - de Vries - Burgers (KdVB) -equation. Here, β is the first order dispersion parameter, measured to be $3.5 \pm 0.3 \times 10^{-17}$ m^3/s along the sapphire c-axis [14]. Eq. (V.1) can be solved numerically. In Sec. V.5, we discuss the initial conditions and the calculation details. For clarity, calculated strain profiles are presented together with the measured traces in Figs. V.1 - V.5.

The one-dimensional propagation is an approximation, since transverse intensity gradients lead to diffraction. In the two-dimensional case (cylindrical coordinate system), a diffraction term has to be added to Eq. (V.1), leading to the Kadomtsev - Petviashvili (KP) - equation. However, for the current pump beam waist of 170 μm, sample thicknesses, and fluences we can safely neglect diffraction [12].

V.3.2 Temperature dependence of damping term

When performing experiments at elevated temperatures, attenuation in the sapphire substrate plays an important role. The damping in sapphire shows a strong temperature dependence. Auld [17] reports a value of $\eta = 6 \times 10^{-4}$ Ns/m^2 at room temperature decreasing linearly with temperature and a frequency dependence $\propto \omega^{1.9}$. Pomerantz [18] and Ciccarello [19] have measured the acoustic attenuation in sapphire in the 0.5 - 10 GHz-range below 130 K, and find a temperature dependence roughly $\propto T^4$ with a frequency dependence $\propto \omega$. The difference between the behaviour at these two temperatures is due to a transition from Akhieser damping to anharmonic phonon decay [20, 21]. Below 10% of the Debye temperature Θ_D (980 K for sapphire), anharmonic phonon decay is considered to be the dominant mechanism. For a sample temperature of 200 K, we may assume that Akhieser damping is still dominant, and extrapolate the room temperature value of η to 4×10^{-4} Ns/m^2.

In the calculation for low temperatures, the damping dependence $\propto \omega$ can be taken into account by replacing the damping term in Eq. (V.1) by $+2\alpha_0 v_s^2 \partial s/\partial x$ [22]. From Ref. [18], we have inferred a value for $\alpha_0 v_s^2$ of 1.0×10^{-1} m at 100 K. This value was extrapolated to obtain values for 60 K and 18 K, other temperatures chosen in experiments.

The typical frequencies that manage to traverse a length d_{sample} in sapphire can

be estimated as $f_{tr} \sim (2\pi\alpha_0 d_{sample})^{-1}$. For $d_{sample} \sim 300$ μm we find $f_{tr} = 1.3$ THz at 100 K, and > 10 THz at 60 K, indicating vanishing attenuation below 60 K. At 77 K, $f_{tr} = 6.5$ THz implying that soliton development and propagation are feasible at LN_2 temperatures in sapphire.

V.3.3 Compressive solitons

In the absence of damping, the wave equation Eq. (V.1) reduces to the well-known Korteweg - de Vries (KdV) - equation. Following the analysis of Ref. [23], we rewrite the KdV-equation into the more general form

$$\frac{\partial \psi}{\partial t'} = 6{\sigma_N}^2 \psi \frac{\partial \psi}{\partial \xi} + \frac{\partial^3 \psi}{\partial \xi^3}, \text{ with} \tag{V.2}$$

$$\sigma_N \simeq \frac{\tau}{\sqrt{8}} \left(\frac{\alpha s_0 v_s}{12 \rho \beta} \right)^{1/2} \tag{V.3}$$

the similarity parameter for a Gaussian derivative input strain waveform. τ is defined as in Ch. III, and normalization of the compressive strain was performed as in Refs. [23, 24]. For the compressive part of the initial strain wavepacket ($s < 0$), exact solutions to Eq. (V.2) can be found [6, 8, 23]. One then finds a family of N so-called *solitons* with index number $i = 1, \ldots, N$. For $\sigma_N \gg 1, \sigma_N \sim N$. The i^{th} soliton is characterized by a single parameter (eigenvalue) λ_i, linking its velocity, amplitude, and width. In real coordinates, these soliton solutions have the form

$$s_i(x,t) = a_i \text{sech}^2 \left(\frac{(x - x_{0,i}) - v_i t}{w_i} \right). \tag{V.4}$$

$x_{0,i}$ is the soliton position at $t = 0$ (virtual, since the solitons have not yet formed at that time). The supersonic velocity v_i (an easily accessible experimental quantity) can be expressed in λ_i as

$$v_i = \frac{8\beta}{{v_s}^2 \tau^2} \lambda_i, \tag{V.5}$$

while the amplitude a_i and temporal width w_i in turn connect to v_i as

$$a_i = \frac{6\rho v_s}{\alpha} v_i \quad (\alpha < 0), \tag{V.6}$$

$$w_i = \frac{1}{v_s}\left(\frac{4\beta}{v_i}\right)^{1/2}. \tag{V.7}$$

For an initially sech^2-shaped compressive part of the strain, the eigenvalues λ_i can be calculated exact [24]:

$$\lambda_i = \left(1 - 2i + \sqrt{1+4{\sigma_N}^2}\right)^2. \tag{V.8}$$

For the tensile part of the strain (with $s > 0$), Eq. (V.2) is not integrable and does not give rise to discrete solutions of Eq. (V.2), but to a continuum of states. The development of the rarefaction part of the wave must therefore be evaluated numerically.

V.4 Experimental results

For all presented measurements, the $t = 0$ point was determined for each sample for low fluences as the point where either the $\delta\varphi$ or ρ signal was maximal, and fixed there for higher fluences.

For interpretation of the measured data, calculated strain traces according to a numerical solution of Eq. (V.1) taking into account the correct damping are presented in Figs. V.1 b) - V.5 b). The corresponding calculated ρ and $\delta\varphi$ traces are shown together with the measurements in Figs. V.1 a) - V.5 a). Here, acoustic reflections at the pump film/substrate and substrate/probe film interface were taken into account. The measured traces were corrected for the reduced interferometer contrast of $\sim 88\%$ for the 123-μm and 307-μm samples (nicely coinciding with the measurements in Chs. II - IV), and $\sim 50\%$ for the 405-μm sample.

V.4.1 Temperature dependence

Fig. V.1 a) shows the measured phase signals $\delta\varphi$ obtained for the 307-μm thick sapphire sample for indicated temperatures in the range 295 K - 18 K. With decreasing temperature, the $t = 0$ point shifts due to small changes in sound velocity [14], but since the sample had to be realigned after each temperature step, we could not determine this variation accurately. The $t = 0$ point is therefore fixed at the point of maximum phase signal $\delta\varphi_{max}$ (as noted earlier) determined for each temperature.

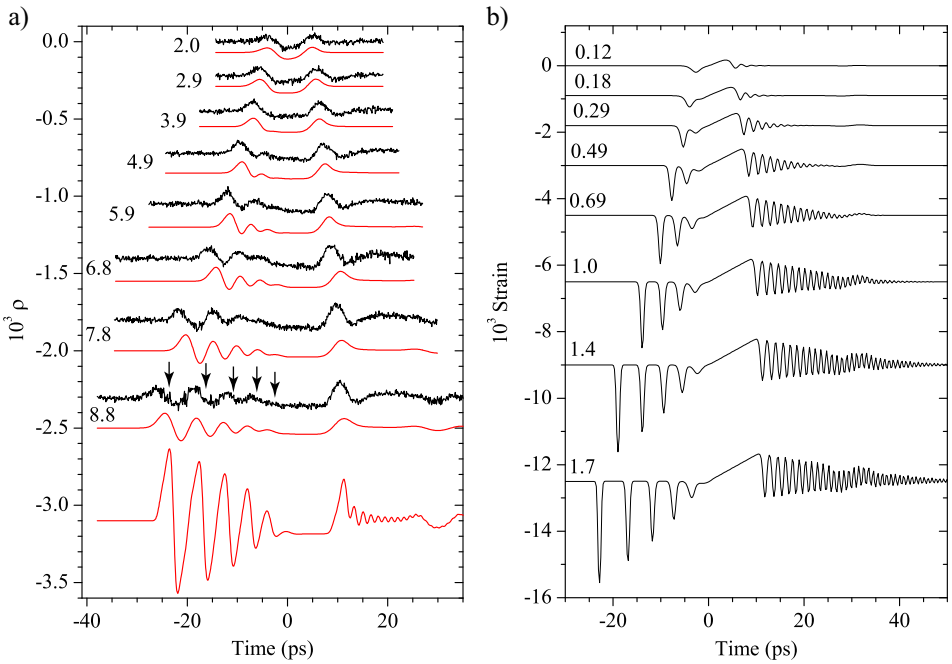

Figure V.2: Amplitude measurements at 18 K for 123-micron sapphire sample
a) Measurements (black line) and calculations (grey line) of amplitude (ρ) signal, for wave propagation through 123 μm of sapphire at a temperature of 18 K. Numbers indicate pump fluence in mJ/cm^2. Bipolar features correspond to arrival of solitons. For 8.8 mJ/cm^2, soliton arrival times are indicated by arrows. In the calculation, corrections for temporal broadening discussed in Sec. V.5 were included. At fluence of 8.8 mJ/cm^2, both uncorrected and corrected signals are shown, demonstrating the relevance of temporal broadening effects. b) Calculated strain profiles after propagation, for an input pulse of $\sim$ 3.6 ps width and indicated strain amplitudes s_0 ($\times 10^3$). At the highest fluence, at least five solitons are formed. Note that the final solitons in the calculation are not resolved in the measurement.

At room temperature we confirm the symmetric, parabolic phase signal observed in Ch. IV, corresponding to a shock wave. Cooling to 200 K, the generation efficiency slightly increases, but the wave shape does not significantly change. At 295 K and 200 K, the damping $\propto \omega^2$ apparently results in overdamped propagation.

At 100 K, however, the wave shape becomes strongly asymmetric. Velocity differences appear between the front and rear of the wave are clear indications

of nonlinear *and* dispersive propagation [25]. The calculations of Fig. V.1 b) demonstrate the formation of (five) acoustic solitons at the front. We note that because of the $\propto \omega$ damping term at 100 K the solitons are critically damped and propagate slower than they would have in the absence of damping.

At 60 K and below, where damping has only a minor influence, clear steps appear at the front of the strain wave. Knowing that the phase signal $\delta\varphi$ is proportional to the integrated strain passing the surface, the steps for $t < 0$ at 60 K and 18 K point to compressive wavepackets separated in space [26], and are characteristic to soliton formation [9]. The calculated soliton arrivals are indicated by numbers in Fig. V.1 a) for the 60 K data. In earlier experiments on samples with a poor metal film quality, these steps did not show up. Here, interface scattering limits transmission from sapphire into the Cr and strong scattering of each soliton in the detection film prevents a well-defined arrival time at the surface [14].

Since the final pulse shape depends critically on the magnitude and the frequency dependence of acoustic attenuation, monitoring nonlinear wave propagation can be used to investigate attenuation of high-frequency phonons in weakly attenuating materials.

V.4.2 Amplitude measurements at 18 K

Before presenting the phase measurements at 18 K, we first consider amplitude (ρ) measurements as a function of pump fluence on the thinnest sample at 18 K. The results are shown in Fig. V.2 a). The signals are qualitatively similar to those measured in Refs. [6, 8, 9].

Since the solitons are unipolar and undergo a sign change upon reflection at the detection interface, convolution according to Eq. (III.1) predicts a bipolar amplitude signal with a width equal to the convoluted soliton width. Such bipolar signals indeed show up prior to $t = 0$ for fluences > 4 mJ/cm^2. At the highest fluence of 8.8 mJ/cm^2, at least four solitons are discernible.

Three typical features of solitons are readily visible. First, their number increases with fluence. This is expected from Eq. (V.3), since $\sigma_N \propto s_0^{1/2}$. Second and third, the velocity of soliton i increases with its number i and with pump fluence. This follows from the calculated eigenvalues Eq. (V.8), and the corresponding supersonic soliton velocities v_i in Eq. (V.5).

The calculated strain waveforms corresponding to the curves fitting the measurements are shown in Fig. V.2 b). At 8.8 mJ/cm^2, the calculated soliton positions are indicated by arrows. Apparently, for all fluences the last one or two

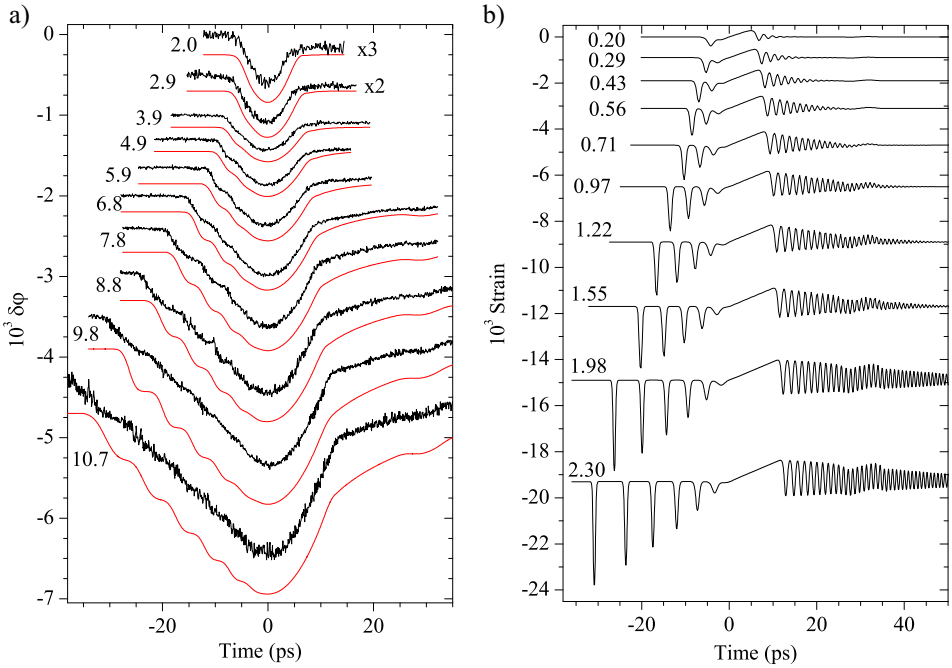

Figure V.3: Phase signals and corresponding strain waveforms at 18 K after propagation through 123 micron of sapphire
a) Measured (black line) and calculated (gray line) phase ($\delta\varphi$) signals for the 123-μm thick sample at 18 K. Numbers indicate fluence in mJ/cm^2. Steps correspond to soliton arrival at the detection surface. In the calculation, broadening effects discussed in Sec. V.5 are taken into account. b) Calculated strain waveform after propagation through 123 μm of sapphire. Numbers indicate input strain amplitude $s_0 \times 10^3$.

solitons are not resolved, because they produce only a very small ρ signal. Arrival time variations further decrease the soliton visibility, and affect detection of the subsonic high-frequency tail even more dramatically. In Fig. V.2 a), for example, the lower two traces show the effects of broadening on the calculated signal for a fluence of 8.8 mJ/cm^2. Apart from these complications, amplitude data yield no information about the soliton amplitude and width.

V.4.3 Phase measurements at 18 K

Figs. V.3 a) - V.5 a) show the collected phase measurements for the 123-μm, 307-μm and 405-μm samples, respectively. The signal-to-noise ratio did not permit

the use of Eq. (III.5), i.e. obtain the strain profile directly by taking the discrete derivative. In all measurements, however, clear steps are visible. Their number increases with fluence, in accordance with Eq. (V.3) and the results from the previous section. In contrast to the amplitude traces, the smaller solitons are resolved in the phase signals. The amplitude of the steps in the phase signal, which is a measure for the soliton volume V_i, increases with soliton number i. In Fig. V.5 c), the steps in the measured trace at 5.9 mJ/cm^2 for the 405-μm sample are shown in more detail. The width of the first step demonstrates that the first soliton fully passes the surface in a time $\sim$ 1.5 ps. The time of passage increases to $\sim$ 2.1 ps and $\sim$ 2.7 ps for the second and third soliton, respectively, in agreement with Eq. (V.7). The expected sharp steps for the first solitons apparently wash out at higher fluences.

The increasing length of the subsonic dispersive tail with increasing pump fluence confirms that the frequencies in the wave packet have increased for higher pump fluences. Fig. V.5 d) shows $\sim$ 500-GHz oscillations at a fluence of 5.9 mJ/cm^2 for the thickest sample, where our temporal resolution at low fluences appeared to be optimal. At higher fluences, where the oscillation frequencies are expected to increase, the oscillation could not be resolved anymore. We can however make an estimate of the frequency content of the tail at the highest fluences. At 405 μm and a fluence of 10.7 mJ/cm^2, the typical length of the tail is $\sim$ 75 ps, leading to a velocity difference Δv of $\sim$ 23 m/s. From the approximation of the first order dispersion term [6], we find that $\Delta v = \beta k^2$. For the typical frequency in the tail $f_{tail} \sim vk/2\pi$ we arrive at 1.5 THz.

V.5 Discussion

The presented data show excellent agreement between experiments and calculations. In this section we discuss the calculation details, in particular the characterization of the generated input pulse width and amplitude. In addition, we take advantage of the inherent properties of solitons to allow for a surprisingly detailed analysis.

V.5.1 Input pulse characterization

The strain pulse launched into the sapphire substrate was calibrated in an experiment as shown in Fig. III.6 d). The width τ was found to be $\sim$ 3.6 ps for all

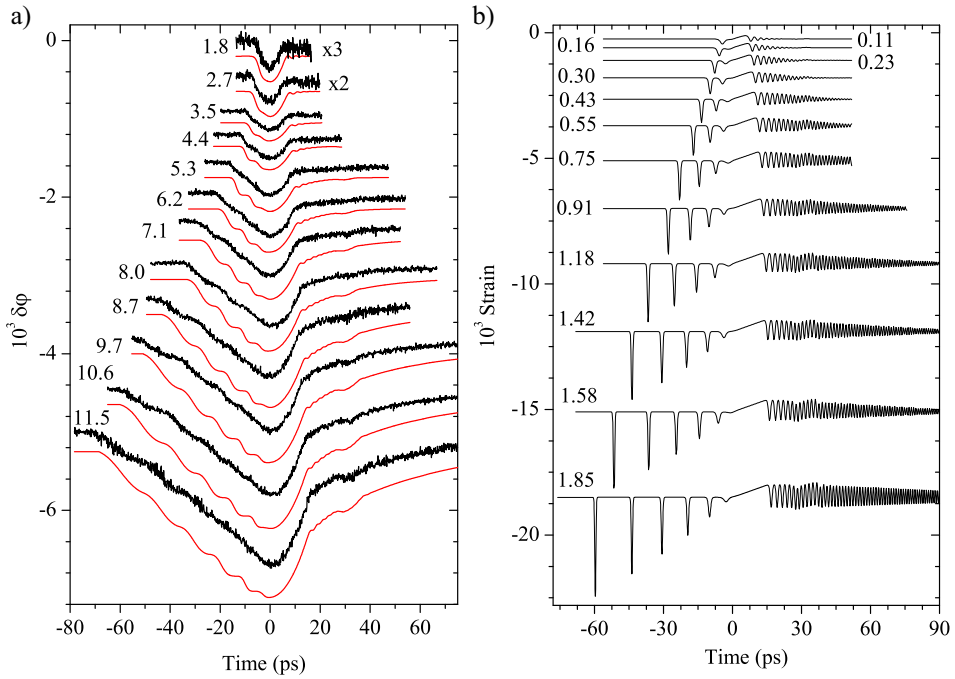

Figure V.4: Phase signals and strain waveforms at 18 K after propagation through 307 micron of sapphire

a) Measured (black line) and calculated (gray line) $\delta\varphi$ signals for the 307-μm thick sample at 18 K. Numbers indicate fluence in mJ/cm^2. In the calculation, broadening effects discussed in Sec. V.5 are taken into account. b) Calculated strain waveform after propagation through 307 μm of sapphire. Numbers indicate input strain amplitude $s_0 \times 10^3$.

fluences. This value is typically 0.6 ps lower than for microcrystalline films, suggesting that the acoustic attenuation is lower, and the film quality better. The relative strain amplitude increases in the relevant fluence range as $\propto {I_0}^{1.7}$, slightly steeper than for the multicrystalline film of Ch. III at room temperature.

The absolute amplitude s_0 was difficult to derive since the elasto-optical parameters appeared to be different from the ones in Ch. III, probably due to temperature effects or the different film structure. An independent estimate for s_0 can be obtained from the maximum phase signal $\delta\varphi_{max}$, which for a Gaussian derivative Eq. (III.6) in absence of damping should equal $-4\pi\sqrt{e}cv_s s_0\tau/\lambda$, with c the interferometer contrast.

In the calculation, s_0 and τ were left as free fit parameters to achieve optimal

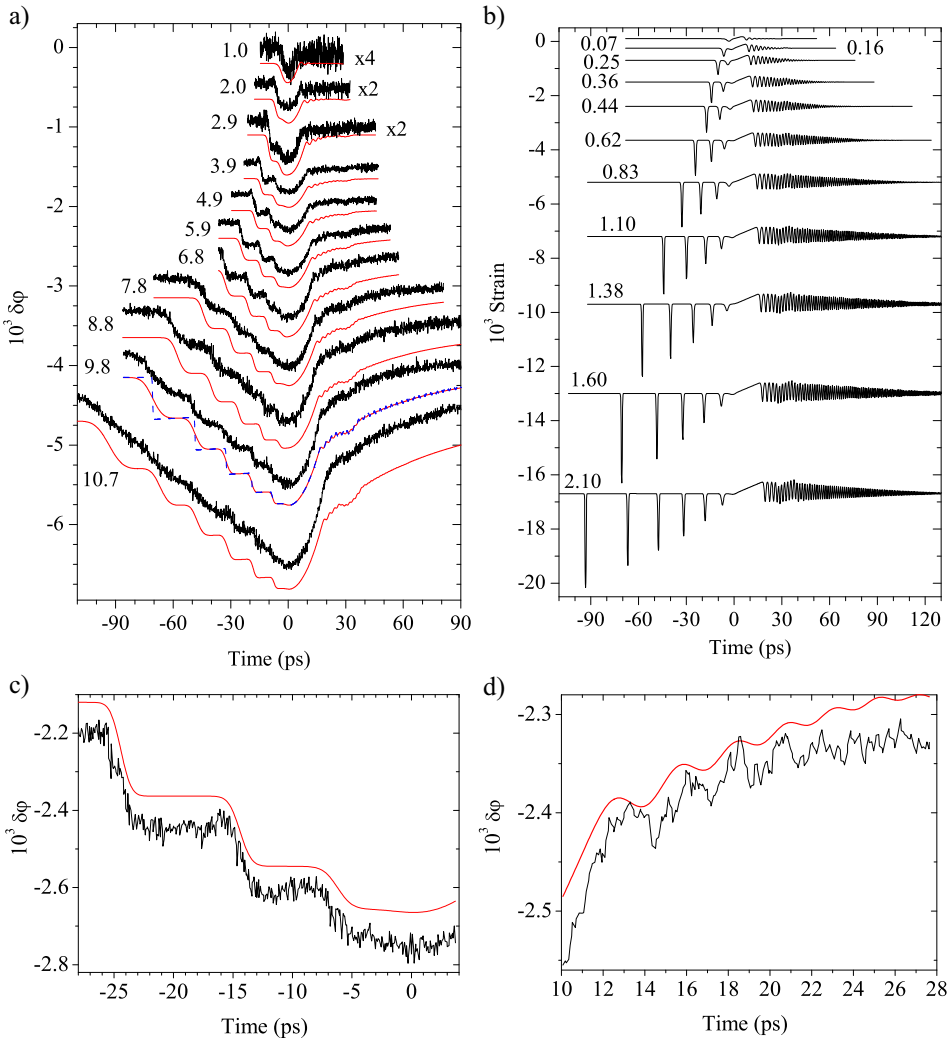

Figure V.5: Phase signals and strain waveforms at 18 K after propagation through 405 micron of sapphire

a) Measured (black line) and calculated (gray line) $\delta\varphi$ signals for the 405-μm thick sample at 18 K. Numbers indicate fluence in mJ/cm^2. In the calculation, broadening effects discussed in Sec. V.5 are taken into account. Calculated data for fluence of 9.8 mJ/cm^2 shows difference between broadened (solid line) and unbroadened (dashed line) signals. b) Calculated strain waveform after propagation through 405 μm of sapphire. Numbers indicate input $s_0 \times 10^3$. c) Detail of measured trace and calculation at 5.9 mJ/cm^2. The width w_1 of the first soliton was measured at $\sim$ 500 fs. d) $\sim$ 500-GHz oscillations in the trailing part of the wave for 5.9 mJ/cm^2, and corresponding calculated results.

agreement with the measured data. The values for τ found from the fit routines agree with the measured ~ 3.6 ps. The values for s_0 found from the fit routine are collected in Fig. V.6 a). Reasonable overlap is obtained for the various sets of measurements. The spread in values for different sets reflects the already mentioned inaccuracy of the pump fluence determination, of the order of $\pm$ 10%. The strain amplitudes and fluence dependence are comparable to those found in the previous chapters. The values for s_0 differed less than 5% from the estimate based on the measured $\delta\varphi_{max}$ for all measurements, except for the 307-μm sample at the highest fluences.

V.5.2 Comparison to measured data

Propagation of the input pulse according to theory discussed in Sec. V.3 was calculated using the known sapphire material parameters [6]. We subsequently use Eq. (III.1) to calculate the ρ signal, and Eqs. (III.3) - (III.4) to calculate $\delta\varphi$. For $\delta\varphi$, the bulk metal film contribution expressed in Eq. (III.2) appeared to be negligibly small.

In the experiments, strong temporal broadening of the calculated signals is observed. There are *linear* broadening effects, which we take into account by convoluting the calculated traces with a Gaussian broadening function with characteristic time $\tau_{br} \sim 1$ ps [27]. At the highest fluences, it is obvious that this 1-ps broadening is by far not enough to account for measured broadening. The characteristic width $w_{meas,i}$ of all detected solitons for the sample thickness of 405 μm was determined, and the result is shown in Figs. V.6 b). A strong connection between pump fluence and/or soliton index number i, and the determined width w_{meas} is found. This suggests *nonlinear* broadening action (Ch. IV).

One cause could be velocity differences due to pump intensity variations as was already encountered in Ch. IV. For solitons, the variation in arrival time t_i, δt_i, can be estimated at $\sim 0.07 t_i$ [28]. For the thickest sample, where $t_1 = -95$ ps, $\delta t_1 \sim 6.5$ ps, exceeding the soliton width ~ 200 fs by an order of magnitude. The calculated δt_i is plotted in Fig. V.6 b) for this sample, and shown to be sufficient to explain the measured temporal broadening up to ~ 10 mJ/cm^2. At the highest fluence of 11 mJ/cm^2, however, additional broadening effects must be invoked. Possibly, higher-order corrections to the dispersion come into play, affecting the stability of the soliton. We note, that at this fluence, the observed soliton volumes also start to deviate significantly from theory (next section), until mere detection of solitons was found to be impossible for higher fluences. Another possibility is

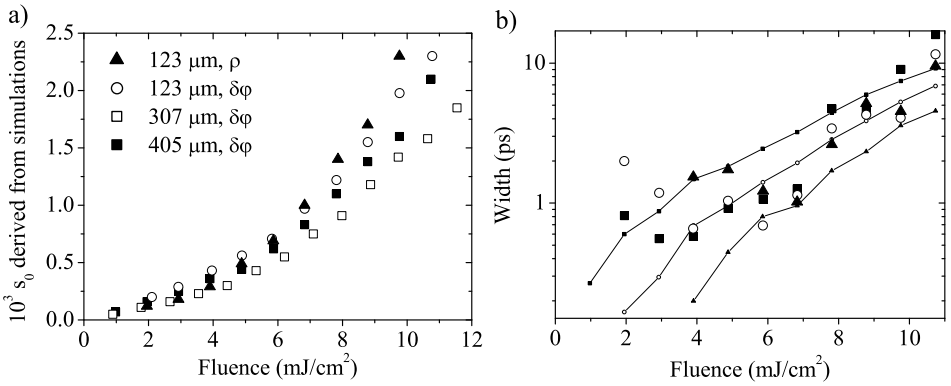

Figure V.6: Strain amplitudes and broadening from simulations
a) Fitted strain amplitude s_0 versus pump fluence at 18 K. Fitted temporal width was 3.6 ps in all cases. b) Temporal width determined for the first three soliton signals (squares, circles, triangles, respectively) and sample thickness 405 μm. Lines are expected nonlinear broadening $\sim 0.07\delta t_i$ based on measured arrival times t_i.

that transverse dynamics comes into play, creating sizable arrival time differences over the probe spot.

The approach works well for the 123-μm ρ and $\delta\varphi$ and 405-μm $\delta\varphi$ data, where temporal broadenings of 0.08 t_i, 0.07 t_i and 0.07 t_i, respectively, are required. For the 307-μm $\delta\varphi$ data a broadening of 0.12 t_i is required. Moreover, for the highest fluences, the first solitons are significantly lower than expected from calculations, while the positions are accurately predicted. This suggests strong scattering at the probe film for this sample.

The broadening corrections were included in the calculated traces in Figs. V.1 a) - V.5 a). To demonstrate the importance of the broadening effect, both corrected and uncorrected signals for the amplitude measurement at a fluence of 8.8 mJ/cm^2 in Fig. V.2 a), and for the phase at a fluence of 9.8 mJ/cm^2 in Fig. V.5 a).

Quite interestingly, at low fluences the 405-μm sample has better temporal resolution than expected, even better than τ_{br} (Fig. V.5 c)). It might be, that the probe is focused at a spot where the Cr detection film is thinner, and/or the front and rear planes are locally more parallel than the (globally) determined value.

V.5.3 Soliton properties

It is interesting to use the measured phase signals at 18 K to analyze the properties of each individual soliton. The integrated phase signal of a soliton of the form Eq. (V.4) reads

$$b_i \left(1 + \tanh \left(\frac{(t - t_i)}{w_{meas,i}} \right) \right). \tag{V.9}$$

The soliton velocity v_i in the moving coordinate system can be estimated from the fitted arrival time t_i by t_i/d_{sample}. Here, one assumes that $x_{0,i}$ from Eq. (V.4) is zero at $t = 0$. For the 405-μm data, where t_i is very large, this certainly is a reasonable approximation. Further, the soliton volume $V_i = 2a_i w_i$ can be calculated from b_i by $V_i = (2b_i\lambda)/(8\pi c)$. Finally, the width $w_{meas,i}$ is the (typically subpicosecond) soliton width w_i, multiplied by the temporal resolution for that soliton, discussed in the previous section.

First, we examine the arrival times t_i for the three sample thicknesses at a fixed initial strain amplitude. The result for $s_0 = 4.3 \times 10^{-4}$ is shown in Fig. V.7 a). Here, $\sigma_N = 3.18$, and three solitons form. The arrival time decreases linearly with sample thickness for each soliton, indicating that the solitons move at a constant supersonic velocity. We determine the slope $\Delta t/\Delta d$ and the supersonic velocity $v_i = v_s^2 \times \Delta t/\Delta d$, and the values are indicated in the figure.

For $s_0 = 1.6 \times 10^{-3}$, six solitons are detected ($\sigma_N = 6.1$). The determined arrival times t_i are presented in Fig. V.7 b). Again, the linear velocity applies. The first soliton at this high fluence has a velocity $v_1 = 23.2$ m/s. Using Eqs. (V.6) and (V.7), we derive a soliton amplitude a_1 of 3.4×10^{-3} ($\sim 2s_0$ [23]), and a width w_1 of only 200 fs.

Next, we analyze the soliton arrival times t_i and volumes V_i for the sample of 405-μm thickness. Using the s_0 derived from simulations, σ_N can be determined for each measurement in Fig. V.5. We have plotted the soliton arrival time t and volume V_i against σ_N in Figs. V.7 c) and d), along with the expected dependence from the theory in Sec. V.3. Excellent agreement is found. For $\sigma_N \gg i$, v_i is determined from Eqs. (V.5) and (V.8) to depend quadratically on σ_N^2. On the other hand, $V_i \propto v_i^{1/2}$ and thus depends linearly on σ_N. Both dependencies are accurately reproduced in Figs. V.7 c) and d).

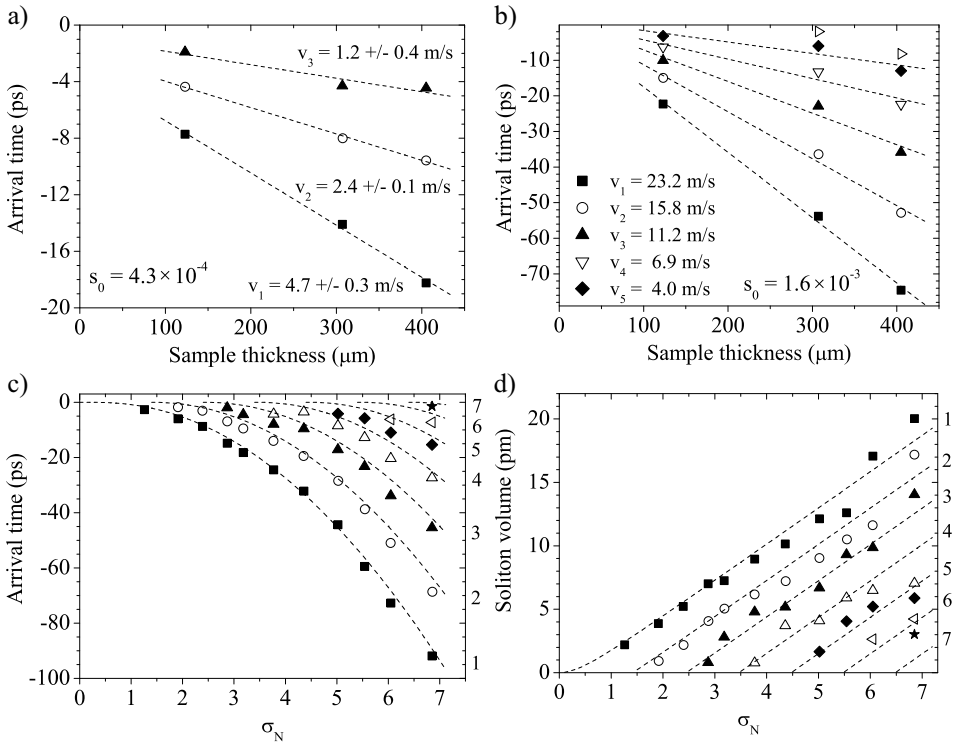

Figure V.7: Soliton velocity and similarity
a) Position of soliton versus sample thickness, for an initial strain wave of amplitude $s_0 = 4.3 \times 10^{-4}$ and width $\tau = 3.6$ ps. Numbers indicate soliton velocity in m/s. b) Like a), but now for $s_0 = 1.6 \times 10^{-3}$. All velocities are determined ± 0.1 m/s. No accurate determination of velocity could be performed for the sixth soliton. c) Position of solitons versus similarity parameter σ_N. dashed lines gives comparison to positions predicted by Eqs. (V.3), (V.5), and (V.8). d) Soliton volume determined from measurements versus similarity parameter σ_N. Dashed lines are soliton volume $V_i = 2w_i a_i$ predicted by theory.

V.6 Conclusions and prospects

In conclusion, we have succeeded in observing soliton formation in sapphire slabs of different thicknesses in low-repetition rate interferometric pump-probe experiments. The parallellism of the sample front and rear planes, and the quality of the Cr detection films appear to be crucial to soliton detection. At 100 K, critical damping occurs and soliton formation is incomplete. Already at 60 K, solitons propagate virtually undamped. Extrapolation of the determined damping at these

temperatures suggests that soliton formation and propagation at liquid nitrogen temperatures in sapphire is possible. This observation may prove to be relevant to the practical use of acoustic solitons in nano-ultrasonic material characterization.

Up to seven solitons in the train are distinguished at the highest fluence of 11 mJ/cm^2, for a strain pulse with initial amplitude 2.1×10^{-3} and temporal width 3.6 ps. At moderate pump fluences, we have directly measured the width of single solitons of only 500 fs, corresponding to 5 nm in sapphire. From accurately measured supersonic soliton velocities a minimal soliton width of 200 fs can be inferred for the highest fluences. Frequencies of 500 GHz are observed in the high-frequency tail, while frequencies up to 1.5 THz can be inferred. Direct observation of the fastest effects is hampered by nonlinear broadening effects related to power fluctuations of the laser.

All measured traces agree excellently with numerical calculations based on the Korteweg - de Vries - equation. Furthermore, the measured properties of the generated solitons agree with the exact relations between soliton amplitude, width, and velocity according to the Korteweg - de Vries solutions.

The quality of the current setup can be further improved by pumping at 800 nm and probing at 400 nm. This decreases the feasible probe beam size and paves the way to larger Gaussian pump spots, thereby limiting lateral effects while at the same time increasing the phase signal by a factor of two (Eq. (III.3)). In the pump, removing the BBO crystal both improves the long-time alignment stability (limited by thermal fluctuations in the BBO), and decreases the intensity variations by a factor of two. The use of a generation film where strain amplitude changes linearly with fluence would further reduce effects of pump intensity variations. Here, nickel (for which efficient strain generation was found in Ch. III) would be a good candidate. Finally, the controlled growth of even thinner detection films should reduce broadening effects due to the metal detection film. In total, these measures should substantially improve temporal and spatial resolution, and resolve effects above strain amplitudes of 2×10^{-3}, in the extremely dispersive regime.

The splitting of the initial wave packet with a typical width of 5 ps into several short acoustic pulses as short as 200 fs (corresponding to < 2 nm width), opens the way to acoustic manipulation of nanometer-sized structures [29] on a subpicosecond timescale. A first experiment where solitons are employed to shift the electronic levels of a quantum well is presented in the following chapter.

References

1. D.J. Korteweg and G. de Vries. On the change of form of long waves advancing in a rectangular canal, and on a new type of long stationary waves. *Phil. Mag.*, 39:422, 1895.
2. A.R. Osborne and T.L. Burch. Internal solitons in the Andaman Sea. *Science*, 208:451, 1980.
3. L.F. Mollenauer, R. H. Stolen, and J.P. Gordon. Experimental observation of picosecond pulse narrowing and solitons in optical fibers. *Phys. Rev. Lett.*, 45(13):1095, 1980.
4. G.O. Ludwig, J.L. Ferreira, and Y. Nakamura. Observation of ion-acoustic rarefaction solitons in a multicomponent plasma with negative ions. *Phys. Rev. Lett.*, 52(4):275, 1984.
5. K.E. Strecker, G.B. Partridge, A.G. Truscott, and R.G. Hulet. Formation and propagation of matter-wave soliton trains. *Nature*, 417:150, 2002.
6. H.-Y. Hao and H.J. Maris. Experiments with acoustic solitons in crystalline solids. *Phys. Rev. B*, 64:064302, 2001.
7. B.C. Daly, T.B. Norris, J. Chen, and J.B. Khurgin. Picosecond acoustic phonon pulse propagation in silicon. *Phys. Rev. B*, 70(21):214307, 2004.
8. W. Singhsomroje and H.J. Maris. Generating and detecting phonon solitons in MgO using picosecond ultrasonics. *Phys. Rev. B*, 69(17):174303, 2004.
9. E. Péronne and B. Perrin. Generation and detection of acoustic solitons in crystalline slabs by laser ultrasonics. *Ultrasonics*, 44(Suppl. 1):e1203, 2006.
10. O.L. Muskens and J.I. Dijkhuis. High amplitude, ultrashort, longitudinal strain solitons in sapphire. *Phys. Rev. Lett.*, 89(28):285504, 2002.
11. O.L. Muskens, A.V. Akimov, and J.I. Dijkhuis. Coherent interactions of terahertz strain solitons and electronic two-level systems in photoexcited ruby. *Phys. Rev. Lett.*, 92(3):335503, 2004.
12. O.L. Muskens and J.I. Dijkhuis. High-amplitude, ultrashort strain solitons in solids. In K.-T. Tsen, editor, *Non-equilibrium dynamics of semiconductors and nanostructures*, pages 15–45. CRC Press, 1st edition, 2005.
13. B.B. Kadomtsev and V.I. Petviashvili. On the stability of solitary waves in weakly dispersing media. *Sov. Phys. Dokl.*, 15(6):539, 1970.
14. H.-Y. Hao and H.J. Maris. Dispersion of the long-wavelength phonons in Ge, Si, GaAs, quartz and sapphire. *Phys. Rev. B*, 63:224301, 2001.
15. F. Watanabe, D.G. Cahill, B. Gundrum, and R.S. Averback. Ablation of crystalline oxides by infrared femtosecond laser pulses. *J. of Appl. Phys.*, 100(8):083519, 2006.
16. J.W. Tucker and V.W. Rampton. *Microwave Ultrasonics in Solid State Physics*. North-Holland Publishing Company, 1st edition, 1972.
17. B.A. Auld. *Acoustic Fields and Waves in Solids*, volume 1. Robert E. Krieger Publishing Company, 2nd edition, 1990.

18. M. Pomerantz. Temperature dependence of microwave phonon attenuation. *Phys. Rev.*, 139(2A):501, 1965.
19. I.S. Ciccarello and K. Dransfeld. Ultrasonic absorption at microwave frequencies and at low temperatures in MgO and Al_2O_3. *Phys. Rev.*, 134(6A):A1517, 1964.
20. E.P.N. Damen, A.F.M. Arts, and H.W. de Wijn. Experimental verification of Herring's theory of anharmonic phonon relaxation: TeO_2. *Phys. Rev. B*, 59(1):349, 1999.
21. C. Herring. Role of low-energy phonons in thermal conduction. *Phys. Rev.*, 95:954, 1954.
22. W. Chen and S. Holm. Fractional Laplacian time-space models for linear and nonlinear lossy media exhibiting arbitrary frequency power-law dependency. *J. Ac. Soc. Am.*, 115(4):1424, 2003.
23. O.L. Muskens and J.I. Dijkhuis. Inelastic light scattering by trains of ultrashort acoustic solitons in sapphire. *Phys. Rev. B*, 70(10):104301, 2004.
24. V.I. Karpman. *Non-linear Waves in Dispersive Media*. Pergamon Press, 1st edition, 1975.
25. H.-Y. Hao and H.J. Maris. Study of phonon dispersion in silicon and germanium at long wavelengths using picosecond ultrasonics. *Phys. Rev. Lett.*, 84(24):5556, 2000.
26. O. Matsuda, T. Tachizaki, T. Fukui, J.J. Baumberg, and O.B. Wright. Acoustic phonon generation and detection in GaAs/$Al_{0.3}Ga_{0.7}$As quantum wells with picosecond laser pulses. *Phys. Rev. B*, 71(11):115330, 2005.
27. The Gaussian function was defined as $(\pi\tau_{br}^2/2)\exp(-2(t-t_0)^2/\tau_{br}^2)$. Here, $\tau_{br} = (\tau_t^2+\tau_p^2+\tau_m^2)^{1/2}$, consisting of contributions
    - τ_t, the probe pulse length, of $\sim$ 180 fs (App. B).
    - τ_p, due to parallelism of the front and rear plane of the sample, specified in Section V.2.
    - τ_m, due to attenuation in the metal film. The attenuation in the metal film effectively only broadens the pulse, but does not give a large decrease in pulse volume. From the value determined in Ch. III for the low-quality Cr films, we estimate τ_m for a 20-nm thick film at 780 fs.

    This way, estimates for τ_{br} of 1.6 ps, 1.4 ps, and 1.0 ps are found for the 123-μm, 307-μm, and 405-μm sample, respectively.
28. We assume that for soliton i, $\delta t_i/t_i = \delta v_i/v_i = \delta a_i/a_i \sim \delta s_0/s_0$. When the variations in pump fluence are $\delta I_0 \sim \pm 2\%$, and taking into account that $s_0 \sim I_0^{1.7}$, we derive for soliton i that $\delta v_i \sim 2 \times 0.02 \times 1.7 \times v_i$.
29. A.V. Akimov, A.V. Scherbakov, D.R. Yakovlev, C.T. Foxon, and M. Bayer. Ultrafast band-gap shift induced by a strain pulse in semiconductor heterostructures. *Phys. Rev. Lett.*, 97(3):037401, 2006.

Chapter VI

Chirping of an optical transition by an ultrafast acoustic soliton train in a semiconductor quantum well

Abstract

Acoustic solitons formed during the propagation of a picosecond strain pulse in a GaAs crystal with a ZnSe/ZnMgSSe quantum well on top lead to exciton resonance energy shifts of up to 10 meV and ultrafast frequency modulation, i.e. chirping, of the exciton transition. The effects are well described by a theoretical analysis based on the Korteweg-de Vries equation and accounting for the dynamical properties of the excitons in the quantum well.

VI.1 Introduction

In the previous chapter, it was shown that the nonlinear elastic properties of solids result in the striking phenomenon of the transformation of a coherent strain wave packet into a train of ultrashort acoustic solitons. Such solitons propagate directionally through the crystal with a velocity slightly above the velocity of longitudinal sound, locally introducing a "nano-earthquake". The first experimental observation of an acoustic soliton by Hao and Maris in 2001 [1] was followed by detailed studies [2, 3, 4, 5, 6] that have shown that a single soliton pulse in such a train can occupy a space as small as a few nanometers, corresponding to durations as short as a few hundred femtoseconds, and may reach strain amplitudes exceeding 10^{-3}. These results were confirmed in Ch. V.

These spatial and temporal characteristics of acoustic solitons are close to the typical sizes of nanostructures (quantum wells, wires and dots) and relaxation

times of their electronic excitations, respectively, which were studied intensively during the last decades. Thus the discovery of acoustic solitons may open up a new research field in solid state physics where subpicosecond and nanometer control of the optical response of nanostructures is achieved by acoustic solitons *without generation of carriers* as unavoidably occurs in standard ultrafast optical excitation schemes. To our knowledge, however, no effects of acoustic solitons on the electronic levels of nanostructures have been observed yet.

In this chapter, we present the first experimental and theoretical study of ultrafast frequency modulation of an exciton resonance in a semiconductor quantum well (QW) by an acoustic soliton train. When the QW is hit by the "nanoearthquake", the exciton resonance experiences an energy shift as high as 10 meV on a picosecond time scale, as is demonstrated via its optical response. The theoretical analysis of this soliton-induced effect takes into account the finite QW width and the exciton coherence time. Excellent agreement between experiment and theory is reached, which paves the way for a new class of quantitative ultrafast acoustic experiments in semiconductor nanostructures.

VI.2 Sample and setup

The idea and scheme of the experiment are shown in Fig. VI.1 a), and all relevant parameters are collected in Table VI.1. The sample used was a (001)-oriented GaAs slab with a thickness l_0 of 114 μm. The heterostructure deposited by MBE on the front side of the slab was a ZnSe QW with a width $a = 8$ nm embedded between $Zn_{0.89}Mg_{0.11}S_{0.18}Se_{0.82}$ barriers. The details of the fabrication and the properties of the structure can be found elsewhere [9]. A 113-nm thick Al film was deposited on the back side of the GaAs slab. This metal film acts as an optoelastic transducer upon excitation by a short laser pulse and injects a strain pulse into the GaAs slab [11, 12]. In these experiments the sample was immersed in liquid helium ($T_0 = 1.8$ K), and the Al film was excited by 200-fs pulses from an amplified Ti-sapphire laser (wavelength 800 nm) with a repetition rate of 250 kHz and a pulse energy of 5 μJ. This pump beam was focused to a 100-μm FWHM spot on the film, creating energy densities I_0 up to 10 mJ/cm^2 per pulse.

The effect of the soliton pulses on the optical response of the QW was studied using ultrafast optical spectroscopy. For this a probe beam was split from the laser beam, passed through a sapphire plate to generate femtosecond white light pulses, and given an optical delay of 20 ns, equal to the travel time of the longitudinal

Parameter	Symbol	Value	Ref.
Thickness of Al generator film	d_{Al}	113 nm	Exp.
Acoustic reflection coeff. Al/GaAs	r_{GaAs}	0.18	Calc.
Thickness of GaAs substrate	l_0	114 μm	
Speed of sound in (001) GaAs	v_{GaAs}	4.8×10^3 m/s	
Nonlinearity parameter for GaAs	α	-3.09×10^{11} N/m^2	[7]
Dispersion parameter for GaAs	β	0.74×10^{-17} m^3/s	[8]
Mass density	ρ	5.31×10^3 kg/m^3	
Temporal width of input wave	τ	6.8 ps	Exp.
Strain amplitude	s_0	7×10^{-5} I_0 (I_0 pump fluence in mJ/cm^2)	Exp.
Acoustic reflection coefficient GaAs/ZnSe	r_{ZnSe}	-0.087	Calc.
ZnSe QW thickness	a	8 nm	[9]
Speed of sound in heterostructure	$\bar{v}_{\mathrm{ZnSe}}$	4×10^3 m/s	[10]
Deformation potential in ZnSe	c	-8 eV	Exp.
Resonance energy of QW	E_0	2.809 eV	[9]
Resonance wavelength	λ_0	441.4 nm	[9]
Resonance linewidth (instrumental)	Γ	0.89 meV	Exp.
Resonance lifetime	T_e	4.6 ps	Exp.
Thickness of cap layer	l_r	53 nm	Exp.

Table VI.1: Material parameters, relevant for the performed analysis
Exp.: determined from this experiment. Calc.: Calculated from tabulated values of physical constants.

strain pulse through the crystal slab. The probe beam was focused on the front side of the slab to a spot with diameter < 50 μm, located precisely opposite the pump spot (Fig. VI.1 a)). The angle between the front and rear plane of the sample was measured at $< 0.018°$. Assuming $w_{probe} \sim 30$ μm, the spread in acoustic arrival time is < 1.9 ps. The specularly reflected probe beam was collected and analyzed by a spectrometer and CCD camera with the readout synchronized with the scanning optical delay line in the pump beam. The overall time resolution of the setup was better than 300 fs.

Figure VI.1 b) shows the reflectivity spectrum in the absence of a pump pulse in the energy range of the heavy-hole exciton resonance in the QW, which was

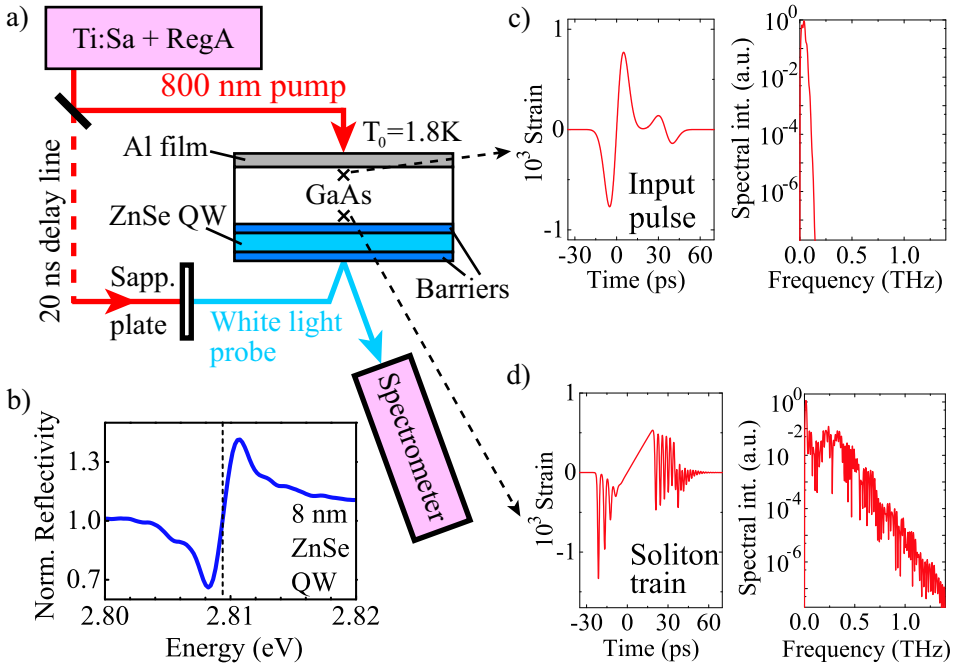

Figure VI.1: Experimental conditions
a) Experimental scheme. b) Measured stationary reflectivity spectrum of the ZnSe QW around the heavy-hole exciton resonance, normalized to the off-resonance background. The vertical dashed line in shows the energy position of the resonance. c) Calculated strain pulse (left) and phonon spectrum (right) as initially generated in the metal film for excitation density $I_0 = 10.2$ mJ/cm^2, and d) its transformation to a soliton train after propagation through 0.114 mm of GaAs. The time in c) is shifted towards that in d) by the sample traversal time t_0.

studied in detail earlier for similar samples [9]. The phase of the reflectivity spectrum is determined by the thickness of the top barrier layer [13]. For our sample, the reflectivity normalized to the off-resonant background can be described by the equation

$$r(E) = 1 + A_0 \frac{E - E_0}{\Gamma^2 + (E - E_0)^2}, \tag{VI.1}$$

with A_0 a constant, E_0 = 2.809 eV (441.4 nm) the static position of the exciton line at this temperature, and $\Gamma \sim 0.9$ meV the phenomenological width of the resonance. This linewidth is determined by the instrumental resolution of the

spectrometer (0.1 nm, corresponding to 0.6 meV) and residual inhomogeneous line broadening, which can then be estimated to be 0.7 meV. These values are in accordance with earlier works [9].

VI.3 Strain propagation

The temporal evolution of the injected strain pulse (Fig. VI.1 c)) was calculated using the known methods of ultrafast acoustics [11, 12] and coincides with results from direct conventional pump-probe measurements [14]. The input pulse is a nearly symmetric bipolar strain wave packet, which can be modeled to a good degree of accuracy by a Gaussian derivative Eq. (III.6) with a width ~ 7 ps, and strain amplitudes reaching 8×10^{-4} in GaAs for the highest pump fluence (we will consider these data in more detail when discussing the simulation results). A typical input strain wave packet is given in Fig. VI.1 c), along with its spectral content.

The temporal and spatial evolution of the strain pulse $s_I(t,x)$ (where x is the distance from the Al film) in the GaAs substrate depend on I_0 and the linear and nonlinear elastic properties of the crystal, and can be calculated numerically by solving the Korteweg-de Vries (KdV) equation [1, 2, 3, 4, 5, 6]. At low pump excitation energy density ($I_0 < 1$ mJ/cm^2), the injected strain pulse propagates linearly through the GaAs slab with the velocity of longitudinal sound ($v_{\mathrm{GaAs}} = 4.8 \times 10^3$ m/s) and reaches the ZnSe/ZnMgSSe heterostructure at a time $t_0 \sim l_0/v_{\mathrm{GaAs}} \sim 24$ ns without any sizable nonlinear or dispersive effects; $s_I(t,x) = s_0(t,x)$.

At excitation densities $I_0 > 1$ mJ/cm^2 on the Al film, however, nonlinear elastic effects start to play a role and the injected strain pulse transforms into a more complicated waveform $s_I(t,x)$. At the medium fluences 1 - 3 mJ/cm^2 the wave develops into a shock wave - an intermediate stage in soliton development. Finally, above 3 mJ/cm^2 dispersive features start to play a role, and the supersonic compressive strain pulse develops into a train of short soliton pulses. Fig. VI.1 d) shows an example trace for $s_I(t,x)$, calculated for our experimental conditions, I_0 = 10 mJ/cm^2 and $x = l_0$. The most apparent characteristics are the development of acoustic frequencies in the THz range, and the formation of solitons at the front of the wave, travelling at a higher velocity than the speed of sound.

In these calculations, it was explicitly assumed that all sources of damping can be neglected at liquid helium temperatures. Defect scattering and anharmonic decay might be limiting factors, but earlier work on longitudinal acoustic phonon

propagation in GaAs [15, 16] suggests that these effects become important at frequencies significantly above 1 THz. Fig. VI.1 d) shows that the spectral intensity at 1 THz is already quite low.

VI.4 Experimental results

The main experimental task of this work was to measure the ultrafast optical response when the soliton train hits the QW. The results for several values of I_0 are shown in Fig. VI.2 as spectral/temporal contour plots. The color and tone in each panel are a measure of the time-dependent reflected spectral intensity normalized to the off-resonant value. The value $t = 0$ corresponds to the arrival time t_0 of the center of the initial bipolar wave packet (Fig. VI.1 c)) at the QW. Animations showing the development of the measured spectrum as a function of time for three fluences can be found at the Physical Review Letters archive [17]. The time intervals $t < -25$ ps and $t > 100$ ps correspond to the situation prior to the arrival of the strain wave packet and after full passage of the heterostructure, respectively. No temporal modulation is observed and the reflectivity spectrum is equal to the one in absence of strain (inset of Fig. VI.2 a), dashed line).

In the time interval $-25 < t < 100$ ps, however, the measurements show strong responses which depend on the pump excitation density I_0. In the linear regime ($I_0 < 1$ mJ/cm^2, Fig. VI.2 a)) and upon arrival of the bipolar acoustic pulse at the QW, the reflectivity spectrum shifts smoothly to higher energies, back to low energies, and recovers to the original position. After reflection of the pulse at the sample surface the same sequence occurs, but in the opposite direction. Qualitatively the optical response tracks the temporal evolution of the exciton resonance in GaAs/AlGaAs QW for strain amplitudes less than 10^{-4} [18]. The important point here is that the shape of the exciton resonance does not change and the exciton resonance energy simply shifts in time (compare solid and dashed lines in the inset of Fig. VI.2 a)). Therefore, the strain-induced shift of the exciton resonance $\Delta E(t)$ can be approximated by $\Delta E(t) = cs^{QW}(t)$, where c is the deformation potential and $s^{QW}(t)$ is the time-dependent strain in the QW, which consists of the sum of the pulse incident from the GaAs slab (taking into account the impedance mismatch, causing an 8.7% amplitude reflection), and a total reflection from the sample/liquid helium interface:

$$s^{QW}(t) = s_0(t) - s_0(t - t_r). \tag{VI.2}$$

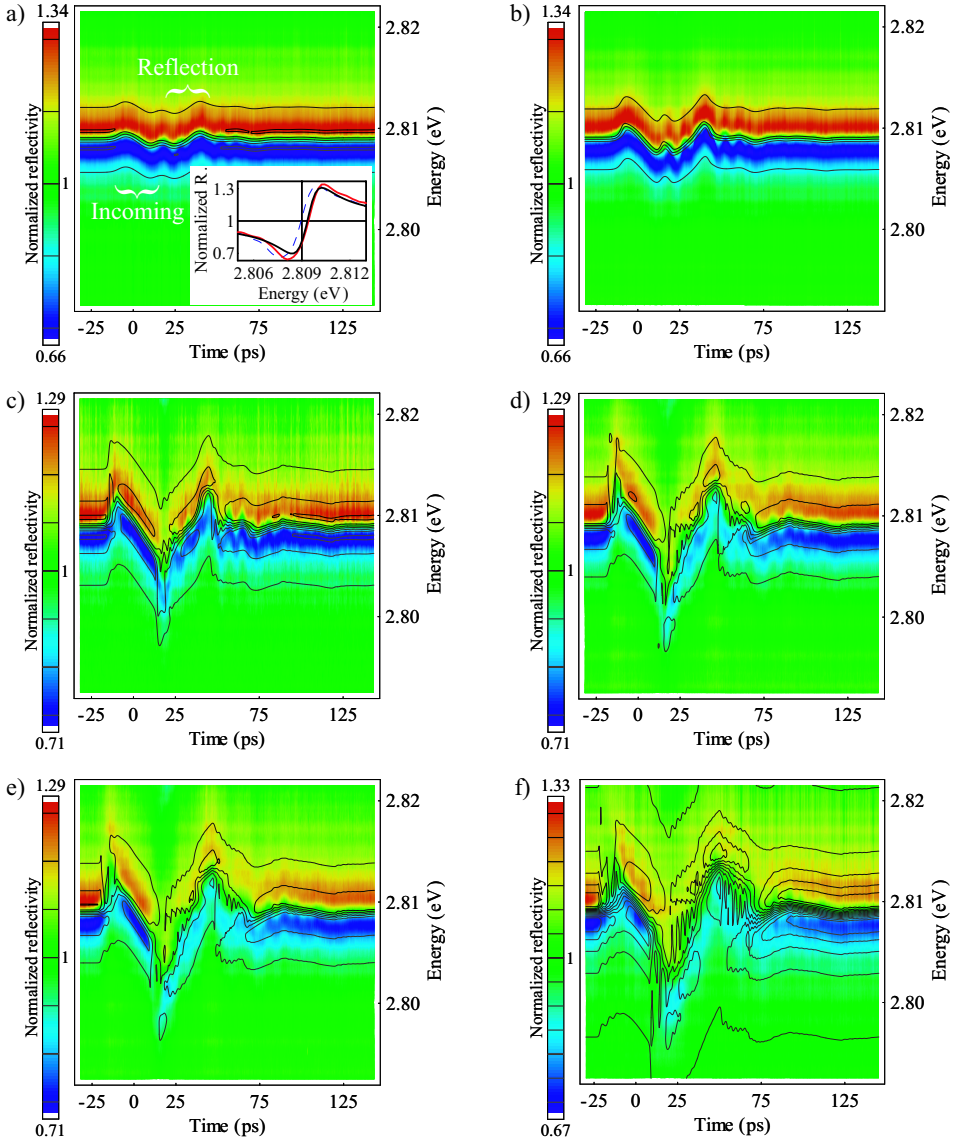

Figure VI.2: Contour plots of time-dependent spectra (Color figure: Fig. 4, p. 205)
Spectral/temporal contour plots of the reflectivity normalized to the off-resonance background, measured for pump fluences of a) 1.0 mJ/cm^2, b) 2.0 mJ/cm^2, c) 5.1 mJ/cm^2, d) 7.1 mJ/cm^2, e) 8.2 mJ/cm^2, f) 10.2 mJ/cm^2. Black lines are calculated contours of equal reflectance changes for corresponding pump fluences. Inset in a) shows the spectral profile of reflectivity: blue (dashed line) is the stationary spectrum, red (light) and black (dark) lines are respectively the measured and calculated spectra at the specified time, for the corresponding fluence.

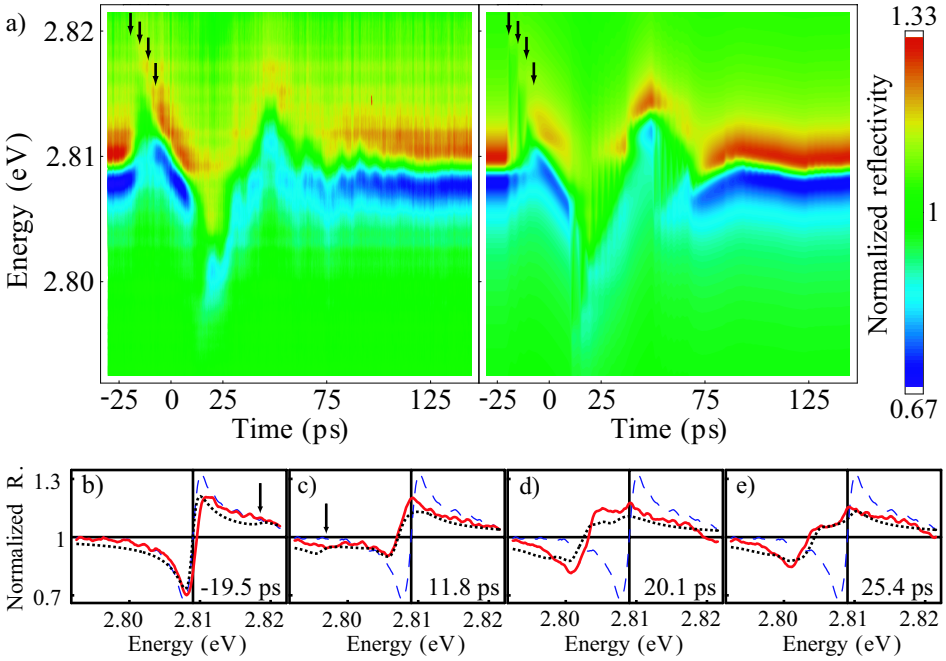

Figure VI.3: Individual spectra for selected fluence (Color figure: Fig. 5, p. 206)
a) Temporal evolution of the reflectivity spectrum measured (left panel) and calculated (right panel) for $I_0 = 9.2$ mJ/cm^2. Arrows indicate the arrival times of acoustic solitons at the QW center. b) - e) Measured (red, solid line) and calculated (black, short dash) reflectivity spectra for $I_0 = 9.2$ mJ/cm^2 at specified times. Arrows in b) and c) indicate the shifted spectral lines due to acoustic solitons. Blue, long dashed lines are unperturbed spectra.

Here, $s_0(t)$ is the strain pulse arriving directly at the QW and $s_0(t - t_r)$ the one arriving after reflection at time $t_r = 2l_r/\bar{v}_{\mathrm{ZnSe}}$ ($l_r = 53$ nm is the distance from the QW to the surface in our sample, and $\bar{v}_{\mathrm{ZnSe}} = 4$ km/s is the mean longitudinal sound velocity in the ZnSe/ZnMgSSe heterostructure [10]). The minus sign between the two strain components in Eq. (VI.2) accounts for the fact that the phase of the strain pulse jumps by π upon reflection at the free surface.

Huge changes in the temporal evolution of the reflectivity spectra are observed for higher fluences I_0 (Fig. VI.2 b) - f)). We have plotted similar data in Fig. VI.3 a), and spectra for specific times in Fig. VI.3 b) - e), for a fluence of 9.2 mJ/cm^2. In Figs. VI.2 and VI.3, some characteristic features can be distinguished:

(i) sharp features in the temporal signal appear;

(ii) the leading edge of the detected signal shifts to earlier times with the increase of I_0 (Fig. VI.2);

(iii) the reflectivity spectrum broadens strongly (Fig. VI.3 b) - e)); and

(iv) doublet structures appear at certain values of time (Fig. VI.3 e)).

Features (i) and (ii) point to ultrafast solitons arriving at the QW. From the simulations we know that the soliton pulses may become of the order of 1 ps (see Fig. VI.1 d)), explaining the sharp features in the temporal evolution of the detected signal at high I_0. Furthermore, the soliton velocity is supersonic, which results in the early arrival of the front of the strain wave packet as observed [1, 4, 6].

VI.5 Numerical calculations

In order to understand the optical response on a quantitative level, the temporal evolution $\Delta E(t)$ of the exciton resonance was calculated upon passage of a soliton train. We use GaAs material parameters (Table VI.1) and numerically calculate the wave shape $s_I^{QW}(t,x)$ arriving at the QW. The strain waveforms arriving at the heterostructure for the fluences shown in Fig. VI.2 are plotted in Fig. VI.4 a).

When calculating the strain profile at the QW, the reflection of 8.7% due to impedance mismatch at the barrier layer/GaAs interface, and the fact that the QW experiences both the strain of the incident pulse and of the pulse reflected at the surface, were included. Due to the small distance between the QW and the surface, the temporal shapes of the incident and reflected strain pulses are taken identical except for the phase jump.

Fig. VI.1 d) shows the presence of THz frequencies in the wave packet, corresponding to wavelengths of 1 ps $\times$ $\bar{v}_{\mathrm{ZnSe}}$ = 4 nm, smaller than the QW width. In the soliton regime the spatial variations therefore become so rapid that we cannot consider the QW as an infinitely narrow object. To analyze this we use the approximation of infinitely high barriers to find the electron wave function $\varphi(x') = \sqrt{2/a}\cos(\pi x'/a)$ ($x' = 0$ at the center of the QW). Effectively, the finite size limits the time resolution to $a/\bar{v}_{\mathrm{ZnSe}} \sim 2$ ps, the travel time through the QW. This decreases the sensitivity of a QW as a detector for very short soliton pulses, where the energy is concentrated mostly in the high-frequency components. In addition, we assume that the strain does not change the potential profile of the

QW significantly. Using perturbation theory, the energy changes of the exciton resonance in the QW in the presence of the strain pulse are found to be equal to

$$\Delta E(t) = c \int_{-a/2}^{a/2} |\varphi(x')|^2 s_I^{QW}(t,x') \mathrm{d}x'. \tag{VI.3}$$

Here we note that Eq. (VI.3) is reminiscent of the equation of matrix elements for the exciton-phonon interaction in a QW [19] that produces a cutoff for high-frequency phonons.

Fig. VI.4 b) shows the arrival times of solitons, for a range of fluences. For low powers, the travel distance l_0 is too short for solitons to be fully formed, see for example 2.0 mJ/cm^2 in Fig. VI.4 a). The resulting shift of the resonance, also taking into account the reflection at the surface, is shown in Fig. VI.4 c) for the highest fluence. Finally, Fig. VI.4 d) shows the resulting contour plot for this fluence. Comparing to the measurement in Fig. VI.2 f), there is a remarkable difference. This is, because one important factor is still missing in the analysis.

The QW interaction is resonant and takes place in a narrow wavelength range, determined by the inhomogeneous linewidth. Therefore, the interaction of the probe light with the exciton system is inherently not instantaneous (as is the case for a metal film, in the previous chapters). Instead, it takes the corresponding exciton coherence time T_e, which in high-quality QWs and at low temperatures is of the order of several picoseconds, close to twice the value of the radiative exciton lifetime [20]. This is an order of magnitude larger than the probe pulse length and the typical soliton widths. Thus a spectral broadening and shift of the exciton resonance are induced by the strain profile arriving at the QW up to a coherence time *after* the incident probe pulse.

To account for this phase memory, the transient reflectivity spectrum $R(E,t)$ is approximated as a convolution:

$$R(E,t) = \frac{1}{T_e} \int_t^\infty r(E - \Delta E(\tau)) \exp\left(-\frac{\tau - t}{T_e}\right) \mathrm{d}\tau, \tag{VI.4}$$

where $r(E)$ and $\Delta E(\tau)$ are given by Eqs. (VI.1) and (VI.3), respectively.

To evaluate $R(E,t)$, we have developed an automated fitting procedure in which the width and height of the input wave and the coherence time T_e are the free parameters. The input wave width of 6.8 ps was determined for the lowest

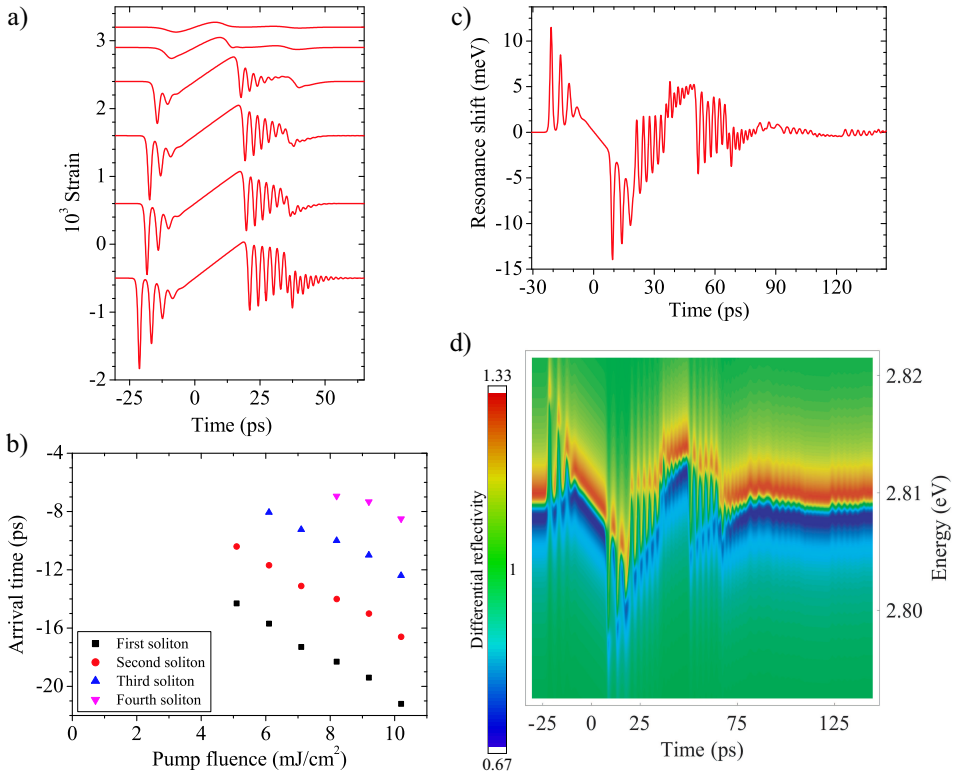

Figure VI.4: Intermediate simulation results (Color figure: Fig. 6, p. 207)
a) Soliton propagation for the fluences depicted in Fig. VI.2. b) Arrival times for solitons, as found in calculations. c) QW resonance energy shift for a pump fluence of $I_0 = 10.2$ mJ/cm^2. d) Calculated contour plots given the resonance shift in c), and exciton lifetime $T_e = 0$.

fluences, and fixed at that value for the higher ones. The best agreement for the values of the shift are obtained for $c = -8$ eV, close to the -6.7 eV reported by Ref. [9]. The results for the amplitude are presented in Fig. VI.5 a). The dependence $s_0 = (7.5 \pm 0.2) \times 10^{-5} I_0$ is in good agreement with the values obtained in the pump-probe measurements mentioned before. Further, for the exponential decay time, we find $T_e = 4.6 \pm 1.3$ ps (Fig. VI.5 b)). This value is close to the measured dephasing time of excitons in similar QWs [21]. The value for T_e found from the fit slightly increases with increasing power, to 7 ps at the highest fluence.

At this point it is useful to briefly discuss other possible broadening effects

that could affect this result. The typical roughness of our Al pump film of 100 nm thick, is ~ 2 nm (estimated from AFM results in Ch. IV). This would lead to an arrival time variation of ~ 300 fs, much smaller than the calculated dephasing time, and independent of power. For the 250-kHz laser system, the pulse stability is better than for the 1-kHz system of Chs. IV and V, and intensity fluctuations can be assumed to have a minor effect. A more important effect is the arrival time difference over the finite probe spot size. Considering the solitons, we know that their velocity depends on their amplitude as $\frac{a_{sol}\alpha}{6\rho v_{\mathrm{GaAs}}}$ with a_{sol} the soliton amplitude [22]. Taking the probe spot size to be 30 μm and the pump spot 100 μm, the spread in amplitude for the first soliton over the probe spot size is roughly 15%, corresponding to a spread in arrival time $(0.15 t_0 v_{sol})/v_{\mathrm{GaAs}} \sim 1.4$ ps for a soliton with an amplitude $\sim 10^{-3}$. Thus, although this effect is considerable, and likely contributing to temporal broadening effects at the highest fluences, it is still much smaller than the coherence time. We checked with simulations that the quality of the fits reduced by a large amount when assuming only Gaussian temporal broadening, signifying the (temporal) coherence present in the measured signals.

VI.6 Discussion

The results of the numerical calculations for the six values of I_0 are shown in Fig. VI.2 a) - f) as solid contour lines of equal reflectivity. The agreement between the experiment and theoretical simulations at low power is excellent. At first sight, the correspondence at high powers seems to be less. We note however, that the large part of this mismatch already depends on the discrepancy between the measured spectrum and the description in Eq. (VI.1), that is apparent mainly at the edges of the spectrum, where the deviations are largest. The sharpening of the leading edges at elevated I_0 signifies the formation of ultrashort strain pulses, i.e. solitons. The arrival time of the solitons decreases with the increase of I_0, as correctly described by the simulations.

The simulations and experiments at the highest energy density show individual soliton pulses, which however seem to be largely washed out. The passage of incident and reflected solitons leads to a strong broadening of the reflectivity spectrum over a broad range of times, reflected as an increase in green areas in Fig. VI.2 c) - f). The reasons for this are that in the present case the duration of individual soliton pulses as well as the delay between different soliton pulses are shorter than T_e. Thus when the soliton train arrives, the exciton resonance is

chirped several times back and forth for each soliton during its coherence time T_e.

The individual spectra, as shown in Fig. VI.3 b) - e), show better agreement than the contour plots suggest. Fig. VI.3 b) shows the spectrum at the passage of the first soliton. The change is mainly unipolar, indicating that we are dealing here with a purely compressive strain. For the first soliton, the shifted exciton line is positioned at the dip indicated by the arrow in Fig. VI.3 b). Since the temporal width of the soliton is an order of magnitude smaller than the coherence time, the full effect is of the order of the CCD noise level and background intensity variations, and it is not possible to discern it in the measurement. In Fig. VI.3 c), the dip caused by the reflection of the second soliton (also indicated by an arrow) is more clearly visible in the measured spectrum, since the shift is smaller and the soliton broader in time.

An even more elucidating example of ultrafast acoustic chirping is presented in Fig. VI.3 e), which shows a clear doublet structure that can be observed around times 25 ps and 52 ps (reflection). We can explain this by the tensile part of the incident wave, shown in Figs. VI.1 d) and VI.4 a). Here, a dispersive tail of high frequency and high amplitude develops. Since the typical phonon oscillation period seen at the highest fluences is 2 ps, the exciton resonance is swept over almost 7 meV in energy a couple of times within its lifetime $T_e \sim 5$ ps. The origin of the doublet can be understood qualitatively by making the analogy with a pendulum, which spends most of the time in its extreme positions.

At high fluences (Figs. VI.2 f), VI.4 c)) both experiment and theory show that the shift reaches almost 10 meV, or 20 times its linewidth, and that this effect is induced at the position where the reflected, initially compressive solitons and the tensile part of the original wave meet in the QW and interfere constructively. We have plotted this event for $I_0 = 9.2$ mJ/cm^2 in Fig. VI.3 d). This interference is absent at low powers and is additional evidence of nonlinear propagation, causing the wave to stretch from its initial width ~ 7 ps to over $2\,t_r \sim 27$ ps at the QW. All experimental results presented in Fig. VI.2 also show minor amplitude oscillations with a period ~ 10 ps after passage of the incident pulse which are not present in the simulated curves, and are not understood yet.

VI.7 Conclusions and perspectives

In this chapter, we have experimentally demonstrated the response of the electronic states of a quantum well nanostructure as it is hit by a train of high-amplitude,

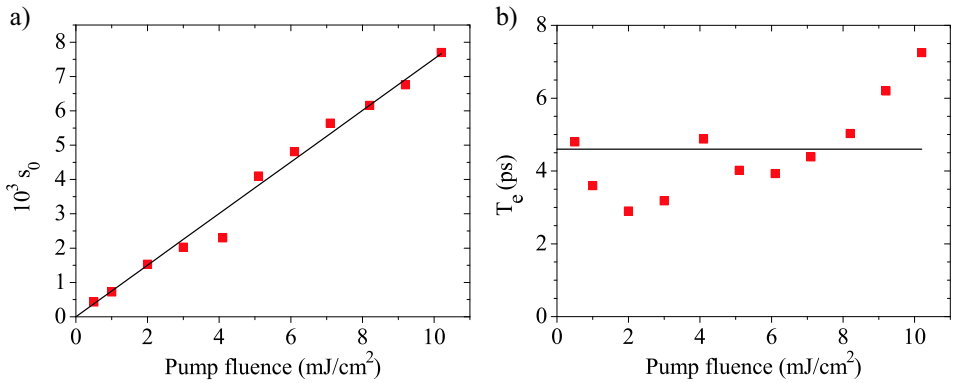

Figure VI.5: Results for free fit parameters
a) Initial strain amplitude s_0 obtained from fit routine versus pump fluence. Solid line is a linear fit to the strain amplitude. b) Calculated exponential decay time of the exciton state T_e versus pump fluence. Solid line indicates average value.

ultrashort solitons. Besides large shifts in energy, significant shape changes of the reflection spectrum are observed, which can be explained by acoustic modulations at timescales shorter than the exciton lifetime. All experimental results are accurately described by calculations of the optical response, taking into account the nonlinear strain propagation in the GaAs substrate, as well as the ultrafast shifts of the exciton resonance this strain induces in a finite-size quantum well.

The presented work uses the QW as the archetypal object of semiconductor nanostructures. The observed constructive interference between incident and reflected strain pulses is analogous to coherent strain control [23] and realizes manipulation of nanostructures by acoustic soliton pulses. The soliton-induced effects in more sophisticated nanostructures (e.g. tunneling devices, shallow QWs, quantum wires, dots and molecules), where the adiabatic approximation for electron and lattice systems is not valid anymore may lead to the discovery of new and ultrafast phenomena at constant carrier densities. The experiments and theoretical analysis show that the effect of acoustic solitons on the electronic state may be used as an ultrafast method for modulating the optical response in nanostructures. The large value of the energy resonance shift may become a basis for picosecond control of emission from nanophotonic devices (semiconductor microcavities, 2D arrays, etc.) and other switching principles in nanoelectronic and -photonic devices.

References

1. H.-Y. Hao and H.J. Maris. Experiments with acoustic solitons in crystalline solids. *Phys. Rev. B*, 64:064302, 2001.
2. O.L. Muskens and J.I. Dijkhuis. High amplitude, ultrashort, longitudinal strain solitons in sapphire. *Phys. Rev. Lett.*, 89(28):285504, 2002.
3. O.L. Muskens, A.V. Akimov, and J.I. Dijkhuis. Coherent interactions of terahertz strain solitons and electronic two-level systems in photoexcited ruby. *Phys. Rev. Lett.*, 92(3):335503, 2004.
4. B.C. Daly, T.B. Norris, J. Chen, and J.B. Khurgin. Picosecond acoustic phonon pulse propagation in silicon. *Phys. Rev. B*, 70(21):214307, 2004.
5. O.L. Muskens and J.I. Dijkhuis. Interactions of ultrashort strain solitons and terahertz electronic two-level systems in photoexcited ruby. *Phys. Rev. B*, 71(10):104304, 2005.
6. E. Péronne and B. Perrin. Generation and detection of acoustic solitons in crystalline slabs by laser ultrasonics. *Ultrasonics*, 44(Suppl. 1):e1203, 2006.
7. Landolt-Bornstein. In K.H. Hellwege and A.M. Hellwege, editors, *New Series: Group III/11*. Springer, 1979.
8. H.-Y. Hao and H.J. Maris. Dispersion of the long-wavelength phonons in Ge, Si, GaAs, quartz and sapphire. *Phys. Rev. B*, 63:224301, 2001.
9. G.V. Astakhov, D.R. Yakovlev, V.P. Kochereshko, W. Ossau, W. Faschinger, J. Puls, F. Henneberger, S.A. Crooker, Q. McCulloch, D. Wolverson, N.A. Gippius, and A. Waag. Binding energy of charged excitons in ZnSe-based quantum wells. *Phys. Rev. B*, 65(16):165335, 2002.
10. B.H. Lee. Elastic constants of ZnTe and ZnSe between 77 K - 300 K. *J. Appl. Phys.*, 41(7):2984, 1970.
11. G. Tas and H.J. Maris. Electron diffusion in metals studied by picosecond ultrasonics. *Phys. Rev. B*, 49:15046, 1994.
12. T. Saito, O. Matsuda, and O.B. Wright. Picosecond acoustic phonon pulse generation in nickel and chromium. *Phys. Rev. B*, 67:205421, 2003.
13. E.L. Ivchenko, P.S. Kopev, V.P. Kochereshko, I.N. Uraltsev, D.R. Yakovlev, S.V. Ivanov, B.Ya. Meltser, and M.A. Kalitievskii. Reflection in the exciton region of the spectrum of a structure with a single quantum well. Oblique and normal incidence of light. *Sov. Phys. Semicond.*, 22:495, 1988.
14. P.J.S. van Capel and J.I. Dijkhuis. Optical generation and detection of shock waves in sapphire at room temperature. *Appl. Phys. Lett.*, 88(15):151910, 2006.
15. A.J. Kent, N.M. Stanton, L.J. Challis, and M. Henini. Generation and propagation of monochromatic acoustic phonons in gallium arsenide. *Appl. Phys. Lett.*, 81(18):3497, 2002.
16. A.J. Kent. Phonon interactions in semiconductor nanostructures. *Phys. Stat. Sol. (b)*, 241(15):3439, 2004.

17. *http://www.aip.org/pubservs/epaps.html*, EPAPS Document No. E-PRLTAO-99-013732.
18. A.V. Akimov, A.V. Scherbakov, D.R. Yakovlev, C.T. Foxon, and M. Bayer. Ultrafast band-gap shift induced by a strain pulse in semiconductor heterostructures. *Phys. Rev. Lett.*, 97(3):037401, 2006.
19. A.V. Akimov. Exciton-phonon interaction in quantum wells. In L.J. Challis, editor, *Electron-phonon interactions in low-dimensional structures*, page 239. Oxford University Press, 2003.
20. E.J. Mayer, N.T. Pelekanos, J. Kuhl, N. Magnea, and H. Mariette. Homogeneous linewidths of excitons in CdTe/(Cd,Zn)Te single quantum wells. *Phys. Rev. B*, 51(23):17263, 1995.
21. H.P. Wagner, A. Schätz, R. Maier, W. Langbein, and J.M. Hvam. Coherent optical nonlinearities and phase relaxation of quasi-three-dimensional and quasi-two-dimensional excitons in ZnS_xSe_{1-x}/ZnSe structures. *Phys. Rev. B*, 56(19):12581, 1997.
22. O.L. Muskens and J.I. Dijkhuis. Inelastic light scattering by trains of ultrashort acoustic solitons in sapphire. *Phys. Rev. B*, 70(10):104301, 2004.
23. Ü. Özgür, Ch-W. Lee, and H.O. Everitt. Control of coherent acoustic phonons in semiconductor quantum wells. *Phys. Rev. Lett.*, 86(24):5604, 2001.

Chapter VII

Generation and detection of high-amplitude strain in InGaN/GaN quantum wells in the saturation regime

Abstract

We detect strains generated by piezoelectric screening processes in ten-period InGaN/GaN multiple quantum well samples with well thicknesses of 1.8, 2.7 and 3.6 nm, using ultrafast pump-probe techniques. At short times, coherent strain oscillations of the multiple quantum well structures are observed, reaching a frequency up to ~ 1 THz for the thinnest quantum wells. The measured vibrational eigenmodes of the multiple quantum wells agree within 10% with the dispersion relation calculations based on the sample parameters. The propagating wave in the GaN buffer layer and sapphire substrate is monitored by time-resolved Brillouin scattering at ~ 100 GHz. The Brillouin oscillation amplitudes saturate when the internal piezoelectric field is fully screened, and scale with the thickness of the quantum wells, as expected. Saturation sets in < 1 mJ/cm^2, i.e. below saturation of the absorption at ~ 2 mJ/cm^2. All these observations are in good agreement with THz electromagnetic emission experiments performed earlier on the same samples.

VII.1 Introduction

The capability of growing high-quality thin layers of semiconductor materials allows the fabrication of a wide variety of single and multiple quantum well and superlattice structures, with tailored bandgap properties. The carrier dynamics in these structures makes them excellent devices for lasing [1]. $In_{1-x}Ga_xN$/GaN quantum well systems have a large bandgap, which makes them suitable for lasing in the blue and green [2]. Inherent to piezoelectric structures such as InGaN/GaN

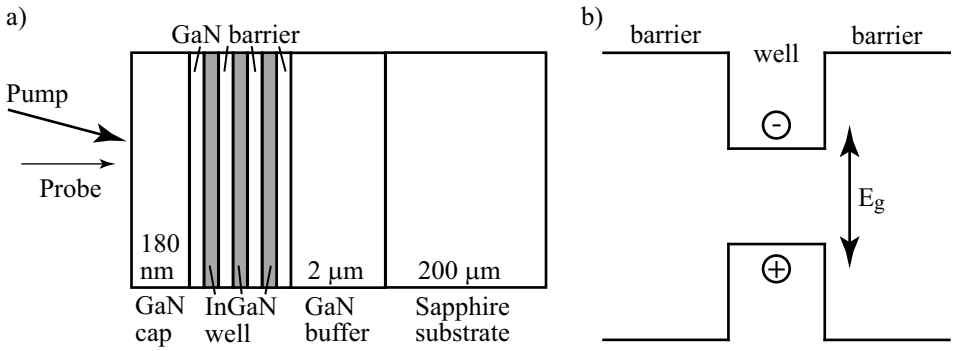

Figure VII.1: Quantum well samples
a) Schematic picture of the multiple quantum well (MQW) samples, consisting of ten periods of GaN/InGaN material. b) Bandstructure of a quantum well, forming a potential well. The electron and hole wavefunctions peak at the same position in space. E_g denotes the energy difference between the lowest electron state and the highest hole state.

quantum wells is the built-in strain due to lattice mismatch, causing an internal piezoelectric field. Optical excitation of such structures leads to THz electromagnetic emission [3, 4] and the generation of high-amplitude acoustic waves [5, 6, 7, 8].

This chapter presents ultrafast pump-probe reflectometry measurements on InGaN/GaN multiple quantum wells (MQWs). The aim of these experiments is to study the acoustic generation by three specific MQW structures with different well thicknesses, and compare it to electromagnetic THz generation studies on the same samples [9]. After discussing the sample properties, the physics of piezoelectric MQWs is reviewed, with emphasis on the generation and detection mechanisms of acoustic strain. Subsequently, the results of pump-probe reflection and transmission measurements are presented. In the analysis of the data, both localized modes in the MQW, and propagating modes in the substrate are considered.

VII.2 Properties of InGaN/GaN quantum wells

VII.2.1 Samples

Fig. VII.1 a) is a schematic picture of the multiple quantum well samples used. Quantum wells consist of typically a few nanometer thick layers of different semi-

conductor mixtures. The well is sandwiched between two layers of semiconductor material with a larger electronic bandgap. This leads to a square well potential, as shown in Fig. VII.1 b). For our samples, GaN (with a bandgap of 3.44 eV at room temperature) acts as barrier and $In_{0.2}Ga_{0.8}N$ (bandgap around 2.55 eV) as well [10].

The quantum well structures are grown on a (0001)-oriented sapphire substrate by low-pressure metalorganic vapor-phase epitaxy. A 2-μm GaN layer between the quantum wells and the sapphire layer buffers the lattice mismatch with sapphire. On top of the quantum wells a 180-nm GaN cap layer is deposited. The MQW structure consists of ten layers of InGaN and GaN, creating a superlattice. We performed experiments on samples with well thicknesses of 1.8, 2.7 and 3.6 nm, all with 7.2-nm thick barrier layers.

VII.2.2 Quantum-confined Stark effect

InN has larger lattice constants than GaN. The fraction of In in the QW therefore increases the lattice unit cell, leading to permanent strain in the structure. Due to the large piezoelectric constant of 0.375 C/m^2 [11], this built-in strain results in piezoelectric fields of 3.1 MV/cm in the well and 0.5 MV/cm in the barriers [9]. These fields are oriented in opposite directions, see Fig. VII.2 a).

The piezoelectric field across the quantum well tilts the band structure. This leads to a modulation of the optical and electronic properties due to the spatial separation of the conduction and valence band wavefunctions (Fig. VII.2 a)), the so-called quantum-confined Stark effect (QCSE) [12]. The transition dipole moment between the valence and conduction band depends on the overlap of these wavefunctions. As a result, the absorption coefficient and recombination rate decrease as a function of electric field strength. The exciton resonance is also red shifted, because the band states penetrate the gap for strong electric fields.

VII.3 Generation and detection of strain in GaN/InGaN quantum wells

VII.3.1 Dynamic screening of the built-in piezoelectric field

When an electron in the quantum well is excited to the conduction band, charge separation takes place due to the piezoelectric field, see Fig. VII.2 a). This charge

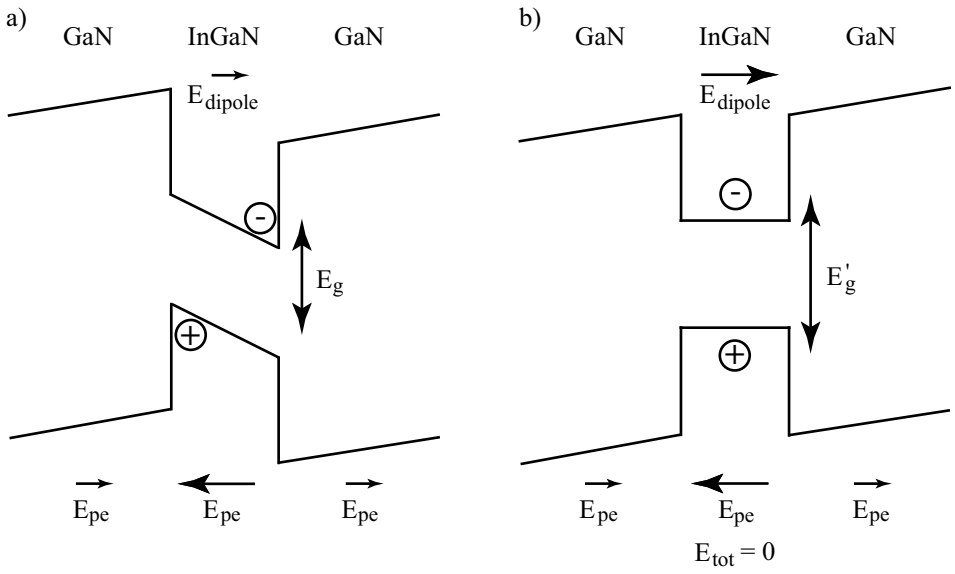

Figure VII.2: Piezoelectric effects in QW samples
a) Schematic picture of a quantum well sample with built-in piezoelectric fields E_{pe}. The electric field tilts the energy levels in the well and shifts the electron and hole wavefunctions in opposite direction. This effectively leads to a decreased gap E_g and a red shift of the luminescence spectra. Upon excitation of carriers, electrons and holes create a dipole field E_{dipole}, which partly screens the piezoelectric field. b) Upon strong excitation, the densities of electrons and holes become large enough to completely screen the piezoelectric field. The wavefunctions of the electron and hole will overlap in space. The resulting optical gap $E_g' > E_g$.

separation creates an opposite electric dipole field and screens the built-in piezoelectric field. If sufficient electrons are excited (Fig. VII.2 b)), the piezoelectric field becomes completely screened, resulting in a flat-band potential inside the well.

Since excitation in our experiments is performed with an intense ultrashort pulse, screening of the piezoelectric field occurs within 100 fs [4]. This ultrafast screening has several consequences. First, the absorption coefficient and recombination rate in the quantum wells increase, because of the increased overlap between the electron and hole wavefunctions [4]. Second, the luminescence from this recombination is blue-shifted, as illustrated in Fig. VII.2 b) [3]. Finally, the ultrafast screening removes the internal field and thus induces a release of elec-

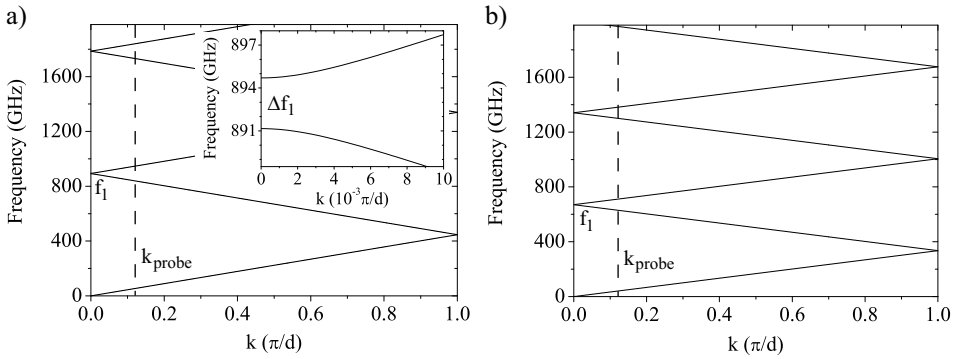

Figure VII.3: Phonon dispersion in MQW systems
a) Dispersion of phonons in the InGaN/GaN MQW with well thickness of 1.8 nm. Inset shows the first bandgap Δf_1 at $k = 0$. b) Like a), but now calculated for the 3.6-nm MQW. Vertical dashed lines indicate the k-vector of 400-nm probe light. f_1 is the lowest frequency for which the dispersion relation crosses $k = 0$.

tromagnetic [9] and acoustic [5] energy on a subpicosecond timescale. In a single quantum well the coherent strain pulse will be emitted directly into the surrounding material [13], while in multiple quantum wells the strain is released via the vibrations of the superlattice [5, 14]. The emitted strain escapes the MQW in two directions, as shown in Fig. VII.4 a). Since acoustic generation occurs due to rapid charge separation, a broad range of wavevectors can be generated. The typical amplitude of the emitted strain reaches values of 0.1% [8].

VII.3.2 Dispersion relation of a superlattice

The acoustic dispersion for low frequencies in bulk GaN is given by the simple relation $\omega = v_s k$, where v_s is the sound velocity in GaN and k is the phonon wavevector. For multiple quantum wells or superlattices, the periodic structure imposes a condition on the dispersion [15]:

$$\omega^2 = {v_s}^2 (k+S)^2, \tag{VII.1}$$

with $S = 2\pi m/d$ the reciprocal superlattice vector, $m = 0, \pm 1, \pm 2, ...$, and d the total thickness of the superlattice structure. The periodicity creates zone-folding of the dispersion relation within the first Brillouin zone (Fig. VII.3), and allows several acoustic modes at each k-vector. Phonon modes with low k (i.e. near the

wavevector of light) are now also present in the THz frequency range. Points at the edges of the first Brillouin zone, $k = 0$ and $k = \pi/d$, correspond to standing waves in the superlattice [16]. At the zone boundaries, small gaps are present in the dispersion relation (Fig. VII.4 a), inset).

To calculate the dispersion of phonons in our InGaN/GaN quantum wells an elastic continuum model can be used, extended with a periodic perturbation [17]. The resulting dispersion relation reads

$$\omega^2 = \frac{{v_s}^2}{2}[k^2 + (k-S)^2] \pm [\frac{{v_s}^4}{4}[k^2 - (k-S)^2]^2 + |V_s|^2 k^2 (k-S)^2]^{1/2}, \quad \text{(VII.2)}$$

with the perturbation V_s given by

$$|V_s| = |\frac{{v_s}^2(\rho_w - \rho_b)}{\rho_0 \pi m} \sin[\frac{m\pi d_1}{d}]|. \quad \text{(VII.3)}$$

Here, d_1 is the thickness of a single QW, ρ_w and ρ_b are the respective mass densities in the quantum well and barrier layer, and ρ_0 and v_s the average superlattice mass density and sound velocity, respectively. The position of the first (nonzero) frequency at $k = 0$ ($m = 2$) is given by

$$f_1 = \frac{m\pi}{\frac{d_w}{v_w} + \frac{d_b}{v_b}}, \quad \text{(VII.4)}$$

with v_w and v_b the sound velocities in well and barrier, respectively.

The calculated dispersion is shown in Fig. VII.3 a) and b) for the 1.8-nm and 3.6-nm thick quantum well, respectively. The bandgap Δf_1 at f_1 is ~ 3 GHz for our quantum well samples (inset Fig. VII.3 a)), too small to detect in ultrafast experiments. For larger QW thickness d_w and constant barrier thickness d_b, the frequency f_1 decreases (compare f_1 positions in Fig. VII.3 a) and b)).

For a finite number of quantum wells, the dispersion is not continuous, but will have discrete vibrational modes at $k = n/N(\pi/d)$, with N the number of QWs ($N = 10$ for our samples), and n ranging from 1 to N. The finite size of the superlattice causes a smearing of these discrete k-modes.

With ultrafast pump-probe spectroscopy it is possible to detect the coherent superlattice vibrations. These vibrations modulate the strain-induced piezoelectric field, and hence the absorption resonance position, through the quantum-confined Franz-Keldysh (QCFK) effect [12].

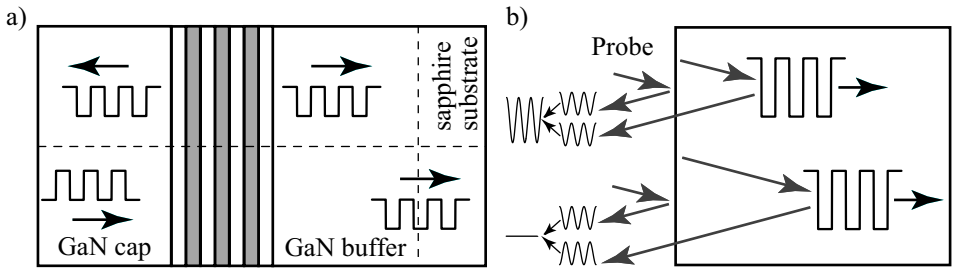

Figure VII.4: Strain propagation, and detection through Brillouin scattering
a) Upon optical excitation, strain is emitted in two directions (upper panel). One contribution travels through the cap layer and reflects at the free surface. The reflected wave travels again through the quantum well structure into the GaN buffer, and finally propagates into the sapphire substrate (lower panel). The other contribution will travel directly in the sapphire direction. b) Principle of Brillouin scattering. The probe beam scatters at a travelling acoustic wave, which interferes with the reflection at the surface. Since the distance between the acoustic wave and the surface changes as a function of propagation time, this interference is observed as an oscillation in the reflected signal.

VII.3.3 Time-resolved Brillouin oscillations

The coherent oscillations of the finite MQW structure are transferred to the surrounding GaN layers. A specific propagating phonon frequency can be observed by time-resolved Brillouin scattering [18]. The principle of Brillouin scattering is depicted in Fig. VII.4 b). An acoustic wave locally changes the refractive index of the material, leading to probe light reflection. This reflected beam will interfere with reflections off the surface, the quantum well structure, and the GaN/sapphire interface. Whether this interference is constructive or destructive depends on the position of the acoustic wave in the sample, and the wavelength of the probe light in the material. Since the acoustic wave moves, it can be observed as an oscillation in the reflection signal. Because this is an interference effect, an increase in reflection is accompanied by a decrease in transmission, *vice versa*. An alternative way to explain this effect, is to say that the oscillatory sensitivity function mentioned in Ch. III is not damped due to the penetration depth in a transparent material ($\kappa = 0$). As a result, the integral Eq. (III.1) therefore shows oscillatory behavior, ultimately limited by the coherence length of the reflecting pulses. Note that in the present case of a buried strain generator, two separate acoustic wavefronts are formed (sketched in Fig. VII.4 a)), leading to multiple interferences.

Although the acoustic pulse contains a broad range of frequencies, only one

QW thickness	R	T	α
1.8 nm	0.29	0.55	0.16
2.7 nm	0.11	0.53	0.36
3.6 nm	0.15	0.44	0.41

Table VII.1: Reflection, transmission, and absorption for the used QW samples
Values were determined for 400 nm, and at low fluence.

frequency, the Brillouin frequency, is Bragg-scattered and detected [18]. This frequency f_0 is given for the case of perpendicular probing by

$$f_0 = \frac{2nv_s}{\lambda}, \tag{VII.5}$$

where n is the refractive index of the material, v_s the sound velocity, and λ the probe wavelength. From Eq. (VII.5), Brillouin frequencies of 107 GHz in GaN and 100 GHz in sapphire are calculated for a probe wavelength of 400 nm.

The amplitude of the Brillouin oscillation is determined by the intensity of the relevant phonon frequency in the wave packet, and the elasto-optic coupling parameter of the material. Since the spectrum of the generated pulse does not depend strongly on pump fluence, we assume that the oscillation amplitude is proportional to the generated strain.

Since interference between the reflection at the acoustic wave and static interface reflections is to take place, spatiotemporal overlap of these probe reflections is required. For long propagation times, this overlap decreases. The coherence time t_{coh} (the time in which the overlap decreases with a factor of $1/e$) is given by $t_{coh} = (c\tau)/(2\sqrt{\ln 2}nv_s)$, with τ the pulse FWHM in time. Assuming that the FWHM of the 400-nm probe pulse is comparable to that of the original 800-nm pulse (App. B), we estimate $t_{coh} \sim 1.5$ ns. Decrease of pulse overlap can therefore be neglected on timescales < 200 ps.

VII.4 Experiment

VII.4.1 Setup

For the pump-probe experiments on the GaN/InGaN quantum wells, we use the reflection-transmission setup described in Ch. II. BBO crystals were inserted in

the pump and probe beam for pumping and probing at 400 nm, i.e. above the optical gap of the MQWs both in the screened and the unscreened case. Pump and probe polarizations are set orthogonally, and polarization filters are used to prevent pump light from entering the detectors. The probe fluence was kept below 0.1 mJ/cm^2 and the pump was varied from 0.1 to 20 mJ/cm^2. In these experiments both the relative changes in reflection $\Delta R/R$ and transmission $\Delta T/T$ were measured, as well as the absolute reflection coefficient R and transmission coefficient T collected in Table VII.1. The absolute values allow for a calculation of the relative changes in absorption $\Delta\alpha/\alpha$ ($\alpha = 1-R-T$):

$$\frac{\Delta\alpha}{\alpha} = -\left(\frac{\Delta R}{R}\times R + \frac{\Delta T}{T}\times T\right)\frac{1}{\alpha}. \tag{VII.6}$$

We note that the reflection also contains some higher-order reflection contributions (at the GaN/sapphire interface and at the sapphire surface), which are further neglected.

VII.4.2 Ultrafast absorption modulation

The measured transmission $\Delta T/T$ and reflection $\Delta R/R$ for the quantum well with a thickness of 3.6 nm for different pump fluences are shown in Fig. VII.5 a) and b), respectively. The background caused by a small fraction of pump light entering the detectors is subtracted from the data and $t = 0$ is set at the position of maximum signal. The inset of Fig. VII.5 b) is a detailed plot of the reflection signal where Brillouin oscillations are clearly visible. The calculated absorption $\Delta\alpha/\alpha$ for this quantum well is shown in Fig. VII.5 c).

The fact that $\Delta T/T$ and $\Delta R/R$ increase and the absorption $\Delta\alpha/\alpha$ decreases, is counterintuitive. One would expect as screening takes place that the absorption increases and thus the reflection and transmission decrease, due to a better overlap between the valence and conduction band states. However, since pumping and probing occurs well above the QW bandgap, saturation is not due to piezoelectric screening but to bleaching of the quantum wells by the pump. In case of high pump fluences, a substantial amount of carriers is generated by the pump and absorption starts to saturate due to depletion of the valence band. As a result, less carriers are excited by the probe than in the case of low pump fluence, and probe absorption decreases. Measurable saturation of the absorption sets in at pump fluences around 2 mJ/cm^2 (Fig. VII.9 b)).

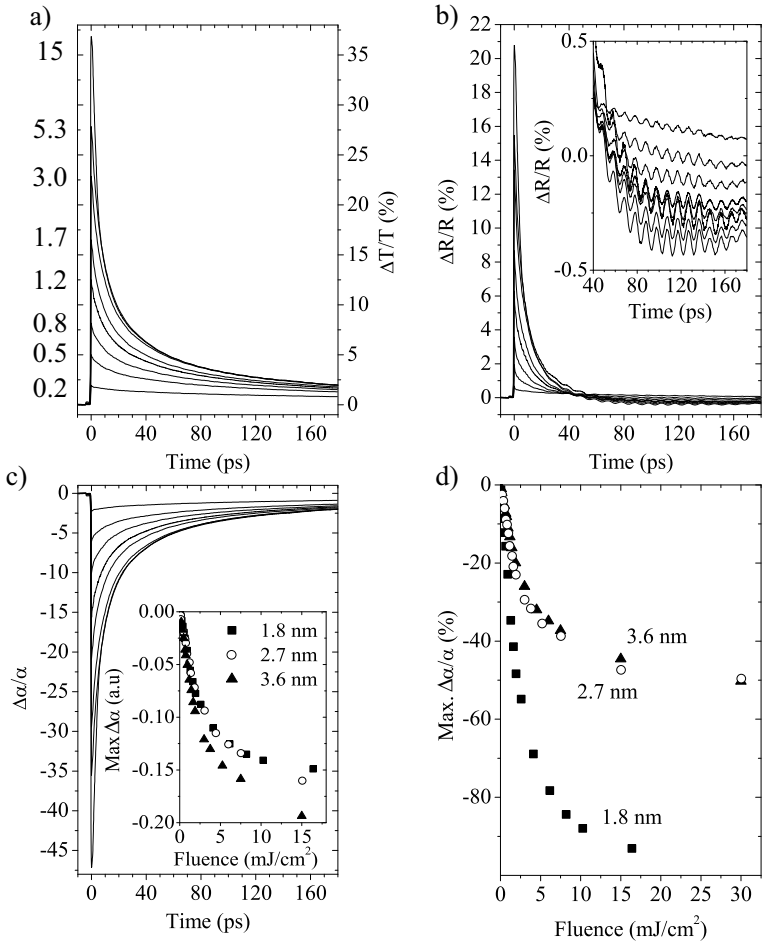

Figure VII.5: Pump-probe response for 3.6-nm MQW
a) Time-dependent transmission changes of the 3.6-nm thick multiple quantum well for different pump fluences (indicated in mJ/cm^2 at the left axis). b) Time-dependent reflection changes of the 3.6-nm thick multiple quantum well for the same pump fluences as a). Inset is a detailed plot, showing clear Brillouin oscillations. c) Time-dependent relative absorption changes for the 3.6-nm thick multiple quantum well for the pump fluences in a). Inset shows the maximum absolute change in absorption $\Delta\alpha$ as a function of pump fluence, for all three MQWs. d) Amplitude of the relative change in absorption at $t = 0$ as a function of pump fluence. The thinnest quantum well, which has the lowest absorption coefficient, has the strongest relative absorption change.

After pump excitation at $t = 0$ the signal decays exponentially with a decay time of ~ 30 ps, by exciton recombination. This implies that screening has vanished and the internal strain is restored. The traces for the 1.8-nm and 2.7-nm MQW samples are similar to that of the 3.6-nm MQW shown in Fig. VII.5 a) - c).

To compare the absorption of the three multiple quantum wells, the amplitude of the peaks in reflection and transmission at $t = 0$ was determined as a function of pump fluence for the three different multiple quantum wells. The absorption $\Delta\alpha$ is presented in the inset of Fig. VII.5 c), and the normalized absorption $\Delta\alpha/\alpha$ in Fig. VII.5 d). For all three samples, the absorbed energies ($\propto \Delta\alpha$) and thus the numbers of carriers generated at a given fluence are about equal. This allows us to compare the acoustic generation results for the different samples presented in the following sections.

VII.4.3 Zone-folded acoustic phonons

During the first 30 ps, fast coherent vibrations of the superlattice are observed, see Fig. VII.8 b). We take a moving average of the original trace over a time interval $\sim 1/f_1$ with f_1 as specified in Eq. (VII.4), and subtract it from the original data to remove the slowly decaying background [19]. The results for the differential reflection and transmission for the 1.8-nm MQW and a pump fluence of 25.6 mJ/cm^2 are shown in Fig. VII.6. This figure shows a fast oscillation of about 1.2 ps period exhibiting a beating pattern. A decay time of ~ 30 ps is observed for these high-frequency components, demonstrating that these acoustic frequencies are not captured in the MQW efficiently, as compared to what one finds for larger numbers of MQW periods [6]. However, this time appears to exceed the travel time of sound through the MQW of ~ 13 ps by some amount.

The absorption modulation through the QCFK effect caused by the vibrating superlattice is shown in Fig. VII.6 b). To analyze the measured fast oscillation, the spectrum of the signal in Fig. VII.6 b) is calculated by Fourier analysis. The result is shown in Fig. VII.7 a), left panel. Several peaks can be observed. These correspond to the allowed discrete vibrational modes $0.1n\pi/d$ ($n = 0, 1, 2, \ldots$) of the MQW, with the frequency of the highest ($m = 2, n = 2$) mode around 1000 GHz. The calculated values are indicated by squares in Fig. VII.7 a), right panel, which shows the phonon dispersion relation of the 1.8-nm thick quantum well as derived from Eqs. (VII.2) - (VII.3). The acoustic Q-factor of the superlattice is very low, resulting in broad spectral modes. The $k = 0$ mode (at 890 GHz) has the highest peak, due to the fact that $\Delta\alpha$ is strongest in transmission.

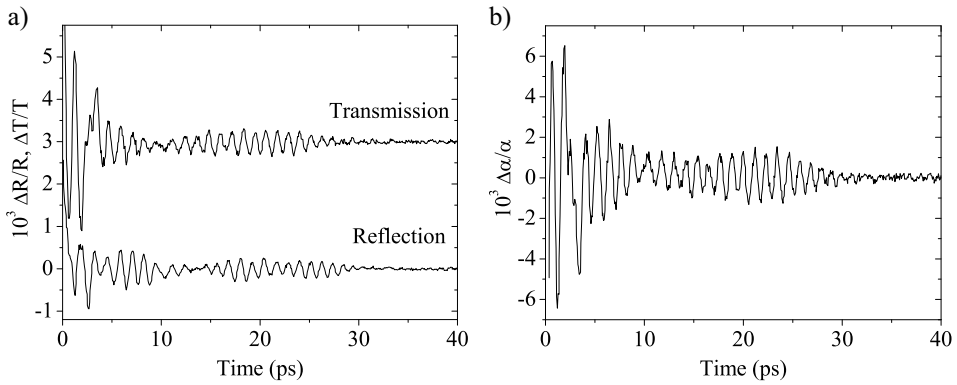

Figure VII.6: Coherent superlattice vibrations
a) Background-subtracted reflection and transmission for short times for the 1.8-nm MQW and a pump fluence of 25 mJ/cm^2. b) Absorption modulation due to the coherent vibrations of the superlattice, derived from a).

In order to compare the generated zone-folded acoustic phonon modes of the three different multiple quantum wells, the (normalized) absorption spectra for all quantum wells are shown in Fig. VII.7 b). The shift of the $k = 0$ oscillation modes to lower frequencies for thicker quantum wells is evident. The higher-order modes can as well be observed in the absorption spectra of the 2.7-nm and 3.6-nm MQW samples, but less pronounced as for the 1.8-nm quantum well due to the lower quality of the measurements. The $k = 0$ modes (indicated by arrows) for the 2.7-nm and 3.6-nm samples are 10% lower than expected. We presume that this is due to slightly different layer thicknesses than determined in the deposition process.

VII.4.4 Brillouin oscillations

A Brillouin oscillation can be observed as the generated acoustic wave travels through the GaN buffer and cap layer. This oscillation is extracted by the same moving average technique as described before, now over a time interval $\sim 1/f_0$. The resulting Brillouin oscillations in reflection and transmission for the 3.6-nm MQW and a pump fluence of 15 mJ/cm^2 are shown in Fig. VII.8 a). The ratio of the two amplitudes reflects the T/R ratio of 1 : 3 (Table VII.1). The reflection and transmission have a 180° phase shift with respect to each other, because the oscillation is an interference effect and not due to absorption $\Delta\alpha$, shown to be

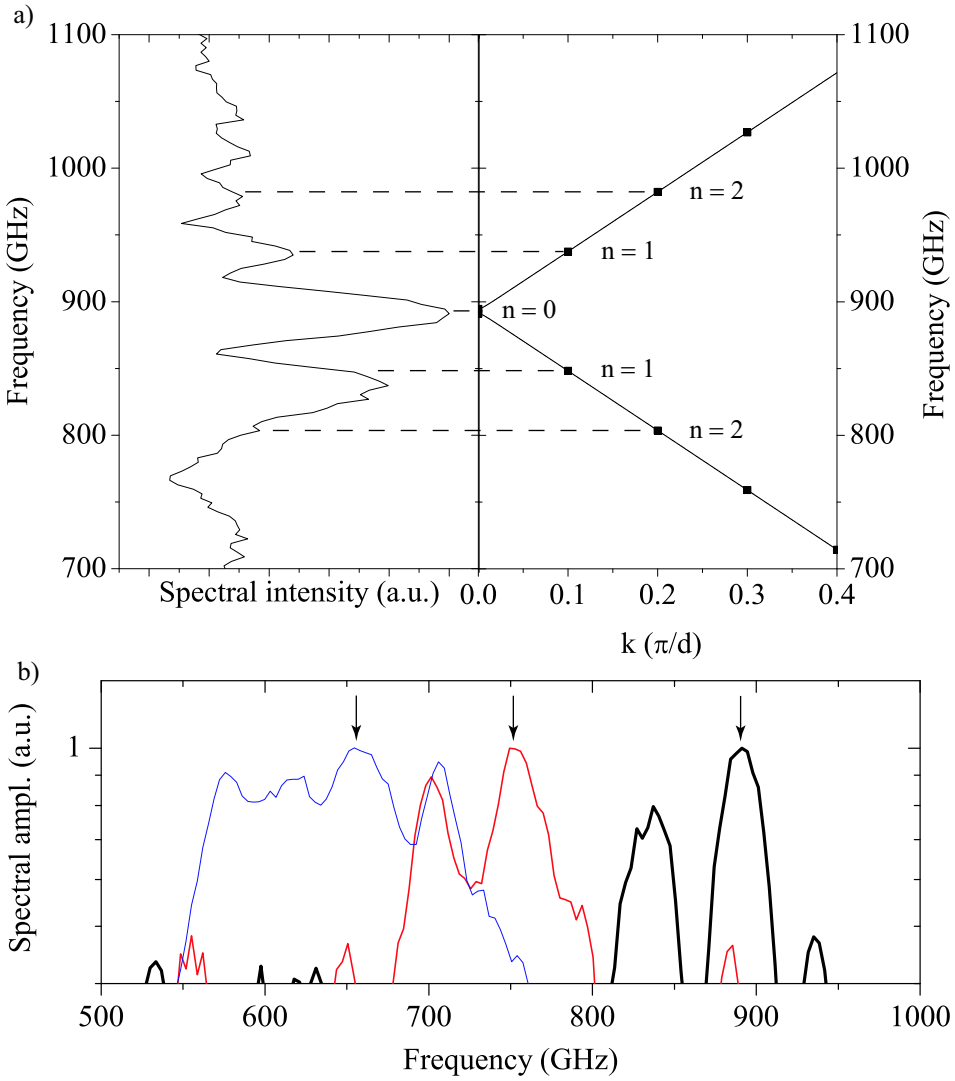

Figure VII.7: Vibrational spectrum of superlattice

a) Plot of the phonon spectrum of the 1.8-nm superlattice vibrations (left panel) obtained by Fourier transformation of $\Delta\alpha/\alpha$ in Fig. VII.6 b), together with the calculated dispersion curve (right panel). In the right panel, squares indicate the discrete modes of the superlattice, calculated by the formalism in Sec. VII.3. b) Phonon spectra of the absorption modulations for the 1.8-nm (thick line), 2.7-nm (medium thick line) and 3.6-nm (thin line) multiple quantum well samples. Arrows indicate the $k = 0$ mode positions.

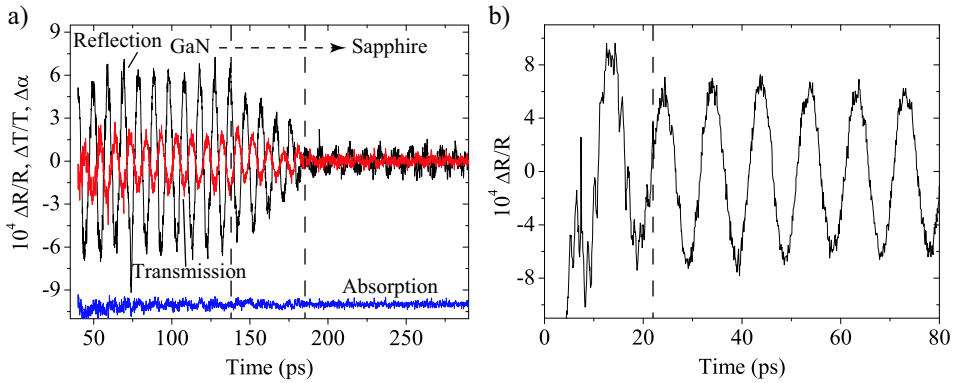

Figure VII.8: Brillouin oscillations
a) Observed Brillouin oscillations in reflection and transmission for the 3.6-nm thick multiple quantum well and an excitation fluence of 15 mJ/cm^2. Electronic background is subtracted from the data. Between 140 and 180 ps, acoustic waves travel from the GaN buffer layer into the sapphire substrate. Bottom line is absorption $\Delta\alpha$ calculated from reflection and transmission data, displaced by -10^{-3}. b) Observed Brillouin oscillations for the 2.7-nm thick multiple quantum well at an excitation fluence of 10.5 mJ/cm^2. Before 22 ps (left of dashed line) generated acoustic waves travel in opposite directions (Fig. VII.4 a), upper panel), after that time both travel in the same direction (Fig. VII.4 a), lower panel).

approximately zero in Fig. VII.8 a).

In Fig. VII.8 a), three different regimes can be distinguished, related to the acoustic wave propagation sketched in Fig. VII.4 a). Between 40 and 140 ps, both acoustic contributions travel through GaN. Since the distance between both waves is constant, the amplitude of the Brillouin oscillation remains constant during travelling. Between 140 ps and 185 ps, the oscillation is decreasing. Here, the first acoustic wave reaches the sapphire layer, while the other returning from the cap layer still travels in the GaN. The amplitude decreases slowly because it takes time for the two contributions (separated by twice the thickness of the cap layer, $\sim$ 360 nm) to fully enter the sapphire. The last regime shows a much smaller oscillation, signifying that both acoustic contributions travel through sapphire, in which the elasto-optic coupling is much smaller [13].

The large and fast decaying electronic background prevents visibility of the Brillouin signals at short times, which are not shown in Fig. VII.8 a). The quantum well with a thickness of 2.7 nm has a lower background in the reflection

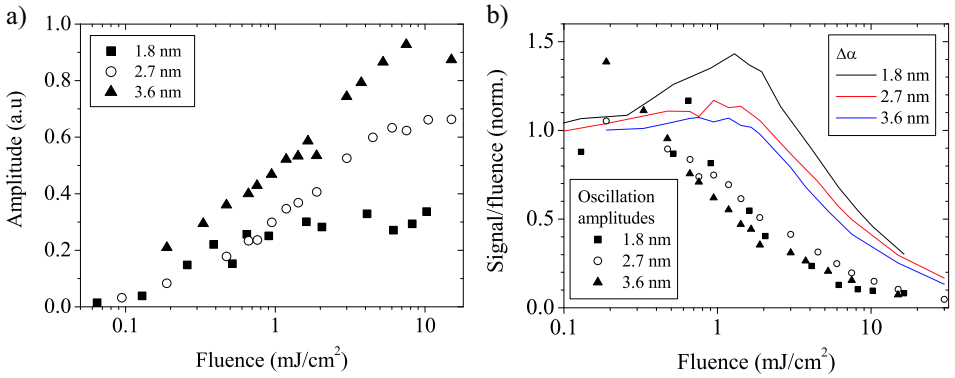

Figure VII.9: Brillouin oscillation amplitudes
a) Amplitude of the Brillouin oscillations observed in the reflection signal as a function of pump fluence, for the three multiple quantum wells. b) Measured Brillouin oscillation amplitudes (points, Fig. VII.9 a)) and maximum absorption (solid lines, Fig. VII.5 c), inset), divided by fluence and normalized to 1. Normalization is performed on the points at lowest fluence.

signal. Fig. VII.8 b) shows a typical Brillouin oscillation for this sample. About 20 ps after arrival of the pump pulse, the amplitude of the Brillouin oscillation changes. This 20 ps corresponds to the travel time (180×10^{-9} m/7.8×10^{3} m/s) of one of the acoustic contributions to the surface. Actually, reflection occurs between 15 and 30 ps because of the $\sim$ 100-nm length of the acoustic wave.

The Brillouin oscillations are fit with a sinusoidal function. From these fits, we calculate an average Brillouin frequency of 103.3 ± 0.2 GHz in GaN. This is slightly lower than the calculated 107 GHz, and is probably related to a lower sound velocity than expected. The oscillation amplitudes found in the reflection signal as a function of pump fluence for the three MQWs are plotted in Fig. VII.9 a). Here, we corrected for the reflection coefficient R, to obtain the absolute reflection change ΔR. The amplitudes scale with the well thickness, which is in accordance with the spectral amplitudes calculated by Fourier transformation of the generation profile. The ratio of maximum amplitude of the Brillouin oscillations between the different quantum wells is about 1:2:3, while the ratio of the quantum well thicknesses is 2:3:4. This can be traced back to the fact that it is not the thickness of the quantum well that determines the amplitude of the strain component at the Brillouin frequency, but rather the spatial separation between electrons and holes. Since the electron and hole wavefunctions are reduced at the

edge of the quantum well [4], this separation distance is $\sim$ 1 nm less than the quantum well thickness, yielding the correct ratio.

Fig. VII.9 b) shows both the Brillouin oscillation amplitude and the determined absorption $\Delta\alpha$ (inset Fig. VII.5 c)) for the three samples, divided by the pump fluence and normalized to 1. The strain generation already starts to saturate at pump fluences around 0.6 mJ/cm^2, comparable to what was derived from calculations and luminescence measurements on these quantum wells [3]. This fluence is lower than the $\sim$ 2 mJ/cm^2 at which the absorption decrease starts to saturate for all quantum wells, indicating that after full screening of the internal field, absorption still takes place. The observation that for thinner MQWs the strain generation saturates at lower fluences [4], cannot be resolved from this series of measurements.

VII.5 Conclusions

In conclusion, we have presented time-resolved pump-probe spectroscopy measurements on InGaN/GaN multiple quantum wells (MQWs) with various quantum well thicknesses. Upon pumping, a strong decrease in probe absorption is observed, related to bleaching effects. The observation of the MQW vibrational eigenmodes demonstrates the generation of a broad range of zone-folded acoustic phonon modes in the 0.6 - 1.0 THz range by pump excitation. The oscillation frequency increases with decreasing well width, consistent with calculated dispersion relations.

The acoustic generation by dynamical screening of the built-in piezoelectric field is demonstrated by monitoring the Brillouin frequency as the emitted strain travels through the surrounding material. The amplitude of the generated strain roughly scales with the thickness of the quantum well. Saturation of the oscillation amplitude takes place as the built-in piezoelectric field is completely screened, at much lower fluences than the saturation of pump light absorption. The saturation fluences for strain generation are in accordance with the ones found in electromagnetic THz emission experiments performed on the same samples.

References

1. R.N. Hall, G.E. Fenner, J.D. Kingsley, T.J. Soltys, and R.O. Carlson. Coherent light emission from GaAs junctions. *Phys. Rev. Lett.*, 9(9):366, 1962.

2. F. Chen, M.C. Cheung, P.M. Sweeney, W.D. Kirkey, M. Furis, and A.N. Cartwright. Ultrafast differential transmission spectroscopy of excitonic transitions in InGaN/GaN multiple quantum wells. *J. Appl. Phys*, 93(8):4933, 2003.
3. D. Turchinovich, P. Uhd Jepsen, B.S. Monozon, M. Koch, S. Lahmann, U. Rossow, and A. Hangleiter. Ultrafast polarization dynamics in biased quantum wells under strong femtosecond optical excitation. *Phys. Rev. B*, 68(24):241307, 2003.
4. D. Turchinovich, B.S. Monozon, and P. Uhd Jepsen. Role of dynamical screening in excitation kinetics of biased quantum wells: Nonlinear absorption and ultrabroadband terahertz emission. *J. Appl. Phys.*, 99(1):013510, 2006.
5. C.-K. Sun, J.-C. Liang, and X.-Y. Yu. Coherent acoustic phonon oscillations in semiconductor multiple quantum wells with piezoelectric fields. *Phys. Rev. Lett.*, 84(1):179, 2000.
6. E. Makarona, B. Daly, J.S. Im, H.J. Maris, and A. Nurmikko. Coherent generation of 100 GHz acoustic phonons by dynamic screening of piezoelectric fields in AlGaN/GaN multilayers. *Appl. Phys. Lett.*, 81(15):2791, 2002.
7. C.Y. Chen, Y.C. Wen, H.P. Chen, T.M. Liu, C.C. Pan, J.I. Chyi, and C.K. Sun. Narrow-band detection of propagating coherent acoustic phonons in piezoelectric InGaN/GaN multiple-quantum wells. *Appl. Phys. Lett.*, 91:133101, 2007.
8. G.D. Sanders and C.J. Stanton. Carrier dynamics and coherent acoustic phonons in nitride heterostructures. *Phys. Rev. B*, 74:205303, 2006.
9. D. Turchinovich. *Study of ultrafast polarization and carrier dynamics in semiconductor nanostructures: a THz spectroscopy approach*. PhD thesis, Albert-Ludwigs-University, Freiburg, 2004.
10. V. Yu. Davidov, A.A. Klochikhin, V.V. Emtsev, D.A. Kurdyukov, S.V. Ivanov, V.A. Vekshin, F. Bechstedt, J. Furthmuller, J. Aderhold, J. Graul, A.V. Mudryi, H. Harima, A. Hashimoto, A. Yamamoto, and E.E. Haller. Band gap of hexagonal InN and InGaN alloys. *Phys. Stat Sol. (b)*, 234(3):787, 2002.
11. V.W.L. Chin, T.L. Tansley, and T. Osotchan. Electron mobilities in gallium, indium and aluminum nitrides. *J. Appl. Phys.*, 75(11):7366, 1994.
12. D.A.B. Miller, D.S. Chemla, T.C. Damen, A.C. Gossard, W. Wiegmann, T.H. Wood, and C.A. Burrus. Band-edge electroabsorption in quantum well structures: the quantum-confined Stark effect. *Phys. Rev. Lett.*, 53(22):2173, 1984.
13. C.-T. Yu, K.-H. Lin, C.-L. Hsieh, C.-C. Pan, J.-I. Chyi, and C.-K. Sun. Generation of frequency-tunable nanoacoustic waves by optical coherent control. *Appl. Phys. Lett.*, 87(9):093114, 2005.
14. A. Bartels, T. Dekorsy, H. Kurz, and K. Köhler. Coherent zone-folded longitudinal acoustic phonons in semiconductor superlattices: excitation and detection. *Phys. Rev. Lett.*, 82(5):1044, 1999.
15. C. Kittel. *Introduction to Solid State Physics*. John Wiley & Sons, 1st edition, 1996.
16. S. Tamura, D.C. Hurley, and J.P. Wolfe. Acoustic-phonon propagation in superlattices. *Phys. Rev. B*, 38(2):1427, 1988.

17. C. Colvard, T.A. Gant, M.V. Klein, R. Merlin, R. Fischer, H. Morkoc, and A.C. Gossard. Folded acoustic and quantized optic phonons in (GaAl)As superlattices. *Phys. Lett. B*, 31(4):2080, 1985.
18. H.-N. Lin, R.J. Stoner, H.J. Maris, and J. Tauc. Phonon attenuation and velocity measurements in transparent materials by picosecond acoustic interferometry. *J. Appl. Phys.*, 69(7):3816, 1991.
19. F. Hudert, A. Bartels, C. Janke, T. Dekorsy, and K. Köhler. Coherent acoustic phonons in phonon cavities investigated by asynchronous optical sampling. *J. Phys. Conf. Ser.*, 92:012012, 2007.

Chapter VIII

Coherent strain generation by optically induced ultrafast phase transitions in YVO_3

Abstract

We study the generation and propagation of acoustic pulses along the *a*-, *b*- and *c*-axes of the semi-transparent material yttrium vanadate (YVO_3) near the generation surface by ultrafast pump-probe techniques, at room temperature and below. To this end, time-resolved Brillouin scattering was measured by a Sagnac interferometer. For propagation along the YVO_3 *b*-axis, no oscillations could be observed. Along the *a*-axis, strong oscillations are measured. These can be described by two Brillouin frequencies of ~ 42 GHz, yielding a measure for the birefringence of the material along the two in-plane *b*- and *c*-axis directions. The amplitude and phase of the Brillouin oscillations show no significant temperature or pump fluence dependences. The strain generation can therefore be attributed to ordinary thermoelastic effects, consistent with slow orbital reordering. The same is true for the *c*-axis, above the spin ordering phase transition at $T_S = 77$ K, which exhibits a strong and sudden volume change. When cooling the crystal below this temperature, we find strong evidence in both the measured Brillouin oscillation amplitude and phase for coherent strain generation through a solid-solid phase transition on the Brillouin period timescale (~ 24 ps) in the YVO_3 surface region. This suggests that when passing T_S orbital reordering occurs at different timescales in the *a* and *c* axial directions.

VIII.1 Introduction

In the previous chapter, the concept of time-resolved Brillouin scattering was introduced. Here, the interaction between probe light and specific coherent acoustic phonon modes in (semi-)transparent materials gives rise to a sensitivity for a single phonon frequency component, typically in the 10 - 100 GHz range. The change in reflection intensity as a function of propagation time arises from con-

structive or destructive interference of waves scattered off the travelling coherent wave and the sample surface reflection. This situation is sketched in Fig. VII.5 b) and Fig. VIII.1. In the frequency domain, Brillouin scattering has been used to detect the population dynamics of selected frequency modes, thereby proving nonlinear acoustic propagation and soliton formation [1, 2]. In the time domain, this technique has for example been applied to measure acoustic attenuation [3], and transparent material growth rates [4].

In this chapter, we use this simple yet powerful technique to study yttrium vanadate (YVO_3) [5, 6, 7, 8, 9]. This material is a perovskite, showing several electronic phase transitions below room temperature, some of which lead to a significant change in lattice constant [10]. In other materials, ultrafast phase transitions induced by optical pumping have been shown to lead to coherent strain emission [11, 12, 13]. The purpose of this chapter is to demonstrate strain generation by inducing phase transitions in YVO_3. By looking at acoustic rather than electronic effects, information is obtained complementary to the phase transition dynamics previously investigated by the electronic response [14].

We first look at the properties of the material relevant to acoustic effects, and the sample specifics. We then turn to the main topic of this chapter, the detection of propagating acoustic waves along the three crystal axes of YVO_3 as a function of temperature and pump fluence, by monitoring the development of the Brillouin component. The measured data will be discussed in a qualitative manner.

VIII.2 YVO_3 and phase transitions

Yttrium vanadate belongs to the group of transition metal perovskite oxides. From a fundamental point of view, these materials show exceptional electronic and magnetic properties [5, 8, 9]. Of particular interest to this research, is that magnetic and electronic reconfigurations at specific temperatures have significant consequences for the crystal structure, affecting for example the frequency of TO phonon modes [6].

In YVO_3 one passes three phase transitions, cooling from room temperature to liquid helium temperatures. At $T_{OO} = 196$ K, an orbital ordering occurs, and the material undergoes a structural phase transition into a Jahn-Teller ordered state. At $T_N = 116$ K, the V^{3+} magnetic moments order, and there is a transition from the paramagnetic to the antiferromagnetic state. Finally, due to a symmetry change (reordering) in the electronic d-band, a first order structural phase transition oc-

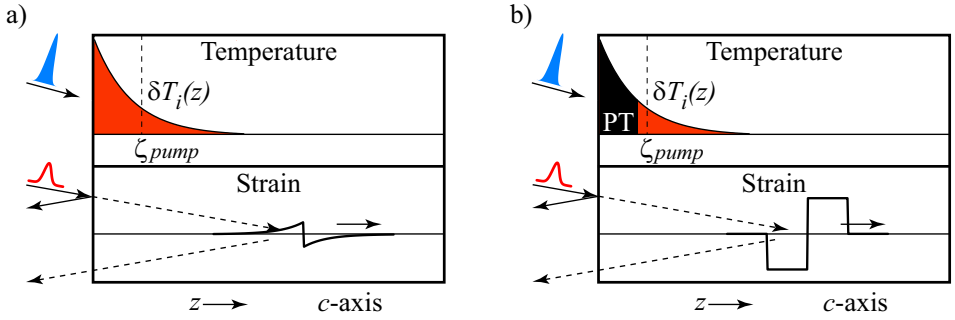

Figure VIII.1: Strain generation mechanisms in YVO_3
a) Sketch of thermoelastic strain generation in YVO_3 along the c-axis, above the strong structural phase transition at $T_S = 77$ K. The pump pulse (upper panel) deposits energy within the penetration depth ζ, and creates a near-exponential temperature profile $\delta T(z)$. The generated travelling strain shown in the bottom panel reflects the exponential profile, in the case that electron diffusion can be neglected, and the thermal expansion coefficient β is weakly temperature dependent. The strain is detected through interference of the two optical probe pulse reflections (solid and dashed arrows). b) Strain generation caused by the phase transition at T_S, when the sample equilibrium temperature is below T_S. The pump pulse heats the sample surface region, and when the threshold energy for reaching T_S is surpassed, up to a certain depth the phase transition will occur (black region indicated by PT), leading to a large and sudden strain contribution (lower panel). The generated strain differs from the thermally generated strain in a) in several ways. Its amplitude does not depend on pump fluence; its width (and therefore its acoustic spectrum) does. Moreover, the phase of the wave is reversed with respect to that of the thermoelastic strain.

curs at $T_S = 77$ K. The latter is the most dramatic when looking at lattice effects, and is accompanied by a sudden volume change (of the order of 0.2%) [10]. The lattice constants predominantly change in the b- and c-axis directions, in a complementary fashion. Recent results suggest that the phase transition at T_S (unlike that at T_N) occurs at very long timescales [14]. This is explained by the fact that the transition is accompanied by a loss of symmetry.

Ref. [10] summarizes the consequences for the temperature dependence of the lattice thermal expansion coefficient $\beta(T)$ along the different crystallographic axes. For the a-axis, the effects at T_S are relatively small compared to the other axes. Furthermore, $\beta(T)$ does not change significantly for $T_S < T < 300$ K. For the c-axis, $\beta(T)$ is near 0 below T_S. At T_S, the impulsive expansion is negative (i.e. contraction), at a value of -2.2×10^{-3}. Between T_S and T_{OO}, $\beta(T)$ is again

positive, and increases gradually to 6×10^{-5} K^{-1} at T_{OO}. Above T_{OO}, the expansion coefficient stabilizes at around 2×10^{-5} K^{-1}. For the *b*-axis, the behavior is qualitatively opposite to what is found for the *c*-axis. We can thus make some important *a priori* observations:

(i) The structural changes connected to the phase transition at T_S are strongly axis-dependent;

(ii) Because of the sign difference between thermal and phase transition strain contributions along all three crystal axes, the generated strains may have a polarity reversal;

(iii) In order to reach the strain amplitudes corresponding to the phase transition at T_S (0.2%) by thermoelastic processes, a temperature difference of several hundreds of Kelvin is required, requiring in general much larger pump fluences;

(iv) The generated coherent phonon spectrum due to the phase transition at T_S depends strongly on pump fluence, because the volume in which the phase transition occurs, increases with pump fluence.

The salient differences between thermoelastic strain generation (Ch. III) and strain generation through the sharp phase transition at T_S by means of ultrashort pulse excitation are sketched in Fig. VIII.1.

VIII.3 Experimental details

The transient reflection measurements (both amplitude and phase) presented in this chapter were performed with the interferometric setup outlined in Ch. III, i.e. pump wavelength at 400 nm and probe at 800 nm.

VIII.3.1 Samples

The YVO_3 sample growth procedure and structural information are supplied in Refs. [5, 6]. After preparation, the samples were polished by hand to optical quality. The experiments were performed on three samples, respectively with the *a*-, *b*-, and *c*-axis in the propagation direction (i.e. perpendicular to the sample surface). The orientation of the remaining two crystal axes in the surface plane is shown in the insets of Figs. VIII.2 a), VIII.3 a), and VIII.6 a).

VIII.3.2 Optical properties

The optical constants $\varepsilon = \varepsilon_1 + i\varepsilon_2$ were extracted from ellipsometry measurements presented in Ref. [6], where for now the differences between the different axes as well as temperature dependences (in the percentage range) are ignored. The values are used to recalculate the optical constants via the definition $\varepsilon = (n + i\kappa)^2$. For the probe wavelength of 800 nm, we arrive at $n = 2.22$ and $\kappa = 0.018$, leading to a $1/e$ intensity penetration depth ζ_{probe} of $\lambda/(4\pi\kappa) = 3.54$ μm. For the pump wavelength of 400 nm, we calculate $n = 2.23$ and $\kappa = 0.296$, leading to a penetration depth ζ_{pump} of 108 nm. The optical reflection coefficients R_{pump} and R_{probe} for 400 nm and 800 nm are calculated to be 0.152 and 0.143, respectively.

VIII.3.3 Brillouin scattering

The basic principle of Brillouin scattering was already discussed in Ch. VII. Given the speed of sound v_s for YVO_3 of around 7.6×10^3 m/s, $n \sim 2.22$, and using Eq. (VII.5), a Brillouin frequency f_0 of 42 GHz is estimated. The observed decay of the oscillation amplitude may be a measure for the acoustic attenuation at this frequency [3]. An important experimental limitation here is the finite pulse length. For a Fourier-limited probe pulse, the distance over which one can follow the acoustic wave in the material l_{coh} (i.e. the distance over which the signal will have dropped to a factor of $1/e$ due to loss of temporal overlap of the two reflections, shown in Fig. VIII.1) is equal to $l_{coh} = (c\tau)/(2\sqrt{\ln 2}n)$, with c the speed of light and τ the pulse FWHM [3]. For a $\tau = 110$ fs pulse, as for this experiment (App. B), the typical length l_{coh} is 8.9 μm. This corresponds to a decay time of $\tau_{coh} = l_{coh}/v_s = 1.2$ ns. The measurements typically extend to up to 1 ns, which means that this source of oscillation amplitude decay cannot be neglected. In the specific case of YVO_3, the limited transparency of the material is the limiting factor. The field penetration depth for the probe is twice the intensity penetration depth ζ_{probe} of 3.54 μm, leading to a decay time for visibility of the acoustic wave $\tau_{pen} = 2\zeta_{probe}/v_s = 960$ ps.

VIII.4 Results

Experiments were performed at $T_0 = 295$ K (room temperature), ~ 200 K, ~ 100 K, and 30 K; the latter three with the sample in a continuous flow cryostat. The pump fluences ranged from 0.1 mJ/cm^2 to 15 mJ/cm^2. Below T_S, the maximum

pump fluence was kept much lower, to reduce the risk of damaging the material.

At liquid helium temperatures, the heat capacity of the material is very low. Since there is also absorption at 800 nm, the probe intensity was minimized. Estimating the probe focus waist to 10 μm, and keeping the probe energy per pulse at the sample below 0.5 nJ, the temperature rise was < 10 K in all cases.

VIII.4.1 Experiments along *b*-axis

An overview of the amplitude measurement results for propagation along the *b*-axis at various temperatures is shown in Fig. VIII.2. There is no sign of Brillouin oscillations. Since these were found for the other axes under the same conditions, and one would in all cases expect thermoelastic strain generation, we conclude that elasto-optic coupling along this axis is negligible.

The decay of the slowly varying background can be fit with three exponentials, with characteristic times τ_1, τ_2 and τ_3. The traces for the *a*- and *c*-axes were also analyzed in this way. The data show no significant temperature or axial dependence. Therefore the results are averaged over all axes and temperatures and collected in Table VIII.1. This three-component decay points to a fast thermalization of the electron gas (τ_1), energy transfer to the lattice and local equilibration (τ_2), and a slow decay due to heat diffusion out of the excited zone into the bulk of the material (τ_3). Comparing to the results of Ref. [14], good agreement for τ_1 and τ_2 is found. The long $\sim$ ns decay time τ_3 is absent in the referred measurements, since $\zeta_{pump} \gg \zeta_{probe}$ in that case, and there is no significant heat diffusion out of the probed region at the picosecond timescale.

The maximum signal amplitude (inset Fig. VIII.2 d)) shows no strong temperature dependence. There is a $\sim 55\%$ increase in signal when cooling from room temperature to lower temperatures, an effect which is also encountered when looking at the Brillouin oscillation amplitudes for other axes.

We have also performed phase measurements (not shown), which would in principle allow observation of propagating strain by surface displacement (Ch. II). Like for phase measurements on the *c*-axis propagation (not presented) however, electronic effects cannot be distinguished from surface displacement, since both occur at relatively long timescales.

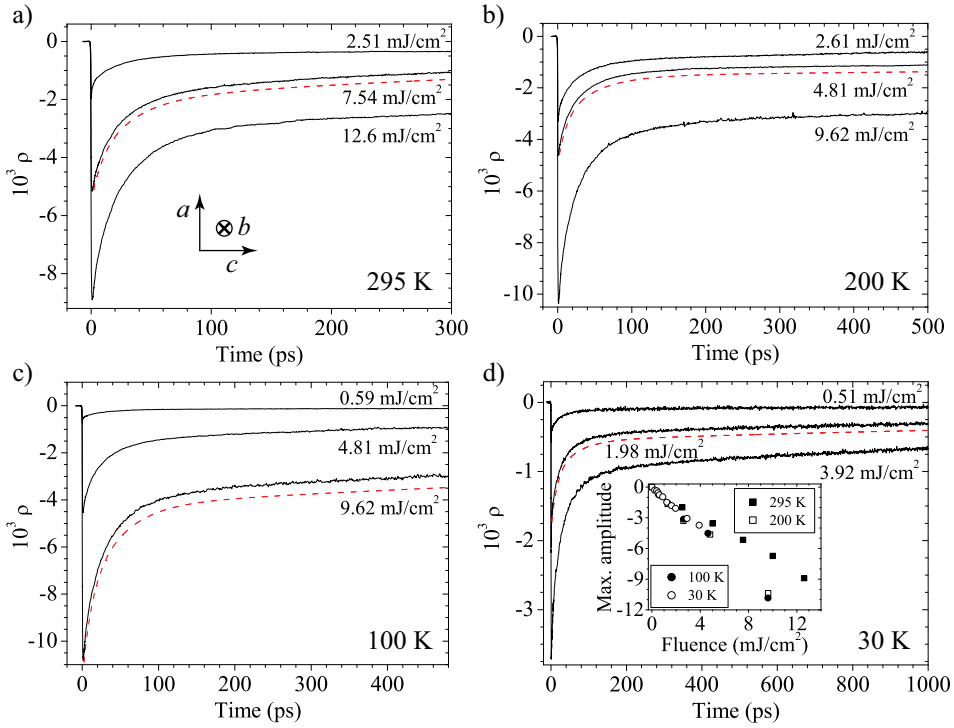

Figure VIII.2: Pump-probe amplitude results for *b*-axis of YVO_3
Selected pump-probe amplitude results $\rho(t)$ for acoustic wave propagation in the *b*-axis direction (inset of a) shows sample orientation), obtained at a) 295 K, b) 200 K, c) 100 K and d) 30 K. Dashed lines indicate three-component exponential decay, with a small offset with respect to the measured trace. In all cases, there is no sign of acoustic wave propagation (Brillouin oscillation). Inset of d) shows the maximum signal change, as a function of fluence and for all temperatures. A 55% signal amplitude increase is found when lowering the temperature from 295 K to 200 K; below that, hardly any change is visible.

Decay time	τ_1 (ps)	τ_2 (ps)	τ_3 (ps)
Value (ps)	4.6 ± 3.1	34.6 ± 4.6	2380 ± 150

Table VIII.1: Extracted signal decay times from *a*-, *b*- and *c*-axis measurements

VIII.4.2 Experiments along *a*-axis

The experiments for propagation in the *a*-axis direction for both amplitude ρ and phase $\delta\varphi$ are shown in Figs. VIII.3 and VIII.4, respectively. First of all, we point to the qualitative differences in background behavior between the 30-K data (Figs. VIII.3 d) and VIII.4 e)) and the data for higher temperatures. There is a strong increase in background level over a time interval of several hundreds of picoseconds, for fluences of ~ 1 mJ/cm^2 and above (getting shorter for higher fluences), saturating at around 4 mJ/cm^2. This is a consequence of the phase transition in the surface region [14]. For higher fluences the phase transition penetrates deeper into the surface layer than the optical probe penetration depth ζ_{probe}, and saturation sets in. The measured settling times of several hundreds of picoseconds are then determined by the time it takes to establish the phase-transformed state. The inset of Fig. VIII.4 e) shows that at high fluences, the background behavior is dominated by ordinary heating of the material also present at high temperatures.

The Brillouin oscillation is clearly visible in both cases, implying that the elasto-optic effect is significantly larger than for the *b*-axis. At low temperatures, beating effects are observed. For example, the data for 100 K, depicted in Fig. VIII.3 c) and Fig. VIII.4 c), show a near-perfect destructive interference around 600 ps. We can explain this effect by the birefringence of the material. Literature data shows, that the index of refraction *n* can differ by several percent for different crystal axes [6]; the same applies to the elasto-optic coupling. Since probing at the sample occurs with circular polarization in our interferometer (Ch. II), the anisotropy in the *b*- and *c*-axis will give rise to a mixing of the effects in these directions in the detection. The inset of Fig. VIII.4 c) shows the Fourier transform of the measured signal in Fig. VIII.4 d), and demonstrates the presence of exactly two frequencies, separated by ~ 1 GHz.

To analyze the Brillouin oscillations, the slowly varying background was subtracted by a moving average over the data, as in Ch. VII. Knowing that the anisotropy can influence both the oscillation amplitude as well as the frequency, the obtained traces were fit by two cosines with different amplitude and frequency but the same damping and initial phase:

$$a(t) = [a_1 \cos(2\pi f_1 t - \phi_0) + a_2 \cos(2\pi f_2 t - \phi_0)] \times \exp\left(\frac{-t}{\tau_{dec}}\right) \times \exp\left(\frac{-t^2}{\tau_{coh}^2}\right). \tag{VIII.1}$$

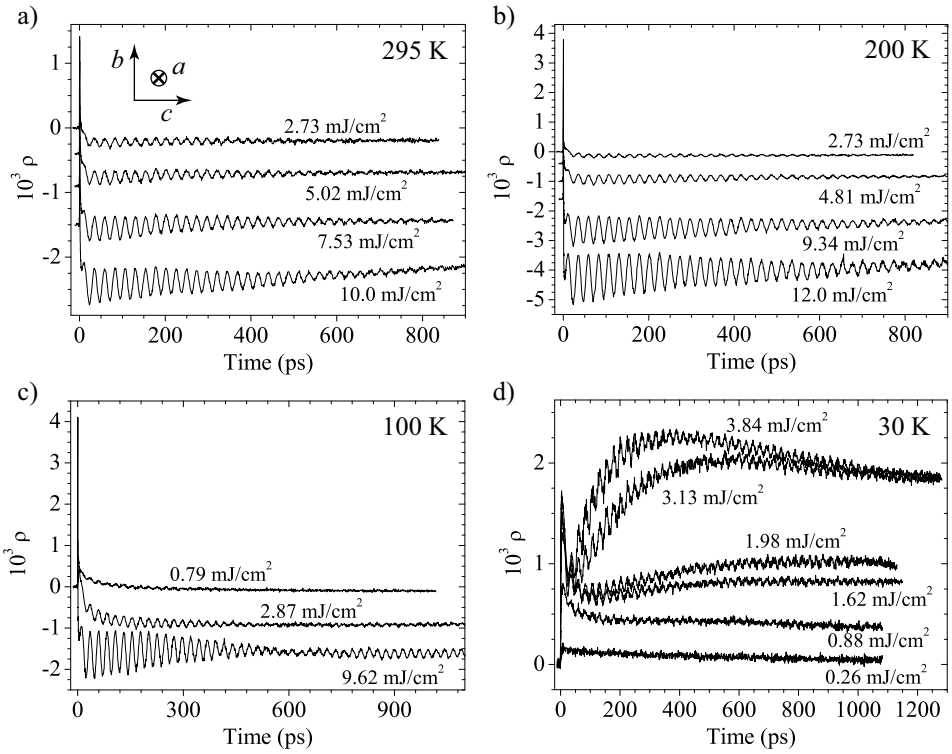

Figure VIII.3: Pump-probe amplitude results for *a*-axis of YVO_3
Selected pump-probe amplitude results $\rho(t)$ for acoustic wave propagation in the *a*-axis direction (inset of a) specifies the sample orientation), obtained at a) 295 K, b) 200 K, c) 100 K and d) 30 K. In a) and b) measured signals have a slight (negative) offset for reasons of presentation. Lowest temperature shows qualitatively different features.

The amplitudes a_1 and a_2, the frequencies f_1 and f_2, the phase offset ϕ_0, and an exponential decay time τ_{dec} (an effective time due to the finite penetration depth and possible acoustic damping) are the free fit parameters. The value of τ_{coh} was fixed to the 1.2 ns established from pulse length measurements. From measurements where the birefringence is large (e.g. at a temperature of 100 K), it was possible to reliably determine the value of τ_{dec}, and it was found to be 960 ± 24 ps, exactly equal to $\tau_{pen} = 960$ ps. We conclude that no detectable acoustic damping is present at this temperature. Test fit routines did not show any pronounced acoustic attenuation at higher temperatures either. Thus we set $\tau_{dec} = \tau_{pen} = 960$ ps for all other traces. The background corrected traces and the

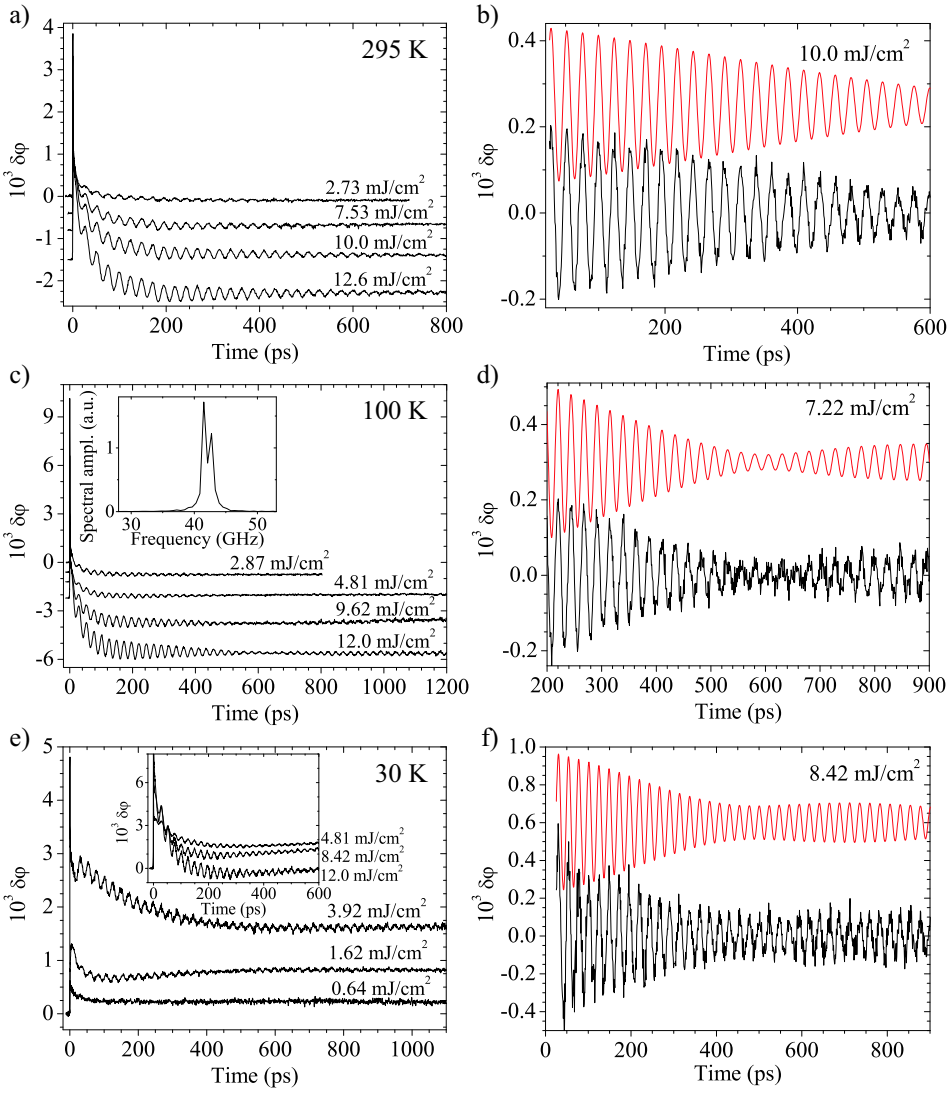

Figure VIII.4: Pump-probe phase results for *a*-axis of YVO_3
a) Phase signals $\delta\varphi(t)$ for 295 K and indicated pump fluences. b) Background corrected signal for a fluence of 10.0 mJ/cm^2 at room temperature, showing only the Brillouin component (lower trace). Upper trace is a fit to the data, according to Eq. (VIII.1). c) Phase signals obtained for a temperature of 100 K. Inset shows the Fourier transform of the measured signal in d), and the two beating frequencies. d) Background subtracted signal (lower trace), and fit (upper trace), for 7.22 mJ/cm^2 at 100 K. e) Phase signals measured at 30 K. Inset shows high fluence data. f) Background subtracted signal (lower trace) and fit (upper trace) for 8.42 mJ/cm^2 at 30 K.

Temp.		f_1 (GHz)	f_2 (GHz)	ϕ_0 (rad)	a_1/a_2
295 K	ρ	42.17 ± 0.01	41.61 ± 0.01	2.94 ± 0.01	1.51 ± 0.09
	$\delta\varphi$	42.17 ± 0.01	41.58 ± 0.01	1.12 ± 0.01	1.57 ± 0.07
200 K	ρ	42.13 ± 0.01	41.73 ± 0.02	2.99 ± 0.02	1.53 ± 0.09
	$\delta\varphi$	42.12 ± 0.02	41.72 ± 0.03	1.56 ± 0.05	1.42 ± 0.39
100 K	ρ	42.61 ± 0.01	41.77 ± 0.01	3.16 ± 0.02	0.71 ± 0.02
	$\delta\varphi$	42.58 ± 0.01	41.78 ± 0.01	1.73 ± 0.02	0.70 ± 0.01
30 K	ρ	42.46 ± 0.01	41.31 ± 0.01	3.27 ± 0.02	2.72 ± 0.18
	$\delta\varphi$	42.46 ± 0.01	41.35 ± 0.02	1.76 ± 0.04	2.81 ± 0.16

Table VIII.2: Brillouin fit information for the *a*-axis, extracted from amplitude and phase measurements

Values are derived from a fit to the measured data according to Eq. (VIII.1). Here, f_1 is always taken to be the largest of the two frequencies. Data per temperature are averaged over typically 4 - 8 different fluences. No fluence dependence was established.

fit results for three $\delta\varphi$-traces at different temperatures are shown in Figs. VIII.4 b), d) and f). These figures show the excellent correspondence of the data to this model.

The results, including the ratio of the amplitudes a_1 and a_2, averaged over around eight curves per temperature, are collected in Table VIII.2. A difference of $\pi/2$ between the values of ϕ_0 for the ρ and $\delta\varphi$ measurements is observed, as expected. The frequencies f_1 and f_2 are found to be around 42 GHz at all temperatures, in accordance with our estimates. The variation in frequency ranges from 0.4 GHz to 1.1 GHz. The ratio a_1/a_2 at 100 K compared to 200 K and 295 K suggests that the birefringence has changed sign, while the value at 30 K shows that the elasto-optical sensitivity in the *b*- and *c*-axis direction have strongly changed. The large temperature steps in our measurements prevent a determination of the relation between the birefringence and the electronic structure as a function of temperature. Additional measurements at intermediate temperatures would yield valuable results complementary to the measurements of the dielectric function collected in Ref. [6].

In Fig. VIII.5 the value of $a_1 + a_2$, which we take to be a fair measure for the strain amplitude, is plotted as a function of fluence and temperature. The total amplitudes for ρ (Fig. VIII.5 a)) and $\delta\varphi$ (Fig. VIII.5 b)) are comparable. In fact, the two measurement types form different ways of looking at the same signal. The

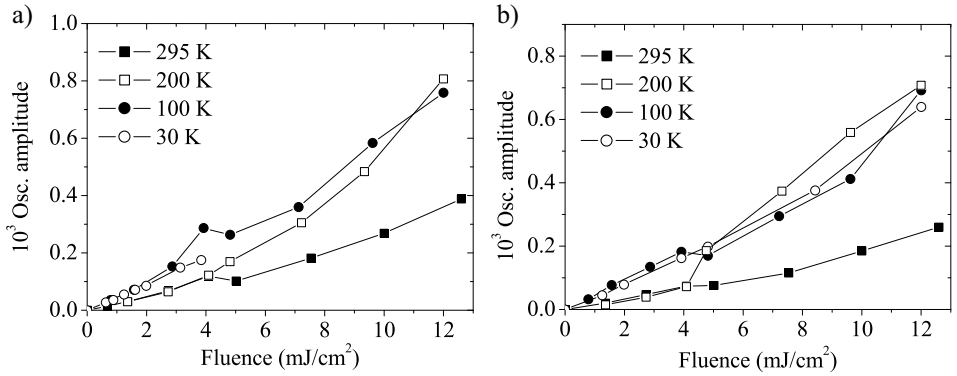

Figure VIII.5: Brillouin oscillation amplitudes extracted from amplitude and phase measurements

a) Amplitude $a_1 + a_2$ of the Brillouin oscillation, derived from ρ measurements, as a function of pump fluence, for the indicated temperatures. b) Like a), but now derived from $\delta\varphi$ measurements. The amplitudes in b) are slightly lower due to the limited contrast of the interferometric setup. When going from room temperature to 200 K and lower, a multiplication factor of ~ 4 can be seen in the Brillouin oscillation amplitude. No differences are observed between results above and below T_S.

values for $\delta\varphi$ are on average slightly lower because the interferometric contrast is less than 100%. From these measurements, the contrast is estimated at 88%, in good agreement with the results found in Chs. II - V.

The amplitudes at room temperature are almost a factor of four lower than at 200 K and lower temperatures, similar to what was found for the *b*-axis (Fig. VIII.2). Knowing that strain generation is not much different for 30, 100 and 200 K, this suggests that at low temperatures the sensitivity for thermal and acoustic effects is larger. Since probing occurs near the optical band gap [6], temperature-induced shifting of the band position may be the cause. Like for the *b*-axis, further cooling does not yield any significant changes in sensitivity.

From these data we can conclude that there is *no* significant contribution to coherent strain generation arising from the phase transition at T_S observed in the Brillouin data for the *a*-axis. This is remarkable because the measured static expansion along this axis predicts a significant contribution, be it smaller than that along the *b*- and *c*-axes [10]. From recent measurements, reproduced in Fig. VIII.3 d), it was concluded that the phase transition along this axis occurs very slowly, on the order of the background variation times shown in Fig. VIII.3 d)

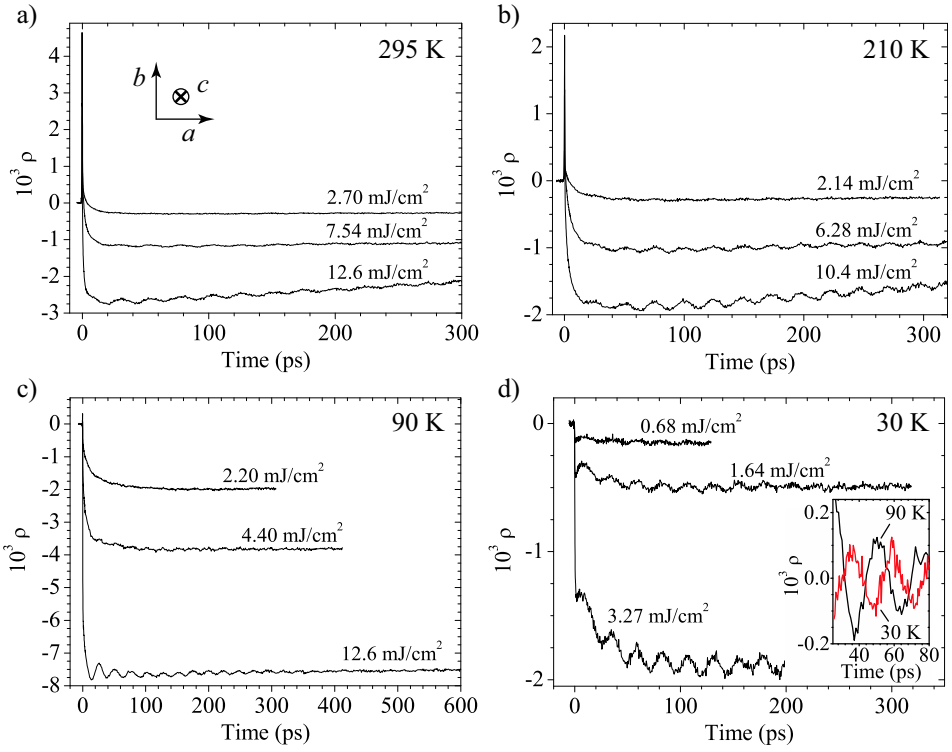

Figure VIII.6: Pump-probe amplitude results for *c*-axis of YVO_3
Selected pump-probe amplitude results $\rho(t)$ for acoustic wave propagation in the *c*-axis direction (crystal orientation is depicted in the inset of a)), obtained at a) 295 K, b) 210 K, c) 90 K and d) 30 K. The inset of d) shows part of the measurements obtained at 90 K and a fluence of 12.0 mJ/cm^2, and at 30 K and a fluence of 3.27 mJ/cm^2, illustrating that both the oscillation amplitude and phase are significantly different for the two temperatures.

[14]. Since the corresponding generated acoustic frequencies are extremely low ($\sim$ 5 GHz, much lower than f_0), it is indeed reasonable to expect no contribution at the Brillouin frequency.

VIII.4.3 Experiments along *c*-axis

In Fig. VIII.6, the amplitude (ρ) data obtained for the *c*-axis for four different temperatures are presented. Clear oscillations are again visible, though the amplitudes are significantly lower than those for the *a*-axis. The slow ($\sim$ 400 ps) shift of the background at the lowest temperature in the *a*-axis results is absent

Temp.		f_1 (GHz)	f_2 (GHz)	ϕ_0 (rad)	a_1/a_2
295 K	ρ	41.55 ± 0.06	40.55 ± 0.06	1.50 ± 0.06	1.20 ± 0.66
210 K	ρ	40.76 ± 0.03	40.76 ± 0.03	0.39 ± 0.07	-
90 K	ρ	41.18 ± 0.13	39.96 ± 0.21	0.72 ± 0.13	1.54 ± 0.12
30 K	ρ	42.45 ± 0.22	41.19 ± 0.07	3.04 ± 0.06	0.57 ± 0.27

Table VIII.3: Brillouin fit information for the *c*-axis, extracted from amplitude measurements

Values are derived from a fit to the measured data according to Eq. (VIII.1). Data per temperature are an average result of 4 - 8 fluences. f_1 is always the largest of the two frequencies. For a temperature of 210 K, no beating is detected, and the trace could well be fitted with a single frequency. Therefore, no value for the ratio could be established.

here. Assuming that this background behavior is connected to the phase transition dynamics, this implies that the phase transition in the *c*-axis direction occurs at a different timescale than in the *a*-axis direction.

The model of Eq. (VIII.1) was used to analyze the Brillouin oscillations. The results are collected in Table VIII.3. For the frequency, slightly lower values are found than for the *a*-axis, which is related to a different refractive index and sound velocity along this axis. A distinct and striking feature appears in the phase ϕ_0 of the acoustic oscillation shown in Fig. VIII.7 a) when passing temperature T_S. For the temperatures of 90 K, 210 K and 295 K, an average value for ϕ_0 of around 0.8 radians (-0.4 rad $< \phi_0 <$ 1.5 rad) is found. ϕ_0, however, makes a sudden jump to a value of 3.04 radians at 30 K. The effect is shown to better advantage in the inset of Fig. VIII.6 d), where the first tens of picoseconds are shown of traces obtained at 90 K and 30 K. Since the data for the *a*-axis does not support the unlikely event of a sign change of the elasto-optic constants, the phase jump demonstrates the sign flip of the acoustic wave. This is expected for an impulsive contribution at T_S along this axis (Sec. VIII.2).

Due to the limited amount of data and small signals, it is not possible to draw conclusions on the results for the ratio a_1/a_2. However, additional evidence for coherent strain generation through a phase transition follows from the sum of amplitudes $a_1 + a_2$, plotted in Fig. VIII.6 f). The amplitudes of the Brillouin component at 41 GHz have significantly increased for 90 K compared to higher temperatures. This can be explained by the strong increase of the thermal expansion coefficient between 100 K and 200 K along this axis [10]. More importantly,

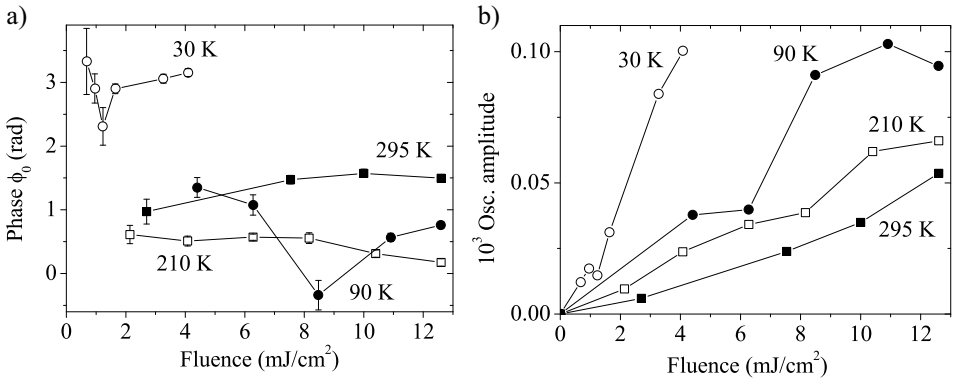

Figure VIII.7: Brillouin oscillation phase and amplitude for *c*-axis of YVO_3
a) Extracted values for the Brillouin oscillation phase offset ϕ_0 as a function of fluence and temperature. There is a clear discontinuity when going from 90 K (above T_S) to 30 K (below T_S). b) Amplitude of the Brillouin oscillations $a_1 + a_2$ as a function of fluence, for the indicated temperatures. There is a sharp increase in oscillation amplitude for the lowest temperatures. The increase for the 90-K case is ascribed to the higher thermal expansion coefficient β between 77 K and 200 K. The additional increase when decreasing temperature to 30 K cannot be connected to the same fact, since β is very small in the temperature range 30 - 70 K.

the amplitude of the Brillouin oscillation increases by about a factor of four for 30 K, relative to high temperature values. For an elasto-optic constant along the *c*-axis independent of temperature below 200 K (as seems to be the case for the *a*- and *b*-axis), this implies that not only the phase of the strain, but also its amplitude has significantly changed.

VIII.5 Discussion

The data in the *a*- and *c*-axis directions show different behavior, both when looking at the electronic and at the acoustic response. All of the observations made here point to the fact that there is an impulsive contribution due to the phase transition at T_S for the *c*-axis at the Brillouin frequency. This fact also signifies that there is strain release at a timescale $\sim 1/f_0 \sim 24$ ps, much faster than what was found for the *a*-axis.

It is still unclear whether the transition effect is due to a full or just a partial reordering, and what the required time to reach the transformed state is exactly. In

order to analyze this problem more quantitatively, a model along the lines of Ch. III is required. A complicating fact is that not all material parameters are known. Furthermore, the spectral intensity at f_0 can depend strongly on the input parameters. An experimental improvement would be to develop an geometry where one looks at the temporal strain profile, rather than at a single frequency component. In the analysis, symmetry considerations are not yet taken into account. If an intermediate state exists where reordering in the *c*-axis direction increases the symmetry of the electron system, this could explain the strong difference in response along the two studied crystal directions.

Additional support for the occurrence of a phase transition would be the presence of a threshold in the fluence dependence. The threshold power can be estimated as

$$\int_{T_0}^{T_S} C_i(T)\mathrm{d}T = \frac{I_{thr}(1-R_{pump})}{\zeta_{pump}}, \tag{VIII.2}$$

with $C_i(T)$ the lattice heat capacity [5, 7]. Due to strong absorption at 400 nm and a low heat capacity in this temperature range, a threshold pump energy I_{thr} of only 0.3 mJ/cm^2 is required to bridge the temperature difference between $T_0 = 30$ K and T_S. This value lies too close to zero to establish threshold behavior. Larger pump wavelengths increase I_{thr} and would allow for a test on threshold behavior.

VIII.6 Conclusions

A large set of interferometric pump-probe measurements on YVO_3 was analyzed as a function of pump fluence and sample temperatures, for three different crystal orientations. The thermal background signal shows a three-component decay, where the $\sim$ 35-ps decay time is identified as the transfer time of heat from the electron gas to the lattice.

Along the *b*-axis, no sign of acoustic propagation was found, indicating a minute elasto-optic coupling. Along the *a*-axis, strong Brillouin oscillations are observed, indicative of a substantial elasto-optic coupling and acoustic wave propagation. The oscillations show a beating pattern due to anisotropy of both the refractive index and the elasto-optic constants for the two probe polarization components. The former gives rise to two slightly different beating frequencies and an accurate determination of the birefringence, the latter to different amplitudes of these beating frequencies. The *a*-axis results can be accounted for by ordi-

nary thermoelastic strain generation, and show no sign of a contribution due to lattice deformation by the orbital ordering phase transition at $T_S = 77$ K. This is consistent with experiments interpreting the electronic response, and proves that the phase transition occurs at much longer timescales than the Brillouin period $1/f_0 \sim 24$ ps.

Along the *c*-axis, the Brillouin oscillation features depend strongly on temperature. The oscillation amplitudes at 90 K strongly increase with respect to higher temperatures, confirming the strong increase of the thermal expansion coefficient between T_S and T_{OO}. At a sample temperature below T_S, the oscillation amplitudes increase by an additional factor of four at low fluences. Moreover, the oscillation phase is opposite to the one above T_S. These facts form conclusive evidence of coherent strain generation through the solid-solid phase transition on a timescale $\leq 1/f_0$. The release of strain occurs first along the *c*-axis, followed by the release in the *a*-axis direction on a much longer (~ 100 ps) timescale.

References

1. O.L. Muskens and J.I. Dijkhuis. High amplitude, ultrashort, longitudinal strain solitons in sapphire. *Phys. Rev. Lett.*, 89(28):285504, 2002.
2. O.L. Muskens and J.I. Dijkhuis. Inelastic light scattering by trains of ultrashort acoustic solitons in sapphire. *Phys. Rev. B*, 70(10):104301, 2004.
3. H.-N. Lin, R.J. Stoner, H.J. Maris, and J. Tauc. Phonon attenuation and velocity measurements in transparent materials by picosecond acoustic interferometry. *J. Appl. Phys.*, 69(7):3816, 1991.
4. S. Kashiwada, O. Matsuda, J.J. Baumberg, R. Li Voti, and O.B. Wright. In situ monitoring of the growth of ice films by laser picosecond acoustics. *J. Appl. Phys.*, 100(7):073506, 2006.
5. G.R. Blake, T.T.M. Palstra, Y. Ren, A.A. Nugroho, and A.A. Menovsky. Neutron diffraction, x-ray diffraction, and specific heat studies of orbital ordering in YVO_3. *Phys. Rev. B*, 65(17):174112, 2002.
6. A.A. Tsvetkov, F.P. Mena, P.H.M. van Loosdrecht, D. van der Marel, Y. Ren, A.A. Nugroho, A.A. Menovsky, I.S. Elfimov, and G.A. Sawatzky. Structural, electronic, and magneto-optical properties of YVO_3. *Phys. Rev. B*, 69(7):075110, 2004.
7. L.D. Tung, M.R. Lees, G. Balakrishnan, and D. McK. Paul. Magnetization reversal in orthovanadate RVO_3 compounds (R = La, Nd, Sm, Gd, Er, and Y): Inhomogeneities caused by defects in the orbital sector of quasi-one-dimensional orbital systems. *Phys. Rev. B*, 75(10):104404, 2007.
8. Y. Ren, T.T.M. Palstra, D.I. Khomskii, E. Pellegrin, A.A. Nugroho, A.A. Menovsky,

and G.A. Sawatzky. Temperature-induced magnetization reversal in a YVO_3 single crystal. *Nature*, 396:441, 1998.

9. G.R. Blake, T.T.M. Palstra, Y. Ren, A.A. Nugroho, and A.A. Menovsky. Transition between orbital orderings in YVO_3. *Phys. Rev. Lett.*, 87(24):245501, 2001.
10. C. Marquina, M. Sikora, M.R. Ibarra, A.A. Nugroho, and T.T.M. Palstra. Lattice effects in YVO_3 single crystal. *Jour. Magn. Magn. Mat.*, 290-291:428, 2005.
11. K. Sokolowski-Tinten, C. Blome, C. Dietrich, A. Tarasevitch, M. Horn von Hoegen, D. von der Linde, A. Cavalleri, J. Squier, and M. Kammler. Femtosecond X-ray measurement of ultrafast melting and large acoustic transients. *Phys. Rev. Lett.*, 87(22):225701, 2001.
12. H. Enquist, H. Navirian, T.N. Hansen, A.M. Lindenberg, P. Sondhauss, O. Synnergren, J.S. Wark, and J. Larsson. Large acoustic transients induced by nonthermal melting of InSb. *Phys. Rev. Lett.*, 98(22):225502, 2007.
13. A. Cavalleri, Cs. Tóth, C.W. Siders, J.A. Squier, F. Ráksi, P. Forget, and J.C. Kieffer. Femtosecond structural dynamics in VO_2 during an ultrafast solid-solid phase transition. *Phys. Rev. Lett.*, 87(23):237401, 2001.
14. D.A. Mazurenko, A.A. Nugroho, T.T.M. Palstra, and P.H.M. van Loosdrecht. Dynamics of spin and orbital phase transitions in YVO_3. *Phys. Rev. Lett. (submitted)*, 2008.

Chapter IX

Ultrafast carrier dynamics in ZnO nanowires

Abstract

This final chapter focuses on the ultrafast optical properties of disordered arrays of ZnO nanowires, grown on sapphire substrates. The nanowire samples were pumped uniformly by 800-nm pulses with fluences I_0 ranging up to 200 mJ/cm^2. Both time-integrated luminescence and time-resolved transmission of a 400-nm probe were detected. The integrated luminescence increases faster than ${I_0}^3$ (i.e. proportional to the carrier density), showing that nonradiative decay gains importance for higher fluences. This superlinear increase with carrier density saturates at the highest pump fluences. The transmission at 400 nm increases strongly directly after arrival of the pump, and rapidly decays with a time constant dependent on fluence, as short as ~ 9 ps at the highest fluence. We explain our results by direct carrier recombination, stimulated emission, and saturation effects. Calculations based on rate equations for carrier and photon densities show good agreement with the measured data.

The results in this chapter were obtained in close collaboration with drs. M.A.M. Versteegh.

IX.1 Introduction

Over the last decade, the use of complex nanostructures as building blocks in electronic and optical circuits has been made possible by advanced growth techniques. Epitaxially grown semiconductor nanowires [1] already find application as polarization-dependent photodetectors [2], light emitting diodes [3], solar cells [4], lasers [5, 6], and subwavelength waveguides [7]. These nanowires typically have lengths ranging from a few up to hundreds of micron and diameters ranging from one up to hundreds of nm [8]. Because of the wide bandgap of zinc oxide (ZnO) of 3.37 eV at room temperature, it is an important material for optical ap-

plications in the UV. Of both fundamental and practical interest are recent claims of polariton lasing in nanowires [5, 9].

The lasing behavior is connected to carrier dynamics on a picosecond timescale [10, 11]. In this chapter, we explore the carrier dynamics in ZnO nanowires in the degenerate electron-hole plasma (EHP) regime by applying our femtosecond pump-probe techniques to in-house grown disordered ZnO nanowire arrays on sapphire. After briefly describing the sample details and the generated carrier densities, luminescence and ultrafast pump-probe transmission experiments are presented. These will be analyzed by a general laser model for semiconductors [10, 12]. Finally, we will discuss some future directions of research on these fascinating structures.

IX.2 ZnO nanowires

This section summarizes the ZnO nanowire growth method and shapes as extensively studied in our Institute [9, 13, 14, 15]. The relevant electronic properties as well as the discussed effects are accurately described in Ref. [12].

IX.2.1 ZnO nanowire structure

The ZnO nanowires were grown in the Debye Institute by H.-Y. Li MSc in the group of Prof. Dr. D. Vanmaekelbergh. The nanowires are grown epitaxially by a vapor-solid mechanism on a sapphire substrate of thickness $d_{sample} = 214\ \mu$m. Here, sputter-deposited gold nanodroplets act as catalyzer [14]. With this technique, a high density of wires is obtained. Fig. IX.1 shows images taken with a scanning electron microscope (SEM) of a typical sample. The wire length is uniform over a large fraction of the sample. For our sample, the wires have an average diameter ~ 100 nm and length $\sim 10\ \mu$m. The crystalline (0001) direction (c-axis) is oriented along the long axis of the wires. The a-axis of the sapphire substrate is oriented perpendicularly to the plane to achieve a minute lattice mismatch at the ZnO/sapphire interface. The nanowire diameter varies between 50 and 400 nm over the sample surface (Figs. IX.1 c), d)) because of the yet uncontrolled Au droplet size. The wires have facets due to the wurtzite crystal structure, clearly shown in Fig. IX.1 f).

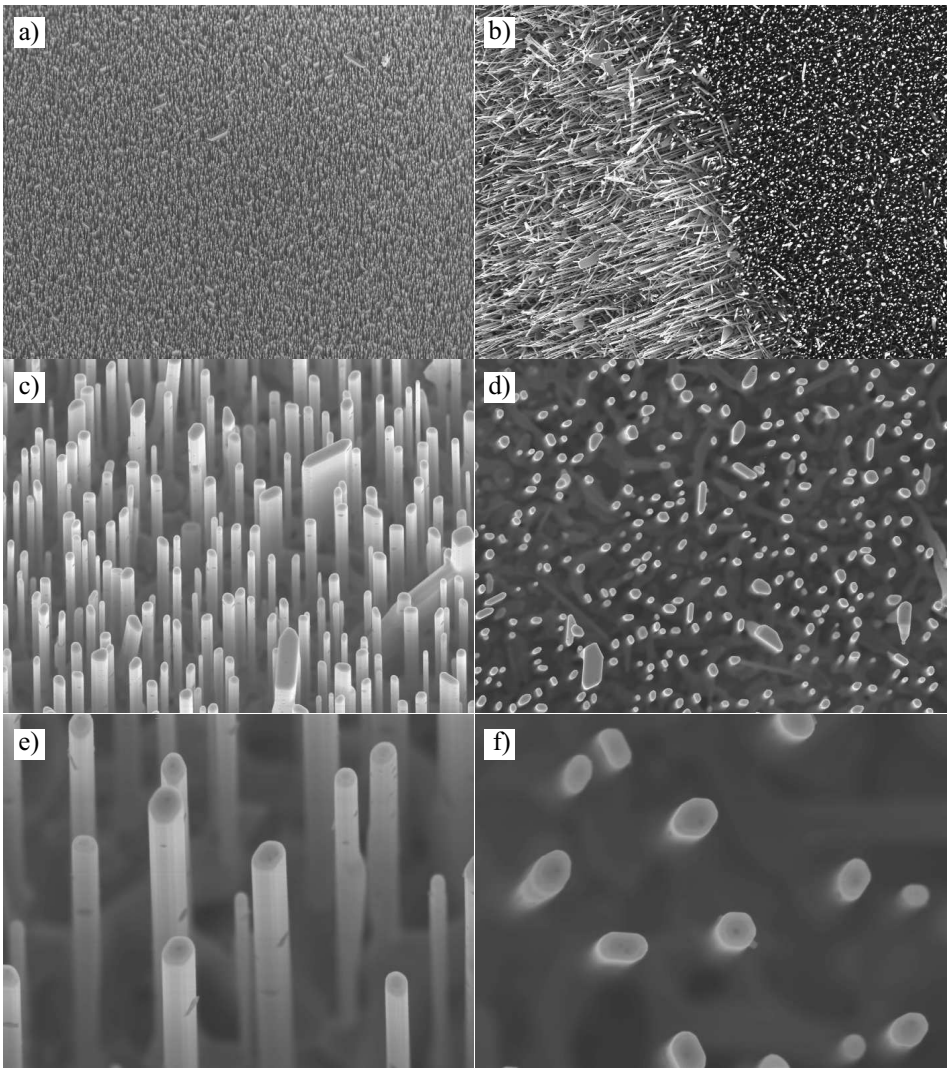

Figure IX.1: SEM images of epitaxially grown ZnO nanowires on a sapphire substrate

a) Overview of the sample. b) Edge of the sample. Note the poor nanowire alignment perpendicular to the sample surface. c) Magnified image of the sample center, with well-aligned nanowires. d) Top view of the sample center, clearly showing the distribution of wire thicknesses. On the sapphire surface lies a thin bulk ZnO layer. e) Detailed image of single nanowires. f) Detailed top view image. The wires are not circular but have the facets of the wurtzite crystal structure.

IX.2.2 Electronic properties

Optical excitation above the band gap (3.37 eV in ZnO at room temperature) in a semiconductor produces electron-hole pairs. Due to the Coulomb attraction between electron and hole, a bound state called an *exciton* can form. The exciton binding energy in ZnO is ~ 60 meV (c.f. at room temperature $k_B T \sim 25$ meV), resulting in stable excitons with a $\sim$ ns lifetime [16]. The exciton Bohr radius r_{eh} is in the range 1.5 - 8 nm, much larger than the lattice spacing, but still much smaller than our typical wire diameters. Therefore, quantum confinement effects do not play a role.

For carrier densities above the Mott density $n_M \sim 5 \times 10^{17}$ cm^{-3}, the density at which the plasma screening length becomes comparable to the exciton Bohr radius, no stable excitons can exist, and an *electron-hole plasma* (EHP) forms [17]. At carrier densities $n_{M'} \sim 10^{19}$ cm^{-3}, more than an order of magnitude above the Mott density, the carriers form a *degenerate electron-hole plasma*. In case of three-photon absorption from an 800-nm pump, experiments and calculations show that the Mott density is reached already at low excitation fluences $\sim$ 10 - 20 mJ/cm^2 [18]. Then, the degenerate EHP is reached at pump fluences $\sim$ 25 - 35 mJ/cm^2. Our experiments are typically performed at fluences above 50 mJ/cm^2, well in the degenerate regime, and therefore at too high carrier densities to investigate exciton-polariton dynamics [5, 9].

IX.3 Experimental results

IX.3.1 Luminescence spectroscopy

Before discussing the time-resolved experiments, we present time-integrated luminescence measurements on the same sample, although not measured simultaneously and at the same position. The nanowires are excited at room temperature by three-photon absorption from 150-fs, 800-nm pump laser pulses. Luminescence spectra are measured for different pump fluences I_0 by a double monochromator and CCD-camera combination. The results are shown in Fig. IX.2 a).

The spectra contain two peaks. First, the broad luminescence peak around 385 nm, attributed to luminescence. This peak shifts for higher pump fluences, because of many-body effects i.e. band gap renormalization largely balanced by degeneration of the carriers [12]. A decrease in peak width at the highest pump fluences in the lasing regime is not observed [19]. However, the distribution of

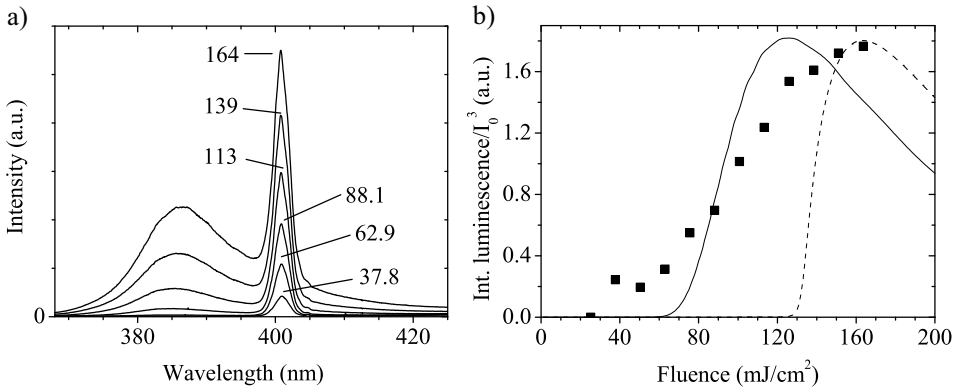

Figure IX.2: Luminescence results
a) Measured nanowire luminescence spectra for pumping at 800 nm at indicated fluences (in mJ/cm^2), in absence of 400-nm probe. Peak at 385 nm is due to luminescence, and peak at 400 nm due to second harmonic generation. b) Squares: integrated luminescence around 385 nm, divided by $I_0{}^3$, as a function of fluence. Lines are calculations according to Eq. (IX.3) using the results from the solution of Eqs. (IX.1) - (IX.2). Dashed line: for a single nanowire diameter, and uniform carrier density. Solid line: for a distribution of nanowire diameters and effective carrier densities.

nanowire thicknesses will broaden the lasing profile and obscure line narrowing effects. Since three-photon absorption is required to excite electrons over the bandgap, the number of carriers is expected to increase as $\propto I_0{}^3$, at least in absence of saturation. In Fig. IX.2 b), the (normalized) integrated luminescence divided by $I_0{}^3$ is shown. Between 40 and 150 mJ/cm^2, the emitted luminescence increases faster than the third power, suggesting that for these fluences radiative decay at the luminescence wavelengths is gaining importance with respect to nonradiative decay channels. Saturation sets in around 150 mJ/cm^2.

The second peak at 400 nm is due to second harmonic generation (SHG) in the nanowires. For the integrated SHG contribution at the sample center $\propto I_0{}^n$ a value for n of 1.57 ± 0.03 was determined, below the (expected) value of two. This suggests significant absorption of 400-nm SHG light in the nanowires for high fluences. This SHG contribution appears in pump-probe experiments as a constant positive background, independent of the delay between the pump and probe pulses.

IX.3.2 Time-resolved pump-probe spectroscopy

Time-resolved pump-probe transmission experiments on the nanowire sample were performed using the reflection-transmission setup described in Ch. II. Transient reflection $\Delta R/R$ is not measured since the reflected intensity was too low to reach an acceptable signal-to-noise ratio. The nanowires are pumped by a 165-μm waist, 800-nm beam via three-photon absorption. The 400-nm probe is focused to 30 μm on the nanowires with a $f = 6$ cm focal distance lens, and is collected after passing the sample with a $f = 6$ cm, 5-cm diameter lens to achieve the largest possible collection angle from the strongly scattering sample. In front of the transmission photodetector, a 10-nm FWHM bandpass filter, centered at the 400-nm probe wavelength, was inserted to reject most of the luminescence at 385 nm.

A selection of the results is shown in Fig. IX.3 a). Signals appear when pumping with fluences $I_0 > 30$ mJ/cm^2, the point at which we also estimate carrier densities $\sim n_{M'}$ at which the EHP becomes degenerate. This supports our assumption that the measured effects originate from a degenerate EHP. The background caused by SHG and residual luminescence is subtracted from the data. Its value as a function of pump fluence is shown in Fig. IX.3 b). The fit of the background data gives $n = 2.0 \pm 0.12$. This value is higher than determined for the SHG peak in the luminescence measurements, probably because not all luminescence is rejected by the bandpass filter.

At $t = 0$, the time that pump and probe arrive at the sample simultaneously, the transmission strongly decreases to approximately -50%, rapidly returning to zero at later times [20]. Echoes of this dip in the signal at 2.6, 5.2, ... ps, correspond to the travel time t_{travel} of the pump light back and forth through the sapphire substrate ($t_{travel} = 2nd_{sample}/c$, with c the speed of light, and $n = 1.78$ the refractive index of sapphire). After about 2 ps, a rapid increase in transmission of up to $+40\%$ is observed. This positive change is followed by a decay with a time constant that strongly depends on pump fluence. The maximum amplitude of the positive signal as a function of pump fluence is plotted in Fig. IX.4 a) and shows a clear threshold behavior. For fluences below 60 mJ/cm^2, the growth of the peak amplitude depends on fluence as roughly $\propto {I_0}^n$ with $n = 6.0 \pm 1.3$ (inset Fig. IX.4 b)). This behavior saturates when increasing the pump fluence to 160 mJ/cm^2. Above 200 mJ/cm^2, the intensity in the center of the Gaussian beam reaches the damage threshold of the nanowires. Permanent damage is probably due to heating of the ZnO to above the melting temperature.

In Fig. IX.4 b), the half-life time $t_{1/2}$ of the enhanced transmission after $t = 2$

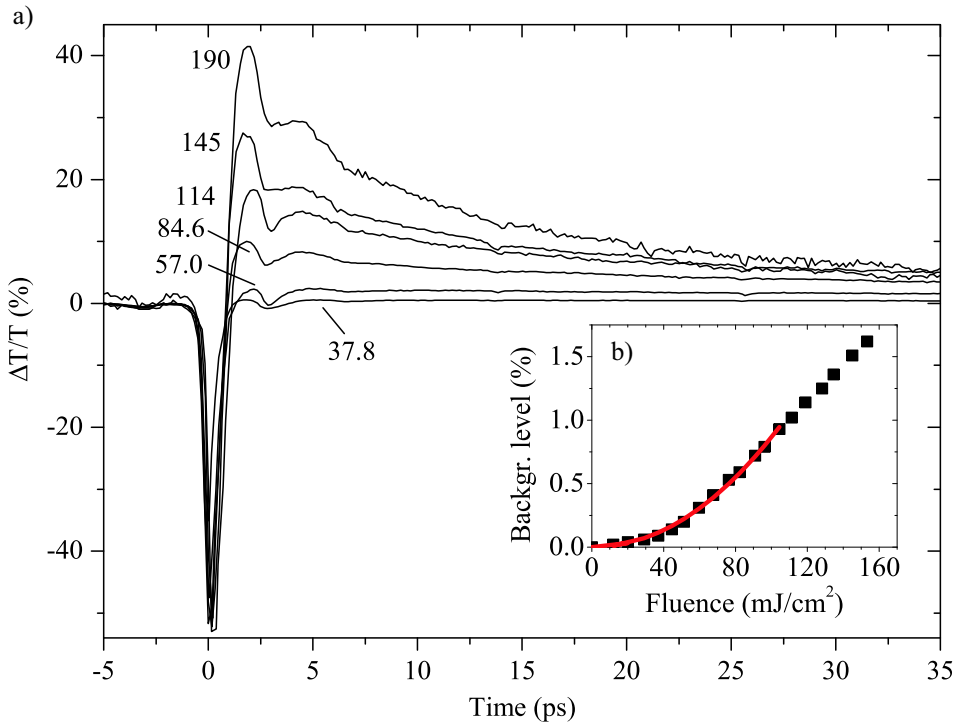

Figure IX.3: Time-resolved transmission results
a) Measurement of the time-dependent 400-nm probe transmission changes, for different 800-nm pump fluences (numbers indicate fluence in mJ/cm^2). b) Background, determined mainly by SHG, subtracted from the data in a), as function of pump fluence. Solid line indicates power law fit to the data for low fluences.

ps is shown. For the lowest fluences, the value of $t_{1/2}$ exceeds 100 ps, consistent with luminescence measurements from literature [16] which suggest up to nanosecond timescales. The decay time becomes shorter for higher pump fluences and saturates above $\pm$150 mJ/cm^2 at a value of 9 ps.

IX.4 Discussion

IX.4.1 Carrier dynamics in ZnO nanowires

In the degenerate EHP regime, direct radiative recombination is the mechanism behind radiative decay [10, 18, 19]. This recombination can be enhanced by stim-

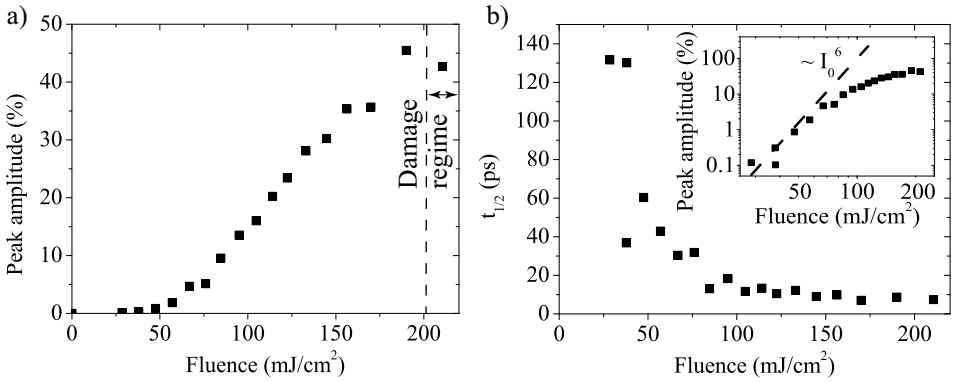

Figure IX.4: Amplitude and decay time as function of fluence
a) Maximum amplitude of $\Delta T/T$ increase in Fig. IX.3 at 2 ps, as a function of pump fluence. b) Half-life time $t_{1/2}$ of increased $\Delta T/T$ signal after $t = 0$, as a function of pump fluence. Inset shows the data of a) in a logarithmic plot, together with a dashed line $\propto {I_0}^6$.

ulated emission due to a large population of low-density optical modes in the nanowire at the luminescence or the probe wavelength. We model these processes by rate equations commonly used for laser processes in semiconductors. Here, we approximate the radiative transition as a single optical mode. With $p(t)$ denoting the optical mode population, and $n(t)$ the carrier density, these equations read

$$\frac{\mathrm{d}n}{\mathrm{d}t} = -(1+p)g(n) - \gamma_{nr} n^2, \tag{IX.1}$$

$$\frac{\mathrm{d}p}{\mathrm{d}t} = \frac{1}{\rho \Delta\nu}(1+p)g(n) - \frac{p}{\tau_p}. \tag{IX.2}$$

The optical mode density is $\rho\Delta\nu = \frac{8\pi\nu^2}{c^3}\Delta\nu = 6.9\times10^{12}\ \mathrm{cm}^{-3}$, with c the velocity of light, ν the mode frequency, and $\Delta\nu$ the gain bandwidth, for which we take the width of the lasing peak for a single ZnO nanowire [21]. The first term on the right side of Eqs. (IX.1) and (IX.2) describes both spontaneous ($\propto n^2$) and stimulated ($\propto n^2 p$) radiative decay, with $g(n)$ the gain. Since two carriers are required for recombination, it is fair to assume that $g(n) = \gamma_r n^2$, with γ_r a proportionality factor [22]. The second term on the right side of Eq. (IX.1) describes losses due to nonradiative decay, also scaling $\propto n^2$ and thus also gaining importance at high carrier densities. However, since the radiative process is stimulated, the radiative decay process potentially becomes the dominant decay mechanism. The second

term on the right side of Eq. (IX.2) describes depopulation of the photon mode, due to outcoupling of light at the nanowire end faces. Since the quality factor of the nanowire "cavity" is very low, τ_p is very short. The gain time for a 10-μm wire is ~ 70 fs, the time required to reach the wire endpoints [10].

In this model, $\Delta T/T$ for $t > 0$ is proportional to the gain $g(n)$ at time t. Then, $\Delta T/T \propto n^2$, the square of the carrier density. Likewise, the integrated (stimulated and spontaneous) luminescence around the maximum at 385 nm equals:

$$I_L = \int_0^\infty (1 + p(t))\gamma_r n(t)^2 \mathrm{d}t. \tag{IX.3}$$

In the following, we numerically evaluate the coupled equations (IX.1) - (IX.2), assuming that a carrier density $n(0) = n_0$ is created instantaneously by the pump at $t = 0$, and make a best fit to the set of $\Delta T/T$ data. The values of γ_r, γ_{nr}, n_0, and an arbitrary scaling factor to convert the calculated quantities to the measured transmission were left as free fit parameters. We assume that $p(0) = p_0 \ll 1$ in all cases and τ_p can be fixed at the value of 70 fs. After fitting the time-resolved traces, we use the determined fluence dependence to calculate the luminescence.

IX.4.2 Comparison to measurements

The carrier dynamics model of Sec. IX.4.1 is first checked against the transmission results. Typical fits according to Eqs. (IX.1) - (IX.2) together with the measured signals are depicted in Fig. IX.5 a) [23]. The already mentioned negative peaks at multiples of 2.7 ps due to subsequent pump reflections (Sec. IX.3) cause deviations between measurement and calculation. Moreover, below a fluence of 130 mJ/cm^2, the measured signal is significantly higher than the calculated ones. The slow variations in the high-fluence measurements are probably due to variations in pump intensity and pointing instabilities (App. A). The latter effects are relatively important in measurements on a chaotic sample like the present one.

The fitted values for the absolute carrier density n_0 are shown in Fig. IX.5 b), together with the saturation curve

$$n_0(I_0) = n_{00}\frac{{I_0}^3}{a + {I_0}^3}, \tag{IX.4}$$

showing good agreement. We compute a value of $n_0 = 1 \times 10^{19}$ cm^{-3} at 35 mJ/cm^2, close to our earlier estimates. In our calculations, the carrier density

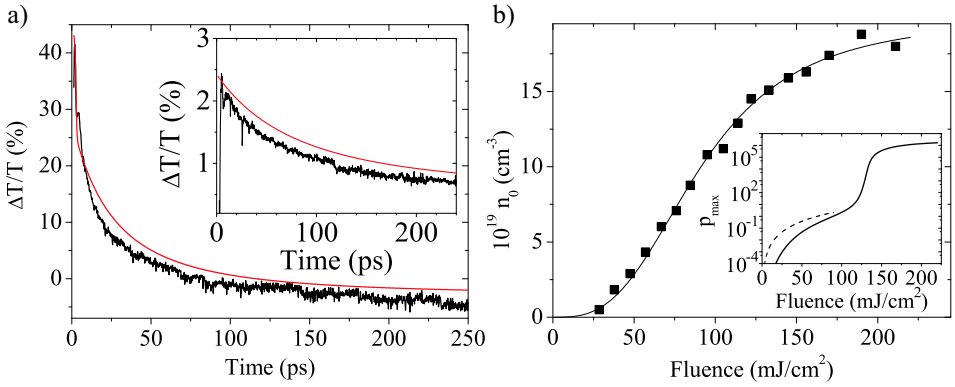

Figure IX.5: Fit results of stimulated carrier decay
a) Measured data for a pump fluence of 190 mJ/cm^2, along with a fit according to the model of Eqs. (IX.1) - (IX.2) (gray line, given a small offset). Inset shows similar data for pump fluence of 57 mJ/cm^2. b) Values of scaled initial carrier density n_0 determined from the fit routine, as a function of pump fluence. Generation of carriers shows clear signs of saturation in this regime. Solid line is a fit along Eq. (IX.4). Inset shows the maximum (solid line) optical mode population p_{max}. Dashed line indicates $\propto {I_0}^3$-dependence.

n_0 starts to saturate significantly around 100 mJ/cm^2, ultimately to a value of $n_S \sim 2 \times 10^{20}$ cm^{-3}. This is much lower than the estimated maximum saturation value $n_{max} \sim 1/2V_0^3 = 1 \times 10^{22}$ cm^{-3} (with V_0 the lattice unit cell volume). Our explanation is, that the calculations assume that n and p are constant over the nanowire cross section. However, for wires with diameter $d < \lambda$, the effective diameter of the optical mode will be much larger than d [24]. In other words, the optical mode will experience an effective carrier density n_{eff} dependent on d, lower than the true carrier density inside the wire. It is very likely that the reason for the deviation between the time-resolved measurement and calculation for fluences < 130 mJ/cm^2 directly after pumping is caused by the fact that stimulated emission starts at lower fluences for thicker wires in the distribution. Another possibility is that less free carriers are available for laser processes in nanowires with a large surface-to-volume ratio, for example by binding of carriers to surface O-defects. Recent experiments on a sample with thicker nanowires showed more than an order of magnitude larger peak heights than in the current experiments [18], demonstrating the importance of the nanowire diameter d [25].

The calculated maximum population of the optical mode p_{max} is plotted versus pump fluence in the inset of Fig. IX.5 b). We can discern three regimes. For

fluences < 50 mJ/cm^2, $p \ll 1$. The p-population is a small fraction of n, and p_{max} increases proportional to ${I_0}^3$. For fluences $50 < I_0 < 120$ mJ/cm^2, $p_{max} \sim 1$ and stimulated emission becomes operative. From the fit routine, we find that $\gamma_r \sim 10^{-4}\gamma_{nr}$ [23]. Above 120 mJ/cm^2 the radiative decay becomes boosted since $p_{max}\gamma_r > \gamma_{nr}$ shortly after the pump pulse. This also results in a stronger decay of the carrier population, as can be seen for $t < 3$ ps in Fig. IX.5 a). The growth of p_{max} in the amplifying regime is limited by the saturation of n_0 shown in Fig. IX.5 b). The population number p depends strongly on the gain time τ_p, which is proportional to the wire length. Experiments using longer wires [18, 26] have demonstrated strong lasing ($p\gamma_r > \gamma_{nr}$) at much lower fluences than in the current experiments.

Next, we have used the calculated $p(t)$ and $n(t)$ to determine the integrated luminescence Eq. (IX.3) as a function of fluence. The result is shown as a dashed line in Fig. IX.2 b). Since p shows a sharp transition around 120 mJ/cm^2, the luminescence follows this sharp increase, which is apparently not found in the measurements. The nanowire distribution, however, is bound to broaden the sharp edge. As a first approximation, we may assume that the effective carrier density $n_{eff} \sim (d/\lambda)^2$. As an example, we have calculated the fluence-dependent luminescence for a Gaussian distribution of wires with an average thickness of 130 nm, and a standard deviation of 40 nm, the solid line depicted in the same figure. Under these assumptions, the calculated profile nicely approaches the measured one. Additional broadening will be produced by a distribution of photon modes, each with a specific gain profile. Deviations can further be caused by the $\pm 10\%$ accuracy in determination of I_0, allowing for slightly different fluence gauges for separate measurements, and by the fact that pumping occurred at different positions on the sample in the luminescence and the pump-probe measurements.

IX.5 Conclusions

In this chapter, a sample with epitaxially grown, chaotically distributed ZnO nanowires at room temperature was pumped via three-photon absorption from an 800-nm beam to create a degenerate electron-hole plasma. Both time-integrated luminescence and ultrafast pump-probe transmission of a 400-nm probe after pumping were measured as a function of pump fluence I_0. The integrated luminescence shows an increase above $\propto {I_0}^3$ and saturates for the highest fluences.

In time-resolved measurements an increased transmission signal of up to $+40\%$

is observed after ~ 2 ps due to stimulated emission at the probe wavelength. The decay time of this signal decreases strongly with fluence, down to ~ 10 ps. These effects can be explained by stimulated emission processes, and are described accurately by coupled rate equations for the carrier density and optical mode population.

IX.6 Prospects

The experiments and theoretical investigations in this chapter are only a first step in a full analysis of ultrafast dynamics in ZnO nanowires. The samples used in the presented experiments consist of nanowires of equal length but with a wide distribution of diameters. This results in a highly scattering sample with strongly varying optoelectronic properties. Improvements in nanowire synthesis leading to higher ordering and a monodisperse size distribution allow resolution of the wire lasing properties with more precision. In addition the possibility arises in highly ordered samples to excite and observe coherence effects between individual nanowires [6].

To reduce sensitivity to ensemble effects, probing can best be performed on single nanowires. A broadband tunable probe beam is needed to characterize the wavelength dependence of ultrafast carrier dynamics in nanowires [26]. The hypothesis of carrier stimulation to the probe wavelength could be tested by simultaneous time-resolved luminescence measurements by a CCD-spectrometer and transmission of the 400-nm probe by a photodetector, as a function of delay time between pump and probe [10]. The stimulated emission at 400 nm should be accompanied by a suppression of luminescence at shorter wavelengths (Fig. IX.2 a)). Very challenging would be to perform local time-resolved probing. For long wires, one can focus on a section of the wire, as was already performed in semi-CW mode [21], and probe position-dependent dynamics.

Finally, returning to the main subject of this thesis, these one-dimensional structures allow for a new class of low-dimensional acoustic wave propagation experiments [27, 28]. By exciting far above the bandgap, a pressure gradient will be generated, analogously to Ch. VIII. The resulting strain propagation in the nanowire long axis direction can subsequently be monitored by time-resolved Brillouin scattering [29]. Using knowledge from Chs. III and IV, large amplitude acoustic pulses can be generated in a planar geometry and sent through ZnO nanowires, sandwiched between two substrates. This way, acoustic waveguiding

effects become experimentally accessible. Quite interestingly, acoustic pulses can be used to modify the electronic properties on ultrafast timescales, analogous to the ZnSe QW experiments in Ch. VII. For acoustic waves of the order of the wire length, strong shifting of ZnO nanowire emission wavelengths can be expected [30], while acoustic waves much smaller than the nanowire length allow for local manipulation.

References

1. D. Appell. Nanotechnology: Wired for success. *Nature*, 419:553, 2002.
2. J. Wang, M.S. Gudiksen, X. Duan, Y. Cui, and C.M. Lieber. Highly polarized photoluminescence and photodetection from single indium phosphide nanowires. *Science*, 293:1455, 2001.
3. M.S. Gudiksen, L.J. Lauhon, J. Wang, D.C. Smith, and C.M. Lieber. Growth of nanowire superlattice structures for nanoscale photonics and electronics. *Nature*, 415:617, 2002.
4. M. Law, L.E. Greene, J.C. Johnson, R. Saykally, and P. Yang. Nanowire dye-sensitized solar cells. *Nature Materials*, 455-459:452, 2005.
5. M.H. Huang, S. Mao, H. Feick, H. Yan, Y. Wu, H. Kind, E. Weber, R. Russo, and P. Yang. Room-temperature ultraviolet nanowire nanolasers. *Science*, 292:1897, 2001.
6. H. Zhou, M. Wissinger, J. Fallert, R. Hauschild, F. Stelzl, C. Klingshirn, and H. Kalt. Ordered, uniform-sized ZnO nanolaser arrays. *Appl. Phys. Lett.*, 91:181112, 2007.
7. L. Tong, R. Gattass, J. Ashcom, S. He, J. Lou, M. Shen, I. Maxwell, and E. Mazur. Subwavelength-diameter silica wires for low-loss optical wave guiding. *Nature*, 426:816, 2003.
8. D.D.D. Ma, C.S. Lee, F.C.K. Au, S.Y. Tong, and S.T. Lee. Small-diameter silicon nanowire surfaces. *Science*, 299:1874, 2003.
9. L.K. van Vugt, S. Rühle, P. Ravindran, H.C. Gerritsen, L. Kuipers, and D. Vanmaekelbergh. Exciton polaritons confined in a ZnO nanowire cavity. *Phys. Rev. Lett.*, 97(14):147401, 2006.
10. J.K. Song, J.M. Szarko, S.R. Leone, S. Li, and Y. Zhao. Ultrafast wavelength-dependent lasing-time dynamics in single ZnO nanotetrapod and nanowire lasers. *J. Phys. Chem. B.*, 109:15749, 2005.
11. J.C. Johnson, K.P. Knutsen, H. Yan, M. Law, Y. Zhang, P. Yang, and R.J. Saykally. Ultrafast carrier dynamics in single ZnO nanowire and nanoribbon lasers. *Nano Lett.*, 4:197, 2004.
12. C.F. Klingshirn. *Semiconductor Optics*. Springer, 3rd edition, 2007.
13. R. Prasanth, L.K. van Vugt, D.A.M. Vanmaekelbergh, and H.C. Gerritsen. Res-

onance enhancement of optical second harmonic generation in a ZnO nanowire. *Appl. Phys. Lett.*, 88:181501, 2006.
14. L.K. van Vugt. *Optical properties of semiconducting nanowires*. PhD thesis, Utrecht University, 2007.
15. S. Rühle, L.K. van Vugt, H.-Y. Li, N.A. Keizer, L. Kuipers, and D. Vanmaekelbergh. Nature of sub-band gap lumineascent eigenmodes in a ZnO nanowire. *Nano Lett.*, 8(1):119, 2007.
16. S. Hong, T. Joo, W.I. Park, Y.H. Jun, and G.-C. Yi. Time-resolved photoluminescence of the size-controlled ZnO nanorods. *Appl. Phys. Lett.*, 83:4157, 2003.
17. C. Klingshirn, R. Hauschild, J. Fallert, and H. Kalt. Room-temperature stimulated emission of ZnO: Alternatives to excitonic lasing. *Phys. Rev. B*, 75(11):115203, 2007.
18. Experiments and calculations of M.A.M. Versteegh. *To be published*.
19. J.M. Szarko, J.K. Song, C.W. Blackledge, I. Swart, S.R. Leone, S. Li, and Y. Zhao. Optical injection probing of single zno tetrapod lasers. *Chem. Phys. Lett.*, 404:171, 2004.
20. Recently, it was proven that this dip is due to multi-photon absorption from pump and probe in the ZnO nanowire [18, 31].
21. L.K. van Vugt, S. Ruhle, and D. Vanmaekelbergh. Phase-correlated nondirectional laser emission from the end facets of a ZnO nanowire. *Nano Lett.*, 6(12):2707, 2006.
22. If reabsorption needs to be taken into account, then one expects that the gain is $\propto n$ [12, 32]. We find that it is not possible to describe all traces reliably with such a gain, proving that reabsorption is of minor importance in small nanowires, unlike in bulk semiconductor lasers.
23. The determined values for the (constant) free fit parameters γ_r and γ_{nr} in Eqs. (IX.1) - (IX.2) are $5.2 \pm 0.3 \times 10^{-27}$ cm^3 ps^{-1} and $1.5 \pm 0.1 \times 10^{-22}$ cm^3 ps^{-1}, respectively. The free multiplication factor was found to be $2.3 \pm 0.1 \times 10^{-13}$. When not considering the times at which echoes of the sharp dip at $t = 0$ disturb the measurement, $\chi^2 < 1$ for all measurements.
24. L. Tong, J. Lou, and E. Mazur. Single-mode guiding properties of subwavelength-diameter silica and silicon wire waveguides. *Opt. Expr.*, 12:1025, 2004.
25. Further evidence that higher carrier densities are excited comes from the determined damage threshold. When 2×10^{20} cm^{-3} carriers are excited, we calculate a temperature rise of the ZnO of only 120 K. Since the melting temperature is roughly 2000 K, the carrier density can be expected to be at least an order of magnitude higher.
26. B. Brenny. Pump-probe spectroscopy of ZnO nanowires. Bachelor's thesis. Utrecht University, 2008.
27. S.N. Jerebtsov, A.A. Kolomenskii, J. Liu, H. Zhang, Z. Ye, Z. Luo, W. Wu, G.G. Paulus, and H.A. Schuessler. Laser-excited acoustic oscillations in silver and bismuth nanowires. *Phys. Rev. B.*, 76:184301, 2007.

28. G.M. Sando, A.D. Berry, and J.C. Owrutsky. Ultrafast studies of gold, nickel, and palladium nanorods. *J. Chem. Phys.*, 127:074705, 2007.
29. P. Kušar and D. Mihajlovic. Sound propagation in a highly damped $Mo_6S_3I_6$ nanowire network measured by femtosecond pump-probe spectroscopy. *J. Appl. Phys.*, 102:013510, 2007.
30. W. Shan, W. Walukiewicz, J.W. Ager III, K.M. Yu, Y. Zhang, S.S. Mao, R. Kling, C. Kirchner, and A. Waag. Pressure-dependent photoluminescence study of ZnO nanowires. *Appl. Phys. Lett.*, 86:153117, 2005.
31. W. Ensing, R. van der Wel and B. Zegers. Enhanced absorption and transmission in ZnO nanowires excited by ultrashort laser pulses. Bachelor's thesis. Utrecht University, 2008.
32. G.P. Agrawal and G.R. Gray. Intensity and phase noise in microcavity surface-emitting semiconductor lasers. *Appl. Phys. Lett.*, 59(4):399, 1991.

Appendix A

Setup electronics and noise characteristics

A.1 Introduction

In standard, typically 80-MHz repetition rate pump-probe experiments, where small variations on a large reflection or transmission background signal are to be detected, improvement of the signal-to-noise ratio is achieved by lock-in amplification at the modulation frequency in the MHz range of the pump signal by an acousto-optic modulator [1]. This leads to a sensitivity for relative changes as good as $10^{-7}/\sqrt{\text{Hz}}$. A recently developed novel technique makes use of two high-repetition laser systems, where the $\sim$ 1-GHz repetition rates are slightly different but coupled, so that with fast electronics and an integration time of $\sim$ 1 second a resolution of 10^{-9} can be reached (the shot-noise limit of the photodiode), at the same time eliminating the need for an optical delay stage [2].

At 1 kHz and lower, lock-in techniques are less efficient since the repetition frequency is very low; in this frequency range, one encounters a large amount of spurious effects (e.g. mechanical vibrations in the table, air turbulence, harmonics of 50-Hz AC power connections). In low-repetition rate experiments such as the ones described in this thesis, one additionally suffers from the fact that less pulses are available for signal averaging.

At this stage it is important to realize that the main reason for 'statistical' detection through lock-in techniques is, that not each pulse in a high-repetition rate can be measured separately, since digitizing electronics at present cannot go below $\sim 1\mu$s integration times while maintaining a high sensitivity. In 1-kHz experiments, one gains the opportunity to decrease the noise not by statistics, but by correcting on a single-shot basis. To this end, some elements specific to this method are required: sensitive timing, a fast digital voltmeter to read out the photodiodes, and efficient data collection. In this appendix, we discuss the developed detection scheme, and its ultimate sensitivity.

A.2 Setup characteristics

A.2.1 Measurement control

Fig. A.1 a) shows the electronics scheme. We use standard Hamamatsu silicon photodiodes (S2386-5K). The voltage on each photodiode is read out by separate Agilent 3458A multimeters. Timing and delay of pulses is done by a Stanford DG535 gate and delay generator. In our setup, we have the possibility to use two delay lines, the Newport ILS250CC fast scanning delay line, and a relatively slow but highly accurate home-built delay line connected to the serial port of the computer. Flow control and overall data acquisition are monitored by a Labview program, able to communicate through GPIB channels and the serial port.

A.2.2 Timing

In Fig. A.1 b), traces 1. - 4., the timing of measurements in our setup is described. A "Hurricane" laser pulse (1.) hits a photodiode in the pump path, behind the chopper (2.), and generates a trigger pulse which is sent to the input of the DG535 delay generator. This trigger signal is delayed by ~ 1 ms (the period between two subsequent laser pulses), and then sent to the multimeters (3.). The multimeter internal clock determines the integration time to obtain the signal voltage V_S on the photodiodes, and the times to start and stop the background measurement to obtain the background voltage V_B (4.). The critical timing is therefore determined by the multimeters, with a jitter ≤ 50 ns [3].

A.2.3 Measurement speed

An overview of the effective scanning rate for a given number of measurements, compared to the initial setup discussed in earlier publications [4, 5] is given in Fig. A.2 b). Great improvements have been made.

When aiming for efficient measurements, one wants to limit data reading and processing time. The reading rate across the GPIB bus was increased by going from single real (SREAL) format to the so-called double-integer (DINT) format, allowing in principle a data transfer speed of 50000 measurements per second [3] (speed of the used GPIB-card: $>$ 1Mbit/s). Multiplication by a scaling factor, which can readily be queried from the multimeter, is required to arrive at the absolute voltages (this step might be skipped, since we are only interested in relative changes, Ch. II). In our case, the net transfer across the bus was roughly 6000

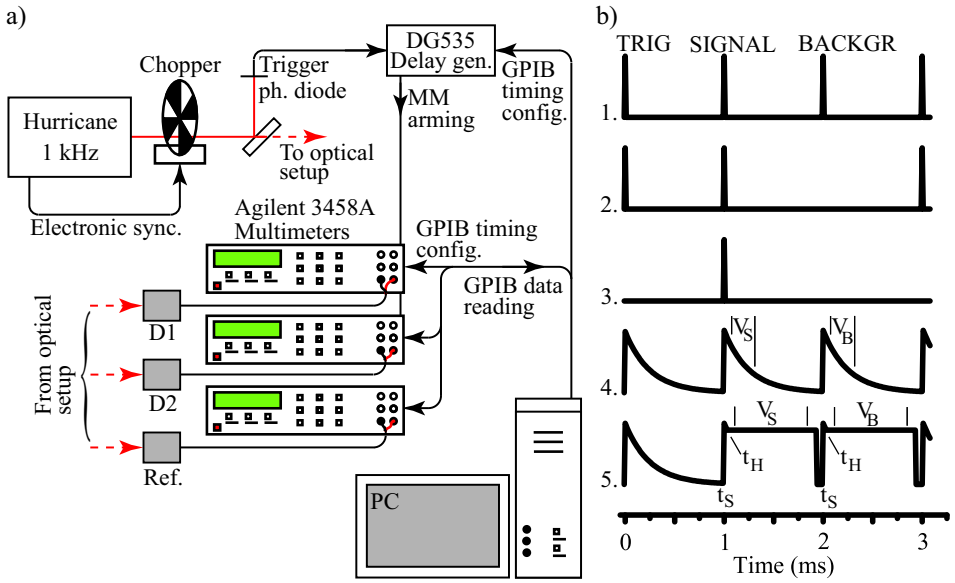

Figure A.1: Properties of the detection scheme
a) Electronics scheme. Connections that are not denoted as GPIB are BNC cables. Cables from photodiodes to the multimeters are shielded. b) Timing configurations. 1. "Hurricane" laser pulses, and their purpose in the measurement. 2. *Idem*, after the chopper. The pulses at 0, 3, ... ms trigger the delay generator. 3. Electronic pulse emitted to the multimeters by the delay generator. 4. Photodiode signals, and integrated time intervals as determined by the multimeter internal clock. 5. Sample-and-hold timing configuration. t_S and t_H are sample time and hold time, respectively, and are determined by the delay generator. Integration interval of the multimeters in this case is also indicated.

measurements per second. This might have to do with subsequently reading multiple 3458A's. In any case, this increased the data transfer rate by roughly a factor of 4, as compared to the previously used SREAL format.

A second improvement was the replacement of the serial delay line by a GPIB-controlled one. Where the full movement cycle (sending the movement command, waiting for the delay line to reach the desired position, waiting for the arrival command, waiting for delay stage stabilization) took about 2.5 seconds for the old delay line and 0.1 mm displacement, the Newport ILS250CC does the same in only 0.13 seconds. This step especially makes measurements with a low number of averages (< 500) efficient.

Finally, shorter measurement acquisition times were achieved by increasing

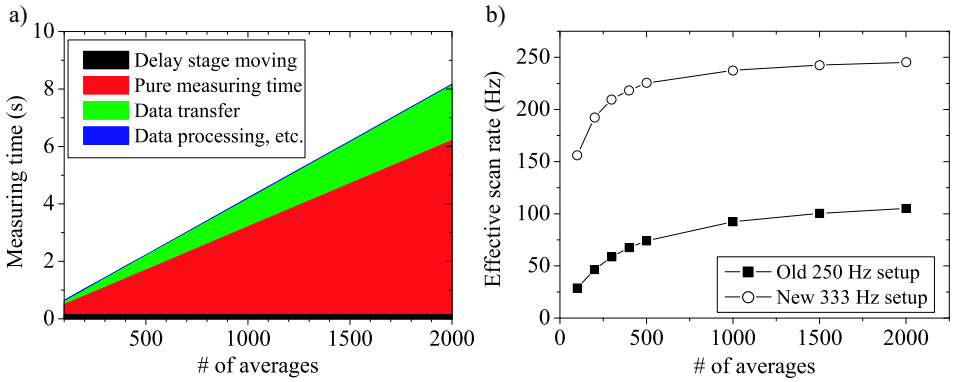

Figure A.2: Detection setup performance
a) Time demand for operations in performing measurements, for a range of averages. b) Effective scan rates, at the start of this research (squares) and at present (open circles).

the repetition rate from 250 Hz to 333 Hz, without influencing the measurement procedure itself. The pump beam is chopped at 333 Hz, giving a three-pulse sequence: the first to trigger the detection sequence, the second to induce an effect on the sample (the measurement with pump, 'signal'), and the third to perform the measurement without pump ('background'), see Fig. A.1 b) (trace 1.).

The time demand for each of these steps is plotted in Fig. A.2 a). The total gain in efficiency can be seen in Fig. A.2 b). A reduction in measurement time of a factor 3 to 6 is reached. We can currently operate the setup at an effective scan rate of around 220 averages per second.

A.3 Noise characteristics

A.3.1 Experimentally determined noise levels

When discussing the experimental noise levels, we first note that the sensitivities mentioned here can only be reached when there is optimal correlation between the probe detector(s) and the reference. There can be no (partly) closed diaphragms in between and the entire beams should be focused on the detectors, so that there are no edge effects.

In the current setup, if no corrections are made, the noise per measured point is roughly 1%. This is of the same order as specified by the pulse-to-pulse intensity variation of the Hurricane laser system [6]. This is by far too large to measure

expected signals on the scale of 10^{-4}, even after a significant number of averages.

For each measured point, the signal and background measurements are normalized by simultaneous measurements at the reference diode. Subsequently, the normalized background measurement are subtracted from the normalized signal measurement and divided by the normalized background to obtain Δ, the differential signal, being reflection (Chs. IV and VII), transmission (Chs. VII and IX), or one of the components of an interferometric signal (Chs. III - V and VIII):

$$\Delta = \frac{\frac{V_{sig,probe}}{V_{sig,ref}} - \frac{V_{bg,probe}}{V_{bg,ref}}}{\frac{V_{bg,probe}}{V_{bg,ref}}} \tag{A.1}$$

$$= \frac{V_{sig,probe} \times V_{bg,ref}}{V_{sig,ref} \times V_{bg,probe}} - 1. \tag{A.2}$$

Close inspection shows, that a double correction takes place [7]. The division of two simultaneous measurements on different multimeters eliminates laser intensity noise. Division of two (signal and background) measurements from the same multimeter eliminates sources specific to this detection channel, which mainly consist of trigger and timing effects in the multimeter, and photodiode characteristics. When looking at the two correction paths, we find that each step is responsible for more than a factor of 5 decrease in noise level. In total, the experimentally found noise level is reduced from 1% per shot to about 4×10^{-4}, or 2×10^{-5} for an integration time of one second. Stated otherwise, if the voltage on a photodiode is typically around 100 mV, we are able to observe effects of around 2 μV for a one-second integration time. This sensitivity is of the same order as can be obtained with a standard low-frequency lock-in, as known from experiments that were also performed in our group [8, 9]. The ultimate sensitivity of our setup is limited by the number of measurements that can be stored in the multimeter memory (~ 2000), and leads to $9 \times 10^{-6} / \sqrt{\text{Hz}}$ over a nine-second integration time. Of course, in this case, one also has to be concerned with changes in the setup over the long collection time of the measurement.

An important problem are the slow variations in pump intensity. The amplifier is an unstable laser source, giving rise to variations on a one-second timescale of the order of 1%, either caused by variations in overall intensity, or by beam pointing varying over time and changing the local intensity at the probe spot. This leads to variations in signal amplitude of the order of 10^{-2} of the total signal per measured point, and makes this method less efficient for detection of small signals

on a large background, as for example measurements shown in Ch. III.

We will now discuss various sources of noise; all contributions are collected in Table A.1. Here, one can observe that for large signal amplitudes, indeed the pump intensity noise limits the detection. Performing a large number of averages is therefore only useful for low signals (typically below 10^{-3}).

Noise source	Typical value per shot
Experimentally found noise limit	2.7×10^{-4}
Photodiode shot noise	6×10^{-5}
Multimeter statistical noise (voltage scale 1 V)	2×10^{-5}
Multimeter trigger timing jitter	$\leq 4 \times 10^{-4}$
Sample-and-hold (expected) (voltage scale 1 V)	3×10^{-5}
Pump intensity fluctuations (for a signal of 5×10^{-3})	5×10^{-5}

Table A.1: Overview of noise sources
These values are valid for a signal derived from two independent multimeters, and an integration time of 100 μs, except for the sample-and-hold sensitivity, where we used an integration time of 800 μs. Pump intensity fluctuations occur for an arbitrary number of averages. The jitter due to timing accuracy in the multimeter is probably the limiting noise source in the current setup.

A.3.2 Photodiode shot noise

The shot noise level of a single photodiode can be calculated as [10]

$$\frac{\sigma_I}{I} = \frac{2e\Delta f}{\alpha P}. \tag{A.3}$$

Here, α is the photosensitivity of the diode (0.55 A/W for a Si photodiode at 800 nm), and the power P around 0.6 μW near saturation. Δf is the detection bandwidth, which can, for a measurement time of 1 second and an integration time of 100 μs every millisecond, be estimated at $1/(.1 \times 1\ \text{s}) = 10$ Hz. For a measurement near saturation of the photodiodes and the former parameters, an ultimate noise level is calculated of 3×10^{-6} per second, or 4×10^{-5} per shot. For two or three multimeter measurements, one should multiply this number with $\sqrt{2}$ or $\sqrt{3}$, respectively.

A.3.3 Multimeter statistical noise contributions

Besides the effects due to timing jitter, the multimeters also show intrinsic, statistical noise errors [3]. These are mainly determined by the limited integration time. From the specifications, we estimate these errors around 16 ppm, or 1.6×10^{-5}. It should be noted here that the multimeters have additional absolute error sources of the order of 10^{-5}, arising from temperature effects and loss of calibration accuracy over time. In the present experiments, these effects are not important due to the fact that we are only interested in relative changes.

A.3.4 Multimeter timing jitter

Since the multimeters can only achieve a high degree of accuracy when integrating signal over a sufficiently long period of time, a long period with stable voltage on the input channel of the multimeters is required. But at the same time, the voltage should be gone after a millisecond, when the next pulse arrives at the diode. In the current version of the setup [5], this was solved by building a RC-circuit. Knowing the capacitance of photodiode and cabling of $\sim$1000 pF, and putting it in parallel with a 150 kΩ resistor, yields a signal decay (RC-) time τ_{RC} of roughly 150 μs, enough to go virtually to zero within a period of one millisecond. The peak voltage reached before photodiode saturation and nonlinear behavior occur is at most 375 mV.

The voltage changes significantly during the integration time of 100 μs, so that limited timing accuracy of the multimeters becomes an origin of noise. We can estimate the magnitude of this source in the following way. Suppose that the voltage drops exponentially during the measurement:

$$V(t) = V_0 \exp -t/\tau_{RC}. \tag{A.4}$$

Assuming that the measurement starts at some time $t = 0$, the voltage $\bar{V}$ determined by the multimeters is then

$$\bar{V} = \frac{1}{t}\int_0^{t'} V_0 \exp\frac{-t}{\tau_{RC}} \mathrm{d}t = V_0 \frac{\tau_{RC}}{t'}\left(1 - \exp\left(\frac{-t'}{\tau_{RC}}\right)\right). \tag{A.5}$$

One can estimate the voltage noise per pulse by calculating the same integration with integration limit variations $\pm\Delta t$, giving $\bar{V}\exp\left(\frac{\pm\Delta t}{\tau_{RC}}\right)$, which, for $\Delta t \ll \tau_{RC}$, is approximately $\bar{V}\frac{\Delta t}{\tau_{RC}}$. With $\Delta t \sim 50$ ns, and $\tau_{RC} \sim 150$ μs, this gives a relative

noise of 3×10^{-4} per shot, and per individual multimeter. When comparing to the experimental noise limit, i.e. the measurements presented in this thesis, one finds that the reported noise is of the order of the effect we describe here.

A.4 Sample-and-hold setup

The previous analysis of noise sources shows that the current noise limit is determined by the multimeter timing accuracy. One can imagine that a sample-and-hold strategy, by which the photodiode voltage (charge) is kept constant during the multimeter integration time, and the diode is unloaded after the measurement but before the next pulse, will give an even more sensitive detection, at least for low signal amplitudes when pump intensity noise is not limiting. This is of course true only if this system can be accurately timed by letting the critical timing be performed by the DG535, with its sub-ns jitter, but more importantly, if it does not introduce any additional noise.

Currently, we are building such a sample-and-hold timing circuit. The new timing configuration is depicted in Fig. A.1 b), trace 5. Central in this circuit is the Analog Devices AD781. The four independent channels on the DG535 are used to alternately switch it to its sample state at time t_S and its hold state at time t_H (see Fig. A.1 b)). Sampling starts before the arrival of the probe pulse at the photodiode (to unload the charge induced by the previous pulse), and stops and is switched to hold at the time where the photodiode signal is approximately largest, and only slowly varying. The multimeters start measuring after the voltage is fixed by the sample-and-hold circuit, with a programmable delay. Since the settling time of the circuit is around 1 ns, the intrinsic delay of the multimeter response to an external trigger [3] is by far enough to stabilize the voltage before starting the measurement.

Because the integration time will be longer, the photodiode shot noise will also decrease, leading to an expected 3×10^{-5} per shot; almost an order of magnitude lower than the current limit. We were unfortunately not able to obtain first results before finalizing this thesis.

A.5 Conclusions

We have discussed the scheme of our 1-kHz pump-probe setup, correcting noise on a shot-to-shot basis. This setup can reach an effective scan rate of around 220

Hz. The sensitivity per average of 2.7×10^{-4} is equivalent to around 1.8×10^{-5} $1/\sqrt{\text{Hz}}$. Signals of the order of 10^{-3} can be excited without being limited by the 1% pump intensity fluctuations. This is a factor of 100 larger than typical results for an 80-MHz laser system. The noise level of 10^{-7} $1/\sqrt{\text{Hz}}$ for the latter, indicates that the signal-to-noise level of this low-repetition rate setup is of the same order as that of conventional high-repetition rate pump-probe experiments. The sensitivity is equivalent to low-frequency lock-in, with the outlook of beating it by integrating the sample-and-hold electronics.

References

1. H.-N. Lin, H.J. Maris, L.B. Freund, K.Y. Lee, H. Luhn, and D.P. Kern. Study of vibrational modes of gold nanostructures by picosecond ultrasonics. *J. Appl. Phys.*, 73(1):37, 1993.
2. A. Bartels, R. Cerna, C. Kistner, A. Thoma, F. Hudert, C. Janke, and T. Dekorsy. Ultrafast time-domain spectroscopy based on high-speed asynchronous optical sampling. *Rev. Sci. Instr.*, 78(3):035107, 2007.
3. Agilent Technologies. *3458A Multimeter user's guide*, 2000.
4. O.L. Muskens. *High-amplitude, ultrashort strain solitons in solids*. PhD thesis, Utrecht University, 2004.
5. E.W. Hesselink. Pump-probe experiments. Master's thesis, Utrecht University, 2005.
6. Spectra Physics. *Hurricane user's manual*, 2000.
7. G.J.A. Vriens. Pump-probe measurements on strain waves. Master's thesis, Utrecht University, 2005.
8. X. Shan, X. Zhang, D.A. Mazurenko, A. van Blaaderen, J.I. Dijkhuis, F. Hudert, and T. Dekorsy. Acoustic vibrations in nanosized gold-shell particles. *Jour. Phys.: Conf. Ser.*, 92:012035, 2007.
9. D. Turchinovich and J.I. Dijkhuis. Performance of combined $\langle 100 \rangle - \langle 110 \rangle$ ZnTe crystals in an amplified THz time-domain spectrometer. *Opt. Comm.*, 270:96, 2007.
10. T. Tachizaki, T. Muroya, O. Matsuda, Y. Sugawara, D.H. Hurley, and O.B. Wright. Scanning ultrafast Sagnac interferometry for imaging two-dimensional surface wave propagation. *Rev. Sci. Instr.*, 77(4):043713, 2006.

Appendix B

Autocorrelation and laser pulse characterization

B.1 Introduction

In ultrafast experiments it is important to have information about and control over the laser pulse lengths. The "Hurricane" laser system, as used in our experiments, has a tunable compression mechanism for output pulse length optimization, but one requires knowledge on what this length is exactly, and also how it changes (stretches) in the remainder of the setup. This is a consequence of dispersion due to transmission through glass elements in the setups presented in Ch. II.

Most pulse length measurement methods use autocorrelation, i.e. the interaction of the pulse with itself, either in collinear (usually interferometric) [1, 2] or non-collinear (second harmonic generation) [3, 4] geometry. For obtaining both temporal and spectral information, commercial systems are nowadays available [5]. For our purpose, where the pulse shape is expected to be roughly Gaussian or sech^2, obtaining only the temporal information suffices.

In this appendix, we briefly discuss the autocorrelator used to determine the pulse length, and the specific results for the experiments presented in this thesis.

B.2 Results

The setup is based on a non-collinear, second harmonic generation technique, and is sketched in Fig B.1 a). The 800-nm pulses are split, and the two parts are focused in the vertical direction by a cylindrical lens on a (KDP) frequency doubling crystal under an angle 2φ (the dispersion due to the splitter can be neglected for pulses longer than 20 fs). One of the arms is of variable length. When phase matching, and temporal and spatial pulse overlap conditions are fulfilled [3, 4], there is not only 400-nm generation in the beam directions, but also at the half angle between both, see Fig. B.1 b). For the present pulse intensities, the resulting

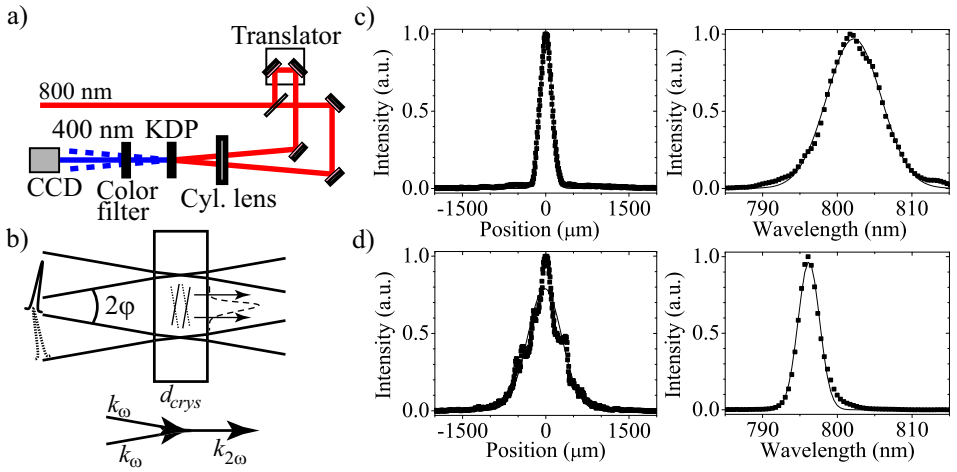

Figure B.1: Autocorrelator operation
a) Overview of the setup. b) Sketch of the geometry in the KDP frequency doubling crystal. Upper part shows the beams crossing in the KDP, and the fact that it is the pulse length that determines the width of the autocorrelation signal. Lower part illustrates phase matching conditions. c) - d) Test measurement results. c) Autocorrelation trace (left) and corresponding spectrum (right) for a compression-optimized pulse. d) Like c), but now for the beam with a 3-nm FWHM interference filter centered at 794.7 nm placed in it. Solid lines are fits to the data, assuming a Gaussian beam shape.

signal is strong enough to capture with a standard line array CCD.

Under the conditions specified in the literature, one can make a reliable determination of the pulse length. In our autocorrelator, with beam waist $w_{beam} \sim 2.5$ mm, $2\varphi \sim 5°$, and a KDP thickness $d_{cryst} \sim 1$ mm and size ~ 1 cm, pulse lengths can be measured from ~ 50 fs up to ~ 500 fs, where eventually the beam size becomes limiting.

The pulse length (FWHM) is given by

$$\delta t = \frac{k\delta x \sin\varphi}{c}, \tag{B.1}$$

with c the speed of light, δx the measured (spatial) width on the CCD, and k a numerical factor, which is $\sqrt{2}$ for Gaussian pulses, and ~ 1.3 for sech^2 pulses. In our calculations, we have further corrected for the finite beam size effects by multiplying the obtained δt by a factor $(1 + (\delta x / w_{beam})^2)$.

	Pulse FWHM (Gaussian, fs)	Spectral width (FWHM, nm)	Pulse FWHM from spectra (fs)
"Hurricane", at laser exit	108 ± 4	8.44 ± 0.07	112 ± 1
Idem, with 3 nm IF filter	362 ± 3	2.72 ± 0.03	342 ± 4
Idem, new 8-pass DL	182 ± 2		
Idem, old 8-pass DL	312 ± 2		

Table B.1: Overview of autocorrelator and pulse spectrum measurements
Pulse temporal FWHM is determined from the width of the autocorrelation traces, and error margins are obtained from the fit routine. The true accuracy is $\pm 5\%$ due to the uncertainty in the determination of φ.

Fig. B.1 c) - d) present test results for the amplifier beam. Fig. B.1 c) shows the autocorrelation trace, and the spectrum (measured by a CCD spectrometer), for the laser pulse directly behind the laser, and Fig. B.1 d) the same, but now with a 3-nm FWHM interference filter with a center wavelength of 794.7 nm placed before the autocorrelator. In the latter case the spectrum has narrowed, while at the same time the pulse length has increased. The non-Gaussian shape of the wider autocorrelation trace in Fig. B.1 d) is likely due to the poor quality of either the amplifier beam or the KDP crystal. Quantitative results are summarized in Table B.1. Values of 108 fs and 362 fs are found for the pulse length for these two cases, assuming a Gaussian pulse shape. Similar fits were performed with a sech^2 shaped pulse, and the results differed less than 5% from the Gaussian values.

It is useful to compare the pulse length as implied by the autocorrelation, to the values implied by the spectral width. To this end the FWHM values were determined for the measured spectra. A correction for the resolution of the CCD spectrometer was included. For a Fourier-transform-limited Gaussian pulse, the FWHM in time and space (δt and $\delta \nu$, respectively) are related as $\delta t \times \delta \nu \sim 0.441$ [6]. So,

$$\delta t = \frac{0.441}{\delta \nu} = \frac{0.441 \lambda^2}{c \delta \lambda}. \tag{B.2}$$

The resulting values for the pulse length as obtained from the spectral information are also stated in Table B.1. From the good agreement between the temporal and the spectral determination we conclude that the original pulse is transform limited, and that the estimates for the pulse lengths are reliable.

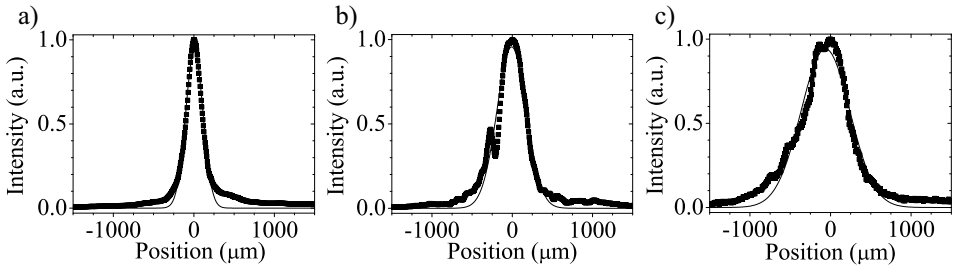

Figure B.2: Autocorrelation traces at several positions in the setup
Measured CCD traces a) directly behind the laser, b) with the new delay line configuration (12 cm of BK7 glass), and c) with the old 8-pass delay line configuration (32 cm of BK7 glass).

The pulse lengths were also measured further on in the setup. Since there is a lot of glass in the setup, we expect to see dispersive effects. During this research project, we decided to replace a prism in the original eight-pass delay line [7] by two mirrors, hereby removing 20 cm of glass from the delay line. The difference in autocorrelation trace can be seen in Fig. B.2 b) and c), and compared to the original trace in Fig. B.2 a). A reduction in pulse length of 40% is the result (Table B.1). The effects of dispersion can be estimated by applying the dispersion parameter of 450 fs^2/cm for BK7 glass [6] to an input pulse of 108 fs. Propagation through 12 cm of glass gives 176 fs, and through 32 cm of glass gives 385 fs. These values agree very well with the results measured with the autocorrelator.

B.3 Conclusions

In conclusion, we have demonstrated the principle of our autocorrelator, and we have made reliable pulse length determinations for the experiments presented in this thesis. In most of the experiments, the pulse length was minimized at BBO frequency doubling crystals in either the pump or the probe (typically after propagation through $\sim$15 cm of glass) to optimize second harmonic generation. The pump pulses might be a little longer due dispersion of 400-nm light in the BBO. For the probe, the propagation length through glass in the remainder of the setup was an additional 12 cm or less in all cases. Therefore, the ultimate temporal resolution for our experiments can be estimated to around 180 femtoseconds, which is by far enough to observe THz acoustic frequencies.

References

1. J.A.I. Oksanen, V.M. Helenius, and J.E.I. Korppi-Tommola. A femtosecond autocorrelator with internal calibration. *Rev. Sci. Instr.*, 64(9):2706, 1993.
2. J.J. McFerran, J. Winterflood, C. Burton, and A.N. Luiten. Resonant interferometric autocorrelator for estimation of laser pulse duration. *Rev. Sci. Instr.*, 76(1):013102, 2005.
3. Y. Ishida, T. Yajima, and A. Watanabe. A simple monitoring system for single subpicosecond laser pulses using a SH spatial autocorrelation method and a CCD detector. *Opt. Comm.*, 56(1):57, 1985.
4. M. Raghuramaiah, A.K. Sharma, P.A. Naik, P.D. Gupta, and R.A. Ganeev. A second-order autocorrelator for single-shot measurement of femtosecond laser pulse durations. *Sãdhanã*, 26(6):603, 2001.
5. *http://swampoptics.com/products_grenoverview.htm*.
6. Spectra Physics. *Mai Tai user's manual*, 2001.
7. O.L. Muskens. *High-amplitude, ultrashort strain solitons in solids*. PhD thesis, Utrecht University, 2004.

Nederlandse samenvatting

Inleiding Dit proefschrift gaat voornamelijk over de voortplanting van geluid in vaste stoffen. Mensen kennen geluid als een van de manieren om dingen waar te nemen, naast bijvoorbeeld licht (zicht) en gevoel. Geluid is een golfverschijnsel, om precies te zijn een drukgolf, waarbij een lokale druk in een medium wordt doorgegeven aan naburige deeltjes. In een vaste stof zijn deze deeltjes atomen, die in een regelmatige structuur zijn gerangschikt.

Het ons bekende geluid bestrijkt een groot frequentie- of toonhoogtegebied, van veel minder dan een hertz (1 trilling per seconde) tot enkele terahertz. Voorbeelden lopen van seismische golven (met frequenties lager dan 1 Hz), via hoorbaar geluid (spraak, omgevingsgeluid, 50 - 20.000 Hz) en ultrasoon geluid (echoscopie en ultrasone materiaalkarakterisatie, 100 kilohertz (kHz) - 100 megahertz (MHz)), naar de ultrasone frequenties die wij onderzoeken (10 gigahertz (GHz) en hoger). Zie Figuur A a) op pagina 187 voor een illustratie van de voor dit proefschrift relevante frequenties en lengteschalen. Voor geluid geldt dat de golflengte λ gelijk is aan v_s/f, met v_s de geluidssnelheid, en f de frequentie. Anders gezegd, hoe hoger de frequentie, hoe korter de golflengte. Van praktisch belang is dat voor golven met terahertz-frequenties, de golflengte in de orde van nanometer ligt. Dit is op dit moment de typische lengteschaal voor bijvoorbeeld componenten op computerchips. Ook zijn de laatste jaren veel technieken ontwikkeld om kunstmatige structuren op deze lengteschaal te vormen die bijzondere optische, electrische, thermische etc. eigenschappen hebben, in populair taalgebruik *nanostructuren*.

Moderne technieken gebruiken licht, in het bijzonder laserlicht met een goed gedefinieerde golflengte en -fase, om kristallen en nanostructuren te bestuderen. Daarnaast is de laser een populair middel om materialen te manipuleren. Dit kan

bijvoorbeeld door verhitting (absorptie) of door gebruik te maken van het electromagnetische veld. Licht en geluid zijn analoge golfverschijnselen. Beide zijn bijvoorbeeld gevoelig voor verstrooiende effecten ter grootte van de golflengte. Licht is makkelijker te meten, als bron eenvoudiger beschikbaar, en heeft verder als voordeel dat het zich buiten een bestudeerde vaste stof kan voortplanten. Geluid kan het medium niet verlaten, en bronnen in het 100-nanometergebied zijn lastiger beschikbaar. Daartegenover kan geluid ook reizen in optisch dichte materialen, waardoor je kunt "waarnemen" op plekken waar licht niet kan komen. Sommige structuren zijn bovendien gevoeliger voor akoestische dan voor optische manipulatie.

Men zou dit proefschrift kunnen opvatten als een poging te onderzoeken in hoeverre hoogfrequent geluid en korte geluidspulsen in vaste stoffen gebruikt kunnen worden, parallel aan optische methodes, voor karakterisatie van vaste stoffen, en daarnaast in hoeverre het haalbaar is om deze geluidspulsen te gebruiken om materialen te manipuleren.

Ultrasnelle akoestische generatie en detectie Een eerste vraag is hoe je deze akoestische golven maakt. De "klassieke" manier om dit te doen, met behulp van een dunne metaalfilm, is ontwikkeld in de jaren '80 en wordt beschreven in Hoofdstuk III. Het experiment is geïllustreerd in Figuur 1 a) op pagina 202. We schieten een korte lichtpuls op een dunne metaalfilm. "Kort" betekent hier van de orde van 100 femtoseconde, zoals gemeten in Appendix B. Verhitting van een dunne oppervlaktelaag door absorptie van licht leidt tot een uitzetting en dus een lokale druk (*stress*), die aanleiding geeft tot een reizende vervormingsgolf (*strain*). Deze bestaat uit een samendrukking (compressie) aan de voorzijde, en een uitrekking (decompressie) aan de achterzijde.

De gegenereerde frequenties hangen samen met de interactietijd tussen het object dat de drukgolf maakt en het materiaal waarin deze wordt gemaakt: hoe korter de contacttijd, hoe hoger de frequenties. Ook: hoe korter de contacttijd, hoe korter in tijd de gegenereerde puls. Om een klok te kunnen laten klinken bij zijn karakteristieke toon is bijvoorbeeld een contacttijd met de klepel nodig van een milliseconde of minder. Met onze 100-femtoseconde "optische klepel" maken we frequenties veel hoger dan een gigahertz. Een bijzonderheid in onze experimenten is dat deze pulsen gedurende deze zeer korte tijd een extreem hoge energie bevatten. Zo heeft de gemiddelde laserpuls waarmee wij onze effecten opwekken in die 100 femtoseconde een vermogen vergelijkbaar met dat van een

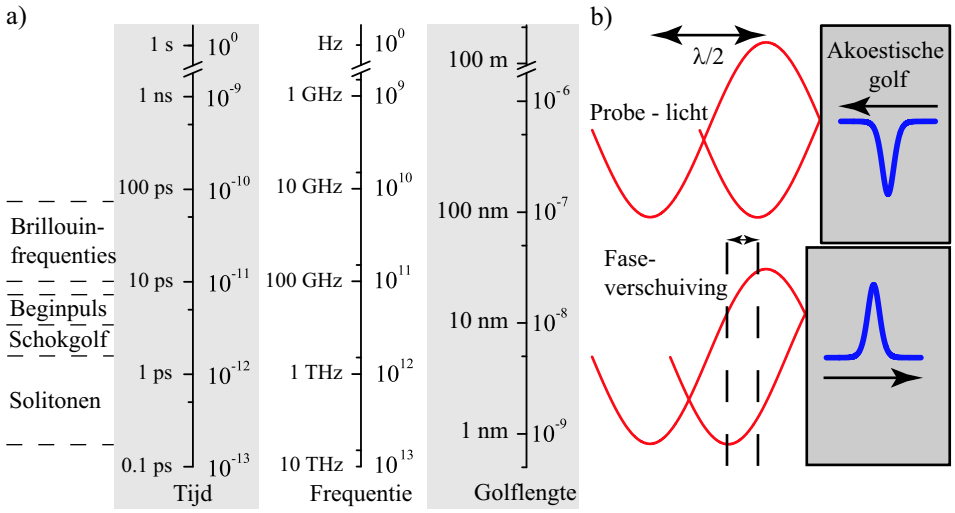

Figuur A: Tijdsschalen en interferometrie
a) Typische tijds-, frequentie- en lengteschalen behorend bij de experimenten in dit proefschrift. Hier:
ns = nanoseconde = 10^{-9} s = 0,000,000,001 s. ps = picoseconde = 0,001 ns.
GHz = gigahertz = 10^{9} Hz = 1.000.000.000 Hz. THz = terahertz = 1.000 GHz.
nm = nanometer = 10^{-9} m = 0,000,000,001 m.
b) Illustratie van de interferometrische techniek. Wanneer een compressive golf naar het oppervlak van een vaste stof reist (bovenste plaatje), zal hij bij reflectie van teken omkeren en als decompressieve golf terugreizen (onderste plaatje). Als gevolg hiervan verplaatst het oppervlak. Wanneer men een lichtpuls op het oppervlak stuurt na reflectie, en deze vergelijkt met een lichtpuls die reflecteerde vóór passage van de akoestische puls, zal de fase van de golven een klein beetje verschillen, evenredig met de oppervlakteverplaatsing. De schaal is zwaar overdreven in de figuur: typisch verplaatst het oppervlak over één tienduizendste van de golflengte, oftewel zo'n 100 picometer. Uiteraard kunnen we ook kijken *tijdens* passage van de akoestische puls, en hieruit valt de pulsvorm af te leiden.

flinke (100-megawatt) electriciteitscentrale. Dit heeft tot gevolg dat er bijzondere, niet-lineaire effecten optreden die bij lage pulsvermogens niet te zien zijn.

De typische eigenschappen van zo'n akoestische puls hebben we onderzocht voor generatie in chroom en nikkel in Hoofdstuk III. De gemeten golven die hieruit kunnen worden afgeleid staan in Figuren III.6 b) en III.7 b) op respectievelijk pagina 46 en 48. De typische tijdsbreedte is zo'n 4 picoseconde, en de typische frequentie zo'n 70 gigahertz, overeenkomend met slechts 25 nanometer.

We kunnen pulsen genereren met een amplitude van 1% (overeenkomend met het verplaatsen van de atomen van hun rustpositie over 1% van de roosterafstand). De typische druk in zo'n golf is maar liefst 20 kilobar.

Een nog niet beantwoorde vraag is hoe je deze golven detecteert. Het ligt voor de hand om een zogenaamd *pomp-probe* experiment te doen, waarbij men op een moment het materiaal exciteert met een lichtpuls ("pomp"), en op een later moment de geïnduceerde effecten "bekijkt" met een zwakke optische puls afkomstig van dezelfde laser ("probe"). De manier waarop deze detectie precies in zijn werk gaat is beschreven in Hoofdstuk II (met schetsen van de opstelling). De technische details staan in Appendix A. De ultieme tijdsgevoeligheid in zo'n experiment is van de orde van de lengte van de optische puls, 100 femtoseconde.

De akoestische golf resulteert in twee effecten die allebei zijn gemeten in onze experimenten. De eerste is een verandering in de hoeveelheid reflectie van de probe. Het probelicht reflecteert in een zeer dun gebiedje aan het oppervlak van de metaalfilm waar de puls in is gegenereerd. De aanwezigheid van een akoestische golf drukt de atomen iets samen (of brengt ze iets verder van elkaar af), waardoor de optische reflectiecoëfficiënt verandert als functie van de positie en vorm van de akoestische golf. Een tweede methode is geavanceerder en is geïllustreerd in Figuur A b). Wanneer een akoestische puls het oppervlak bereikt, keert hij om van teken en reist de film weer in. Hierdoor verandert de positie van het oppervlak van de metaalfilm, en dus ook de fase van het reflecterende probelicht (onderste plaatje). De akoestische puls kan nu gekarakteriseerd worden door de fase van deze gereflecteerde puls te vergelijken met de fase van een optische referentiegolf die reflecteerde wanneer er niets aan de hand was (bovenste plaatje).

Merk op dat voor een enkele verzameling meetpunten, zoals in vele figuren in dit proefschrift weergegeven, een meting van typisch een half uur nodig is, waarin hetzelfde fysische proces zich afspeelt op een tijdsschaal van enkele tientallen picoseconde, enkele honderdduizenden keren, en met de regelmaat van een Zwitsers uurwerk. Deze experimenten vormen daarmee een voorbeeld van de extreme controle die in een modern fysisch experiment kan worden bereikt.

Schokgolven Nu de gegenereerde golven gekarakteriseerd zijn, willen we de voortplanting in het substraat bekijken. In Hoofdstuk IV bekijken we het gedeelte van de golf dat het substraat inreist (Figuur 1 b)). Saffier is een ideaal substraat, omdat het van alle bekende en gangbare substraten de laagste akoestische demping heeft. Hierdoor bereikt de golf na tientallen nanoseconde slechts

licht gedempt de overzijde van het substraat, dat typisch 0.1 millimeter dik is. Aan deze kant is opnieuw een (chroom of aluminium) metaalfilm gedeponeerd, en hierop meten we de reflectie en de faseverschuiving.

Het blijkt, dat bij hogere amplitudes er niet alleen demping optreedt, maar ook een vervorming van de golf ten gevolge van niet-lineaire voortplanting. De voorkant (compressieve gedeelte) van de golf gaat hierdoor "sneller reizen" (supersoon), en de achterzijde (decompressief) "langzamer" (subsoon). Figuur IV.3 op pagina 72 laat het resultaat zien van een serie berekeningen. Er vormt zich een *schokgolf*, ook wel *N-golf* genaamd (een logische naam kijkend naar de figuur).

Bij hoger pompvermogen wordt deze schokgolf breder, maar ook worden de fronten steeds scherper, tot het uiteindelijk nog maar 9 roosterafstanden (10 nanometer) duurt om van bijna geen tot maximale vervorming te komen. De typische frequenties in de golf gaan hierdoor omhoog naar zo'n 500 gigahertz.

Akoestische solitonen In een discrete structuur als een kristalrooster komt bij hoge frequenties het effect van dispersie in het spel. Dit betekent dat hoge frequenties effectief een lagere geluidssnelheid hebben. Bij kamertemperatuur worden de hoogste frequenties gedempt, zodat dispersie niet wordt waargenomen. Wanneer we het kristal afkoelen naar zo'n -250 °C, worden de hoge frequenties nagenoeg niet gedempt, en gaat dispersie de voortplanting van de golf beïnvloeden. Nu reist bij niet-lineaire voortplanting de voorzijde van de golf sneller, maar dit is tegelijkertijd het gebied met de hoogste frequenties (dus effectief langzamer). Hierdoor ontstaat er een bijzonder evenwicht, leidend tot zogenaamde akoestische *solitonen* aan de voorzijde van de originele puls.

De eigenschappen van solitonen werden al in 1895 berekend door de Nederlandse wiskundigen Korteweg en De Vries. Een bijzondere eigenschap van deze solitonen is dat de snelheid, breedte en amplitude nauwkeurig met elkaar samenhangen. In Hoofdstuk V presenteren we metingen (Figuren V.3 tot V.5 op pagina's 90 tot 93), waarin maximaal zeven solitonen te zien zijn. Uit deze metingen kunnen het volume en de snelheid van deze solitonen worden afgeleid. Vanuit de gemeten snelheid van deze solitonen (die zoals gezegd samenhangt met de breedte) kunnen we afleiden dat de minimale breedte zo kort is als 200 femtoseconde (2 nanometer)!

Nanostructuren manipuleren met akoestische solitonen Nu is gedemonstreerd dat deze zeer korte solitonen zich kunnen vormen, kunnen we ook kijken of we ze kunnen gebruiken om structuren te manipuleren op zeer korte tijdsschaal. De resultaten zijn weergegeven in Hoofdstuk VI. Als modelsysteem nemen we een zogenaamde *quantum well*, Figuur VII.1 b) (pagina 118). Dit is een enkele nanometers dikke, gegroeide laag waarin gebonden electrontoestanden bestaan. Bij een bepaalde golflengte heeft deze quantum well een specifiek reflectiepatroon (bij de zogenaamde excitonresonantielijn), getoond in Figuur VI.1 b) op pagina 104. Door de structuur iets samen te drukken of uit te rekken, verschuift de golflengte waar dit patroon optreedt. Deze verschuiving kan ook bereikt worden met korte optische pulsen (door absorptie en verhitting), maar het duurt vaak relatief lang voordat de structuur weer afgekoeld is en terugkomt in de originele toestand.

Inderdaad zien we een verandering van het reflectiespectrum. Bij "langzame" manipulatie (langer dan de ongeveer 4 picoseconde die de reflectie duurt) zien we dat de resonantielijn onder invloed van de drukgolf verschuift. Nu is het mooie, dat wanneer we de *quantum well* bestoken met akoestische solitonen (die zoals eerder is opgemerkt veel korter zijn dan vier picoseconde), we een zogenaamd *chirping*-effect waarnemen: het reflectiepatroon wordt dan vervormd doordat de resonantielijn heen en weer wordt geschoven binnen de duur van de reflectie (*chirping* kan vertaald worden als "tsjilpen", zoals van een vogel. Ook in dat geval verandert de frequentie tijdens het fluiten). Hier tonen we dus aan dat het mogelijk is om met behulp van geluidspulsen de optische eigenschappen van een nanostructuur te veranderen op een tijdsschaal van slechts enkele picoseconde.

Generatie van akoestische golven in door nanostructuren Tot nu toe hebben we gebruik gemaakt van de "klassieke" manier om akoestische pulsen van picoseconde lengte te genereren, namelijk met behulp van een metaalfilm. Een "moderne" manier is door hiervoor bijvoorbeeld een gegroeide nanostructuur te gebruiken. Een zeer interessante structuur is dan een gallium nitride/indium gallium nitride meerlaags *quantum well* (Hoofdstuk VII). De structuur heeft een ingebouwde vervorming, die vrijkomt wanneer deze met een korte laserpuls gepompt wordt. Bij dit pompen zendt deze structuur niet alleen akoestische golven, maar ook electromagnetische golven uit, in hetzelfde frequentiegebied (rond 1 terahertz).

We gebruiken drie meerlaags *quantum well*-systemen met verschillende diktes. De gegenereerde golven worden op twee manieren bekeken. Allereerst kijken we naar de vibraties van de *quantum well*-structuur. De vibratiefrequentie hangt

samen met de dikte van de structuur, en verschilt inderdaad voor de drie gebruikte structuren. Deze resultaten laten zien dat er frequenties worden gegenereerd in de orde van 700 tot 900 gigahertz. Interessanter is de waarneming van de 100-gigahertz *Brillouinfrequentie*. Wanneer de gegenereerde golf uit de nanostructuur reist en het omringende materiaal in (Figuur VII.4 a) op pagina 123), ontstaat er een constructieve dan wel destructieve interferentie tussen de reflectie van licht op de golf, en de reflectie op het oppervlak van het materiaal, zie Figuur VII.4 b). In de meting zien we dit als een oscillatie. Door te kijken naar de amplitude van deze oscillatie vinden we dat de akoestische emissie en de verzadiging ervan voor hoge pompvermogens overeenkomen met verwachtingen op basis van de verschillende diktes, en bovendien met eigenschappen als gemeten in experimenten waarbij men kijkt naar de emissie van electromagnetische straling.

Akoestische emissie door faseovergangen Yttriumvanadaat (YVO_3) is een bijzonder materiaal. Wanneer het afgekoeld wordt van kamertemperatuur tot 30 kelvin (-243 °C), gaat het door enkele electronische faseovergangen. Hierbij verandert de electronische configuratie van het materiaal. Bij 77 kelvin treedt een faseovergang op waarbij ook de roosterafstand tussen atomen sterk verandert. Door middel van verhitting door optische excitatie met een pompppuls, kunnen in zeer korte tijd deze reconfiguraties in tegenovergestelde richting doorlopen worden. De roosterafstand kan dan ook zeer snel veranderen, wat gepaard gaat met emissie van een drukgolf.

In Hoofdstuk VIII is de amplitude van de eerder genoemde Brillouinoscillatie gebruikt om de emissie als functie van pompvermogen te meten langs de drie verschillende kristalassen (a, b en c). We meten asymmetrisch gedrag voor de verschillende richtingen. Eén as (de b-as) laat niets zien. Interessanter zijn de a- en c-as. De a-as laat bij verhitting vanaf lage temperaturen geen bijzondere effecten zien in de amplitude van de Brillouinoscillatie, maar wel een zeer langzame verandering van het achtergrondsignaal, waarschijnlijk veroorzaakt door een *langzame* reconfiguratie van het rooster. De c-as echter laat bij deze temperaturen niet alleen een vier keer hogere amplitude van de Brillouinoscillatie zien, maar ook nog eens een fasesprong van deze frequentie. Dit is volledig in overeenstemming met in de literatuur gemeten roostervervormingen bij de faseovergangstemperatuur van 77 kelvin, en betekent dat in deze richting de reconfiguratie *snel* is. Hier is derhalve aangetoond dat ook een akoestische puls gemaakt kan worden middels een faseovergang.

Ultrasnelle dynamica in zinkoxide nanodraden Dit hoofdstuk is een buitenbeentje in dit proefschrift, en bekijkt ultrasnelle electronische effecten in zinkoxide nanodraden. Nanodraden (zie Figuur IX.1 op pagina 155 voor plaatjes) zijn structuren met een lengte van enkele micrometers, en met een diameter van typisch 100 nanometer. Bijzonder aan deze draden is dat ze *laserwerking* kunnen vertonen, dus een versterkte emissie van licht bij een gegeven golflengte door gestimuleerde processen. De laserwerking bij zeer hoge pompintensiteiten is gekarakteriseerd met behulp van de eerder besproken pomp-probe technieken. Tenslotte inventariseren we een aantal mogelijkheden om ook in deze structuren akoestische propagatie te bestuderen.

Conclusies en vooruitzichten Het is terecht de vraag te stellen hoe de mensheid nu verder is geholpen met dit onderzoek.

Op een fundamenteel niveau hebben we een aantal materialen gekarakteriseerd middels hun akoestische respons op ultrasnelle optische excitatie. Het gaat hier zowel om de generatie van de vervorming (Hoofdstukken III, VII en VIII), als de propagatie ervan (Hoofdstukken IV, V). Het uitvoeren van de solitonexperimenten van Hoofdstuk V bij hogere pompvermogens geeft wellicht de mogelijkheid om golfpropagatie te onderzoeken in extreem dispersieve media.

De solitonresultaten van Hoofdstukken V en VI bieden mogelijkheden tot praktische toepassingen. In feite hebben we hiermee de beschikking gekregen over een bron van akoestische pulsen met een lengte van enkele nanometer. De mogelijkheden van optische gepulste systemen kunnen met enige beperkingen worden nagebootst in het akoestische veld. Een optie is materiaalkarakterisatie met nanometer en picoseconde precisie. Impliciet hebben we dit al gedaan door de akoestische transmissie van metaalfilms van verschillende kwaliteit te vergelijken in Hoofdstukken III - V. De resultaten van Hoofdstuk VI vormen een eerste voorbeeld van ultrasnel *akoestisch schakelen*. Zonder veel problemen kan deze techniek worden uitgeprobeerd op andere nanostructuren.

Dankwoord

Wanneer men de ontwikkeling van het dankwoord in proefschriften door de jaren heen bekijkt, valt op dat de lengte langzamerhand een aantal maal is toegenomen (en het is een geluk voor de promovendus dat voor de rest van het proefschrift niet hetzelfde geldt). Dat is hoogstwaarschijnlijk niet (alleen) omdat er meer mensen te bedanken zijn dan voorheen, maar vooral omdat het erkent dat een project als dit diepere wortels heeft dan het dagelijkse wetenschappelijke werk. Ik zal mijzelf hier niet inhouden (dat heb ik elders tenslotte ook niet gedaan), en proberen recht te doen aan al diegenen die belangrijk zijn geweest in de periode vóór dit onderzoek, gedurende het onderzoek, en, zo hoop ik van harte, ook in de periode erna.

Allereerst dank ik mijn promotor Jaap Dijkhuis. Waar ik degene was van de lange dagen, meetsessies en berekeningen, en een natuurlijk streven naar complexiteit, was hij degene van het bewonderenswaardig snelle, intuïtieve inzicht dat doorbraken genereerde wanneer ik vastliep, de vaardigheid om de resultaten om te zetten in heldere figuren en teksten, en het vermogen om de zaak begrijpelijk te houden. Onze "complementaire" benadering heeft mijns inziens geleid tot een mooie verzameling goed onderzoek.

The research in this thesis contains a remarkably large Russian contribution. I owe great thanks to Andrey Akimov, who taught me the basics of experimental physics in my first half year. He is also the one to connect our soliton work to the experiments Alexey Scherbakov performed in the group of Manfred Bayer in Dortmund, resulting in a fruitful collaboration and a nice publication (Ch. VI). The presence of Dmitry Turchinovich as post-doc in Utrecht was very stimulating. He supplied the ideas and samples for the research in Ch. VII. I thank Dmitry Mazurenko for his hospitality in St. Petersburg during the Phonons conference in 2004, and for initiating the experiments on YVO_3 of Ch. VIII.

Otto Muskens, die de standaard voor onderzoek op het gebied van ultrasnelle akoestiek zeer hoog heeft gezet, bedank ik voor zijn hulp in de aanloopfase van mijn onderzoek, en voor de leuke tijd in Triëst.

Ik wil hier graag mijn leescommissie, bestaande uit de professoren Schropp, Stoof, Van der Straten en Vanmaekelbergh, bedanken voor haar inspanning om in korte tijd én gedurende de zomermaanden mijn proefschrift te beoordelen.

Heng Yu Li has grown the ZnO nanowire samples that were studied in Ch. IX. I thank Peter Liljeroth for the AFM measurements used for sample characterization in Ch. IV. Daarnaast dank ik de CMI-groep van het departement Scheikunde voor het uitlenen van de CCD-camera, gebruikt voor Hoofdstuk IX en voor veel meer karakterisatiemetingen. Peter van der Straten dank ik voor zijn hulp bij het opstellen van een aantal belangrijke Fortran-rekenroutines.

Van het triumviraat van de koude gassen bestaande uit Johan Keizer, Jan van Eijk en Nico Kuipers is alleen de laatste nog werkzaam. Zij allen (en in de laatste maanden ook Paul Jurrius) bedankt voor het leveren van enkele duizenden liters vloeibaar helium. Peter de Graaf en medewerkers van de Glasinstrumentmakerij van Scheikunde hebben de meeste van de samples geprepareerd die in Hoofdstukken III - V zijn gebruikt. Paul Graf dank ik voor het regelmatig oplappen van onze "Hurricane".

Cees de Kok vormde niet alleen een onmisbare factor bij het oplossen van problemen rondom optica en electronica, maar ook een uitstekende sparringpartner in discussies over vele andere (Haagse, aardse en hemelse) zaken.

Wanneer ik met een verzoek voor een mechanisch onderdeel (met een opzetje waar ik al gauw een uurtje over had nagedacht) naar hem toeging, had Paul Jurrius al tijdens het stellen van de vraag een beter werkend en eenvoudiger alternatief bedacht. Daarnaast heeft hij voor mij veel samples van dunne metaalfilms voorzien. Zijn opgeruimde humeur en praktische instelling vormen de smeerolie van menig onderzoek in onze groep.

Masterstudent Henrik Porte heeft nagenoeg op eigen kracht de resultaten van Hoofdstukken VII en IX bij elkaar gemeten. Hij is de enige student die ik ken die ook nachten doorwerkte om zijn resultaten bij elkaar te meten, ondertussen geduldig zijn repen wegkauwend. Ik ben ervan overtuigd dat hij een goed promotieonderzoek zal afleveren bij Dmitry in Kopenhagen. De intellectuele en praktische bijdragen van bachelorstudenten Gerard Vriens en Gido van der Star in het karakteriseren, begrijpen en optimaliseren van de opstelling hebben een cruciale rol gehad in latere experimenten, toen de resultaten pas echt binnen begonnen te

stromen. Marco Stoffelen tenslotte heeft na mijn vertrek uit het lab een moedige poging gedaan om de interferometrische opstelling te leren gebruiken, en nog een aantal leuke resultaten bij elkaar gemeten.

Mijn kamergenoot op de gezelligste kamer van de afdeling, Lennart Karssen, heeft veel grote en kleine programmeer- en computerproblemen opgelost, en was altijd bereid om mee te doen in een discussie over onderzoek in de breedste zin van het woord. Als prominent oud-lid van de groep-Karssen zorgde Robert Meppelink ("de Maestro" voor tafeltennis-intimi), voor de (meestal) nodige afleiding van het werk. I would like to thank Marijn Versteegh and Xinjian Shan for the nice time at the Summer School in Cargèse and the Phonons conference in Paris. Marijn wens ik daarnaast veel succes bij het scheppen van verdere orde in het onderzoek aan de nanodraden. Uiteraard bedank ik ook de nog niet eerder genoemde (ex-)collega's Michiel, Driss, Dries, Erik, Richard, Johnny, Silvio, Louise, Clarien, Frits en Hans voor de prettige (en op zijn tijd een beetje gekke) sfeer op de afdeling.

Mijn afstudeerbegeleider Jeroen Bakker wil ik bedanken voor het (destijds onverwachte) inzicht dat experimenteel onderzoek leuk is, en dat een oprechte interesse voor het onderwerp je een heel eind kan brengen. Het voorbereiden en geven van de werkcolleges TF2, VAST en MIF, onder leiding van respectievelijk Toine Arts, Arjen Vredenberg en Wim Westerveld, was voor mij regelmatig even leerzaam als voor de studenten die deze colleges volgden.

Ik heb me gedurende mijn studie en onderzoek regelmatig kunnen optrekken aan de inspirerende sfeer op de A.U.S.R. Orca, waar ik veel vrienden en bekenden heb opgedaan via wedstrijdroeien, MAC en FAC. Ik ben er trots op dat ik mij straks mag verdedigen met mijn paranimfen Markus en Martijn, als de harde kern van Zwaar '97.

Het is altijd een plezier om op kwekerij Brouwer, waar de academische humor met de paplepel werd ingegoten, wat te rommelen met planten of bouwmaterialen. Van het Noorden-front wil ik ook Nico en Joke noemen, bij wie ik altijd graag mag bijpraten over ditjes en datjes.

Mijn familie, en hiertoe mag ik sinds kort ook Albert, Janneke, Jessica en verdere schoonfamilie rekenen, dank ik voor de algemene interesse in het onderzoek en mijn voortgang daarin. Dit hoewel het mij eigenlijk nooit goed lukte om uit te leggen wat ik nu precies aan het doen was (in de samenvatting heb ik nog eens een goede poging gewaagd).

In het bijzonder wil ik opa en oma Pieterse en opa en oma Van Capel noemen. Hun liefde in mijn jonge jaren heeft mij in hoge mate gevormd. Ik vind het heel

jammer dat zij niet meer allemaal mijn promotie, die ik toch beschouw als de afronding van mijn jeugd, mogen meemaken.

Roel en Linda, en Marleen en Benjamin, jullie bedankt voor de leuke verjaardagen en feestdagen, en voor jullie hulp en aanwezigheid op de belangrijke momenten.

Mijn ouders hebben altijd voor me klaar gestaan, en hebben ons vooral rondom de zoveelste (ongewenste) verhuizing regelmatig uit de brand gered. Aan hen dank ik daarnaast mijn arbeidsethos, dat tijdens dit onderzoek onmisbaar is gebleken. Papa en mama, ik hoop dat jullie net zo trots zijn op wat ik voor elkaar krijg, als ik dat ben op wat jullie allemaal doen.

En dan tot slot mijn lieve Stella. Ik heb je regelmatig tegen mijn (en jouw) zin avonden en nachten alleen moeten laten omdat de natuur zich helaas vaak niet binnen kantoortijd liet dwingen. Bedankt voor alle kussies, (stomme) grapjes, bakjes, zondagochtend-ontbijtjes, en zoveel meer grote en kleine dingen die mij de afgelopen jaren op de been hielden. Maar vooral bedankt voor het uitzicht op een mooie, lange toekomst samen.

Curriculum Vitae

Peter van Capel werd geboren op 24 maart 1978 in het pittoreske dorpje Noorden. Van 1990 tot en met 1996 volgde hij het Atheneum aan het Minkema College te Woerden. Hierna startte hij de studie Natuurkunde aan de Universiteit Utrecht. Deze werd in 2003 afgerond in twee afstudeerrichtingen, te weten Experimentele Natuurkunde en Grondslagen van de Natuurkunde, beide met genoegen.

Van 2003 tot en met 2008 was hij in dienst van de Stichting FOM en onderzocht de generatie en propagatie van geluidsgolven van zeer hoge amplitude in vaste stoffen middels ultrasnelle, tijdsopgeloste interferometrie. De resultaten van dit onderzoek zijn beschreven in voorliggend proefschrift. Gedurende het onderzoek zijn twee bachelorstudenten en één masterstudent begeleid. Daarnaast zijn als onderwijstaken gedurende een aantal jaar de werkcolleges Thermische en Statistische Fysica, Moderne Gecondenseerde Materie, Meten in de Fysica, en enkele practica begeleid.

Buiten deze studie- en onderzoeksactiviteiten was hij van 1996 tot en met 2001 wedstrijdroeier bij de A.U.S.R. Orca, en van 1997 tot en met 2008 actief in vele commissies aldaar. In 2003 werd hem voor alle activiteiten de Beker van Verdienste toegekend. Sinds 2008 is hij penningmeester van Stichting de Driewerf, beheerder van de roeiloods.

Per 1 september is hij in dienst van TMC Physics, en werkzaam bij TNO Industrie en Techniek in Delft.

Publications and presentations

List of publications

- P.J.S. van Capel and J.I. Dijkhuis. Optical generation and detection of shock waves in sapphire at room temperature, *Appl. Phys. Lett.*, 88(15):151910, 2006 [Ch. IV], and
  P.J.S. van Capel and J.I. Dijkhuis. Erratum: Optical generation and detection of shock waves in sapphire at room temperature [Applied Physics Letters (2006) 88 (151910)], *Appl. Phys. Lett.*, 89(13):139903, 2006 [Ch. IV].
- A.V. Scherbakov, P.J.S. van Capel, A.V. Akimov, J.I. Dijkhuis, D.R. Yakovlev, T. Berstermann and M. Bayer. Chirping of an optical transition by an ultrafast acoustic soliton train in a semiconductor quantum well, *Phys. Rev. Lett.*, 99(5):057402, 2007 [Ch. VI].

Additional publications on Chs. III and V - IX are in preparation.

Conference proceedings

- P.J.S. van Capel, O.L. Muskens, E.W. Hesselink and J.I. Dijkhuis. Towards ultrafast pump-probe spectroscopy on trains of strain solitons, *Phys. Stat. Sol. (c)*, 1(11):2753, 2004.
- P.J.S van Capel, H.P. Porte, G. van der Star and J.I. Dijkhuis. Interferometric detection of acoustic shock waves, *J. Phys.: Conf. Ser.*, 92:012092, 2007 [Ch. IV].
- A.V. Akimov, A.V. Scherbakov, P.J.S. van Capel, J.I. Dijkhuis, T. Berstermann, D.R. Yakovlev and M. Bayer. Acoustic solitons in semiconductor nanostructures, *J. Phys.: Conf. Ser.*, 92:012002, 2007 [Ch. VI].
- A.V. Akimov, A.V. Scherbakov, T. Berstermann, D.R. Yakovlev, P.J.S. van Capel, J.I. Dijkhuis, and M. Bayer. Ultrafast piezospectroscopy in semiconductor nanostructures, *Proc. SPIE*, 6892:689205, 2008 [Ch. VI].

List of presentations

- *Generation and detection of THz acoustic solitons*, FOM Waves in Complex Media workshop, Universiteit Twente, Enschede, 2 December 2004
- *Shock waves in sapphire studied by picosecond ultrasonics*, FOM Decemberdagen, Veldhoven, 13-14 December 2005
- *Direct observation of ultrafast acoustic solitons by semiconductor heterostructures*, Physics@Veldhoven, Veldhoven, 23-24 January 2007
- *Interferometric detection of acoustic shock waves*, 12th International Conference on Phonon Scattering in Condensed Matter, Paris (France), 15-20 July 2007

List of posters

- P.J.S. van Capel, O.L. Muskens, E.W. Hesselink and J.I. Dijkhuis, *Towards ultrafast pump-probe spectroscopy on trains of strain solitons*, 11th International Conference on Phonon Scattering in Condensed Matter, St. Petersburg (Russia), 25-30 July 2004
- *Idem*, FOM Waves in Complex Media workshop, Universiteit Twente, Enschede, 2 December 2004
- *Idem*, Wetenschappelijke vergadering voor de Gecondenseerde Materie, Veldhoven, 14-15 December 2004
- P.J.S. van Capel and J.I. Dijkhuis, *Ultrafast pump-probe spectroscopy on high-amplitude strain solitons*, Gordon Research Conference on Photoacoustic and Photothermal Phenomena, Trieste (Italy), 26 June-1 July 2005
- P.J.S. van Capel, A.V. Akimov, A.V. Scherbakov, A. Waag, D.R. Yakovlev, M. Bayer and J.I. Dijkhuis, *Interferometric detection of high-amplitude strain waves*, Summerschool Son et Lumière: from microphotonics to nanophononics, Cargèse (France), 16-28 October 2006
- P.J.S. van Capel, A.V. Akimov and J.I. Dijkhuis, *Simulations of acoustic soliton-induced chirping of exciton resonances*, 12th International Conference on Phonon Scattering in Condensed Matter, Paris (France), 15-20 July 2007
- H.P. Porte, P.J.S. van Capel and J.I. Dijkhuis, *Ultrafast generation and detection of high-amplitude strain in GaN/InGaN quantum well structures*, Physics@Veldhoven, Veldhoven, 22-23 January 2008

Awards

- Award for best poster at the 12th International Conference on Phonon Scattering in Condensed Matter, Paris (France), 15-20 July 2007

Color figures

Current chapter	Reference
Figure 1	Figure I.1, p. 14
Figure 2	Figure III.11, p. 57
Figure 3	Figure III.12, p. 59
Figure 4	Figure VI.2, p. 107
Figure 5	Figure VI.3, p. 108
Figure 6	Figure VI.4, p. 111

Table 1: Reference table for reprinted color figures.

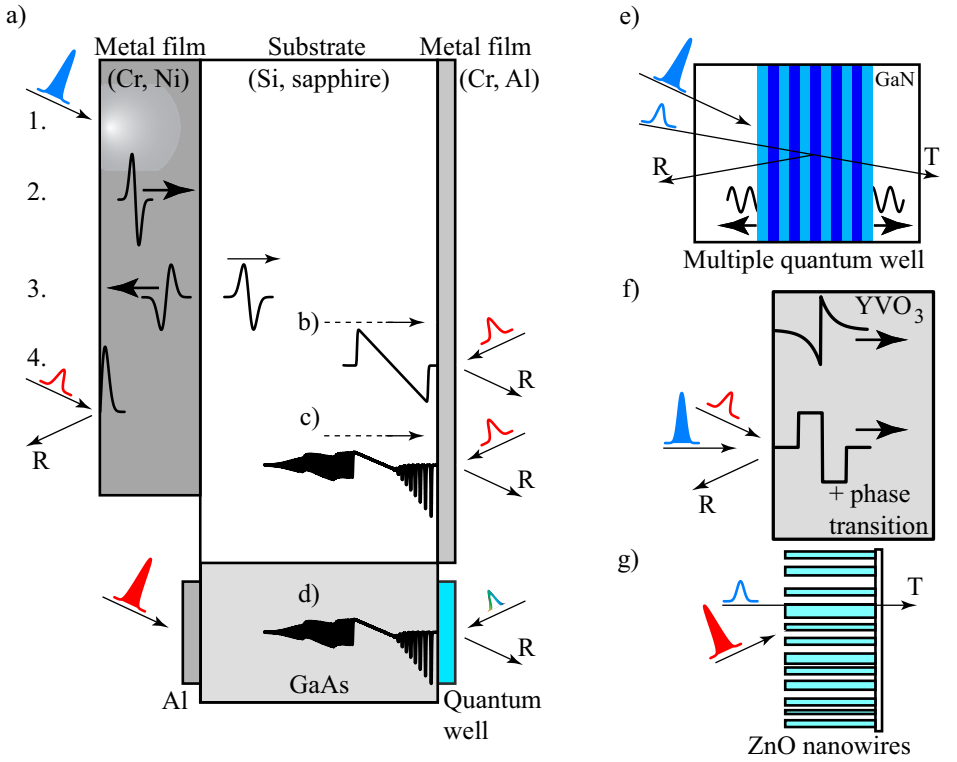

Figure 1: Ultrafast pump-probe experiments in this thesis in a nutshell (Fig. I.1, p. 14)

a) Picosecond ultrasonics technique (Chs. II, III). 1. Absorption of energy from pump beam, and heating of the surface region. Coherent strain is generated by thermal expansion of the lattice. 2. The generated strain travels into the film. 3. Part of the wave is reflected at the metal/substrate interface. 4. The part that returns to the interface is detected by a delayed, weak probe pulse. b) Propagation of the high-amplitude acoustic wave launched into the substrate at room temperature: due to nonlinearity, the wave transforms into a N- or shock wave. The shock wave is detected at the other side by the same technique as in Fig. I.1 a). c) Like b) but now at low temperatures: the wave develops into a train of solitons, and high-frequency tail. d) Detection of soliton train by analyzing wavelength dependent reflection of a broadband colored pulse on a quantum well with a spectrometer. e) Reflection and transmission of multiple gallium nitride - indium gallium nitride quantum wells. Pumping leads to coherent vibrations, and acoustic wave propagation in the surrounding material. f) Generation of low-frequency, high amplitude acoustic waves in yttrium vanadate through structural phase transitions. g) Pump-probe transmission experiments on zinc oxide nanowires. First attempts are made to access the ultrafast carrier dynamics.

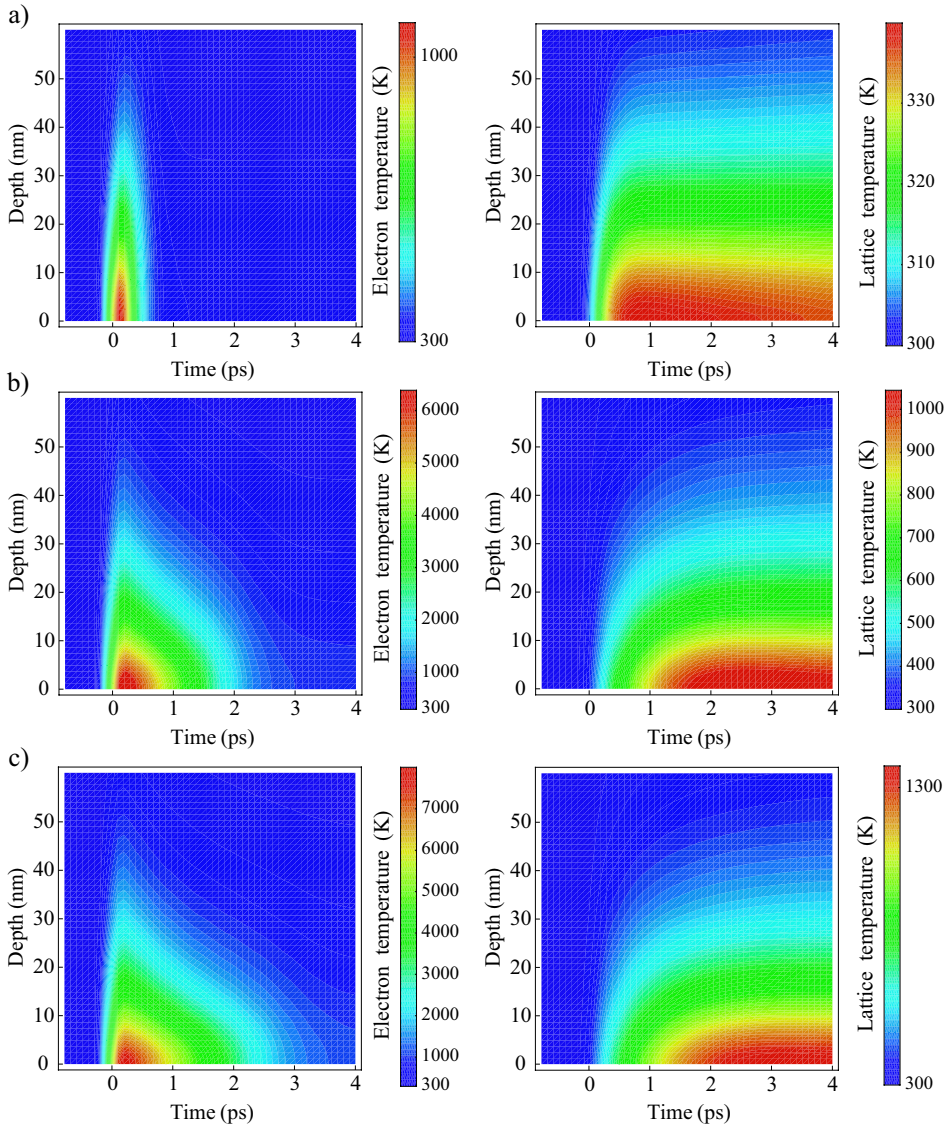

Figure 2: Nonlinear temperature dynamics in Cr (Fig. III.11, p. 57)
Electron (left panel) and lattice (right panel) temperatures for Cr as a function of time and position in the film, for pump fluences a) $I_0 = 0.83$ mJ/cm^2, b) $I_0 = 14.0$ mJ/cm^2, and c) $I_0 = 20$ mJ/cm^2.

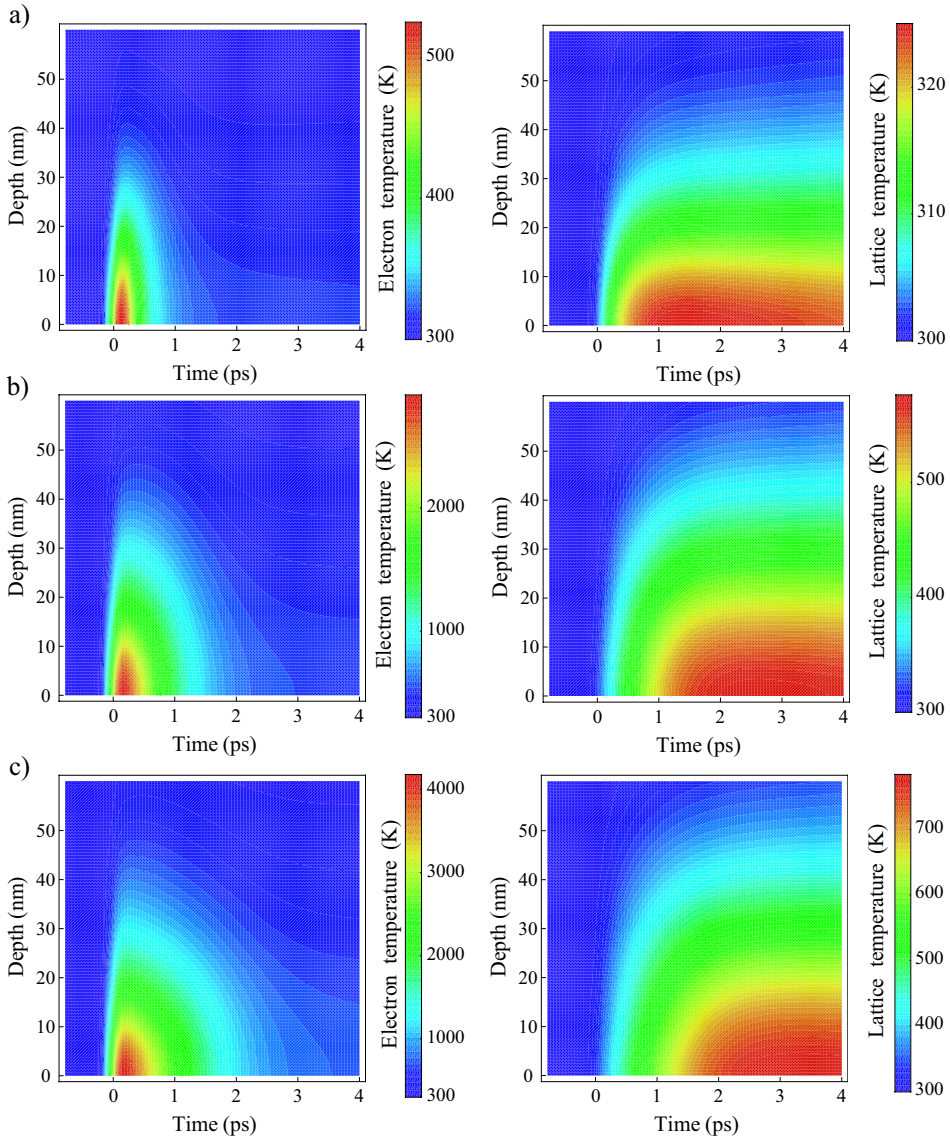

Figure 3: Nonlinear temperature dynamics in Ni (Fig. III.12, p. 59)
Electron (left panel) and lattice (right panel) temperatures for Ni as a function of time and position in the film, for pump fluences a) $I_0 = 0.54$ mJ/cm^2, b) $I_0 = 8.56$ mJ/cm^2, and c) $I_0 = 14.1$ mJ/cm^2.

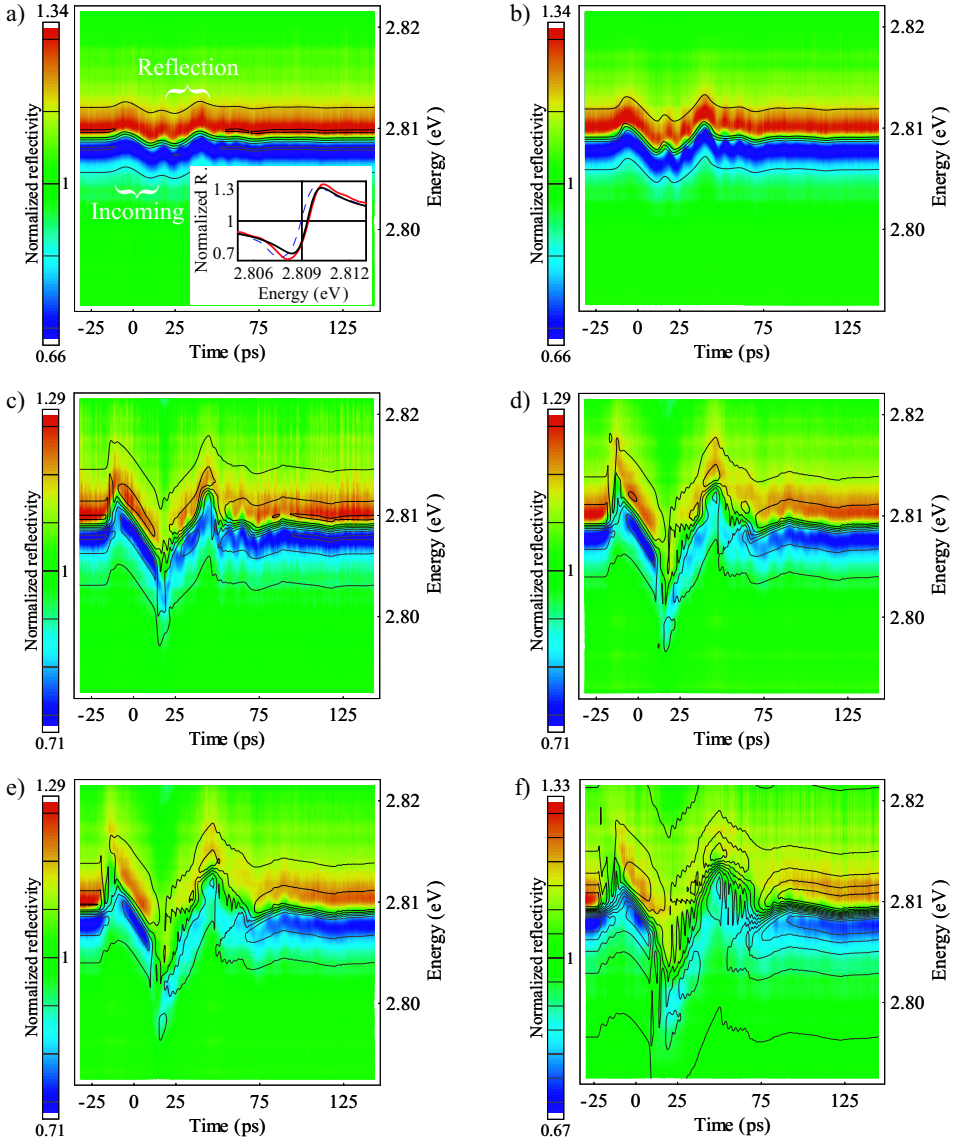

Figure 4: Contour plots of time-dependent spectra (Fig. VI.2, p. 107)
Spectral/temporal contour plots of the reflectivity normalized to the off-resonance background, measured for pump fluences of a) 1.0 mJ/cm^2, b) 2.0 mJ/cm^2, c) 5.1 mJ/cm^2, d) 7.1 mJ/cm^2, e) 8.2 mJ/cm^2, f) 10.2 mJ/cm^2. Black lines are calculated contours of equal reflectance changes for corresponding pump fluences. Inset in a) shows the spectral profile of reflectivity: blue (dashed line) is the stationary spectrum, red (light) and black (dark) lines are respectively the measured and calculated spectra at the specified time, for the corresponding fluence.

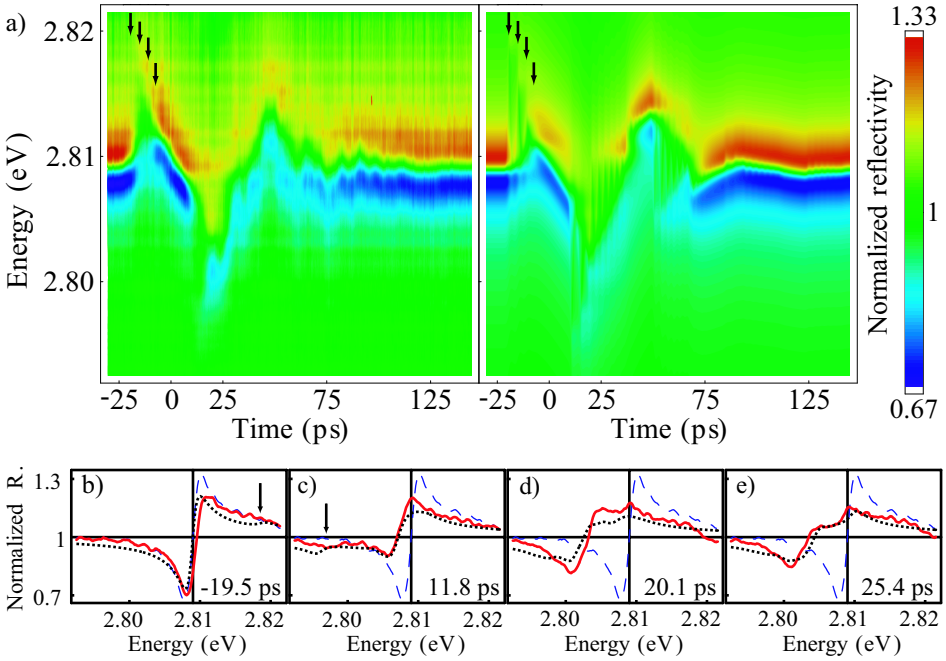

Figure 5: Individual spectra for selected fluence (Fig. VI.3, p. 108)
a) Temporal evolution of the reflectivity spectrum measured (left panel) and calculated (right panel) for $I_0 = 9.2$ mJ/cm^2. Arrows indicate the arrival times of acoustic solitons at the QW center. b) - e) Measured (red, solid line) and calculated (black, short dash) reflectivity spectra for $I_0 = 9.2$ mJ/cm^2 at specified times. Arrows in b) and c) indicate the shifted spectral lines due to acoustic solitons. Blue, long dashed lines are unperturbed spectra.

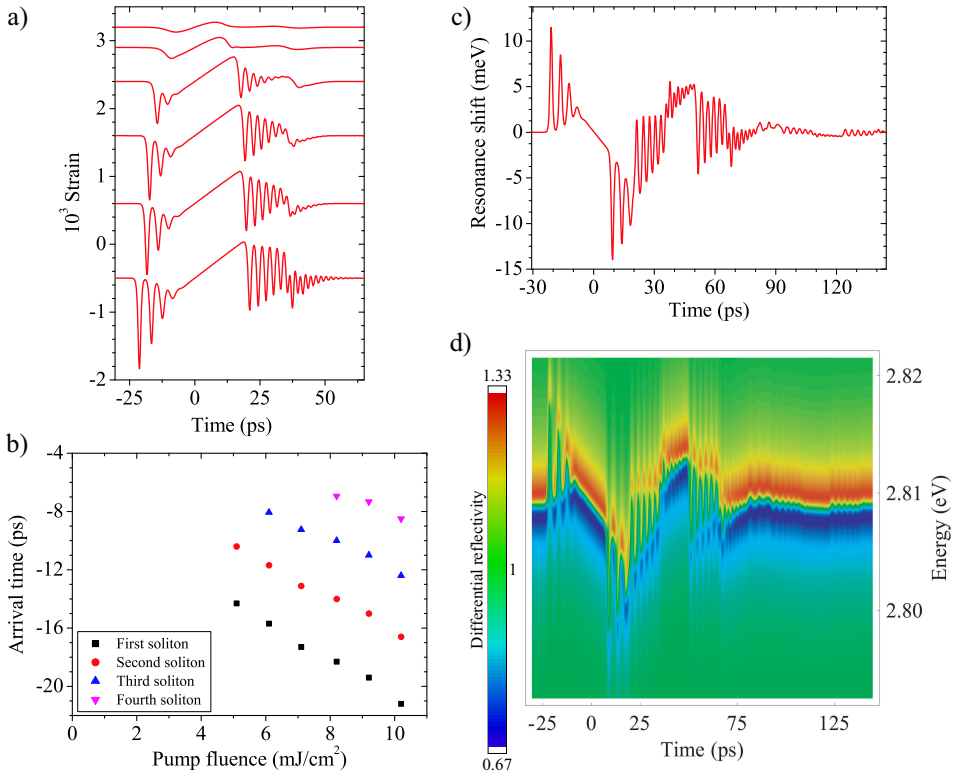

Figure 6: Intermediate simulation results (Fig. VI.4, p. 111)
a) Soliton propagation for the fluences depicted in Fig. VI.2. b) Arrival times for solitons, as found in calculations. c) QW resonance energy shift for a pump fluence of $I_0 = 10.2$ mJ/cm^2. d) Calculated contour plots given the resonance shift in c), and exciton lifetime $T_e = 0$.